Searches for Diboson New Physics and the L1Calo Software Development with the ATLAS Detector

Chiao-Ying Lin
of Peterhouse

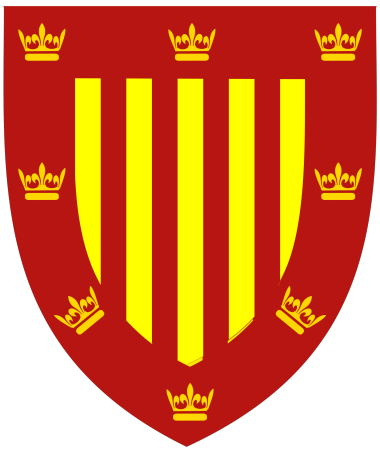

A thesis submitted to the University of Cambridge
for the degree of Doctor of Philosophy
Aug 2019

Declaration

This thesis is the result of my own work, except where explicit reference is made to the work of others, and has not been submitted for another qualification to this or any other university. This thesis does not exceed the word limit for the respective Degree Committee.

Chiao-Ying Lin

Abstract

The Standard Model has been a successful theory in describing the behaviour of fundamental particles, but there are still problems remaining unsolved. New theoretical models are therefore proposed to answer those questions with either new interactions or new particles. This thesis is presenting the searches for new physics with diboson signatures in these two ways from LHC $\sqrt{s} = 13\ TeV$ collisions with the ATLAS detector with the data collected in 2015 and 2016 corresponding to an integrated luminosity of 36.1 fb^{-1}. The searching strategy was performed with the Monte Carlo simulation for the SM background modelling and a data-driven method for the multijet background estimation. The final result was interpreted by a comparison between background modelling and data by a CLs method. For the resonance search, no new particle was discovered, and mass limits are therefore set on the new particles from models taken as the interpretation benchmarks. For the study on new interactions in the signatures of vector boson scattering, the first measurement of this process with the semileptonic decay was given with a significance of 2.7σ in reasonable agreement with the SM prediction

Both the LHC and ATLAS detector are now going through the upgrades for operations in 2021 with the $\sqrt{s} = 14\ TeV$ collisions. The ATLAS hardware calorimeter trigger is part of the upgrade project for the implementation of three new object processors: eFex, jFex, and gFex. This thesis will also present the construction of simulation system along with the expected performance of proposed object reconstruction algorithms for this new infrastructure.

Acknowledgements

The three and half years of PhD has been a wonderful adventure, and here is to present my appreciation for the people who are part of my journey.

Firstly, I want to thank my supervisor, Christopher Lester. The whole work of my PhD will not be possible without his support and help. And, I also want to show my gratitude to my college, Peterhouse, for funding my PhD and enriching my life out of research.

Then, I would like to thank Takuya Nobe, Viviana Cavaliere, and Lailin Xu as the convenors for the analysis works I was involved in. Those tasks are complicated like a maze, and they provide the guidance to show where is the way to go to have the final results. I would also like to thank Ben Carlson for all my L1Calo works, because I cannot keep working on the L1Calo upgrade project without his support. I also want to present my appreciation to John Chapman, John Hill, and Will Buttinger for all the helps on the technical problems I encountered when dealing with varied software tools.

For my social life during PhD, I am glad to be part of the friendly Cambridge HEP group, and I want to thank everyone in the group for the sweet tea time and nice chats. Especially, I want to thank James Cowley, Alison Tully, Ben Brunt, Jonathan Rostén, Holly Pacey, and Herschel Chawdhry for the company. They have made the research work not so intense, as I can always have fun with those people. I also want to say thank you to the Cambridge Taiwanese Society, especially Cheng-Tai Lee, because this is where I can still keep the connection to where I am from even though I am thousands of miles away from home. Most importantly, I can get rid of the stress by complaining in my mother tongue with those people.

For the last part of this list, I would like to thank my family for supporting me to be away for the pursuit of this degree.

Contents

"We are just an advanced breed of monkeys on a minor planet of a very average star. But we can understand the Universe. That makes us something very special."

— Stephen Hawking

Chapter 1.

Introduction and Motivation

"We can't focus on what's going wrong, there's always a way to turn things around."

— Joy, Inside Out

Particle physics is the subject to study the fundamental structure of the universe. It is now based on the theory called the "Standard Model" (SM). It interprets the universe as the composition of tiny particles interacting with each other by the exchange of force carriers (another type of particle). In July 2012, the discovery of Higgs boson made by the ATLAS and CMS collaborations [1, 2] completed SM 50 years after being predicted for the existence. By now, it has been deemed as one of the most successful theories in modern physics.

However, there are still some conflicts between the SM and factual results. For example, in the SM, neutrinos are supposed to be massless, but the discovery of neutrino oscillation support the fact that neutrinos are massive, and the SM cannot explain it. New theories are proposed in order to resolve those conflicts, and they indicate the existence of some new particles or the deviation from SM predictions. This thesis is dedicated to the work in search for this kind of new physics.

1.1. Standard Model [3, 4]

The SM is a quantum field theory (QFT). In the QFT, the universe is filled with different fields, and all fundamental particles (particles without further substructure) are the forms of quantized fields. They make up the matters and also mediate interactions between them, which is the foundation how this universe operates. Those fundamental particles could be classified into two types: fermions and bosons. Fermions are the matter builders, while bosons are the force carriers exchanged between particles (for both fermions and bosons).

Fermions

Fermions are quantized from fermionic fields following Dirac-Fermi statistics with half integer spin number, $\pm\frac{1}{2}$. Under the statistic characteristics, fermions exclude each other with the same quantum status in a bound state, which makes them different from bosons.

All fermions have their antiparticles which have opposite charge and chirality. Those fermions are called "Dirac Fermions". They can be presented as Weyl spinors of four components composed of one left-handed spinor and one right handed spinor following the Dirac equation. However, neutrinos, a sub-specie of fermions, have no anti-partner with opposite chirality found[1], so they are now taken as candidates of "Majorana Fermions": they are their own antiparticle following the Majorana euqation. They could be presented as Majorana spinors in Majorana equation.

Dirac Equation: $i\hbar\gamma^\mu\partial_\mu\psi - mc\psi = 0$

Majorana Equation: $i\hbar\gamma^\mu\partial_\mu\psi - mc\psi_c = 0$

ψ is the fermion field with charge conjugate ψ_c, and γ^μ is the gamma matrix and

[1] Due to being neutral, although neutrinos and anti-neutrinos were discovered, neutrinos (anti-neutrinos) only have the left-handed (right-handed) chirality.

m is the particle mass.

Fermions can then be further categorized into two types, quarks and leptons, by the interactions they participate in. Quarks are the only particles involved in the strong interaction, so they cannot exist alone, and, instead, they are always in bound state with two or more quarks.

Quarks have three generations and six flavours. In each generation are quarks with different charges: $\frac{-1}{3}$e and $\frac{2}{3}$e with e as the electric charged carried by electrons. The first generation are the lightest: up and down. Strange and charm are in the second generation. The third generation has bottom and top with highest mass. Quarks change their flvaours via the weak interaction, and the couplings between flavours is described by the CKM matrix which is shown in Fig.1.1. A stronger coupling between two quarks indicates a higher possibility that the heavier quark would decay to the lighter one.

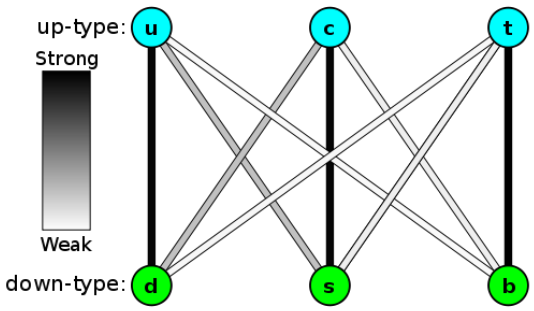

Figure 1.1.: The coupling strengths between quarks are determined by CKM matrix taken from [5]

Similar to quarks, leptons also have 3 generations and 6 flavours. In each generation, there is one neutral neutrino and corresponding charged particle with charge -1. The three generations are electrons, muons and taus with their neutrino partners. The flavour change is via the weak interactions which has one charged lepton with its partner neutrino and a W boson participating in the process. The neutrinos could

also change their own flavours via neutrino oscillation described by the PMNS matrix without the company of other particles. Leptons participate in weak interaction, quantum electrodynamics(except for neutral neutrinos) and gravity.

Interaction and Bosons

Under the SM, the interactions between particles are induced by gauge fields which could be quantised into gauge bosons. Different from fermions, those bosons follow Bose-Einstein statistics with their spin as integer numbers, which means more than one boson is allowed to occupy a single quantum state in a bound state. They mediate interactions between particles including themselves.

Although there are four fundamental forces in the universe, only three of them are in the SM, because they are quantizable: electromagnetic, weak and strong interactions. The challenge of quantizing gravity is still not achieved in the modern physics. Each interaction has a corresponding term in the SM Lagrangian.

The electromagnetic interaction is the best known among the four interactions. It is explained by quantum electrodynamics in the SM. The interaction is induced by electromagnetic field which could be seen as the interaction between photons and charged particles, under which the electric charges are conserved as an invariance of $U(1)$ symmetry. In electromagnetic interactions, photons don't interact with neutral particles at the leading order [2]. The coupling constant (a number that determines the strength of the force exerted in an interaction) in the interaction is:

$$\alpha_{EM} = \frac{e^2}{4\pi\epsilon_0\hbar c} = \frac{1}{137.036...} \tag{1.1}$$

with e as electric charge of electron, $\hbar$ as reduced Plank constant and c, the speed of

[2] With a loop diagram, it can still be achieved by exchanging charged fermions between photons

light. Its part in the SM Lagrange could be written as:

$$\mathcal{L} = \bar{\psi}(i\gamma^{\mu}D_{\mu})\psi - F^{\mu\nu}F_{\mu\nu} \tag{1.2}$$

with ψ as the Wyle spinor of spin, $\pm\frac{1}{2}$, and $D_{\mu} = \partial_{\mu} + ieA_{\mu} + ieB_{\mu}$ representing the gauge covariant derivative with A_{μ} as the field induced by the particle itself and B_{μ} as the field from external source. In the equation, $F_{\mu\nu}$ is the electromagnetic field tensor.

All the left-handed particles participate in the weak interaction. It is mediated by three different bosons: the W^{+}, W^{-} and Z^{0} bosons. They are massive gauge bosons which obtain their mass via the electroweak symmetry breaking. The flavour change of a particle is through the weak interaction mediated by W bosons which would also involve the change of electric charge (the neutrino oscillation is an exception, as the neutrinos change their flavour without the involvement of W bosons), while Z boson is involved in the neutral current interactions within which both the electric charges and particle flavours are conserved. In the weak interaction, a quantity, weak isospin, is conserved under $SU_L(2)$ symmetry. Its definition is similar to the spin numbers of a pair of electrons in the same orbital. For two fermions in the same generations, they could be grouped into a weak isospin doublet with $I_3 = \pm\frac{1}{2}$. As right-handed fermions do not participate in weak interaction, their weak isospin is 0. The weak isospins of fermions are showed in Table.1.1.

Table 1.1.: Weak Isospin of Elementary fermions

1st Generation	I_3	2nd Generation	I_3	3rd Generation	I_3
e^{-}	$-\frac{1}{2}$	μ^{-}	$-\frac{1}{2}$	τ	$-\frac{1}{2}$
ν_e	$\frac{1}{2}$	ν_{μ}	$\frac{1}{2}$	ν_{τ}	$\frac{1}{2}$
u	$\frac{1}{2}$	c	$\frac{1}{2}$	t	$\frac{1}{2}$
d	$-\frac{1}{2}$	s	$-\frac{1}{2}$	b	$-\frac{1}{2}$

The coupling constant for weak interaction is defined as:

$$\alpha_W = \frac{g_W}{4\pi\hbar c} \approx \frac{1}{29} \tag{1.3}$$

with g_W as the W weak charge strength. In terms of the interactions via Z boson, it is substituted by Z weak charge, g_Z. A unification between the weak and electromagnetic interactions is achieved with another new parameter called electroweak hypercharge defined as $Y_w = 2(Q - I_3)$ where I_3 is the isospin and Q is the electric charge under $SU_L(2) \times U(1)$ symmetry in the scale of high energy. In the SM, the symmetry is spontaneously broken by the Higgs field to give particles mass. It will be discussed in the next section.

Only quarks are involved in the strong interaction which is described by quantum chromodynamics (QCD). The conserved quantity in the interaction is the colour charge, with gluons as the force carrier boson under $SU(3)$ symmetry. There are three different colours: red, blue and green along with their anti-colour partners. Similar to the colour principle of light, the colour would be neutral (white) when the three colours are mixed together or with their anti-colour, and it is the condition for a stable state in QCD. However, each quark is only allowed to carry one colour, and this is an unstable state. It needs to be bound with another quark(s) to stabilize the system, which is called colour confinement. In QCD, gluons have 8 types with different colour combinations:

$$(r\bar{b} + b\bar{r})/\sqrt{2}, \quad -i(r\bar{b} - b\bar{r})/\sqrt{2} \tag{1.4}$$

$$(r\bar{g} + g\bar{r})/\sqrt{2}, \quad -i(r\bar{g} - g\bar{r}/\sqrt{2}) \tag{1.5}$$

$$(b\bar{g} + g\bar{b})/\sqrt{2}, \quad -i(b\bar{g} - g\bar{b}/\sqrt{2}) \tag{1.6}$$

$$(r\bar{r} - b\bar{b})/\sqrt{2}, \quad (r\bar{r} + b\bar{b} - 2g\bar{g})/\sqrt{6} \tag{1.7}$$

with r, red charge, b, blue charge, and g, green charge.

Its part of the SM Lagrange is shown as:

$$\mathcal{L}_{QCD} = \bar{\psi}(i(\gamma^\mu D_\mu)_{ij} - m\delta_{ij})\psi_j - \frac{1}{4}G^a_{\mu\nu}G^{\mu\nu}_a \tag{1.8}$$

with

$$G^a_{\mu\nu} = \partial_\mu \mathcal{A}^a_\mu - \partial_\nu \mathcal{A}^a_\nu + g f^{abc} \mathcal{A}^b_\mu \mathcal{A}^c_\nu \tag{1.9}$$

with ψ_i, the quark field in $SU(3)$ representation indexes of i,j, ..., $G^a_{\mu\nu}$, the gluon field also in $SU(3)$ representation indexed of a, b... from 1 to 8. f^{abc} is the structure constant, $\mathcal{A}_\mu$ is the spin 1 gluon field and $g = \sqrt{4\pi\alpha_s}$ is the QCD coupling strength with α_s as the fine structure constant. It should be noted that the coupling strength is not a constant in QCD but dependent on colour-charged particle energy due to the effect of the gluon self-interaction. It leads to the result that the interaction between colour-charged particles are strong, when they carry lower energy. In the other opposite way, the quarks would behave like free particles when they have higher energy, as the interaction strength is weak in this scenario, which is called "asymptotic freedom".

All the elementary particles with their basic properties are shown in Fig. 1.2. The 3 interactions with their conserved quantities makes the SM a gauge quantum field theory containing the internal symmetries of the unitary product group, $U(1) \times SU(2)_L \times SU(3)$.

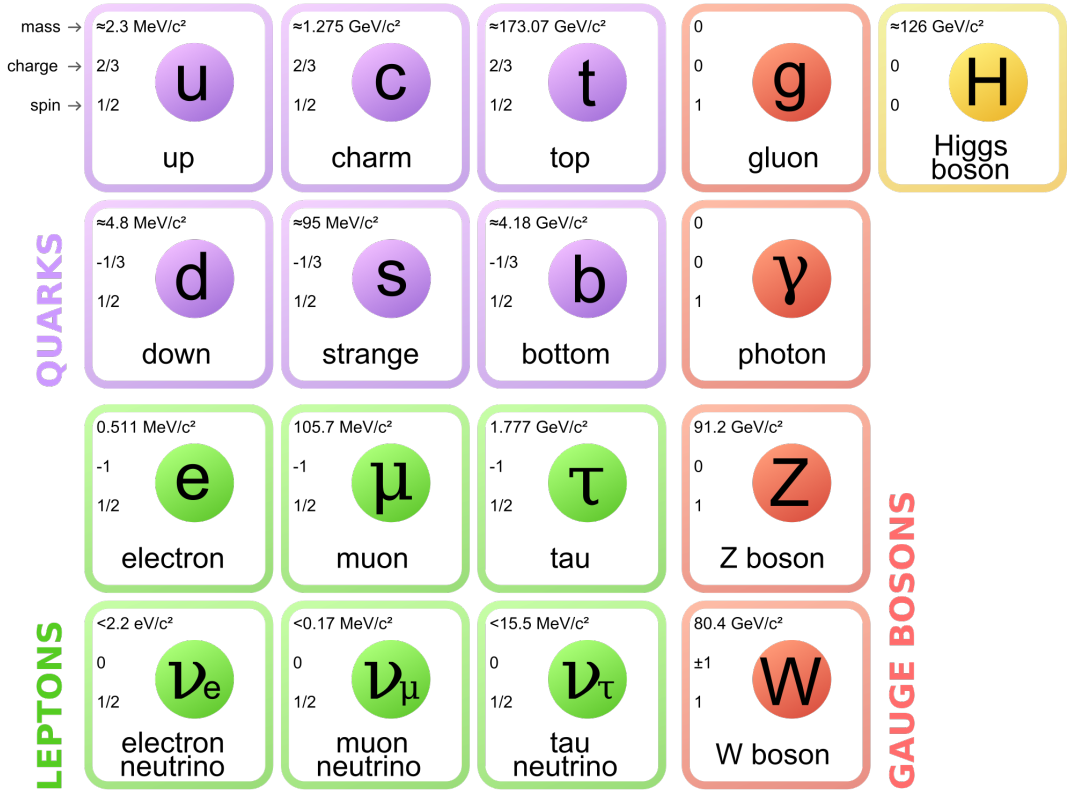

Figure 1.2.: Elementary particles and properties taken from [6]

1.2. Electroweak Symmetry Breaking

One particle in Fig. 1.2 is not mentioned yet: Higgs boson, the last discovered fundamental particle in the SM. It arises from quantised Higgs field which was proposed by three groups in early 1960s: Robert Brout and Francois Englert [7], Peter Higgs [8] as well as Gerald Guralnik, C. R. Hagen, and Tom Kibble [9]. It induces spontaneous electroweak symmetry breaking via the "Brout-Englert-Higgs mechanism". The Higgs boson discovery was announced on 4th July 2012 and confirmed on 14 March 2013 with spin 0 and + parity by the ATLAS and CMS collaborations.

The Higgs field is defined as the scalar gauge field in a complex scalar $SU(2)_L$ doublet.

$$\Phi = \begin{pmatrix} \phi^+ \\ \phi^0 \end{pmatrix} \tag{1.10}$$

with both ϕ^0 and ϕ^+ as arbitrary imaginary numbers representing the neutral and charged components. The potential for this field is then given as:

$$V(\Phi) = \mu^2|\Phi^\dagger\Phi| + \lambda(|\Phi^\dagger\Phi|)^2 \tag{1.11}$$

Here, μ and λ are arbitrary constants, and some choices of them could make the potential minimum at $\Phi = 0$. For this case, the shape of potential would be seen in Fig. 1.3 (this is a simplified plot, and the real one should be in 4 dimensions). In this potential, the symmetry is not broken with the minimal value at $\Phi = 0$.

In an alternative scenario for $\mu^2 < 0$, the potential shape becomes Fig. 1.4. The minimal expected value of the potential is not at 0 but at:

$$\langle\Phi\rangle = \sqrt{-\frac{\mu^2}{2\lambda}} \begin{pmatrix} 0 \\ 1 \end{pmatrix} \equiv \frac{v}{\sqrt{2}} \begin{pmatrix} 0 \\ 1 \end{pmatrix} \tag{1.12}$$

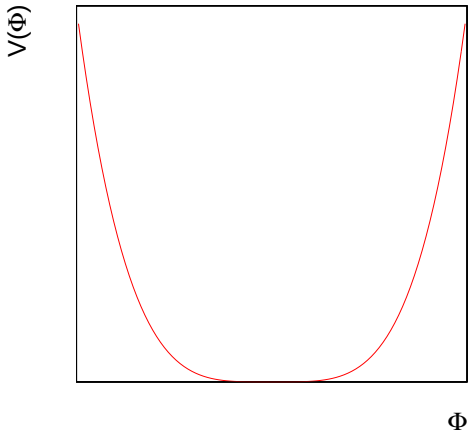

Figure 1.3.: Scalar potential with $\mu^2 > 0$

with ν as the "vacuum expected value" (VEV). It could be noted that the term of $\phi+$ is shifted to zero with a rotation on the phase space of (ϕ^+, ϕ^0). To maintain a stable state, particles are only allowed to stay in the lowest potential, the valley part. This makes the degree of freedom of the particles decrease from four to one and breaks the $SU_L(2) \times U(1)$ symmetry with isospin and hypercharge to $U(1)$ symmetry with electric charge. In high energy regime above the valley (excited state), electromagnetic

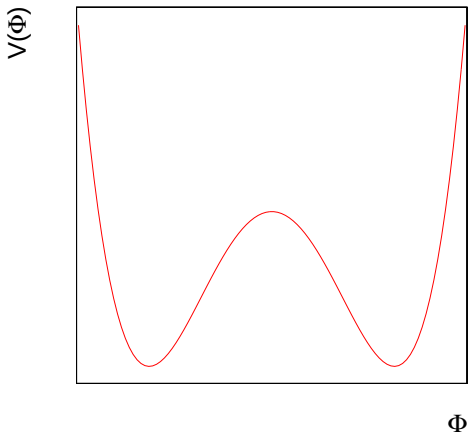

Figure 1.4.: Scalar potential with $\mu^2 < 0$

and weak interaction are mixed together to form three $SU_L(2)$ gauge bosons, W^i_μ with $\mu = 1, 2, 3$ and one $U(1)$ gauge boson, B_μ. They are not SM particles, but they could be taken as the excited form of SM gauge bosons. The Lagrangian for the interaction

between them and Higgs field is:

$$\mathcal{L} = (D^{\mu}\Phi)^{\dagger}(D_{\mu}\Phi) - V(\Phi) \tag{1.13}$$

with

$$D_{\mu} = \partial_{\mu} + i\frac{g}{2}\tau \cdot W_{\mu} + i\frac{g'}{2}B_{\mu}Y \tag{1.14}$$

g and g' are the coupling constants between the fields respectively, τ is the Pauli matrix and Y is the hypercharge.

A unitary gauge transformation on the Higgs field can remove Goldstone bosons[3] after the symmetry breaking. The Higgs field is thus shifted with the new gauge as:

$$\langle\Phi\rangle = \frac{v+h}{\sqrt{2}}\begin{pmatrix} 0 \\ 1 \end{pmatrix} \tag{1.15}$$

with h, the physical Higgs sector, as a real number.

After inserting the new Higgs field into and rearranging SM Lagrangian, the SM gauge bosons could be shown as:

$$W_{\mu}^{\pm} = \frac{1}{\sqrt{2}}(W_{\mu}^{1} \mp iW_{\mu}^{2}) \tag{1.16}$$

$$Z^{\mu} = \frac{-g'B_{\mu} + gW_{\mu}^{3}}{\sqrt{g^2 + g'^2}} \tag{1.17}$$

$$A^{\mu} = \frac{gB_{\mu} + g'W_{\mu}^{3}}{\sqrt{g'^2 + g^2}} \tag{1.18}$$

[3]Unitary gauge transformation is to select the fixed gauge which sets the Goldstone boson terms into 0

with particle masses:

$$M_W^2 = \frac{1}{4} g^2 v^2 \tag{1.19}$$

$$M_Z^2 = \frac{1}{4} (g^2 + g'^2) v^2 \tag{1.20}$$

$$M_A = 0 \tag{1.21}$$

From the expression, it turns out that Z boson and photon are both the mix of B and W^3 bosons with different phases which could be shown as:

$$\begin{bmatrix} A \\ Z \end{bmatrix} = \begin{bmatrix} \cos\theta_W & \sin\theta_W \\ -\sin\theta_W & \cos\theta_W \end{bmatrix} \begin{bmatrix} B \\ W^3 \end{bmatrix} \tag{1.22}$$

With $\cos\theta_W = \frac{g}{\sqrt{g^2+g'^2}}$ and $\sin\theta_W = \frac{g'}{\sqrt{g^2+g'^2}}$. Here, θ_W is called the weak mixing angle or Weinberg angle. By this, the electroweak parameter, ρ, is defined:

$$\rho = \frac{m_W}{m_Z \cos\theta_W} \tag{1.23}$$

with the comparison between Eq. 1.2 and Eq. 1.14 with Eq. 1.22, the electric charge could be defined as:

$$e = g \sin\theta_W = g' \cos\theta_W \tag{1.24}$$

This relation gives the access to a precision measurement of ρ, which is now given 1.0008, a litte deviation from expectation of 1 in the SM because of the loop diagram correction.

In terms of degrees of freedom, before symmetry breaking, it comes with four degrees

from Higgs complex scalar doublet, six degrees from $SU(2)_L$ gauge fields, W_i, and two degrees from $U(1)_Y$ gauge field, B, which makes 12 degrees in total for all the massless fields. After symmetry breaking, the number of degrees of freedom does not reduce with nine degrees from three massive vector boson, Z and $W_\pm$, two degrees from massless photon, A, and one degree from physical real scalar field, h.

Not only granting mass to bosons, the interaction between fermions and Higgs boson is also part of the Brout-Englert-Higgs Mechanism. The left-handed fermionic field is defined as a doublet:

$$Q_L = \begin{pmatrix} u_L \\ d_L \end{pmatrix} \tag{1.25}$$

For right-handed ferions, the representation would be in a singlet, u_R and d_R, due to the fact that they have different transformation under the $SU(2) \times U(1)$ gauge symmetry.

Their interaction with Higgs field are through Yukawa couplings[4]

$$\mathcal{L} = -\lambda \bar{Q}_L \Phi d_R + h.c. \tag{1.26}$$

with λ as the coupling constant. The Lagrangian can lead to the fermionic mass as:

$$m_d = \frac{\lambda v}{\sqrt{2}} \tag{1.27}$$

This mechanism would change the chirality of a fermion, when it is giving the mass. However, no right-handed neutrino and left-handed anti-neutrino were measured, which leaves it as one of the unsolved problem in SM. (More details are given in next section.)

[4]Yukawa coupling means the couplings betweent fermionic and bosonic fields

1.3. Unsolved Problems in SM

With SM, we have understood most behaviours of the fundamental particles. However, it still failed explaining some experimental results. The following is part of them the work in the thesis is trying to answer.

Higgs Mass Naturalness [10]

In quantum field theory, all the experimental observables could be presented as:

$$O = a_1 + a_2 + a_3 + ... \tag{1.28}$$

where O corresponds to the physical observables like the invariant mass of particles, and $a_n^{'}s$ are the independent contributions to the observables. For naturalness of the observable, it is expected that $a_n \leq O$. For any case that $a_n >> 0$, the further fine-tuning needs to be introduced for proper correction on theory, and it also indicates the defect in the theory.

The form for the observable of Higgs mass is:

$$m_h^2 = 2\mu^2 + \delta m_h^2 \tag{1.29}$$

where δm_h^2 for the contribution from coupling to top quark is:

$$\delta m_h^2 \simeq \frac{3}{4\pi^2}\left(\lambda_t^2 + \frac{g^2}{4} + \frac{g^2}{8\cos^2\theta_w} + \lambda\right)\Lambda \tag{1.30}$$

where λ_t is the top-quark Yukawa coupling, and Λ is the energy cut-off to divergent loop integrals. With the observed Higgs boson mass at 125 GeV, Λ is estimated to be around 1 TeV, and that is also roughly the limit to keep the naturalness of this observable.

However, many models beyond the SM predict the existence of particles at the TeV

scale, which means the naturalness would be broken in the scenario. For this reason, a correction to Brout-Englert-Higgs Mechanism is needed, or there is possibly a heavier Higgs boson to complete the theory.

The Hierarchy Problem and Quantum Gravity [11]

The hierarchy problem is defined in two ways: the unreasonable discrepancy between theoretical prediction and experimental result, or two comparable parameters. Higgs mass is one instance for the first definition. For the second one, it is generally referred to the gap between coupling strengths of weak interaction and gravity in the order of 10^{16}.

When a hierarchy problem occurs, the "so-called" fine-tuning is introduced to correct the discrepancy between two parameters. However, the fine-tunning could only be performed with enough understanding on the quantum effect of related parameters, and quantum gravity is still an unsolved problem. In the case, no solution is available.

Neutrino Mass

Brout-Englert-Higgs Mechanism is the process to make particles massive within which the chirality of fermions would be changed. This implies that massive fermions of right-handed and left-handed chirality shall both exist, but no evidence is found for right handed neutrinos (or left-handed anti-neutrinos). Therefore, they are supposed be massless with SM. However, with the measurement of neutrino oscillation [12] induced by the difference of neutrino mass and flavour eigenstates, they are practically massive particles. The conflict between SM and experiment still remains unsolved.

1.4. Thesis Overview

To solve the problems in SM, analyses are performed in two ways, direct and indirect searches which are corresponding to two different signatures in physics: new particles

or new interactions. The thesis will present how the experiment is set up to see the signatures of new physics in Chapter 2, and the following three chapters are dedicated to show the analyses of these two types of signatures with 2015+2016 data corresponding to the integrated luminosity of 36.1 fb^{-1} for which I made the contributions to the multijet background estimation, study on trigger performance, data background comparison, analysis framework development, and the statistical interpretation. The last chapter is for the simulation of the upgrade of the LHC and ATLAS detector which will start to operate in 2021 for which I made the contribution to the construction of the simulation framework and also the study for the preliminary missing transverse energy (E_T^{miss}, the definition will be shown later) trigger.

Chapter 2.

Experimental Setup

"Adventure is out there!"

— Ellie, Up

The accelerators are utilised to recreate the high energy environment rich in new physics like the hot early universe. In this thesis, Large Hadron Collider (LHC) is used for this purpose, and the ATLAS detector (A Toroidal LHC ApparatuS) is taken to probe the potential signatures of new physics.

2.1. Large Hadron Collider [13]

LHC is a circular collider with a circumference of 27 km for hadrons (it could be either protons or lead ions) hosted by CERN at the border of France and Switzerland in the depth varied between 50m to 175m. It accelerates protons (lead ions) to the speed of Lorentz Factor of 10540 (32) and smashes them together to recreate the "hot" environment right after the big bang which corresponds to 6.5 TeV (2.5 TeV) energy. However, before a proton reaches the targeted energy, it has a long way to go.

Ionization

At the beginning, hydrogen is released from a tank and ionised into the state of proton-electron plasma. It then experiences the electric field to separate electrons as well as protons like Fig. 2.1. The protons are then sent into the LINAC2, a linear accelerator. After reaching the energy of 50 MeV, the protons are fed into circular accelerators in the order of the PSB, PS and SPS to further increase the energy until they reach 450 GeV (Fig. 2.2). By this stage, the protons are ready to be injected into the LHC.

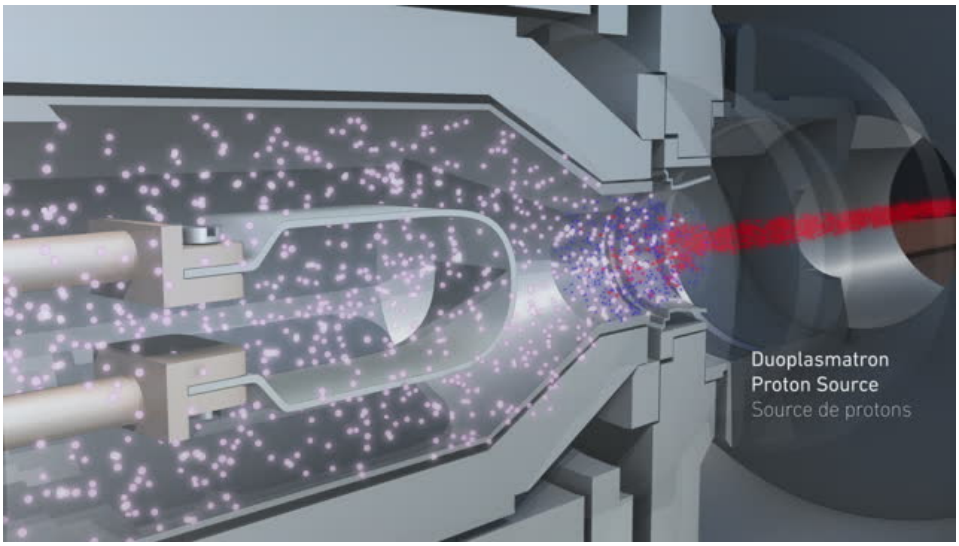

Figure 2.1.: The hydrogen plasma is separated into electrons (blue) and protons (red), and the protons are injected into LINAC2. This image is taken from [14].

Magnets

While accelerating the protons, they would repel each other due to the same electric charge they are carrying, so the quadrupole magnets are implemented in LHC to focus them by the effect of magnetic lens. In addition to the quadrupole magnets, the other magnet system in LHC is the superconducting dipole magnets working to bend the protons to keep them staying in the circular pipe of the LHC. For the ATLAS operation from 2015 to 2018, the dipole system provide a 8.3 T magnetic field to bend the proton beam at an energy of 6.5 TeV.

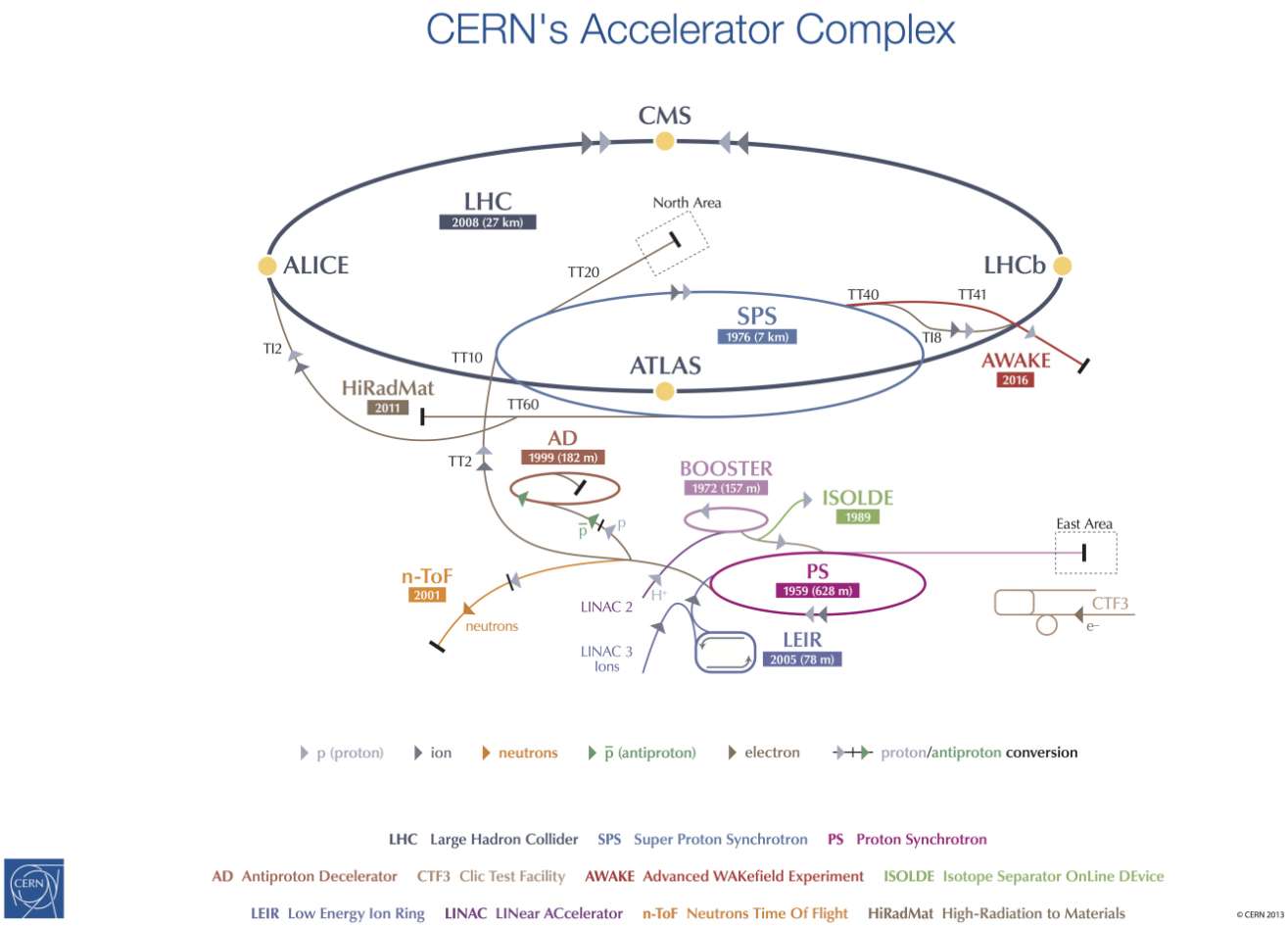

Figure 2.2.: Before the LHC, protons go through several boosting facilities. This material is taken from [15]

Radiofrequency Cavity [16]

The "radiofrequency cavity" (RF cavity) is in charge of the acceleration. Protons would experience electric field when going through RF cavities which are installed in the LHC like beads along a string. The field is induced by an alternating current of a frequency of 400 MHz and resonates as a standing wave in the cavity. This wave decelerates faster protons and accelerates slower ones, which makes the protons squeeze into bunches as demonstrated in Fig. 2.3., until they reach the targeted energy. When the beams are kept in the same speed, they are called "stable beams" and ready for the collision.

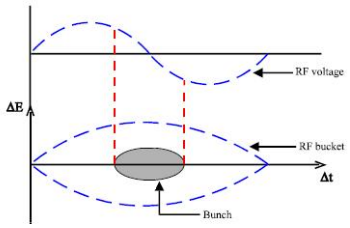

Figure 2.3.: The protons are formed into a bunch in the EM wave. This image is taken from [17]

Each LHC beam could have up to 3564 bunches with $N \approx 10^{12}$ protons in each bunch for a spacing of 25 ns, but not all of them are filled. For the LHC 2018 operation, the "filling scheme" has around 1000-2500 bunches filled, while the remaining ones are left empty (filling scheme most of time is constrained due to technical issues). A series of continuous bunches is called a "bunch train". This scheme would then be used to configure the trigger and data acquisition system for the active window of detector operation.

Collision

The LHC has two beams going in opposite directions with the same configuration (bunch structure, luminosity and energy), and the two beams cross at locations where four detectors are sited: ALICE [18], ATLAS [19], CMS [20], and LHCb [21]. Before stable beams, the two beams pass each other where they are supposed to cross. When both of the beams are ready, the two beams are slightly shifted to target on each other for the collisions. The crossing angle between the two beams plays an important role in detector performance. It should not be too big, or it would have an impact on physical object reconstruction (see section. 2.3) which assumed a zero crossing angle. However, it also should not be too small, or the two beams would interfere with each other. The crossing angle is kept optimized during LHC operation even when the detectors are taking data for physics.

When collisions happen, the two crossed bunches usually have more than one pair of interacting protons. In physics, only the one leaving signatures with the highest energy

sum gets the attention for study, while the other ones are background contributions called "pile-up events". For the ATLAS operation in 2017, the measured pile-up events could number up to 70 per bunch crossing, and it is now a major challenge of analyses to suppress this type of background.

The collisions are then taken as the “instantaneous luminosity” for the measurement on the amount of data:

$$\mathcal{L}_{inst} = \frac{N}{\Delta t \times S^{eff}} \tag{2.1}$$

with N as the number of collisions and S^{eff} as the effective area of the LHC beams for the collisions [1] in a time duration, Δt. Then, the total collected data with time is presented as:

$$\mathcal{L} = \int \mathcal{L}_{inst} dt \tag{2.2}$$

2.2. ATLAS Detector

The ATLAS detector [19] is designed as a general purpose detector[2] aiming for most high energy physics topics in the energy scale LHC provides like SM precision measurements and searches for new physics.

The ATLAS detector is in a cylinder shape with dimensions of 44 m in length and 25 m in diameter. Its inner structure is like an onion with multiple layers from the inner most tracking system to the outer part of muon spectrometer functioning to capture different physical objects which will be explained in the following. In the purpose of measuring the particle mass and charge, ATLAS also has two magnetic systems (a solenoid and a toroid) located outside inner tracking system and muon spectrometer.

[1] $S^{eff} = 4 \times \pi \times (1.6 \times 10^{-5})^2 [m^2]$ for the LHC configuration.

[2] The other general purpose detector hosted by LHC is Compact Muon Solenoid (CMS). The discovery of any new physics shall be verified by both the ATLAS and CMS collaborations

The diagram of the whole ATLAS detector is shown in Fig. 2.4 with the two minimum bias trigger scintillators (MBTS) at both ends.

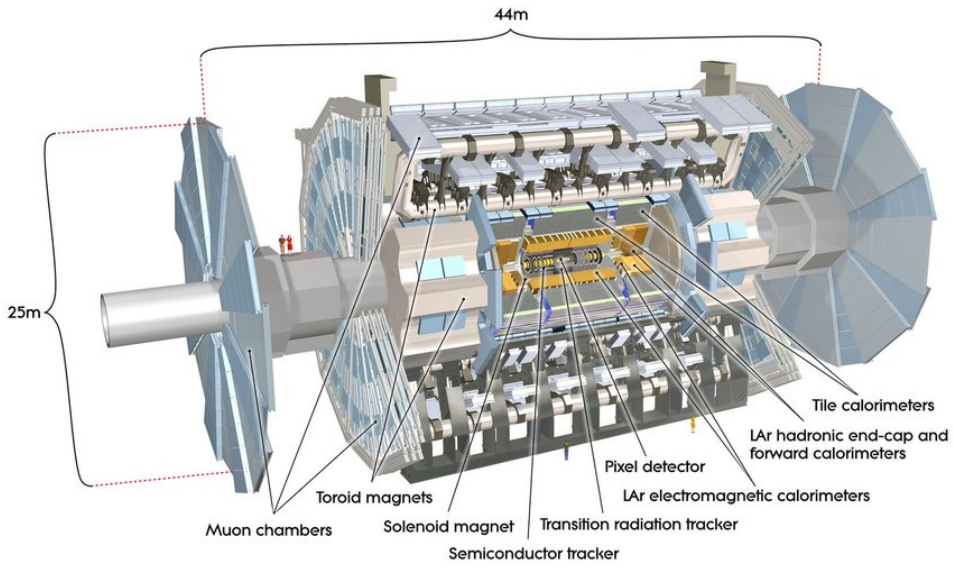

Figure 2.4.: The diagram of the ATLAS detector taken from [22]

To define the object positions inside this massive and complicated giant, the Cartesian coordinate is applied as shown in Fig. 2.5. The x-axis is defined as pointing to the centre of the LHC, while the z-axis is the cylinder axis toward the direction of solenoid magnetic field. Then, the y-axis could be found with the right-hand rule. However, this Cartesian coordinate is not convenient in a cylinder, so, instead, an alternative coordinate system (θ: angle related to z-axis, ϕ: angle related to x-axis) is adopted in terms of physics. However, in the experimental particle physics, θ is interpreted into pseudorapidity, η:

$$\eta = -\ln \tan \frac{\theta}{2} \tag{2.3}$$

because the particle production is approximately constant as a function of η. And, the differences in η between particles is also a Lorentz invariance, so the relative kinematic variables like $\Delta\eta$ are not dependent on the particles' energy. With this definition, the variation of η is different from θ, which can be seen in Fig. 2.6. This quantity is

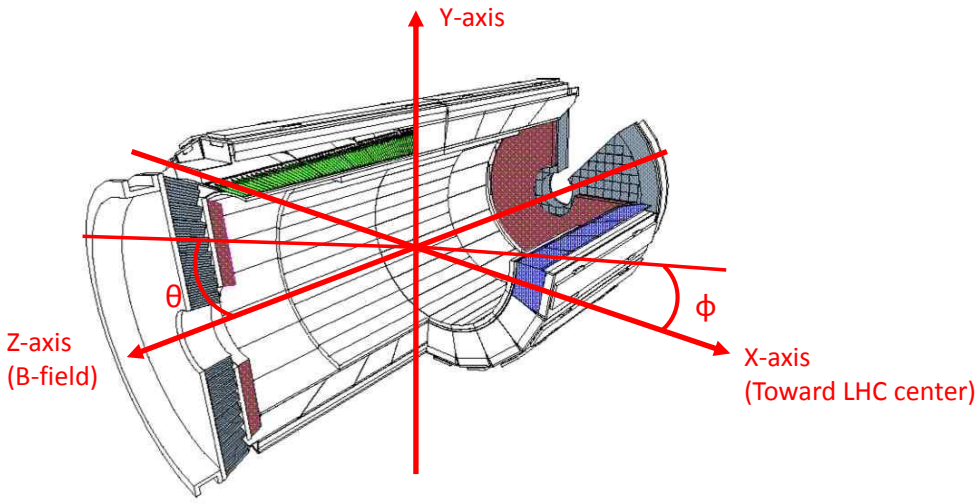

Figure 2.5.: The coordinate system used in the ATLAS detector

important, because the distance between two particles in the detector is defined as:

$$\Delta R = \sqrt{\Delta\eta^2 + \Delta\phi^2} \tag{2.4}$$

For the same ΔR, the separation would be actually larger in the high η region especially at $|\eta| > 3.2$ ("endcap" and "forward" regions).

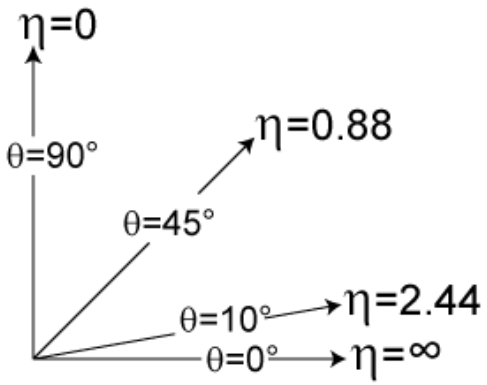

Figure 2.6.: The Psedorapidity varied with θ from [23]

2.2.1. Inner Detector (ID) [24]

The design of a general detector usually consists of two types of system: "trackers" and "calorimeters". The tracker is used to record the charged particle trajectories inside the detector with the lowest disturbance on their energy, while calorimeters trap the particles to measure their total energy sum, E.

The ATLAS Inner Detector is designed as a "tracker", so it is used to record the tracks of particles from the collisions. It stands at the inner most part of the detector and spans from 3 cm to 108 cm in radius with several layers from three subsystems which are the pixel detector (in the following content, it might be just written as "pixel"), semiconductor tracker (SCT) and transition radiation tracker (TRT) as shown in Fig. 2.7.

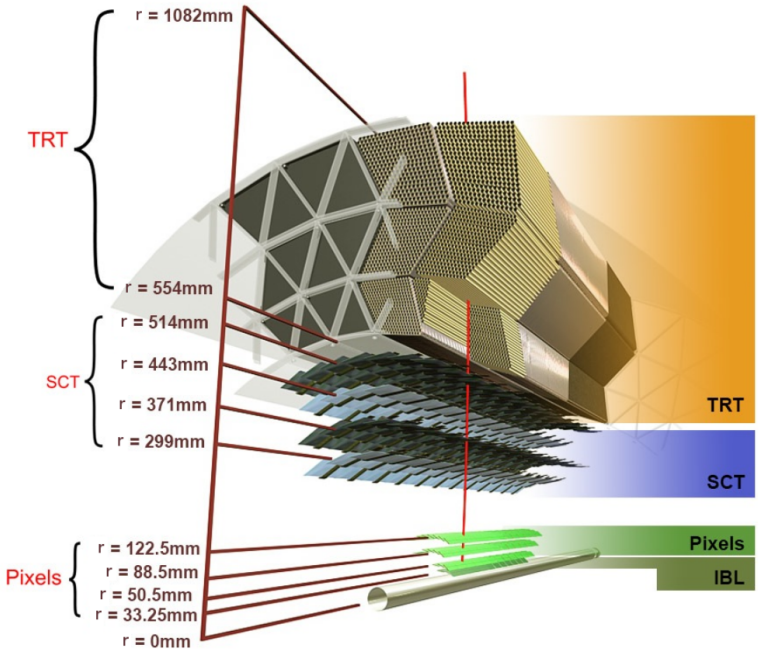

Figure 2.7.: The diagram for the ATLAS inner detector from [25]

Each layer has cells of well-defined granularity. When particles are passing through the Inner Detector, they leave "a hit" per cell on each layer. The tracks are then defined

as the link through hits on each layer which are curved lines due to the existence of magnetic field from solenoid, so the curvature of a track is taken to evaluate the particle momentum and charge. After all tracks are reconstructed, the vertices are then defined as where the tracks cross. The resolution of particle momentum projected on the transverse plane (x-y plane), transverse momentum (p_T), depends on the particle p_T and η, and it can be presented as:

$$\sigma_{p_T} = \sqrt{a^2 p_T^4 + b^2 p_T^2} \tag{2.5}$$

with a and b, the coefficients, depending on track quality and η. From MC simulation for the track with at lease seven hits (a track crossing all layers from pixel and SCT) within $0.25 < |\eta| < 0.5$, a and b are estimated to be 0.00034 GeV^{-1} and 0.0015 respectively.

Pixel [26]

The pixel detector is the innermost system of ATLAS, and it has the structure of three concentric barrels enclosed by three disks at each end, so all the particles coming out from the collision must pass through all the layers (giving three hits). It provides the best position resolution in the ATLAS detector with a granularity of 50 $\mu m \times 400$ μm for each cell in the $r\Delta\phi \times z$ plane with the coverage of $|\eta| < 2.5$ which is used to define the barrel region which has a spatial resolution of 14 $\mu m \times 115$ μm

In 2014, a new layer of pixel detector called insertable b-layer (IBL) [27] was installed at 3.3 cm to the beam pipe in addition to the original three layers. Its design is aiming to find the vertices of particles which decay near the primary vertex (the definition is in Sec. 2.3) like the b quarks, so it has an even better granularity of 50 $\mu m \times 250$ μm with a extended coverage to $|\eta| < 3$. The improved granularity also helps to reduce the uncertainty on impact parameter of collisions (the particle trajectory distance to the primary vertex).

Semiconductor Tracker

Outside the pixel detector is the semiconductor tracker with four layers in its barrel and nine disks at each end. The sensors are double sided, so when a particle passes through four layers, it leaves totally eight hits in the SCT which form four spacepoints. Different from the pixel detector which has one sensor on each module, the SCT modules have two strip sensors with the width of 80 μm which cross at an angle of 40 $mrad$ giving a spatial resolution of 17 $\mu m \times 580$ μm in the $r\Delta\phi \times \Delta z$ plane.

Transition Radiation Tracker

The last part of the inner detector is the TRT detector. It does not have a multiple layer structure as the pixel or SCT detectors but just a single thick layer stacked of straw drift tubes. Each straw has the diameter of 4 mm (with the drift time correction, the spatial resolution from each measurement is 130 μm) and is filled with the gas mixture of Xe, CO_2 and O_2. The gas mixture is used to optimize the absorption of transition radiation. (Due to the gas leaking problem found in the ATLAS operation from 2009 to 2012 [28], part of the gas was replaced by cheaper Ar-based gas.) When a charge particle passes through the gas, the emitted photon (transition radiation) induces a "charge avalanche". This detector allows to distinguish between electrons and charged pions (because light particles emit more transition radiation).

Magnets

The ATLAS detector has two superconducting magnet systems different from the CMS experiment with only one solenoid magnet. The inner one is the solenoid magnet located between the TRT detector and the calorimeter, while the toroid magnet is situated in the muon spectrometer system. The advantage of this design is to have the light material (solenoid) inside the detector for transparency, and the toroid still provides the magnetic field to further improve the resolution of momentum measurement [29] on the muons.

The solenoid magnet has a diameter of 2.56 m and length of 5.8 m. The magnetic field inside the solenoid is almost uniform of 2 T along the z-axis as shown in Fig. 2.8 to give the momentum and charge measurement in the Inner Detector.

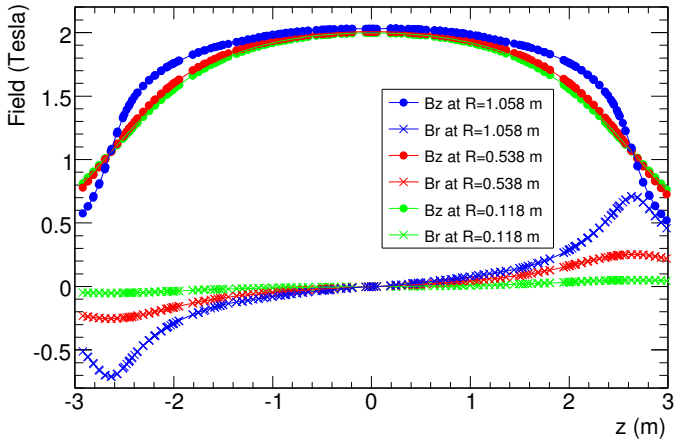

Figure 2.8.: The magnetic field inside the solenoid taken from [30]

The toroid magnet is composed of the barrel and endcap toroids, and both of them have eight coils providing the magnetic field varied between 2 T and 8 T in the muon spectrometer. The toroid magnet has the advantage that the particle trajectories in the transverse plane are always perpendicular to the magnetic field, so the momentum measurement is simplified. The toroid magnet is for the measurement of muon momentum in the muon spectrometer.

2.2.2. Calorimeter

Outside the inner detector is the calorimeter, an energy sampling system. In the ATLAS analyses, there is the need to distinguish the fundamental particles with their energy, so two systems of calorimeters are applied to trap particles with different interactions to materials: the electromagnetic calorimeter (ECAL) for electrons and photons as well as the hadronic calorimeter (HCAL) for the hadronic particles. Both ECAL and HCAL have the coverage up to $|\eta| < 4.9$. For the range of $|\eta| < 2.5$ in the barrel

region, two types of calorimeter, the liquid argon (LAr) and tile detectors, are used for the ECAL and HCAL, while in the endcap and forward regions is only the LAr detector. To fit into the cylinder shape of the ATLAS detector, the LAr calorimeters are accordion-shaped from the cross section side. The full diagram of the calorimeter system is presented in Fig. 2.9. The energy resolution for the calorimeter could be

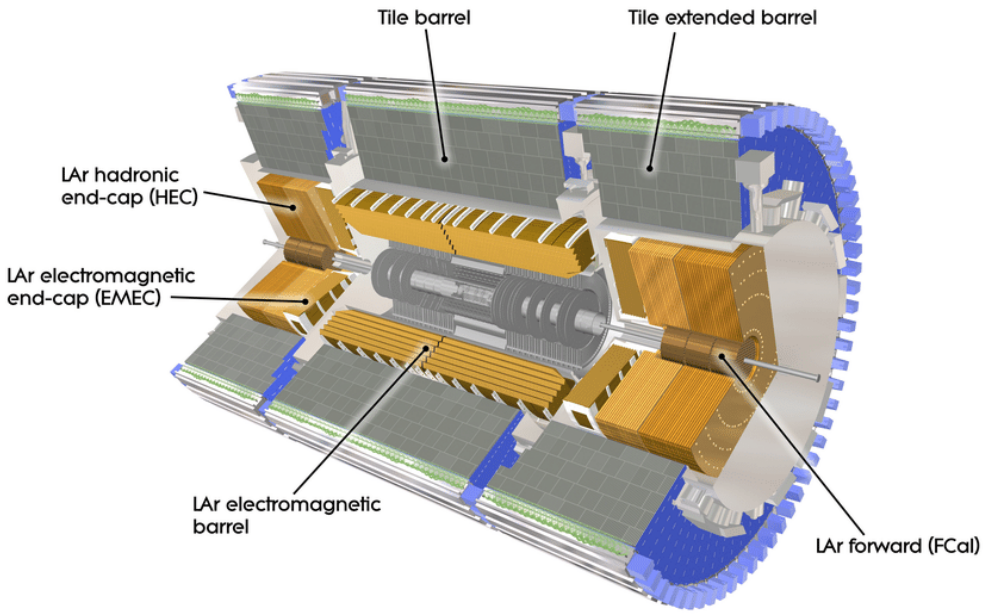

Figure 2.9.: The calorimeter system of the ATLAS detector from [**?**]

presented as:

$$\sigma(E) = \sqrt{a^2 + b^2 E + c^2 E^2} \tag{2.6}$$

where a, b, and c are the coefficients. The first term is due to the electronic noise (constant), and the second term is from the shower development of the Poisson fluctuation for the number of shower particles, while the third term is for the calorimeter non-uniformities (linear to the true shower energy). From the test beam data, the coefficients for the ECAL are 0.4 GeV, 0.1 $\sqrt{GeV}$ and 0.0017 for a, b, and c. In terms of the HCAL, the resolution is a bit worse with 1.6 GeV, 0.52 $\sqrt{GeV}$ and 0.03. The degraded resolution is partially due to the complexity of measurement on hadronic objects like the energy contribution from neutrinos or binding energy between partons.

Electromagnetic Calorimeter

In ATLAS, the ECAL is made up of the LAr detector [31] each module of which has one absorber and one electrode, and liquid argon is the medium between them. When a particle hits the absorber, it induces the shower, and the shower electrons ionize liquid argon atoms. All the electrons from the interactions would then be collected by the electrodes. The measured current is used to estimate the energy of the incoming particle. The process could be seen in Fig. 2.10.

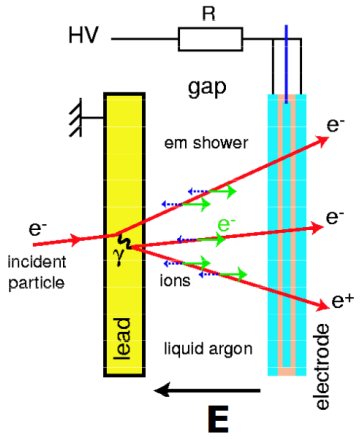

Figure 2.10.: The interaction between an electron and the LAr calorimeter taken from [32]

The barrel LAr detector has three sampling layers with different depth and granularity. An extra presampler (layer 0) was added for $|\eta| < 1.8$ which has no absorber but only a thin LAr sampler to recognize photons from π^0 decays. The best granularity is at the strip layer (layer 1) for 0.0031×0.1 ($\Delta\eta \times \Delta\phi$) [3], while the last layer is coarse for 0.05×0.025 in terms of $\Delta\eta \times \Delta\phi$. For the energy absorption, the depth is what matters most. The full depth of the three sampling layers could correspond to ~ 22 lead radiation lengths ($22X_0$) or 2 nuclear interaction length (2λ).[4] When the ECAL is

[3] the granularity for $\Delta\phi$ is a approximation, as it has to complete a circle of an irrational number.

[4] the radiation length is defined by the electron energy loss (the distance that an electron loses $(e-1)/e$ [e is the natural constant] energy), while the nuclear interaction length is defined as the mean distance before undergoing an inelastic nuclear interaction when a hadronic object is traveling though materials.

extended to the region of $2.5 < |\eta| < 3.2$, only the last two layers would remain, but they still have $18X_0$ in total.

Hadronic Calorimeter

Behind the LAr detector is the three-layer tile detector covering $|\eta| < 1.7$ with a crack[5] at $1.37 < |\eta| < 1.52$. It operates in the similar way to the LAr detector, but the absorber material is scintillator instead of lead used in the LAr detector. Each sensor of this system is coarser as compared to LAr ones with 0.1×0.1 ($\Delta\eta \times \Delta\phi$) for the first two layer and 0.1×0.2 at the third layer. To ensure the absorption of all the hadronic objects, the depth for all three tile layers corresponds to 8λ.

In the endcap region ($1.7 < |\eta| < 3.1$), another type of LAr detector with copper absorber is used as the HCAL. It contains four layers which have the same granularity for 0.1×0.1 ($\Delta\eta \times \Delta\phi$) in the region, $1.7 < |\eta| < 2.5$, and 0.2×0.2 in $2.5 < |\eta| < 3.1$

Forward Calorimeter [33]

The calorimeter is designed to have the widest coverage in the ATLAS detector, so the missing energy carried by invisible particles could be estimated by energy conservation within the detector. Therefore, a forward detector is installed at $3.1 < |\eta| < 4.9$, and it makes the calorimeter have the best coverage among the ATLAS subsystems.

The type of detector used here is the third type of LAr detector with tungsten absorber. It has three layers with the first one for ECAL and the last two for HCAL with the total depth of 10λ (ECAL+HCAL).

[5] The crack is for the supporting structure and output cables

2.2.3. Muon Spectrometer [34]

The outermost detector is the muon spectrometer (MS). Because of their large mass and lack of strong interactions, only muons could travel through the calorimeter and leave signatures here. The muon spectrometer is composed of four types of detectors: thin gap chamber (TGC), resistive plate chamber (RPC), monitored drift tubes (MDT), and cathode strip chamber (CSC) with the toroid magnet system.

In this subsystem, the MDT and CSC are the two detectors providing the tracking measurement with a three-layer structure. In the coverage of $|\eta| < 2.0$, all the three layers are composed of the MDT detectors, while the innermost layer is replaced by the CSC detectors in the extent of $2.0 < |\eta| < 2.7$ for the effectiveness of high particle density environment. The overall tracking measurement has the spatial resolution of $35\mu m$.

However, the precise tracking measurement of the MDT and CSC comes with the cost of a poor temporal resolution, so the RPC ($|\eta| < 1.05$) and TGC ($(1.05 < |\eta| < 2.7)$) are interspersed in tracking layers with the time resolution of 25 ns (with the consideration of uncertainty from cosmic muons). With the fast response, they are part of the ATLAS hardware trigger system. The overall detector performance is summarised in Tab. 2.1.

Table 2.1.: Muon Spectrometer Subdetector Performance

Type	Function	coverage	z/R resolution	$r\Delta\phi$ resolution	time resolution
MDT	tracking	$\|\eta\| < 2.7$	35 μm(z)	N/A	N/A
CSC	tracking	$2.0 < \|\eta\| < 2.7$	40 μm(R)	5 mm	7 ns
RPC	trigger	$\|\eta\| < 1.05$	10 mm(z)	10 mm	1.5 ns
TGC	trigger	$1.05 < \|\eta\| < 2.7$	$2-6$ mm(R)	$3-7$ mm	4 ns

2.2.4. Trigger System

The LHC has the collision rate at 40 MHz, which leads to the data rate over 60 TB per second. However, most of the events have no physical interest, because they are

just the products of low energy hadronic interactions. Therefore, the trigger system is developed to select events which are going to the storage.

For data-taking, the ATLAS trigger system has a two-level structure: the hardware-based L1 trigger (L1) and the software-based high level trigger (HLT). The L1 system is based on the front-end electronics with the logic of selection written by FPGAs. Its feature is to make a fast reconstruction of physical objects with a degraded resolution, and it delivers the events at the rate of 100 kHz (100k events per second). As the detector signatures from the calorimeter and MS are irrelevant to each other, they have their independent L1 trigger systems: L1Calo and L1MU. After the physical objects are reconstructed in the two systems, they are then sent to the L1Topo system for the estimation on the topological relation between them. The final trigger decision would eventually be made at the central trigger processor (CTP) by whether a event contains the objects with energy or topological parameters fulfilling the defined criteria. Afterwards, the detector signatures in the readout buffer will be further processed with a more complicated reconstruction algorithm to give the HLT trigger decision, and the output event rate is reduced to $\sim 5\,kHz$. The full trigger system is shown in Fig. 2.11.

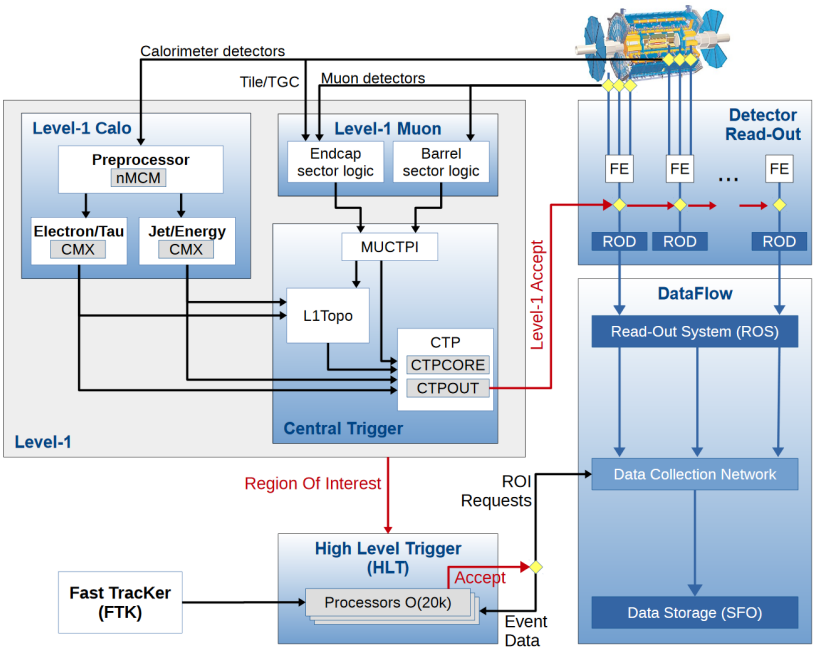

Figure 2.11.: The ATLAS trigger system from [35]

L1Calo

When the detector signatures are received from the calorimeter, they are firstly sent to the readout buffer and the L1Calo system. The first component in the L1Calo electronic system is the preprocessor where the signatures are processed into trigger towers with degraded granularity and sent to the processors for physical object reconstruction. Electrons, photons and taus are reconstructed with the trigger tower of $0.1 \times 0.1(\Delta\eta \times \Delta\phi)$ in the cluster processor (CP), while hadronic objects and missing transverse energy ($E_T^{missing}$)[6] are processed in jet energy processor (JEP) with a coarser granularity of 0.2×0.2.

L1MU

The L1MU system is taking the data from the RPC and CSC which have great time resolution as fast as 1.5 μs but with a poor spatial resolution. It receives signatures from the MS barrel and endcaps where they are processed respectively. To further suppress the rate contributed by fake muons, the L1 muons are reconstructed and matched to the hits from the TGC in the endcap ($1.05 < |\eta| < 2.7$).

HLT

When the trigger decision is made to accept an event, the regions of interest (ROI) with the original detector granularity are passed to the HLT. The HLT runs on a CPU farm where the more complicated algorithms are deployed to reconstruct the physical objects. Due to the finer granularity and longer latency, it provides better precision on both energy and spatial resolution. When the events fulfil the HLT criteria, they are then sent to storage.

[6] As the protons only have the longitudinal momentum, the transverse direction momentum should be conserved after collisions

ATLAS Trigger Menu

An ATLAS trigger is generally a trigger chain composed of L1 and HLT items. When an HLT trigger is fired, there is always a corresponding L1 trigger decision. For example, HLT electron trigger shall only be passed when a L1 electron trigger is also fired:

$$L1\_e24 \rightarrow HLT\_e26\_lhtight\_nod0\_ivarloose \tag{2.7}$$

where the numbers are the trigger thresholds in the unit of GeV, while the *lhtight* and *ivarloose* are to define the electron quality with the calorimeter activities in the surrounding region of this electron (see more details in Sec. 2.3) . The threshold of triggers might not be kept the same during operation periods. Because the LHC keeps pushing its performance on instantaneous luminosity, the increase of events from both pile-ups and interactions from physics of interest enhances the trigger object energy. This makes the trigger rate go above the allowed bandwidth for data storage. To make better suppression on the trigger rate, the thresholds are therefore raised during some operation periods.

The defined triggers would then be made into "streams" where the events are categorized for different purposes. Physics analyses shall use the triggers contained in the "*physics_main*" stream, and there are also the dedicated streams composed of "prescaled" triggers for hardware calibrations. Those calibration triggers usually have lower thresholds in the contrast to the ones in *physics_main*. A random sampling is applied to only pick a fraction of events passing those triggers, which makes them not ideal for most physics analyses due to a complicated calibration scheme for the simulation.[7] The total allowed output rate from all streams is 5 kHz with 1 kHz for *physics_main*.

[7] There are still analyses using prescaled triggers like the studies in b-physics, or low energy signatures.

2.2.5. Run 2 Operation Overview

For the ATLAS operation from 2015 to 2018 which is called Run 2 (with respect to Run 1 from 2009 to 2012), the average data recording efficiency is around 95% with respect to LHC delivery efficiency. From the measurement with the Luminosity Cherenkov Integrating Detector (LUCID, one of the forward detectors of ATLAS) [**?**,36], the integrated luminosity is $\sim 36\ fb^{-1}$ for 2015 and 2016, $\sim 46\ fb^{-1}$ for 2017 and $\sim 63\ fb^{-1}$ for 2018 which gives the total data of 140 fb^{-1}. The performance from 2011 to 2018 is summarized in Fig. 2.12

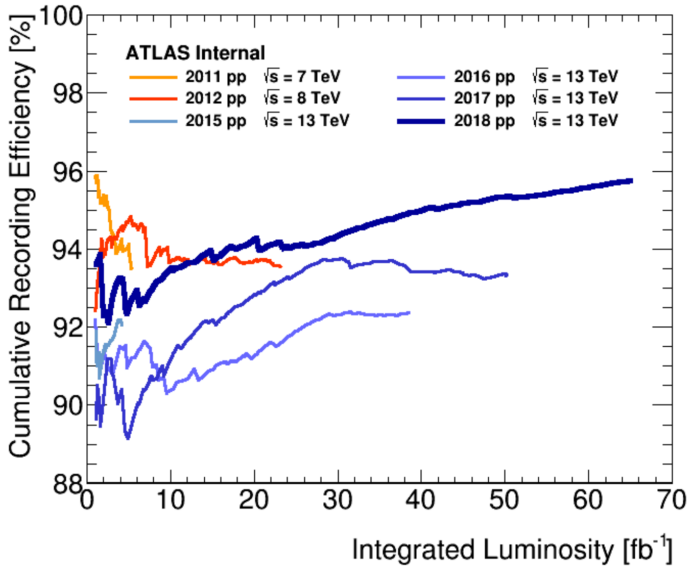

Figure 2.12.: The ATLAS recording efficiency and luminosity [37]

2.3. Object Reconstruction

When the events are passed into the permanent storage, they are still in the format of raw data which contains only the information of hits (the spacepoints from the inner detector and muon spectrometer) and calorimeter energy towers (the energy deposited in the calorimeter cells). They need to go though the full reconstruction (offline reconstruction, which is different from the online construction performed in the hardware) to be interpreted into the objects with physical meanings as the SM

particles like electrons or muons. The reconstruction will be based on the principles of interactions between detectors and particles:

1) Only charged particles leave tracks in the inner detector

2) The particles involved in electromagnetic interactions shall deposit energy in the ECAL, and the light ones are stopped here.

3) All the particles except for muons are supposed to be stopped in or before the HCAL.

4) Only muons could reach the muon spectrometer.

After the reconstruction of all objects, a further correction on energy scale (the peak of the energy pulse shape) is applied on both data and simulation samples to take in the effect of energy loss from the radiation, the contamination from other objects, or the detector effect (like dark current, hot noise, or material inhomogeneities). The final procedure is to remove the overlapped objects by the priority defined by the analyses.

Primary Vertex & Tracks [38]

A pattern recognition is performed in the SCT to find the helical trajectories with at least 3 spacepoints and $p_T > 500\ MeV$ which are taken as the track seeds. A Kalman Filter algorithm is then performed to extend the track seeds to the pixel layers. To resolve the reconstruction ambiguity, a tracking score system is taken to reject the shared spacepoints or fake tracks. When a track is reconstructed with more hits and less "holes" (missing hits in some layers), it is given a higher score. The track candidates from the SCT and pixel shall all have at least seven hits (three spacepoints from SCT and four hits from pixel). To complete the track reconstruction in the full inner detector, the drift tubes in the TRT are integrated into the track, if they are with 10 mm of the route projection of a reconstructed track from the outermost SCT spacepoint. Afterwards, one addition track reconstruction (outside-in) from the TRT is

performed to recover the tracks from late decays or photon conversions. The unused TRT segments are then rematched to the SCT and pixel hit remanent.

The tracks which fulfil the following requirements are taken into the interaction point (vertex) reconstruction with the reconstructed beamspot which is assume to be where the two proton beams cross each other on the transverse plan [39]:

- p_T>400 MeV, $d_0 < 4\ mm$ (transverse distance to the beamspot)
- $\sigma(d_0) < 5mm$ (uncertainty on the d_0 measurement);
  $\sigma(d_z) < 5mm$ (uncertainty on the measurement of distance between the track and beamspot on the z-axis)
- at least four hits in the SCT
- at least nine hits in total from the SCT and pixel
- no hole in the pixel

The input tracks are then taken into an iterative algorithm [39] to reconstruct the interaction points (where the protons collide into each other) called vertices. The vertex associated with the highest p_T^2 sum is then defined as the primary vertex. All the reconstructed objects should origin from the primary vertex which is verified by d_0 and d_z, or they are taken as "minimum bias" background.

Electrons

Electrons are charged light particles, so they leave tracks in the inner detector and energy clusters in the ECAL. The two types of signature are combined to reconstruct electrons.

The first stage of the reconstruction is to build the energy cluster as an electron seed [40, 41]. A window of 3×5 ECAL layer-2 cells (corresponding to 0.075×0.125 in $\Delta\eta \times \Delta\phi$) is used to scan through ECAL layer-2 to find the electron seeds. If the transverse energy sum (E_T) inside the window is above $2.5GeV$, the cells inside this

window are selected, and the electron position is defined as the energy weighted η and ϕ (barycentre) of this window. Then, this window is extended along the R-direction to sum over the energy in other layers with the adjusted window size (detailed in [41]). The cells taken in the cluster are then removed to avoid the duplication into other electrons. With the estimation from $Z \to ee$ simulation sample, this algorithm has the electron reconstruction efficiency of 95% ($> 99\%$) for $E_T \sim 7\ GeV$ ($E_T > 15\ GeV$).

The reconstruction of tracks associated to electrons is performed independently from the mentioned reconstruction . A track seed of $p_T > 1GeV$ is firstly reconstructed with three spacepoints from the SCT layers . Then, based on the pion hypothesis (pion energy loss pattern in the ID materials), it is verified whether this track seed can be extended to pixel with four hits and matched to a calorimeter cluster. If it fails, the electron hypothesis is applied for the same verification. The hits from both hypotheses are then fitted using "ATLAS Global χ^2 Track Fitter" [42] into tracks, and the tracks failing the pion track hypothesis are then tested again with electron hypothesis. The tracks passing the electron hypothesis are then taken as potential electron tracks. This algorithm is also integrated in the standard track reconstruction with the least interference to the reconstructed tracks.

The track and cluster are then associated with a loose ΔR matching which considers the electron bremsstrahlung and the number of hits in the inner detector. The matched track-cluster pairs are then refitted with optimised "Gaussian Sum Filter" (GSF) [43] to take non-linear bremsstrahlung into account.

To have further separation between signal-like and background-like electrons, the electron identification is then performed on $Z \to ee$ (signal) and dijet (background) MC samples. It is a multi-variable analysis (MVA) based on the likelihood discriminant defined as:

$$d_{\mathcal{L}} = \frac{\mathcal{L}_S}{\mathcal{L}_S + \mathcal{L}_B} \quad \text{and} \quad \mathcal{L}_{S(B)}(\vec{x}) = \prod_{i=1}^{n} P^i_{S(b)}(x^i) \tag{2.8}$$

where $P^i_{S(b)}(x^i)$ is the probability density function for signal (background) for a specific input variable x^i, and $\vec{x}$ is the vector formed by those variables in the likelihood phase space (all the input variables could be found in [44]). Three working points are therefore defined by $d_{\mathcal{L}}$: *Tight*, *Medium* and *Loose*[8]. The signal efficiency from this selection process is as a function of electron E_T, and the plateau of efficiency could be reached at $E_T = 70GeV$ with $\sim$97% (95%) [91%] for the *Loose* (*Medium*) [*Tight*] working point.

In addition to the reconstruction quality, the electrons are also required to be "isolated" from all the other tracker and calorimeter signatures, because of the concern that the nearby detector activities might affect the electron measurement. The isolation is defined in two ways:

- the calorimeter isolation (Iso^{E_T}): it is defined as the cluster E_T sum within a cone with $\Delta R = 0.2(0.3)$ centred at the reconstructed electron inside which a central cluster subset in a rectangle of 0.125×0.175 ($\Delta\eta \times \Delta\phi$) is subtracted. This will be denoted as topoetcone20(30)
- the track isolation (Iso^{p_T}): it is defined as the p_T sum of tracks from primary vertex within a cone of $\Delta R = min(0.2(0.3), 10GeV/E^e_T)$ centred at the electron but without the electron associated tracks. This will be denoted as ptvarcone20(30)

The isolation discriminant is then applied as Iso^{E_T}/E_T or Iso^{p_T}/p_T. The recommendation working points on the discriminant are given as a function of electron E_T or fixed cut which are summarised with the muon isolation working points in Tab. 2.2.

Muons [45]

Muons can travel through the calorimeter and reach the MS, and the reconstruction is mainly based on the tracks in the inner detector and the MS.

The MS track segments are firstly built from the hits within each MS module, and the reconstruction coordinates are different for each subsystem due to the varied detector architectures: the MDT reconstruction is on the coordinate of the toroid magnetic

[8] *Tight* selected electrons are the subset of *Medium*, and *Medium* is the subset of *Loose*

bending plane, while the RPC and TCG have the coordinate orthogonal to it, and the CSC is only using the detector η-ϕ coordinate. A loose criteria is applied in the segment building algorithm to verify the compatibility to a full track. Then, the segments in the middle layer of the MS are taken as the track seed and extended to the inner and outer layers. If two segments could be fitted with enough hits by matching from their relative position and angle, they are integrated into the same track. The exception is in the transition region between the barrel and endcap, and a standalone and good-quality segment could be kept as a single track.

An overlap removal is afterwards applied to remove the shared hits in the tracks with poor fitting quality, but they could still be kept only if the fitting criterion is fulfilled. Two tracks could share maximally two hits in the inner two layers and have no same hit in the outer layer for the concern of close-by muons.

The hits along the tracks are then taken into the global χ^2 fitting. The hits with great deviation from the fitted MS trajectory are removed, and the fit is applied again to derive the new track. If there are hits not included in the track but within the allowed deviation from the track, they are also taken into the track, and the fitting is repeated.

The final MS tracks are taken as the seed to match to the inner detector tracks to reconstruct the combined muons. A further global fitting is conducted to extrapolate the muons with the flexibility to add in or remove the MS hits to improve the fitting quality with the ID tracks. The primary algorithm in the fitting is performed outside-in from the MS to the inner detector, and a complementary algorithm of inside-out is also applied to guarantee the robustness of the reconstruction. For the muons outside of the inner detector coverage ($2.5 < |\eta| < 2.7$), they can be reconstructed from only MS tracks, but the criteria are more stringent.

Similar to electrons, muons also have the identification procedure with three parameters: q/p significance (the ratio of charge and momentum measured in the ID and MS over the quadrature sum of their uncertainties), ρ' (the ratio of momentum differ-

ence between the ID and MS measurements over the combined measurement) and the normalised combined track fit, χ^2. The working points for the muons identification have the definition individually as below:

- *Medium* muons: they are defined within the range of $0.1 < |\eta| < 2.5$ with at least two MDT layers of ≥ 3 hits. If it is within the range, $0.1 < |\eta|$, it is allowed to have hits in only one MDT layer, but there shall be no hole in the MS track reconstruction. As the muons go beyond the coverage of the inner detector (i.e. $2.5 < |\eta| < 2.7$), they shall have the MS tracks reconstructed from all three layers. An extra requirement of q/g significance above seven is also applied on this muon quality.

- *Loose* muons: those muons are defined with the most loose requirement. They are generally *Medium* muons, but the selection is loosen for the range of $|\eta| < 0.1$ due to the missing coverage of the MS (where a gap is present for the service of the ID and calorimeter). When an ID track is found within this range and matched to a calorimeter cluster which is identified as a deposit by "minimum-ionization" particles, they are also accepted as loose muons to recover the reconstruction efficiency.

- *Tight* muons: all of them must have the tracks reconstructed from two layers in the MS (either MDT or CSC) with *Medium* muon hit selection. To enhance the purity of muons, a further requirement on the ID to MS track fitting is also added into the selection for $\chi^2 < 8$. An additional two-dimension cut on q/g significance and ρ' is also applied to improve the background rejection for muons with $p_T < 20\ GeV$.

For the muon isolation, the definition is similar to the electron ones, but they have different working points. The recommended working points for electrons and muons are shown in Tab. 2.2.

Table 2.2.: Electron/Muon Isolation Working Points (ϵ means the efficiency)

Working Point	**Object**	**Calo Iso**	**Track Iso**	Combined Iso
LoseeTrackOnly	all leptons	-	99%	99%
Loose	all leptons	99%		99%
Gradient	all leptons	$\epsilon = (0.1143 * p_T[GeV] + 92.14)\%$		$\epsilon(25GeV) = 90\%$ $\epsilon(60GeV) = 99\%$
GradientLoose	all leptons	$\epsilon = (0.057 * p_T[GeV] + 95.57)\%$		$\epsilon(25GeV) = 95\%$ $\epsilon(60GeV) = 99\%$
FixedCutTight	Electrons	topoetcone20/p_{T} <0.06	ptvarcone20/p_{T} <0.06	-
FixedCutTight	Muons	topoetcone20/p_{T} <0.06	ptvarcone30/p_{T} <0.06	-
FixedCutTightTrackOnly	Electrons	-	ptvarcone20/p_{T} <0.06	-
FixedCutTightTrackOnly	Muons	-	ptvarcone30/p_{T} <0.06	-
FixedCutLoose	Electrons	topoetcone20/p_{T} < 0.2	ptvarcone20/p_{T} < 0.15	-
FixedCutLoose	Muons	topoetcone20/p_{T} < 0.3	ptvarcone30/p_{T} < 0.15	-
FixedCutHighPtCaloOnly	Electrons	topoetcone20 < 3.5 GeV	-	-

Jets

When quarks or gluons are travelling in the space, they go through the process called "fragmentation" or "hadronisation" for "colour-confinement" of QCD. This leads to the multiplication of quarks, gluons (i.e. partons), or even leptons and photons, and they eventually form the bound states as hadrons leaving complicated signatures in the detector. One quark from a collision might leave more than one hundred tracks in the inner detector and several clusters in the calorimeter, and jets are defined as the ensemble of those signatures. To properly collect those tracks and calorimeter clusters into the same jets, the reconstruction algorithm is designed to ensure the infrared safety and collinear safety. The infrared safety means that the soft radiation from hadronic objects in a jet would not change the jet width or orientation, while the collinear safety indicates that the nearby particles with higher p_T in the collinear direction of the splitted parton would not affect the jet reconstruction. To achieve both of the two requirements, the jet reconstruction algorithm [46] employs the following

two parameters for the jet definition:

$$d_{ij} = min((p_T^i)^a, (p_T^j)^a) \times \frac{R_{ij}^2}{R} \quad \text{with} \quad d_{iB} = (p_t^i)^a \tag{2.9}$$

where p_t^i and p_t^j are p_T of ith and jth entities which could be calorimeter clusters (a patch of energetic cells in the calorimeter), tracks, or the truth particles in the simulation, R_{ij} is the distance between the $i-th$ and $j-th$ entities, and R is the parameter to customize the algorithm for performance (i.e. cone size), while a corresponds to three algorithms which are sensitive to different jet properties. $a = -2$ is for anti-k_t algorithm, and it has the advantage for better stability of jet structure during reconstruction with high sensitivity to hard objects and ignorance for the jet substructure as well as pile-up events. $a = 0$ and $a = -2$ are used for Cambridge-Aachen algorithm and k_t algorithm respectively which are more sensitive to jet substructure but with high dependence on pile-up events and soft objects. When $d_{ij} < d_{iB}$, the i^{th} and j^{th} objects are merged into the same cluster with the position defined as their barycentre. If no new pair could be found meeting this condition, the cluster is then defined as a jet.

For the jets in the ATLAS experiment, anti-k_t algorithm is preferred with $R = 0.4$ and $R = 1.0$. $R = 1.0$ is for the scenario that two jets are close to each other, and $R = 0.4$ could not have the separation power to distinguish them. The input entities for jet reconstruction is the ECAL clusters in the range of $|\eta| < 4.9$, the calorimeter coverage, with the energy 2σ above the quadrature sum of pile-up events and electronic noise, while the cluster to initiate the clustering (the seed) has higher requirement of 4σ. The hadronic energy deposit from HCAL is added to the ECAL clusters through "local cell weighting" (LCW) [47] which is to calibrate the jet energy scale by the MC simulation and the data from the single particle test beam. The final reconstructed jets are then used in analyses after the selection of "jet vertex tagger" (JVT) [48] to guarantee that they originate from the primary vertex.

b-Tagging [49]

In the SM, $\sim$58.5% of Higgs bosons decay to two bottom quarks (b-quark), and

almost all top quarks decay to b-quarks (BR($t \to bW$)=100%) which is the major background for most ATLAS analyses. Therefore, how to recognize the jets from b quarks is an important task for physics purposes.

Different from the signatures other stable SM particles leave in the detector, b-quarks have a longer lifetime as compared to the other unstable particles which decay almost at the locations of vertices, so the jets of b-quarks have a displaced vertex several mm away from the primary vertex. The b-jet identification depends on this property and the b-quark decay chain. The following three algorithms are used:

- **Impact-Parameter-Based Algorithms**: given their displaced vertex, b-jet associated tracks should tend to have a greater impact parameter in both transverse and longitudinal directions. The impact parameters are used as inputs for the probability density function for b-quark and light-flavour quark hypotheses. The ratio of the two possibilities are then taken into a single log likelihood ratio discriminant (LLR).

- **Secondary Vertex Finding Algorithm**: to reconstruct the secondary vertex, a preselection on tracks within a jet based on the kinematic and topological properties is adopted. This is to reject the tracks from photon conversions, hadronic interactions, etc. The survived tracks are then taken into the reconstruction of a single vertex with outlier tracks iteratively removed.

- **Decay Chain Multi-Vertex Algorithm**: this algorithm is also called "jet finder". Its purpose is to find the full chain of "$PV \to b \to c$". A Kalman filter is applied to link the vertices to approximate the trajectories of this jet with which the vertices of b- and c-quarks could be resolved even with only one-track link.

The output of those algorithms are then given to a multi-variable analysis (MVA) of Boosted Decision Tree for the final discriminant. It is trained with the sample of $t\bar{t}$ which contains b-jets and the background composed of 10% c-jets and 90% other light-flavour jets. The final outcome variable, MV2c, is then applied as a simple cut to select b-jets, and the suggested working points are shown in tab. 2.3. The rejection rate is defined as the inverse of the background acceptance rate.

Table 2.3.: b-Tagging Working Points

Cut Value	b-jet Efficiency[%]	c-jet Rejection	light-flavour-jet Rejection
0.4496	60	21	1900
−0.0436	70	8.1	440
−0.4434	77	4.5	140
−0.7787	85	2.6	28

Missing Transverse Energy (E_T^{miss})

The design of the ATLAS detector utilises electromagnetic and hadronic interactions to capture particles. If particles are only involved in weak interactions, they leave no signatures in the detector like neutrinos or some new particles predicted by BSM theories. In this case, the only way to measure their energy is via the momentum conservation.

When two protons collide into each other in the LHC, both of them have no momentum on the transverse plane, so the transverse momentum sum of collision products is supposed to be zero. Therefore, the definition for sum of transverse momentum from invisible particles could be presented as:

$$\vec{E}_T^{miss} = \sum_{\text{visible objects}} -\vec{p}_T^{\,i} \tag{2.10}$$

where E_T^{miss} is supposed to be called missing transverse momentum, but it is called "missing transverse energy" out of historical reason. The explicit form is:

$$\vec{E}_T^{miss} = -(\sum \vec{p}_T^{\,e} + \sum \vec{p}_T^{\,\mu} + \sum \vec{p}_T^{\,\gamma} + \sum \vec{p}_T^{\,jet} + \sum \vec{p}_T^{\,\tau} + \sum \vec{p}_T^{\,soft}) \tag{2.11}$$

with p_T contributed from different objects passing loose selection (the notations in the equation are e as electrons, μ as muons, *gamma* as photons, *tau* as tau lepton). Even though tau, τ, and photon, γ, are not used in this analysis, they are still reconstructed

and applied in E_T^{miss} estimation. The last term ($\vec{p}_T^{soft}$) is referred to the detector soft signatures which are not used in the reconstruction of any objects. They could be either from tracks (track soft term, TST) or clusters (cluster soft term, CST). The track soft term considers only the remaining tracks from the primary vertex, so it has lower dependence on the pile-up events, while it cannot deal with the contribution from neutral objects which, instead, could be recovered by the CST. In ATLAS Run2 analyses, TST is preferred, because it delivers smaller uncertainty with the high pile-ups. As E_T^{miss} is only calculated on the transverse plane, it has no η information.

2.4. Simulation

For the two analyses in this thesis, the SM background estimation comes from the Monte Carlo simulation. It is performed in several steps: event generation → event overlapping with "minimum bias" (MB) events → detector response simulation → digitisation → physical object reconstruction → physics analysis.

Event generation is through the generators designed by theorists with the input of theoretical parameters for interactions: $pp(\rightarrow X) \rightarrow Y$. X is intermediate particles with a short lifetime, and it will eventually decay to Y as final stable particles which leave signatures in the detector. With the example of $t\bar{t}$ event simulation, the process would be taken as $pp \rightarrow t\bar{t} \rightarrow b\ell\nu bqq$ with X as the intermediate particles, $t\bar{t}$, and Y as the final state particles, $b\ell\nu bqq$. The total cross section of an interaction will then be evaluated by this equation [50]:

$$\sigma_{pp\rightarrow Y} = \sum_{a,b} \int dx_1 dx_2 f_a(x_1, \mu_1) f_b(x_2, \mu_2) \hat{\sigma}_{a+b\rightarrow X}(x_1, x_2, \mu_R) \tag{2.12}$$

with a,b as the proton partons (quark or gluon) involved in the interaction, and x_1 and x_2 are the momentum fraction of the partons relative to the whole proton, $\hat{\sigma}_{a+b\rightarrow X}$ is the cross-section calculated perturbatively of the process, $a + b \rightarrow X$, and f_a, f_b are the parton distribution function (PDF) for the corresponding parton which determines the possibility of momentum transfer from partons, a and b, to the output particle, X. μ_1,

μ_2, and μ_R are the parameters which decide how the PDF depends on x_1 and x_2.

For the ATLAS simulation, two processes are simulated in one event: pile-ups, $pp \rightarrow jj$, and hard-scattering, $pp(\rightarrow X) \rightarrow Y$ with X and Y as particles of interest. Generally, hard-scattering is generated with a specific generator which can give the best accuracy of simulation, and the events are then passed to $PYTHIA8$ [51,52] for the generation of pile-up events and the hadronizaton of the hadronic objects which are stored in the "HITS" files.

The next step is to simulate the interaction between the particles and the detector. The detector is described by $GEANT4$ [53] with the input parameters like materials and physical design. The detector description is stored in the ATLAS Geometry database which has low flexibility to change the content, while an additional database, COOL, is used to keep the information changed with time like dead channels and LAr high voltage settings. The particles are then parametrized to interact with the detector, which gives the digitalised output of raw data objects (RDO) like tracks and calorimeter clusters . After the same physical object reconstruction from the detector signatures as data, the simulation samples are ready for the physical analyses in the data format called "analysis object data" (AOD). The full procedure could be seen in the diagram of Fig. 2.13 .

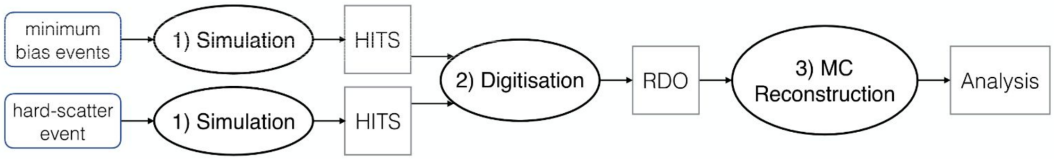

Figure 2.13.: The full procedure of the ATLAS simulation

Chapter 3.

Resonance Searching Strategy

"The wilderness must be explored!"

— Russell, Up

The search for resonance signatures is applying a general strategy with three benchmarks for exotic particles of different spins: the narrow-width-approximation scalar boson (NWA, spin=0), the heavy vector triplet (HVT W', Z' bosons, spin=1), and the Randall-Sundrum graviton (RSG, spin=2).

In the study of this thesis, WW and WZ are the two medium states of interest through the production of gluon-gluon fusion (ggF), Drell-Yan process (DY), or vector boson fusion (VBF). The vector boson fusion is the fusion process of two vector bosons (W or Z) emitted from two incoming quarks, and the two quarks are then scattered into two energetic jets with a wide η separation and high invariant mass, which is taken as the key signature to select VBF events (details in event selected section). The production processes could be seen in Fig. 3.1 as Feynman diagrams, and it should be noted that DY and ggF are indistinguishable from detector signatures. The strategy herein considers only final states in which one W boson decays leptonically ($W \to l\nu$) into an electron or muon accompanied by a neutrino of the corresponding flavour, while the other boson,W or Z, is chosen to decay hadronically into two quarks reconstructed into two $R = 0.4$ jets or one $R = 1.0$ jet ($W/Z \to jj$ or $W/Z \to J$). The events with W

bosons decayed into taus are not considered in this analysis. The benefit of choosing this final state is to have the high branching ratio from the hadronic decay and suppress the QCD contamination by the leptonic decay. This study is conducted to search for particles in a wide mass range from 300 GeV to 5 TeV. If the mass of a resonance particle is high enough ($m > 1$ TeV), the bosons would be highly boosted. In this scenario, the two quarks decayed from boosted bosons get too close to each other which is beyond the resolution of anti-k_T algorithm with $R = 0.4$, so they are not resolved as two jets, and a larger cone of $R = 1.0$ is applied to collect their signatures into a single fat jet.

This search was performed with the 36.1fb^{-1} data collected by the ATLAS detector in 2015 and 2016 with pp collisions at $\sqrt{s} = 13$ TeV (s is a Mandelstam variable meaning the square energy sum of the two quarks involved in a collision).

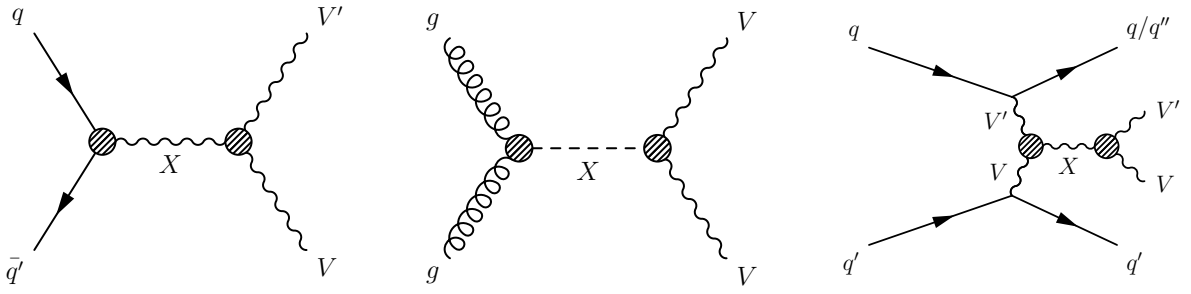

(a) Drell-Yan Process **(b)** gluon-gluon Fusion **(c)** Vector Boson Fusion

Figure 3.1.: The Feynman diagrams of different production mechanisms for particle X which decays into two SM bosons.

3.1. Signal Models

In the SM, bosons are the force carriers and also maintain the conservation of certain physical quantities associated with underlying symmetries. To seek for the solution of unsolved problems of the SM, many new models predict the existence of new bosons corresponding to unknown interactions or symmetries, and they also have the strong

coupling to the SM bosons which provide the access to verify those theories. However, the existing new models are constructed with many free parameters, and each set of them needs a dedicated analysis from the experimental side, which is impossible in reality. Therefore, a simplified model with only the kinematic parameters related to resonance mass is introduced for which experiments provide precise measurements for on-shell bosons.

This strategy could scan through many models, so it is defined as a general search. However, to give a better separation between signal and background, three benchmarks are applied in this analysis for sensitivity optimization as mentioned before.

Narrow-Width-Approximation Higgs Boson

Some extended models predict the existence of high mass Higgs bosons (BSM Higgs boson) to solve the problems of Higgs boson naturalness. However, as only kinematic properties are concerned, the interpretation model chosen in this analysis is the SM Higgs boson but with higher mass. To have further simplification, the decay of the Higgs boson is forced to be always at the mass pole with the narrow width approximation. This means the transferred momentum, q, from the proton partons is exactly the mass of the resonant particle under the assumption, which gives the narrow resonance width, $\Gamma/m_H << 1$ (Γ is the mass width on Higgs boson mass spectrum with m_H as the new mass of Higgs boson), and the interference to the SM Higgs boson is taken to be negligible [54]. Therefore, the relativistic Breit–Wigner distribution could be written as:

$$f(q) = \frac{k\pi}{m_H\Gamma}\delta(q^2 - m_H^2) \tag{3.1}$$

where k represents:

$$k = \frac{2\sqrt{2}m_H\Gamma\gamma}{\pi\sqrt{m_H^2 + \gamma}} \tag{3.2}$$

and $\gamma = \sqrt{m_H^2(m_H^2 + \Gamma^2)}$. This is then used to evaluate the cross-section of the Higgs boson production.

Heavy Vector Triplet

Heavy vector bosons are predicted by many new BSM theories with the coupling to quarks, leptons, SM vector bosons and Higgs bosons. To examine the suitable theories, this study attempts to investigate all the couplings with a set-up of one neutral heavy boson, Z', and two degenerate charged bosons, $W'^{\pm}$, with the given coupling constant, g_V. For optimization, two models are taken as the benchmarks [55,56]. Model A is with an additional symmetry breaking to SM, $SU_1(2) \times SU_2(2) \times U(1) \rightarrow SU_L(2) \times U(1)$ giving a weak coupling: $g_V \sim \mathcal{O}(1)$. For the scenario of a strong SM boson coupling, the Minimal Composite Higgs Model is taken as model B with the symmetry breaking, $SO(5) \rightarrow SO(4)$ for $4\pi \geq g_V \geq 1$. However, because the decay width is proportional to the coupling constant, and the focus of this search is for the narrow resonance, only $6 \geq g_V \geq 1$ is considered with $\Gamma_{V'}/m_{V'}$ below 10%.

To simplify the models, the coupling strength to all fermions are equal with the scale of $g^2 c_F/g_V$ where g is the $SU_L(2)$ gauge coupling, and c_F is the dimensionless coefficient between bosons and fermions defined as a free parameters of order one (ranged between one and ten) in the phase space of interest. As the fermionic coupling scale is proportional to $1/g_V$, model A turns to be more sensitive to the fermionic production with Drell-Yan process, but it is suppressed in model B. In contrast, the coupling to bosons is governed by $c_H g_V$ with c_H as the universal coupling among bosons. Therefore, model B has higher branching ratio of the diboson decay channel and also the production rate from vector boson scattering in this analysis than model A. For the interpretation, the two parameters, $g^2 c_F/g_V$ as well as $c_H g_V$, construct a two-dimension phase space across which production rates and decay branching ratios vary significantly.

As the coupling to all bosons are the same ($c_H g_V$), the neutral and charged heavy

bosons (Z' and $W'^{\pm}$) have the same decay branching ratio to all SM bosons:

$$BR(Z' \to ZH) = BR(Z' \to W^{\pm}W^{\pm}) = BR(W'^{\pm} \to W^{\pm}Z) = BR(W'^{\pm} \to W^{\pm}H) \tag{3.3}$$

However, with the small mixing angle (between SM and BSM bosons), the coupling in the transverse component of a field is well suppressed, and the dominant contribution is from the longitudinal component. For the same reason, the couplings to neutral dibosons and $W\gamma$ are also so weak that those channels are ignored in this analysis. For the case of coupling to HH, this interaction is forbidden due to the conservation of momentum and angular momentum.

Randall-Sundrum Graviton

As discussed in Chapter 1, extra dimensions were proposed as one of the solutions [57] to the hierarchy problem. It leads to the result that the effective Planck scale, $M_{pl} = 2 \times 10^{18} GeV$, is determined by the existence of extra dimensions from the orginal scale, M, and the extra-dimension geometry. The relation between M_{pl} and M is:

$$M_{pl}^2 = M^{n+2} V_n \tag{3.4}$$

where n is the number of dimensions which are not yet observed, and V is the volume constructed from the extra dimensions regardless of the four-dimensional spacetime. Therefore, the visible spacetime is just a manifold under $(4 + n)$ dimensions.

Under Randall-Sundrum model, only one more dimension is needed, which hypothesises that the fifth dimension in addition to the spacetime four dimensions is constrained with boundary condition of the ϕ periodicity ranged between $-\pi$ to π called the "warped bulk". It bridges two four-dimensional manifolds at $\phi = \pi$ and $\phi = 0$. The "Hilbert-Einstein"actions under the set-up could be presented as:

$$S = S_{gravity} + S_{obs} + S_{hid} \tag{3.5}$$

$$S_{gravity} = \int d^4x \int_{-\phi}^{\pi} d\phi \sqrt{G} \left[-\Lambda + 2M^3 R \right] \tag{3.6}$$

$$S_{vis(hid)} = \int d^4x \sqrt{-g_{vis(hid)}} \left[\mathcal{L}_{vis(hid)} - V_{vis(hid)} \right] \tag{3.7}$$

with Λ as the cosmological constant, R as the scalar spacetime curvature, and g's are the determinants of metric tensor matrix, $g_{\mu\nu}$, V_{vis}, and V_{hid} are the constant gravitational potentials taken out from the Lagrangian vacuum energy for the visible and hidden spacetimes. After inserting the terms into the Einstein Field Equation, it leads to the solution for the spacetime description in terms of the line element:

$$ds^2 = e^{-2\sigma(\phi)} \eta_{\mu\nu} dx^\mu dx^\nu + r_c^2 d\phi^2 \tag{3.8}$$

with

$$\sigma(\phi) = k r_c |\phi| \quad k = \sqrt{\frac{-\Lambda}{24M^3}} \tag{3.9}$$

where η is the Minkowski metric, and r_c is the constant independent of ϕ taken as the "compactification radius" of the extra dimension on the orbifolding. As a result, the extra dimension only has the dimensional interval, πr_c, at $\phi = \pi$ in the visible spacetime. Taking the space description into Eq. 3.4, the relation between r_c and M_{pl} could be derived as:

$$M_{pl}^2 = \frac{M^3}{k} \left[1 - e^{-2kr_c\pi} \right] \tag{3.10}$$

This expression indicates that M_{pl} depends on kr_c, and the weak gravity could be explained with a proper choice of r_c. Under the solution, the existence of graviton (the gravitational field) is then taken as the tensor fluctuation on Minkowski metric: $\eta_{\mu\nu} \rightarrow \eta_{\mu\nu} + \bar{h}_{\mu\nu}(x)$. To estimate its mass, the new spacetime geometry is inserted into the Higgs sector in the SM Lagrangian, and it gives the result: $m = e^{-kr_c\pi} m_0$ with m_0 as the original mass scale in the visible manifold, and m as the one in the five-dimensional spacetime. (This relation could also be applied to SM particles.) If $e^{kr_c\pi}$ is of the order 10^{15}, the mass scale would be in the scale of TeV under this

mechanism, which offers the signature verifiable to the LHC energy scale with the couplings to SM particles derived the same way.

3.2. Simulation Samples and Derivation

Each SM background process and each signal sample are simulated by the procedure mentioned in Sec. refsec:simulation. To make a proper comparison between simulation and data, the event numbers are normalised to the theoretical cross section and total data luminosity. However, the modelling of interactions between the ATLAS detector and particles is not perfect, and it leads to discrepancy in efficiency measurements including the particle reconstruction, lepton isolation, trigger, and jet b-tagging efficiency. To recover this disagreement, scaling factors are estimated from the comparison between data and the simulation from a Monte Carlo method (MC) and applied as event weights on the simulation samples.

Another disagreement comes from the inconsistency in distribution of interaction numbers per bunching crossing, μ. To eliminate the effect, one more scale factor is applied through the process called "pile-up reweighting" (PRW) to make the simulated μ distribution agree with data.

After considering all the factors for the data-MC comparison, the final simulation event yield is reweighted to data by:

$$N_{yield} = \mathcal{L} \times \sigma \times \epsilon_{rec} \times \epsilon_{iso} \times \epsilon_{trigger} \times \epsilon_{b-tagging} \times \epsilon_{prw} / N_{mc} \tag{3.11}$$

where N_{mc} is the total event weight from simulation, σ is the cross-section for the interaction, and ϵ's stand for the scaling factors of different contributions like trigger or reconstruction efficiency. $\mathcal{L}$ and σ are the integrated luminosity and cross-section of the interaction.

Background Simulation

Some of the SM processes have the same final state to the new physics of our interest: one lepton, one neutrino and multiple jets, and they are called "irreducible" background which could not be well-suppressed by selection cuts. This type of backgrounds are estimated from the MC simulation contributed from W+jets ($W \to l\nu$), $t\bar{t}$ ($t \to bW \to bjj$ and $t \to bW \to bl\nu$), diboson ($WW/WZ \to l\nu jj$), Z+jets ($Z \to ll$), and single top interactions.

The events of W/Z+jets are simulated by SHERPA v2.2.1 [58], with the PDF configuration of NNPDF30NNLO [59] as the baseline generator, and the simulation uncertainty is taken by the comparison to other generators detailed in next chapter. With the complicated process of hadronisation including the broad range of jet p_T and involved quark flavours, the simulation is done respectively with multiple slices of $max(h_T, p_T(W/Z))$ (h_T is the scalar sum of p_T from all jets) and different number of bottom and charm quarks. The involved matrix element for the simulation are up to 2 partons at NLO (next to leading order) and 4 partons at LO (leading order) which is followed by merging into the Sherpa parton shower. The resulting cross section for normalisation is estimated to NNLO (next next to leading order) of QCD.

$t\bar{t}$ events are generated through POWHEG-BOX [60] v2 with the matrix element calculation provided by CT10 PDF [61] with the top quark mass set at 172.5 GeV, and the HDAMP parameters for high p_T radiation is set at $1.5m_t$. Different from SHERPA as a self-contained generator to do parton shower itself, the simulation from POWHEG-BOX is then interfaced through MADSPIN [62] and PYTHIA8.186 tuned by Perugia 2012 (P2012) [63] and CTEQ6L1 PDF [64] sets for spin correlation preservation of top quark decays and the following parton shower, fragmentation and underlying events. The renormalisation and factorisation scale of the whole process are determined by $\sqrt{m_t^2 + p_T^2(t)}$. The $t\bar{t}$ cross section used for normalisation is calculated using TOP++ 2.0 [65] with the precision up to NNLO in QCD. To take in the contribution from soft gluon terms, a re-summation with next-to-next-to-leading logarithmic (NNLL) is applied to make further correction.

Single top events are generated through three processes: s-, t- and Wt-channel productions (Feynman diagrams are presented in Fig. 3.2). For the simulation of Wt and s-channels, the same recipe from $t\bar{t}$ generation is adopted, while the t-channel one is through POWHEG-BOX v1 with fixed four-flavour CT10F4 PDF [66] set but also followed by the same procedure for decay and parton showering from $t\bar{t}$ generation. The renormalisation and factorisation scales are set respectively for the three channels with:

- s-channel & Wt-channel: m_t
- t-channel $4 \times \sqrt{m_q^2 + p_T^2(q)}$ (q is the quark associated with the single top quark production)

The cross section for each production is calculated separately with the description in [67,68].

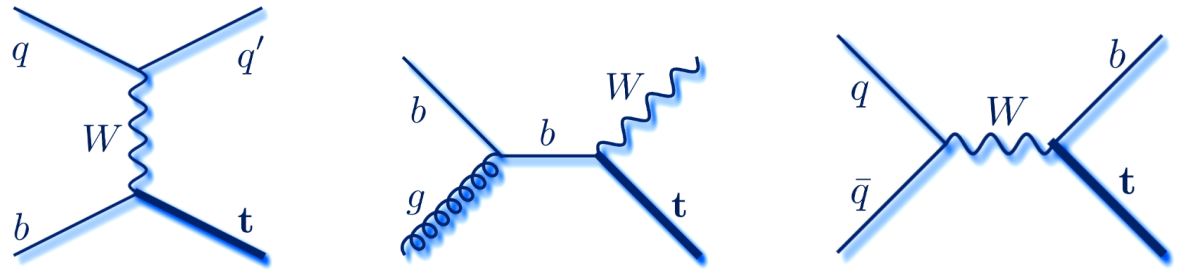

(a) t-channel **(b)** Wt-channel **(c)** s-channel

Figure 3.2.: The Feynman diagrams of three channels for single top production.

The generation of WW/WZ events are also through SHERPA v2.2.1 for the event production and the hadronisation.

Signal Simulation

HVT samples are generated via MADGRAPH5 [69] interfaced to PYTHIA8 [52] with the resonance mass points ranged from 300 GeV to 5 TeV with 100 GeV spacing. For simplicity, $g_V = 1$ and $g_V = 3$ are set for model A and model B respectively.

RS graviton events are also simulated through MADGRAPH5 and PYTHIA8, and only the ggF production is considered for this signal. Within the simulation, $r_c = 1$ is set as the default for the simulation, but it is also reweighted in the resonance mass distribution at parton level for $r_c = 0.5$ [1] This is for the comparison with the result from the CMS collaboration. The decay width of graviton mass with this configuration is expected to be $\approx 6\%$. The decay widths and cross-sections of HVT and RS graviton are summarised in tab. 3.1.

For the NWA Higgs boson, its interference to the SM Higgs boson (125 GeV) is assumed to be negligible as discussed in 3.1. Its narrow decay width is set as a constant at 4.07 MeV for all mass points which is beyond the experimental resolution with the production of ggF and VBF, which are simulated separately. The simulation is done by POWHEG-BOX v2 showered with PYTHIA8 under CTEQ6L1 PDF set.

Table 3.1.: The decay width and cross section of HVT and RSG at 800 GeV, 1.6 TeV, and 2.4 TeV mass points

	HVT W′ and Z′			RS $G*$	
m	Γ	$\sigma \times BR(Z' \to WW)$	$\sigma \times BR(W' \to WZ)$	Γ	$\sigma \times BR(G* \to WW)$
$[TeV]$	$[GeV]$	$[fb]$	$[fb]$	$[GeV]$	$[fb]$
0.8	32	354	682	46	301
1.6	51	38.5	79.3	96	4.4
2.4	74	4.87	10.6	148	0.28

Derivation

For practical reasons, the analyses were not run on AODs directly. Instead, they went through the "derivation" procedure composed of "trimming" and "slimming" to drop down variables and events of no interest first [70], which outputs the data format called derived AOD (DAOD). For the broad variety of analysis types, a couple of derivation schemes are applied, and the analyses with similar final states share the

[1] Reweighting is a feature of Madgraph. For similar configurations of simulations, the samples can be obtained by altering the weight of existing samples based on the kinemtic properties.

same derivation scheme.

With the final state of this analysis, "HIGG5D2" is chosen with the derivation scheme as the following:

- trigger: passing at least one unprescaled electron, OR muon, OR E_T^{miss} trigger
- lepton: one electron OR muon with $p_T > 15\ GeV$
- jet: two small R jets with $p_T > 20\ GeV$, OR one small R jet with $p_T > 100\ GeV$, or one large R jet with $p_T > 150\ GeV$

3.3. Physical Object Definition

Because the LHC is using protons as the beam source, it leads to the enormous production of hadronic jets. Within the environment, most reconstructed objects have the potential to suffer from great contamination from jet misidentified as other objects. Therefore, the definition on the signal objects selection as well as the loose object rejection for this analysis is to keep the signal efficiency and significant suppression of misidentification of the intended objects at the same time.

Electron

The electrons in this analysis are defined as two types, loose and signal, and each event only has exactly one signal lepton without additional loose one. Signal electrons are required to have p_T above 27 GeV to reach the trigger efficiency turn-on plateau, and $|\eta| < 2.47$ is applied on both electron types within the acceptance of inner detector with the crate region vetoed ($1.37 < |\eta| < 1.52$). The impact parameter cut is required to suppress the electrons contributed by pile-up events by the cuts on the distance between the electron and the primary vertex on the transverse plan and the z-axis. The selection criteria for signal and loose electrons are shown in Tab. 3.2.

In addition to the fundamental quality requirement, the overlap removal is applied

afterwards to prevent the objects reconstructed from the same detector signature. When an electron shares inner detector tracks with any muon candidate, the electron is discarded. The existence of a nearby jet defined by:

- $0.2 < \Delta R(e, j) < min(0.4, 0.04 + 10\ GeV / p_T(e))$

also makes the electron removed. The final requirement on electron is that it shall be consistent with the trigger level electron which fired the required electron trigger to suppress the QCD background.

Table 3.2.: Selection for electron candidates used in the analysis. Loose and signal electrons are defined.

	Electrons	
	Loose	Signal
p_T	$> 7\ GeV$	$> 27\ GeV$
$\lvert\eta\rvert$	$< 2.47 \notin [1.37, 1.52]$	
Identification	LooseLH	TightLH
Isolation	LooseTrackOnly	FixedCutTight
$\lvert d_0/\sigma(d_0)^{BL}\rvert$	< 5	
$\lvert z_0 \sin\theta\rvert$	< 0.5 mm	

Muon

Similar to electrons, loose and signal muons are defined with p_T and $|\eta|$ cuts in the consideration of trigger turn-on curve plateau and inner detector coverage. The requirement on muon impact parameters is tightened for better rejection to the cosmic muons. The selection criteria are shown below in Tab. 3.3

Different from the electrons, muons are kept, when it is close to small-R (R=0.4) jets. And, those jets are discarded, if they fulfil either of the following conditions:

- $\Delta R(\mu, j) < 0.2$
- number of associated tracks is smaller than 2 (the ghost-association algorithm mentioned in large-R jet definition in the following)

- $p_T^{\mu}/p_T^{j} < 0.5$ with $\Delta R(\mu, j) < min(0.4, 0.04 + 10\ GeV/p_T(\mu))$
- $p_T^{\mu}/\sum_1^n p_T^{trk} < 0.7$ with $\Delta R(\mu, j) < min(0.4, 0.04 + 10\ GeV/p_T(\mu))$

If a jet pass the above selection with a distance po the muon with $\Delta R(\mu, j) < min(0.4, 0.04 + 10\ GeV/p_T(\mu))$, the muon is discarded instead.

The last selection in muon is that it shall be spatially consistent to the trigger muon if muon trigger is fired in the event.

Table 3.3.: Selection for muon candidates used in the analysis. Veto and signal electrons are defined.

	Muons	
	Loose	Signal
p_T threshold	7 GeV	27 GeV
$\|\eta\|$	< 2.7	< 2.5
Identification	Loose	Medium
Isolation	LooseTrackOnly	FixedCutTightTrackOnly
$\|d_0/\sigma(d_0)\|w.r.t.BL$	< 3	
$\|z_0 \sin\theta\|$	< 0.5 mm	

Small R Jets [R=0.4]

In the intended final states, the jets (denoted as j) come from the decay of W bosons ($W \to jj$) or the remnant quarks from the vector boson fusion ($jj \to WWjj$ or $jj \to WZjj$). Because of the kinematic properties, the two types of jets are selected respectively. The full selection criteria are in Tab. 3.4.

The pair of VBF jets are supposed to be a high mass dijet system with wide separation, so they have a tighter p_T selection of $p_T > 30\ GeV$ but a looser $|\eta|$ cut, $|\eta| < 4.5$. For signal jets (the jets from the boson decay), they are only required to have $p_T > 20\ GeV$, and only the ones within the acceptance of inner detector ($|\eta| < 2.5$) are taken as jet candidates for event selection. The jet quality requirement is to remove the "fake jets"

from calorimeter noise pulse, cosmic ray, or non-collision background (like beam-halo), which is called "jet cleaning" [71].

Table 3.4.: Selection for small-R jets

	Small-R Jets	
	Signal Jets	VBF Jets
Algorithm	anti$-k_t$, $R = 0.4$	
p_T	$> 20\ GeV$	$> 30\ GeV$
$\lvert\eta\rvert$	< 2.5	< 4.5
Quality	not "bad" jet	
JVT	< 0.59 ($\lvert\eta\rvert < 2.4$ && $p_T < 60$ GeV)	
b-Tagging	`MV2c10`, 85% efficiency	

Large R Jets [R=1.0]

When the W or Z boson is highly boosted and decayed from a heavy particle, the outcoming quarks would be close to each other. In this case the small R jets would not have enough resolution power to reconstruct them individually, so the large R jets (or called "fat jets" and denoted as J) are reconstructed to collect the energy deposits from the close-by quarks. The full selection on the fat jets could be seen in Tab. 3.5. With this topology, the jet mass and p_T would need a further correction due to the limited calorimeter spatial resolution. This is performed with the track-assisted mass, m^{TA} [72], as the calorimeter cannot provide enough spatial resolution. m^{TA} is estimated from the tracks left by charged jet partons inside the fat jets defined as:

$$m^{TA} = m^{trk} \times \frac{p_T^J}{\sum p_T^{trk}} \tag{3.12}$$

Here, m^{trk} is the reconstructed mass of the tracks taken as massless particles, and p_T^{trk} is the vector sum from p_T of tracks. The ratio of p_T between the jet and tracks is to take in the neutral-to-charge fluctuations. It could then be combined with the calorimeter

mass, m^{calo}, into the combined mass, m^{comb}, by this definition:

$$m^{comb} = \frac{\sigma_{calo}^{-2} m^{calo} + \sigma_{TA}^{-2} m^{TA}}{\sigma_{calo}^{-2} + \sigma_{TA}^{-2}} \tag{3.13}$$

with σ_{calo} and σ_{TA} as pre-estimated mass resolutions for the calorimeter and track-assisted mass which are assumed to be uncorrelated. From Fig. 3.3, it could be seen that the calorimeter mass has better performance in the low $p_T(W)$ regime benefited from the great energy resolution, but it is degraded as $p_T(W)$ increases, while the track-assisted mass performed in an opposite way. The combined mass takes the merits of these two mass definitions and provide the best mass resolution ($\sim 10\%(15\%)$ at jet $p_T = 1\ TeV(2.5\ TeV)$). It is taken as the nominal fat jet mass in this analysis with the selection of $m^{comb} > 50\ GeV$. The jet p_T is the corrected by $p_T^{comb} = p_T^{calo} \times m^{comb}/m^{calo}$

Table 3.5.: Selection for large-R jets

	Signal Large-R Jets
Algorithm	anti$-k_t$, $R = 1.0$
p_T	>200 GeV
$\lvert\eta\rvert$	< 2.0
Mass threshold	50 GeV
W/Z Tagger	$D_2^{\beta=1}$&m^{comb}

However, the combined mass is still not proficient to select the W/Z decayed fat jets precisely, so the substructure of jets is needed to improve the boson tagging. This extra information is extracted with the subjets of $R = 0.2$ from a k_T algorithm performed on the clusters used to reconstruct small-R jets. Those tiny jets are then taken as the new entities to be "ghost-associated" with the fat jets, which mean the $anti - k_T$ algorithm is performed on the $R = 0.2$ subjects p_T selected by the threshould, $p_T^{R=0.2}/p_T^{R=1.0} > 0.05$, for a re-clustering. The jet substructure information could then be given by the discriminant, $D_2^{\beta=1}$, for the W/Z boson recognition [73] which is

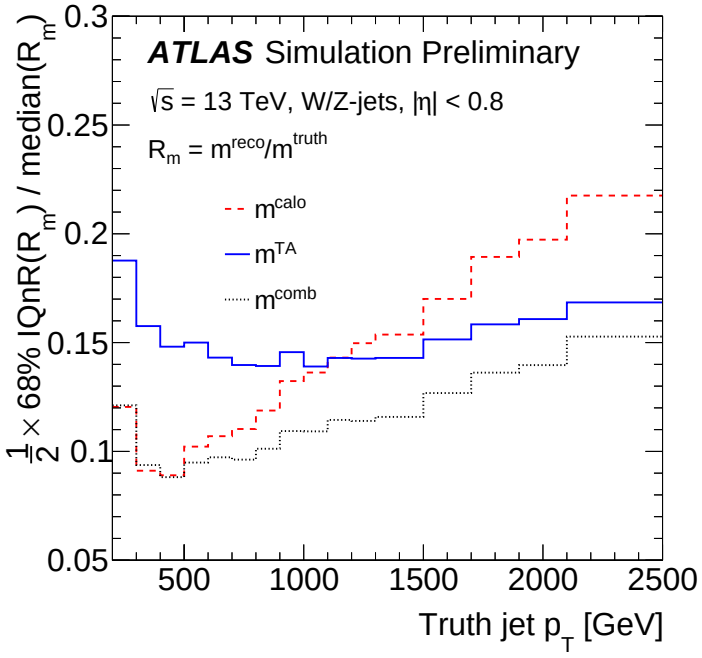

Figure 3.3.: The jet mass resolution as a function of jet p_T for jets produced from boosted W boson [72]. Three different jet mass reconstruction algorithms are displayed: the calo-jet mass (m^{calo}), the track-assisted mass (m^{TA}), and the combined TA+calo mass (m^{comb}).

defined as:

$$D_2^{\beta=1} = \frac{e_3^\beta}{e_2^\beta} \tag{3.14}$$

with e_2^β and e_3^β as:

$$e_2^\beta = \frac{1}{(p_T^{jet})^2} \sum_{i<j\in J} p_T^i p_T^j (\Delta R_{ij})^\beta \tag{3.15}$$

$$e_3^\beta = \frac{1}{(p_T^{jet})^3} \sum_{i<j<k\in J} p_T^i p_T^j p_T^k (\Delta R_{ij}\Delta R_{jk}\Delta R_{ik})^\beta \tag{3.16}$$

where ΔR is the distance between two $R = 0.2$ jets with i, j, and k as the indices for subjets. The boson tagging requirement is then done by a 2D cut on both $D_2^{\beta=1}$ and m^{comb} as a function of p_T shown in Fig. 3.4 with two working points (WPs), 50% and

80%, for the tagging efficiency. The curves are smoothed, but the cuts are applied in different bins.

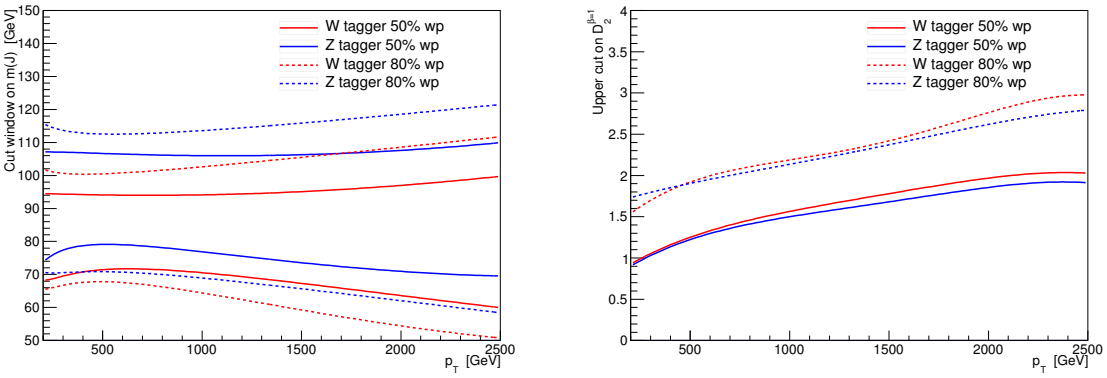

(a) **(b)**

Figure 3.4.: The thresholds of the mass window cut (m^{combo}) (a) and the upper cut on $D_2^{\beta=1}$ (b) as a function of p_T used in this analysis. The cuts for W-(Z)-boson tagging is shown by red (blue) lines.

Missing Transverse Energy

Although $E_T^{missing}$ is supposed to be reconstructed as shown in Sec. 2.3, hadronically decayed taus and photons are treated as jets for the intended final state in this analysis.

The cut on E_T^{miss} will be discussed in the next section.

3.4. Event Selection

The event selection in this analysis is performed to define signal regions which is expected to be enriched with events of new-physics-like (signal-like) detector signatures as well as the control regions enriched with the SM events which is to give constrains in the SM background contributions in signal regions when the simultaneous fit is performed(details in the next chapter). For this analysis, two control regions are defined

corresponding to two dominant background, W+jets (WR) and $t\bar{t}$ (TR) interactions, whose events are orthogonal to each other.

As discussed before, the signal regions are defined into four categories by production channels (VBF and ggF/DY) and jet topologies (single merged jets or two resolved jets): VBF merged, VBF resolved, ggF/DY merged, and ggF/DY resolved, and they are defined as the following:

- VBF: the existence of a jet pair with high invariable mass and broad η separation (the selection criteria is in the following)
- ggF/DY: no VBF jet pair is found
- Merged: at lease one large-R jet is found fulfilling the definition mentioned in Sec. 3.3.
- Resolved: no fat jet is found.

By this definition, the four categories are orthogonal to each other, and the category priority is given as: VBF merged $\rightarrow$ VBF resolved $\rightarrow$ ggF merged $\rightarrow$ ggF resolved. This scheme is performed to give the category with less background contamination higher priority. Furthermore, each categories have WW and WZ signal regions due to different charges of signal particles ($W' \rightarrow WZ$, and $G/H/Z' \rightarrow WW$) which are selected by the mass of hadronically decayed bosons. For WW signal regions, the fat jet or the dijet system should have the mass in the W mass window, while they are in the Z mass window for the WZ signal region. (It should be noted that WW and WZ signal regions are not orthogonal to each other).

If a event fails the signal region selection and passes either the control region selections, it would be recycled into the control regions. Then, the same event categorisation is performed in control regions , which gives each signal category a corresponding control region. The priority of event categorisation for both signal and control could be seen in Fig. 3.5.

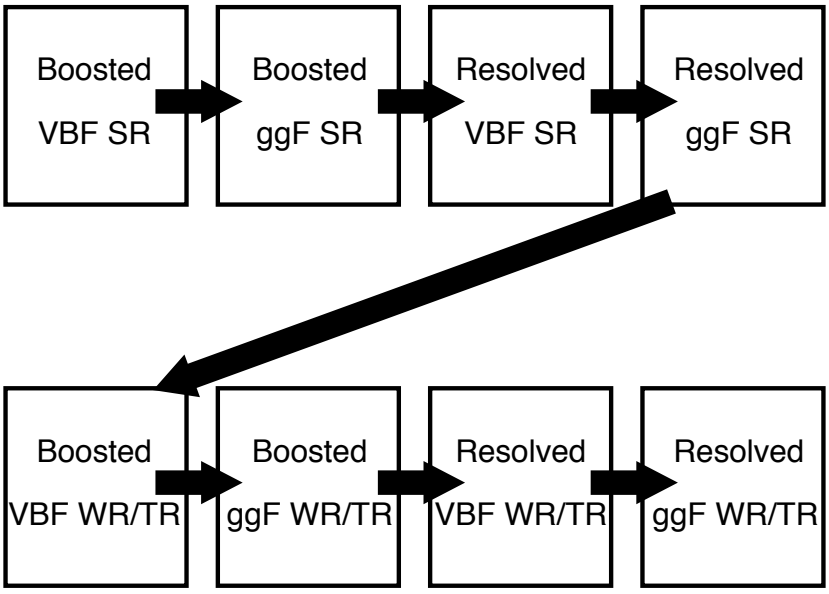

Figure 3.5.: Illustration on the priority of event categorisation for both signal and control regions.

3.4.1. Trigger

The first applied criterion on event selection is the trigger. The recorded data is a broad collection of different physical signatures, and our final state only accounts for a small fraction of them, so the trigger is used to choose the events with signatures of interest. Hereby, the chosen triggers for this analysis are single electron triggers, single muon triggers, and E_T^{miss} triggers. Because of the increasing luminosity provided by LHC, the trigger thresholds were enhanced in 2016 to reduce the trigger rate. For the MC samples, the run number is randomly generated, and the events shall only pass the triggers available in the random run number. The full trigger set used in this analysis is shown in Tab. 3.6

Three electron triggers are used in electron channel including the unprescaled lowest threshold one to maximize the signal efficiency. The other two triggers are used to select high p_T electrons with looser isolation requirement. The combined performance of the triggers is around 90% efficiency at the turn-on plateau as a function of p_T, which was studied by a dedicated $Z \to ee$ sample [74].

Table 3.6.: The list of triggers used in the analysis.

Data-taking period	Electron channel	Muon channel	
		$p_T, (\mu\nu) < 150\,GeV$	$P_T, (\mu\nu) > 150\,GeV$
2015	HLT_e24_lhmedium_L1EM20 HLT_e60_lhmedium HLT_e120_lhloose	HLT_mu20_iloose_L1MU15 HLT_mu50	HLT_xe70
2016a (run < 302919) ($L < 1.0 \times 10^{34}\,cm^{-2}\,s^{-1}$)	HLT_e26_lhtight_nod0_ivarloose HLT_e60_lhmedium_nod0 HLT_e140_lhloose_nod0	HLT_mu26_ivarmedium HLT_mu50	HLT_xe90_mht_L1XE50
2016b (run ≥ 302919) ($L < 1.7 \times 10^{34}\,cm^{-2}\,s^{-1}$)	same as above	same as above	HLT_xe110_mht_L1XE50
Total int. lumi. [fb^{-1}]	36.1	35.6	35.9

In muon channel, E_T^{miss} and muons triggers are both used, which depends on the transverse momentum sum of muon and E_T^{miss} denoted as $p_T(\mu\nu)$. For the scenario of $p_T(\mu\nu) < 150\ GeV$, two unprescaled single muon triggers are used with the logic of "OR": one for single isolated muons passing the lowest threshold, and another one with for single muon passing a higher threshold without the requirement on isolation. Otherwise, E_T^{miss} triggers are chosen for events with $p_T(\mu\nu) > 150\ GeV$, because the combined performance of muon triggers can only reach 70% efficiency on the plateau with the study on signal samples.

However, the E_T^{miss} cut in this analysis is below the plateau, so there might be the inconsistency between data and simulation in terms of the efficiency. Therefore, a "tag and probe" method is applied to study the trigger efficiency as a function of $p_T(\mu\nu)$ (because muons are invisible in the L1Calo system, so E_T^{miss} in the hardware trigger level is actually $p_T(\mu\nu)$). This study is performed on boosted and resolved channels respectively. The tagged events are required to fulfil the following conditions for the resolved (boosted) channel:

a) one muon with $p_T > 27\ GeV$

b) at least 2 signal jets (1 fat jet) selected for resolved (boosted) category

c) the unprescaled lowest threshold muon trigger is fired

d) $p_T(\mu\nu) > 75GeV$

Then, the probe is performed by the selection on the tagged events by whether the events pass the E_T^{miss} trigger. The efficiency is therefore taken as the ratio of probed event number over the tagged event number. The result for data and simulated $t\bar{t}$ events are shown in Fig. 3.6 for boosted channel and Fig. 3.7 for the resolved channel. They are presented as a function of $p_T(\ell\nu)$, and it could be seen that the efficiency reaches the 100% plateau at $pT(\mu\nu) \sim 200\ GeV$. However, E_T^{miss} trigger is applied for the case of $p_T(\mu\nu) > 150\ GeV$, and there is the efficiency discrepancy between data and simulation sample. To recover the discrepancy, the scaling factor is applied as an extra weight on simulated events for a proper modelling of background estimation from simulation. In the concern of the orthogonality, signal regions are a small fraction of events used in this study, so the interference is negligible.

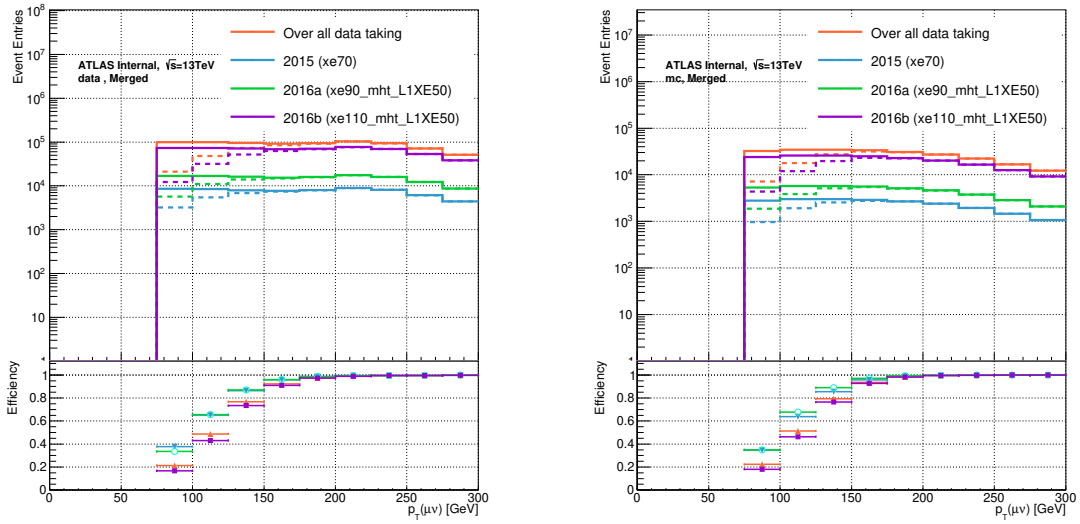

(a) **(b)**

Figure 3.6.: The upper plot is $p_T(\mu\nu)$ distribution of tagged (real) and probed (dotted) events in boosted channel for data (a) and $t\bar{t}$ events (b). The lower plots is the efficiency as a function of $p_T(\mu\nu)$

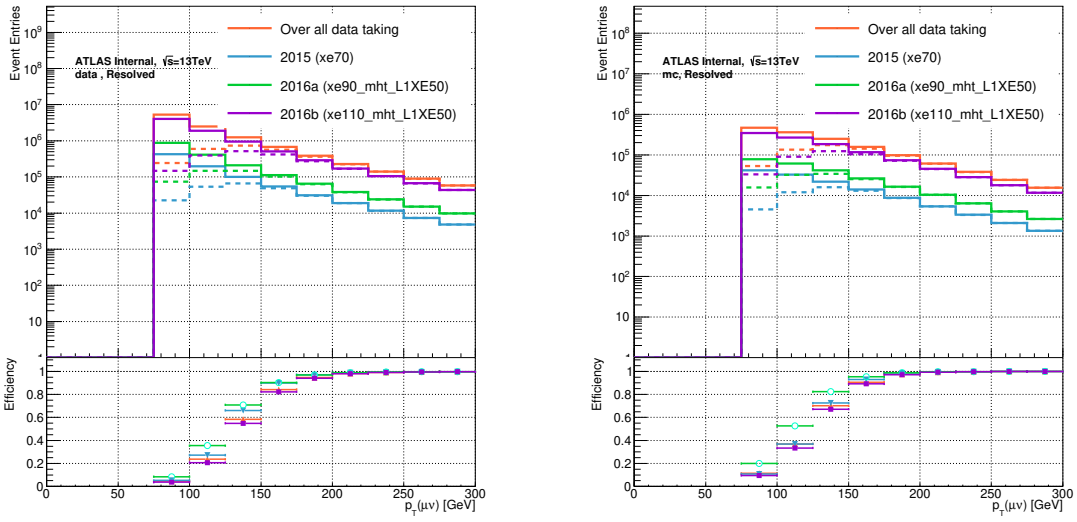

(a) **(b)**

Figure 3.7.: The upper plot is $p_T(\mu\nu)$ distribution of tagged (real) and probed (dotted) events in resolved channel for data (a) and $t\bar{t}$ events (b). The lower plots is the efficiency as a function of $p_T(\mu\nu)$

3.4.2. Event Cleaning and Preselection

After the trigger, the event "quality" is verified by a series of flags in data determining the suitability of an event for physical analyses. The following is the list:

- **Good Run**: when the detector operates in a proper status without intolerable defects like dead channels in the colorimeter covering a significant region, the runs go into the good run list (GRL). Only the events contained in the GRL are considered in this analysis.
- **Primary Vertex**: because all the physical objects are required to origin from the primary vertex, its existence is essential. Events without a proper primary vertex (defined in Sec. 2.3) are discarded.
- **Tile Error Veto**: part of the channels in tile detector are broken. If they accept any physical objects, this flag would be marked, and the events are vetoed.
- **LAr Error Veto**: part of the channels in LAr detector are broken. If they accept any physical objects, this flag would be marked, and the events are vetoed.

- **SCT Error Veto**: part of the channels in SCT detector are broken. If they accept any physical objects, this flag would be marked, and the events are vetoed.
- **Core Error Veto**: during data-taking periods, the ATLAS central DAQ system might suffer from some glitches which broke the data recording, and the flag is marked for events. They are also vetoed in this analysis.

3.4.3. Reconstructed Mass of Signal Objects, m_{WV}

This analysis is searching for the mass resonance of exotic particles. If there is the existence of signal particles with the narrow width assumption applied in this analysis, a peak should be spotted in the mass spectrum of reconstructed from signal objects (two jets, one lepton, and one neutrino) denoted as m_{WV}. Therefore, m_{WV} is taken as the discriminant to input to the statistic interpretation which will be discussed in the next chapter. However, the longitudinal momenta of neutrinos, p_z^ν, are not measured, so the mass resolution is degraded. To improve it, p_z^ν is solved with the assumption that all neutrinos are coming from the process, $W \to l\nu$, so E_T^{miss} could be taken equally as transverse component of neutrino momentum, p_T^ν. Therefore, the equation of energy conservation of W boson decays can be written down as:

$$m_W^2 = m_l^2 + 2E^l\sqrt{{p_T^\nu}^2 + {p_z^\nu}^2} - 2\vec{p}_T^{\,l} \cdot \vec{p}_T^{\,\nu} - 2p_z^l p_z^\nu \tag{3.17}$$

with the four-vector of leptons as (m_l, p_T^l, p_z^l) where m_l and p_T^l could be written as:

$$p_T^l = \sqrt{{p_x^l}^2 + {p_y^l}^2} \tag{3.18}$$

$$m_l = \sqrt{{E^l}^2 - {p_T^l}^2 - {p_z^l}^2} \tag{3.19}$$

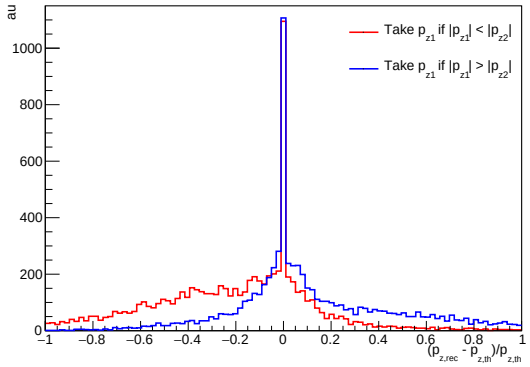

Figure 3.8.: The p_z^ν resolution with absolute values of the solutions, bigger (blue) and smaller (red) one.

In SM, W bosons have the mass of 80 GeV (m_W), so m_l for electrons and muons is negligible. This leads to the quadratic equation with p_z^ν:

$$4{p_T^l}^2{p_T^\nu}^2 - 4\left(m_W^2 + 2\vec{p}_T^{\,l}\cdot\vec{p}_T^{\,\nu}\right)p_z^l p_z^\nu - \left(m_W^2 + 2\vec{p}_T^{\,l}\cdot\vec{p}_T^{\,\nu}\right)^2 + 4{p_T^l}^2{p_T^\nu}^2 = 0 \tag{3.20}$$

If the solutions are complex, only the real terms are taken into this analysis, and the imaginary term is discarded. If both solutions are real, the resolutions are compared with the absolute value of solutions (bigger one and smaller ones) to determine which solution to use. It is defined as:

$$\sigma = \frac{p_z^{truth} - p_z^\nu}{p_z^{truth}} \tag{3.21}$$

with p_z^{truth} as the neutrino longitudinal momentum at generator level (MC truth). The result could be seen in Fig. 3.8, and it indicates the bigger one has slightly better performance in terms of the mass resolution, so it is kept. The similar assumption is also made on the hadronically decayed objects. The two selected signal jets are also assumed to always originate from a W or Z boson, so the reconstructed mass of two selected signal jets, m_V, is supposed to be sim80 GeV (sim91 GeV) for W (Z) boson. Therefore, the invariant mass and transverse momentum of this di-jet system, m_{jj} and

$p_T(j,j)$, are taken to correct the transverse momentum of the di-jet system, p_T^{corr}:

$$p_T^{corr} = p_T(j,j) \times \frac{m_V}{m_{jj}} \tag{3.22}$$

With the two corrected boson systems ($W \to \ell\nu$ with p_z^ν correction and m_W, and $V \to jj$ with p_T^{corr} and m_V), the invariant mass of the diboson system, m_{WV}, is evaluated. A comparison for the evaluations with and without this "mass-constraint" correction could be seen in Fig. 3.9 with NWA Higgs boson samples of 300 GeV, 500 GeV, and 700 GeV, and the ones with this correction has a better resolution.

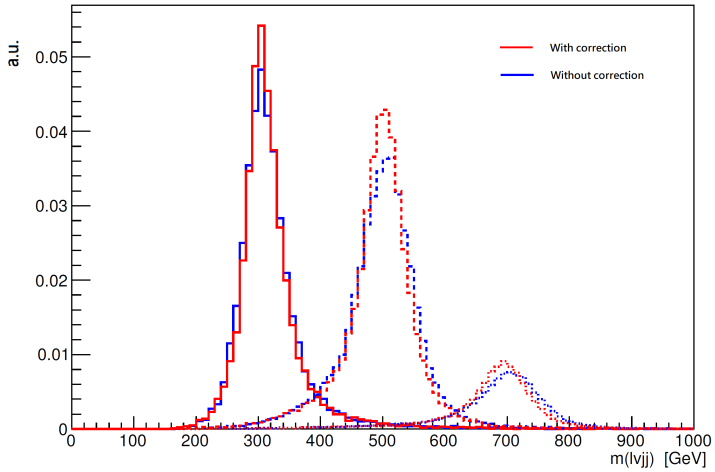

Figure 3.9.: m_{WV} distributions for $gg \to H \to WW$ signals at $m = 300\ GeV$ (solid), 500 GeV (dashed) and 700 GeV (dot), with (red) and without (blue) W-mass constraint to $W \to jj$ system.

3.4.4. VBF Event Selection

As VBF signal regions have better sensitivity than ggF/DY ones, the selection criteria play an important role in this analysis. The optimization on the selection is conducted in three steps. First, all VBF events are required to have at least 4(2) jets in the resolved (boosted) channel. Second, the two jets in the dijet system are chosen as the pair with the highest mass, opposite η signs, and not b-tagged. This pair was chosen prior to the $W/Z \to jj$ signal jet selection and removed from signal jet candidates. Then, the optimization is performed on a 2-dimensional phase space constructed by $\Delta\eta(j,j)$

and $m(j,j)$ which are two most evident signatures of this production process. The performance of the cuts on the two variables is determined by signal significance, σ, which is evaluated on the m_{WV} distribution which is defined as:

$$\sigma^2 = \sum_{i}^{N^{bin}} \left(\frac{s_i}{s_i + b_i + (\Delta b_i)^2} \right)^2 \tag{3.23}$$

Here, s_i and b_i are the signal and background event numbers in the $m_W V$ distribution with the binnings shown in Eq. 4.2 and 4.3, and Δ is set at 1.5% taken as the hypothesised systematic uncertainty. Fig. 3.10 shows the result of the optimization performed on the signal sample with 700 GeV HVT, and the best significance could be achieved by:

- $\boldsymbol{m_{jj}^{VBF} > 770\ GeV}$
- $\boldsymbol{\Delta\eta(jj) > 4.7}$

The other reason to choose this set of cuts is to make it consistent with $WZ/ZZ \rightarrow lljj/\nu\nu jj$ analysis [75] for the combination in next chapter. In the following of this thesis, the reconstructed mass of two VBF jets is denoted as m^{VBF}.

3.4.5. Boosted Event Selection

In the boosted channel, the most important selection above the others is that at least one large R jet fulfils the W/Z boson 80% efficiency tagging working points. Then, those events are further categorized into high purity and low purity regions determined by whether the 50% tagging working points are passed. The full selection is seen in Tab. 3.7. It should be noted that W and Z boson taggers are applied respectively in signal regions to separate the $W \rightarrow J$ and $Z \rightarrow J$ events, which gives the WW and WZ signal regions for each signal region category.

For the other boson system which decays leptonically, the requirement is that exactly one signal lepton is selected with E_T^{miss} above 100 GeV to suppress the multijet back-

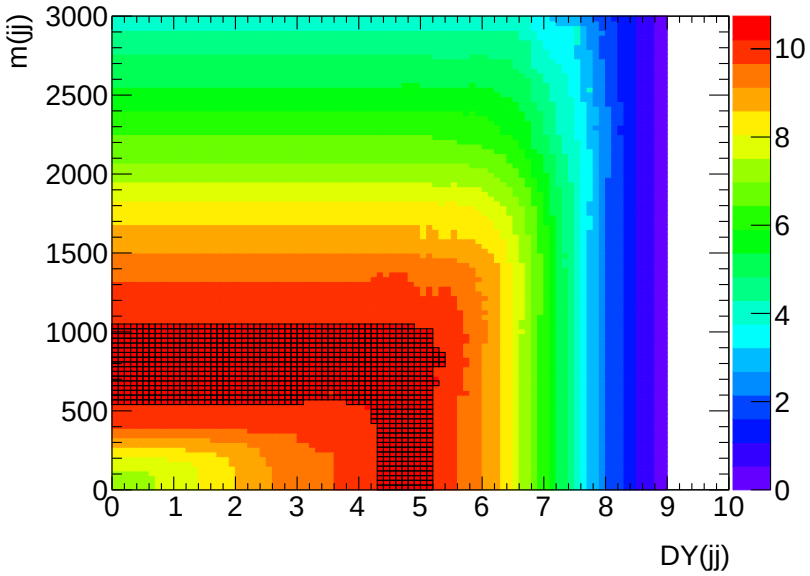

Figure 3.10.: The signal significance for the VBF WW signal as a function of the VBF cuts on $\Delta\eta(j_1, j_2)$ (which is shown as DY(jj) in the plot) and $m(jj)$ for signal mass 700 GeV respectively. The black outlined bins are those whose values vary from the maximum by less than 5%.

ground. The additional requirements on the leptonical decay system is two topological cuts with the study on the simulation samples:

(a) $E_T^{miss}/p_T(e,\nu) > 0.2$

(b) $p_T(\ell,\nu)/m_{WV} > 0.3(0.4)$ for VBF (ggF) category

(a) is only for the electron channel to reduce multijet background of which electrons and E_T^{miss} are irrelevant, so the events tend to have smaller ratio of met over $p_T(e,\nu)$ (transverse vector sum of met and electron p_T). For the case of (b), because the two reconstructed bosons in SM background events are not correlated, the ratio of $p_T(ell,\nu)$ over m_{WV} has smaller number. Therefore, the cut is deployed to suppress the SM background contribution. [76] These criteria are consistent across signal and control regions.

On the side of the hadronically decayed boson is only the large R jet. In addition to the requirement in the last section, the high purity regions (HP) (for both signal and control regions) demand the fat jet boson-tagged at 50% WP, and it is the most sensitive region to signal. Events with fat jets failing 50% but passing 80% WPs go

Table 3.7.: Summary of the selection criteria in the definition of the signal region (SR), W+jets control region (W CR) and $t\bar{t}$ control region ($t\bar{t}$ CR), in the high-purity (HP) and low-purity (LP) categories.

Selection		SR		W CR		$t\bar{t}$ CR	
		HP	LP	HP	LP	HP	LP
$W \to l\nu$	Num of signal leptons	1					
	Num of vetoed leptons	0					
	E_T^{miss}	$> 100GeV$					
	$p_T(l\nu)$	$> 200GeV$					
$W/Z \to J$	Num of large-R jets	≥ 1					
	$D_2^{(\beta=1)}$ 50 % WP	pass	fail	pass	fail	pass	fail
	$D_2^{(\beta=1)}$ 80 % WP	—	pass	—	pass	—	pass
	W/Z mass 50 % WP	pass	fail	—	—	pass	fail
	W/Z mass 80 % WP	—	pass	fail	fail	—	pass
Topology cuts	$p_T(l\nu)/m_{WV}$ $p_T(J)/m_{WV}$	$> 0.3(0.4)$ for VBF (ggF) category					
Top-quark veto	Num of b-tagged jets	0				≥ 1	
Multi-jet BG Cleaning Cut	$E_T^{miss}/p_T(l\nu) > 0.2$	Electron channel only					
Existence of VBF jets		yes (no) for VBF (ggF) category					

into the low purity region (LP). By doing this, the combined sensitivity of the HP and LP signal regions is improved by around 10%. [76] If the fat jet only fails mass cut and pass the $D_2^{\beta=1}$ of boson tagging, this event would not be discarded but chosen into W+jet control region instead. Finally, p_T of the fat jet is also required to be above $0.3(0.4)m_{WV}$ for the energy balance in VBF(ggF) category. The event categorization of signal and W+jet control regions for both high and low purity categories is illustrated in Fig. 3.11. To reduce the $t\bar{t}$ background contribution, the subjets associated to the selected large R jet shall not be b-tagged in the W+jet control region and signal region. If any of them or the small R jets ($R = 0.4$) pass the 85% b-tagging WP, the event would go into the top control region.

Fig. 3.12 and Fig. 3.13 are the m_{WV} distributions for the comparison of signal and background events in high purity and low purity signal regions for electron and muon channels respectively.

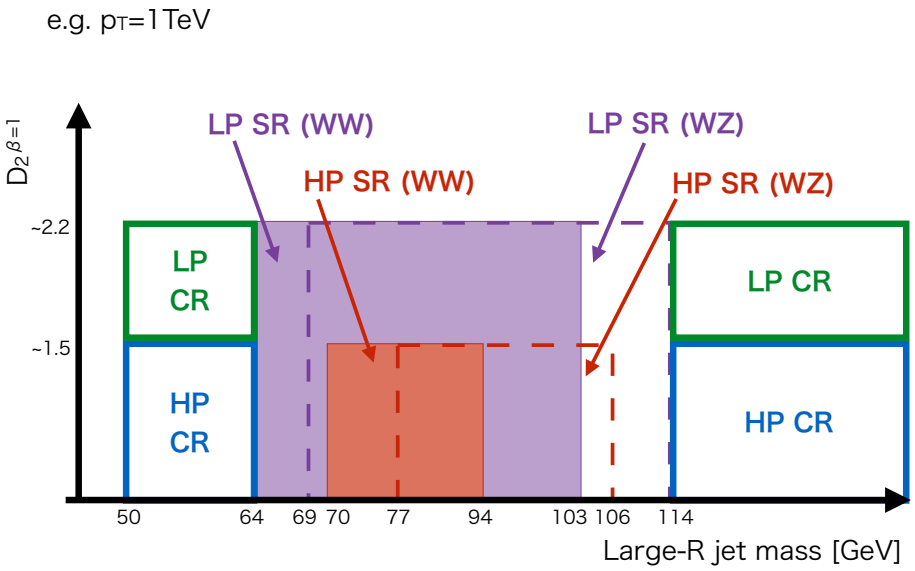

Figure 3.11.: Definitions of signal region (SR) and W+jets control region (CR) for the event with the large-R jet of $p_T = 1\,\text{TeV}$ based on fat jet boson tagging parameters, $D_2^{\beta=1}$ and fat jet mass.

3.4.6. Resolved Event Selection

The resolved channel has a lower sensitivity than the boosted channel, but it still helps to recover the events lost in the lower energy regime. If the event has no fat jet fulfilling the selection criteria, it goes to the resolved category. The full selection for resolved signal and control regions can be seen in Tab. 3.8.

As in the boosted channel, the leptonically decaying W boson has a signal lepton fulfilling the object definition of the last section. However, the E_T^{miss} cut here is lowered to 60 GeV for the less energetic system as compared to the boosted channel. For the energy balance, the ratio between $p_T(l,\nu)$ and m_{WV} shall be over 0.3 (0.35) for VBF (ggF) category.

On the hadronic side, the two signal jets are selected after VBF jets, and they are required to have p_T above 60 GeV (45 GeV) for the leading (subleading) one to suppress the SM background. Similar to the boosted event selection, to recognize the

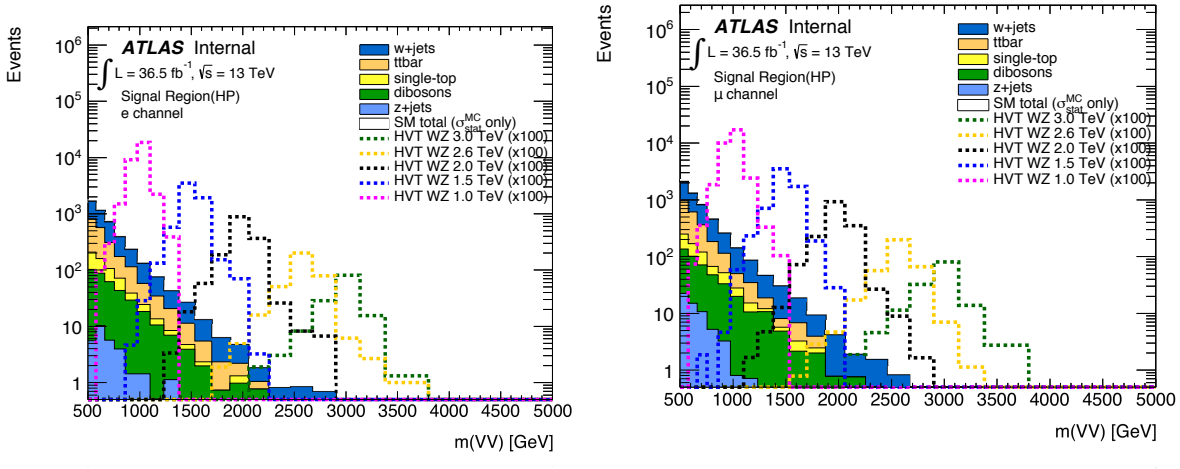

(a) **(b)**

Figure 3.12.: The m_{WV} distribution (denoted as m(VV) in the plots) in the HP signal region for (a) electron and (b) muon channels for SM background from simulation which is normalized to the integrated luminosity of 36.5 fb^{-1}.The HVT WZ signals with mass of 1.0 TeV, 1.5 TeV, 2.0 TeV, 2.6 TeV and 3.0 TeV are overlaid and scaled to 100 $\times$ the cross section.

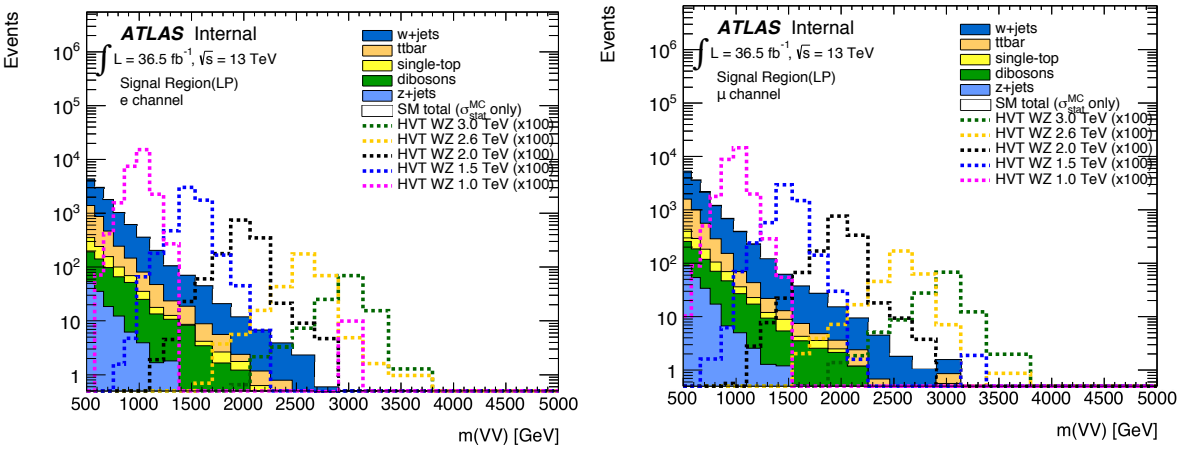

(a) **(b)**

Figure 3.13.: The m_{WV} distribution (denoted as m(VV) in the plots) in the LP signal region for (a) electron and (b) muon channels for SM background from simulation which is normalized to the integrated luminosity of 36.5 fb^{-1}.The HVT WZ signals with mass of 1.0 TeV, 1.5 TeV, 2.0 TeV, 2.6 TeV and 3.0 TeV are overlaid and scaled to 100 $\times$ the cross section.

boson which decays to the two jets, two mass windows are applied respectively to select WW and WZ signal regions, which are $[66, 94]$ GeV for WW signal region ($W \rightarrow jj$)

Table 3.8.: Summary of the selection criteria of the resolved analysis for the WW and WZ signal regions (SR), W+jets control region (WR) and $t\bar{t}$ control region (TR).

cuts		WW SR	WZ SR	WR	TR
$W \to \ell\nu$ selection	Number of signal leptons	1			
	Number of veto leptons	0			
	E_T^{miss}	$> 60GeV$			
	$p_T(\ell\nu)$	$> 75GeV$			
$W/Z \to jj$ selection	Number of small jets	≥ 2			
	$p_T(j1)$	> 60 GeV			
	$p_T(j2)$	> 45 GeV			
	m_{jj}	[66, 94]GeV	[82, 106]GeV	$< 66GeV$ or [106, 200]GeV	[66, 106]GeV
Topology cuts	$\Delta\phi(j,\ell)$	> 1.0			
	$\Delta\phi(j, E_T^{miss})$	> 1.0			
	$\Delta\phi(j,j)$	< 1.5			
	$\Delta\phi(l, E_T^{miss})$	< 1.5			
	$p_T(e\nu)/m_{WV}$ $p_T(jj)/m_{WV}$	$> 0.3(0.35)$ for VBF (ggF) category			
Top veto	Number of b-tagged jets in W/Z	≤ 1	≤ 2	≤ 1	≥ 2
	Number of other b-tagged jets	0			or ≥ 1
Existence of VBF jets		yes (no) for VBF (ggF) category			

and $[82, 106]$ GeV for the WZ signal region ($Z \to jj$). The top control regions don't have the WW and WZ regions separated, so the mass window is applied with $[66, 106]$ GeV as the OR condition of W and Z mass windows. Events with a dijet mass which falls into the side band region of W and Z boson mass ($[0, 66]$ GeV or $[106, 200]$ GeV) are taken into the W+jet control region. The energy balance requirement here is the same as the leptonic system: $p_T(jj)/m_{WV} > 0.3(0.35)$ for the VBF (ggF) category. The two selected jets in the W(Z) mass window are allowed to have one(two) of them b-tagged. The existence of any additional b-tagged jets would then make the event go into the top control region.

Different from the boosted channel, the resolved channel has the abundant background contribution from multijet events (details in next section), so they are suppressed by a series of topological cuts with the optimization by the study on the dijet MC samples, which are listed below [76]:

- $\Delta\phi(j,l) > 1.0$
- $\Delta\phi(j, E_T^{miss}) > 1.0$

- $\Delta\phi(j,j) < 1.5$
- $\Delta\phi(l, E_T^{miss}) < 1.5$

Fig. 3.14 is the m_{WV} distributions for comparison of signal and background in resolved signal regions for ggF and VBF categories respectively. The signal samples are with lower mass, because resolved channel has better sensitivity to them.

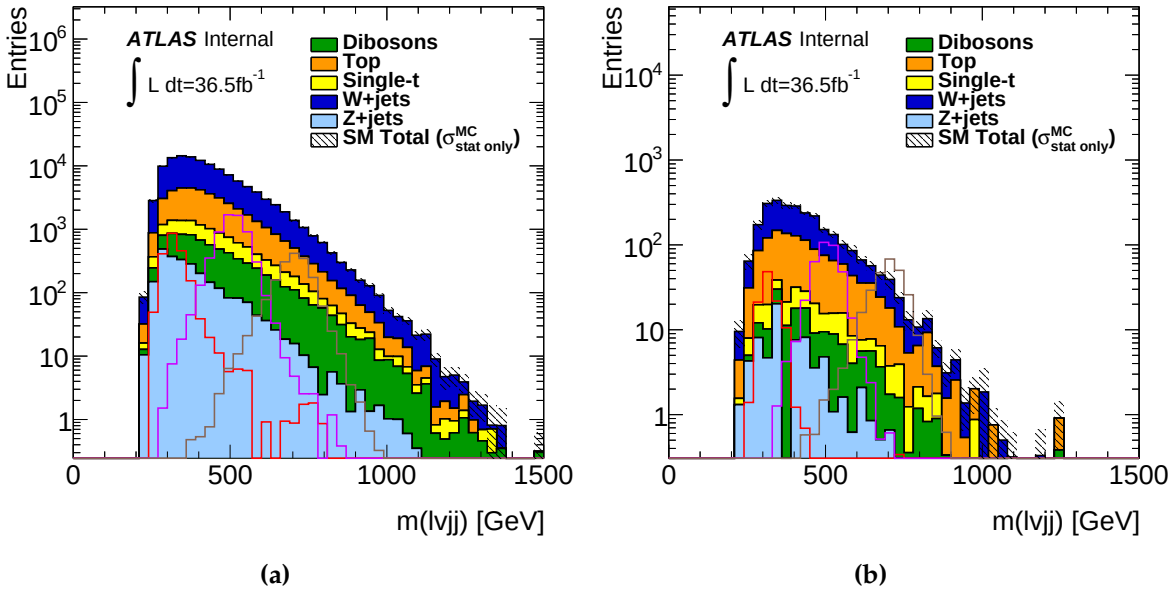

Figure 3.14.: The m_{WV} (denoted as m(VV) in the plots) distribution in the resolved signal region for (a) ggF and (b) VBF channels for SM background from simulation which is normalized to the integrated luminosity of 36.5 fb^{-1}.The HVT WZ signals with mass of 300 GeV, 500 GeV, and 700 GeV are overlaid and scaled to 100 $\times$ the cross section..

3.4.7. Multijet Background Estimation

As discussed above, the SM backgrounds are estimated from Monte-Carlo simulation and constrained in the dedicated control regions. However, the multijet processes is poorly modelled in MC simulation due to the lack of understanding of QCD, so simulation is not feasible for this background contribution. Its contribution is from the following sources:

- **Photon Conversion**: When photons are travelling through detector material, the interaction between photons and nucleus induces the pair production which has the products of a electron-position pair. The electrons from this source are difficult to distinguish from the signal ones decayed from Z bosons. This contribution is considered only in the electron channel.
- **Lepton Misidentification**: Soft charged hadrons could be blocked at ECAL and leave no signature in HCAL, which is identical to electron signatures. In this case, they are reconstructed as electrons instead of jets. This source only contributes to electron channel.
- **Heavy Hadron Decay**: The decay products of heavy hadrons also include leptons. If their decay is close to the primary vertex, the decayed leptons are not distinguishable from the prompt ones. Both electrons and muons have the contribution from this source.

This background contribution is only considered in resolved channel, while it is negligible in boosted channel. [76]. Different from the SM background, the multijet background estimation is performed with fake factor method, a data-driven approach. The details of this method can be found in the ATLAS Run2 VHbb analysis [77, 78].

Methodology

The fake factor method is one type of ABCD methods with an illustration in Fig. 3.15. Two uncorrelated parameters are chosen to divide the data events into four categories, A, B, C, and D which are orthogonal to each other, and A is taken as the signal or control region. If the event contributions are the same across all the regions, the following equation should be held true:

$$\frac{N_A}{N_B} = \frac{N_C}{N_D} \tag{3.24}$$

N stands for the event numbers in each region. With a proper choice on the parameter A and parameter B, the multijet events are enriched in region B, C, and D, and the multijet contribution in region A could then therefore be estimated with the equation

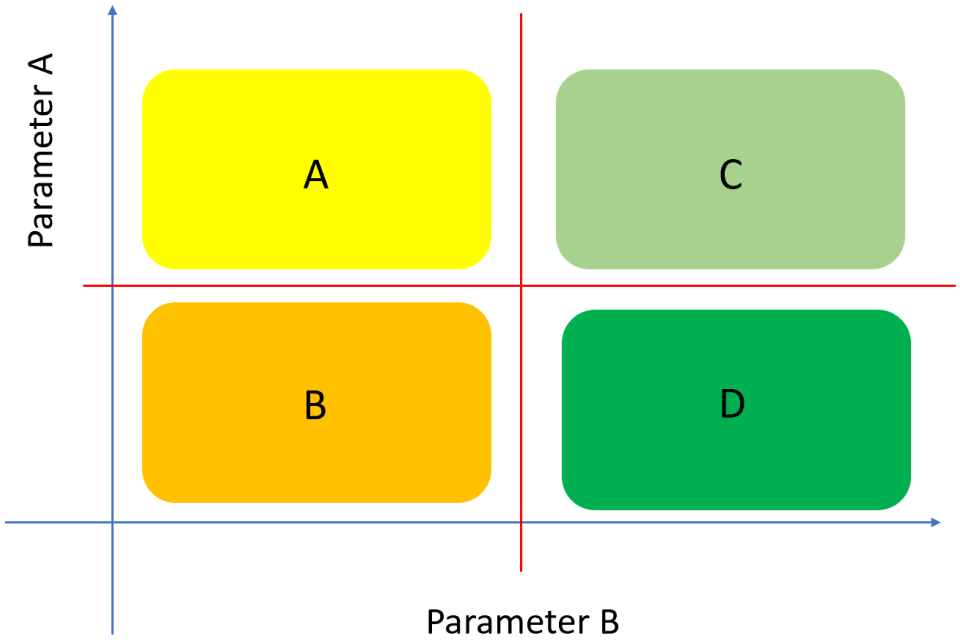

Figure 3.15.: The illustration of ABCD method with two uncorrelated parameters, A and B, to divide events into four categories, A, B, C, and D, and A is the signal/control region.

shown above. The ratio of event numbers of C and D regions is called "fake factor".

In this analysis, the number of small R jets is taken as parameter B, while the muon isolation (electron identification) is chosen to be parameter A for the muon (electron) channel. The fake factors are estimated from data in the region with only one small R jet selected called single jet control region (region C+ region D) which is orthogonal to signal regions which demands two or more jets. The events with any existence of fat jets passing the selection is vetoed ($p_T^J > 200\ GeV$ && $m^J > 50\ GeV$) to keep the orthogonality to boosted regions. This region is then further divided into two subregions by muon isolation and electron identification. The first subregion has the same lepton selection as the signal region with signal leptons, while the second one has the inverse requirement on leptons with inverse leptons. The lepton definition could be seen in table 3.9. With $p_T(\mu\nu) < 150\ GeV$, an isolated muon trigger is applied with a requirement on isolation of $ptvarcone30/p_T^\mu < 0.07$. In this case, the isolation requirement for inverse muons is tightened to the same upper limit to keep the consistency of muons reconstructed at trigger and offline levels. E_T^{miss} triggers instead of

muon triggers are applied in the region of $p_T(\mu\nu) > 150GeV$, so the isolation issue is not present. Therefore, the isolation upper limit is loosen to 0.15. Then, the fake factor is defined as the ratio of event numbers of these two subregions:

$$f = \frac{N_{event}(CR(1j, \ell\,[signal]))}{N_{event}(CR(1j, \ell\,[inverse]))} \tag{3.25}$$

Furthermore, to achieve a better accuracy, this was performed in the binnings presented in Tab. 3.10. The fake factors have the dependence on lepton η (this dependence is for the consideration of detector homogeneity) and lepton p_T (the multijet background contribution source varies with lepton p_T). Additional binning on the E_T^{miss} is applied in electron channel. For both channels, the fake factor is estimated in two different regions with $p_T(\mu\nu) < 150\ GeV$ and $p_T(\mu\nu) > 150\ GeV$, because they have different amount of multijet contamination. Fake factors are shown as a function of lepton p_T in Figure 3.16 for the region of $p_T(l\nu) > 150\ GeV$ for which it could be noticed that fake factors for electron channel are just up to $p_T = 190\ GeV$. To have the multijet background estimation for high p_T electrons with $p_T > 190\ GeV$, fake factors are roughly evaluated in p_T bins only for this p_T range which is shown in Fig. 3.17.

Table 3.9.: Definition of leptons in the single jet control regions

	Signal Lepton	Inverse Lepton
electron	TightLH	MediumLH (!TightLH)
muon($p_T(l\nu) > 150GeV$)	$Iso_{trk} < 0.06$	$0.06 < Iso_{trk} < 0.15$
muon($p_T(l\nu) < 150GeV$)	$Iso_{trk} < 0.06$	$0.06 < Iso_{trk} < 0.07$

The fake factors are then applied on events from the "inverse leptopn" control regions. They have the same event selection as the signal and control regions, but the only lepton in those events is required to be an inverse leptons with the same definition as shown in Tab. 3.9 (Region B in Fig. 3.15). With Eq. 3.24, it could be seen that the multijet event number in the region of interest (N_A) could be presented as:

$$N_A = N_B \times f \tag{3.26}$$

Table 3.10.: Binning for electrons and muons to evaluate fake factor

channel	$p_T(GeV)$	$\|\eta\|$	$E_T^{miss}(GeV)$
electron	27-115	0, 1.37, 1.52, 2.47	0, 60, 75, ∞
	115-135		0, 38, 52, ∞
	135-155		0, 26, 43, ∞
	155-190		0, 25, 45, ∞
	Fig. 3.17 (190-∞)	NA	NA
muon	27, 42, 59, 76, 99, ∞	0, 1.05, 1.5, 2.5	N/A

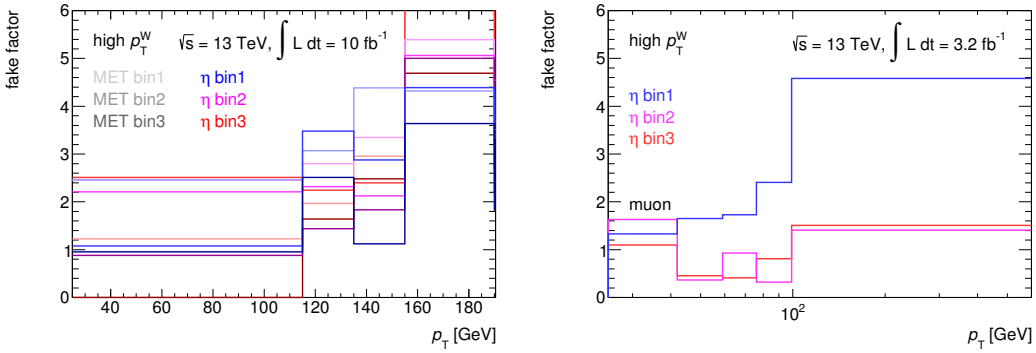

(a) **(b)**

Figure 3.16.: Fake factors for the corresponding binnings (shown in text) in electron (a) and muon (b) channels

with f from Eq. 3.25. Therefore, fake factors could be used as event weights applied on events from inverse lepton control regions, which then gives the multijet event number in the signal/control regions.

Electroweak Subtraction

Electroweak interactions ($t\bar{t}$, W/Z+jets, diboson and single top) could also contribute to multijet events in addition to the multijet background, so they might be double counted from the fake factor method and background simulation. To avoid this issue, those events are removed by employing fake factors on events from the simulation in

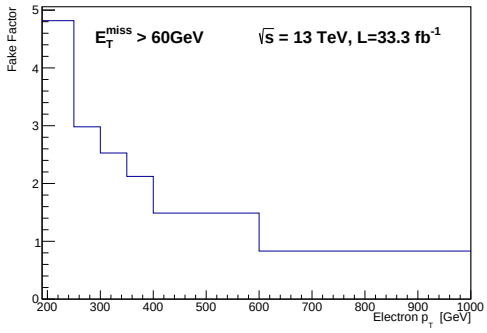

(a)

Figure 3.17.: Fake factors for high p_T electrons

the inverse lepton control region, which could be expressed as the following equation:

$$N_{events}^{MJ} = N_{events}^{data} - N_{event}^{MC} \tag{3.27}$$

It means that the multijet background events (N_{events}^{MJ}) are given by removing the estimated SM multijet contribiton (from simulation) (N_{event}^{MC}) from the estimated multijet events (from data)(N_{events}^{data}), and it is anticipated that $N_{events}^{data} \approx N_{event}^{MC}$ with $E_T^{miss} > 150\ GeV$. A control region was defined to verify this with a simple selection of at least two small-R jets with $p_T > 20\ GeV$ and exactly one signal electron or muon. This region is overlapped with signal regions, while the signal events just account for a small fraction, so this doesn't bias the final result. The comparison between data and the SM background from the MC simulation in this control region is shown in Figure 3.18 and Figure 3.19 for electron and muon channels respectively. The observed discrepancy was contributed by the multijet events. However, unfortunately, an inconsistency remains in the region of $E_T^{miss} > 150\ GeV$. That means the multijet events from the SM backgrounds (electroweak interactions) are not well-modelled. In this case, the electroweak subtraction is applied with a scale factor derived from the ratio of events from data and simulation in the bin of $150GeV < E_T^{miss} < 250\ GeV$ defined as:

$$f = \frac{N_{event}(data)}{N_{event}(MC)} \tag{3.28}$$

It is applied as an additional correction on fake factors for events with $E_T^{miss} > 150GeV$ from simulation to correct this MC mis-modelling. The electroweak subtraction factors

for electron and muon channels are shown in Tab 3.11. For the $E_T^{miss} < 150\ GeV$ region, the simulation sample has the performance as what we expected, so this correction is not applied.

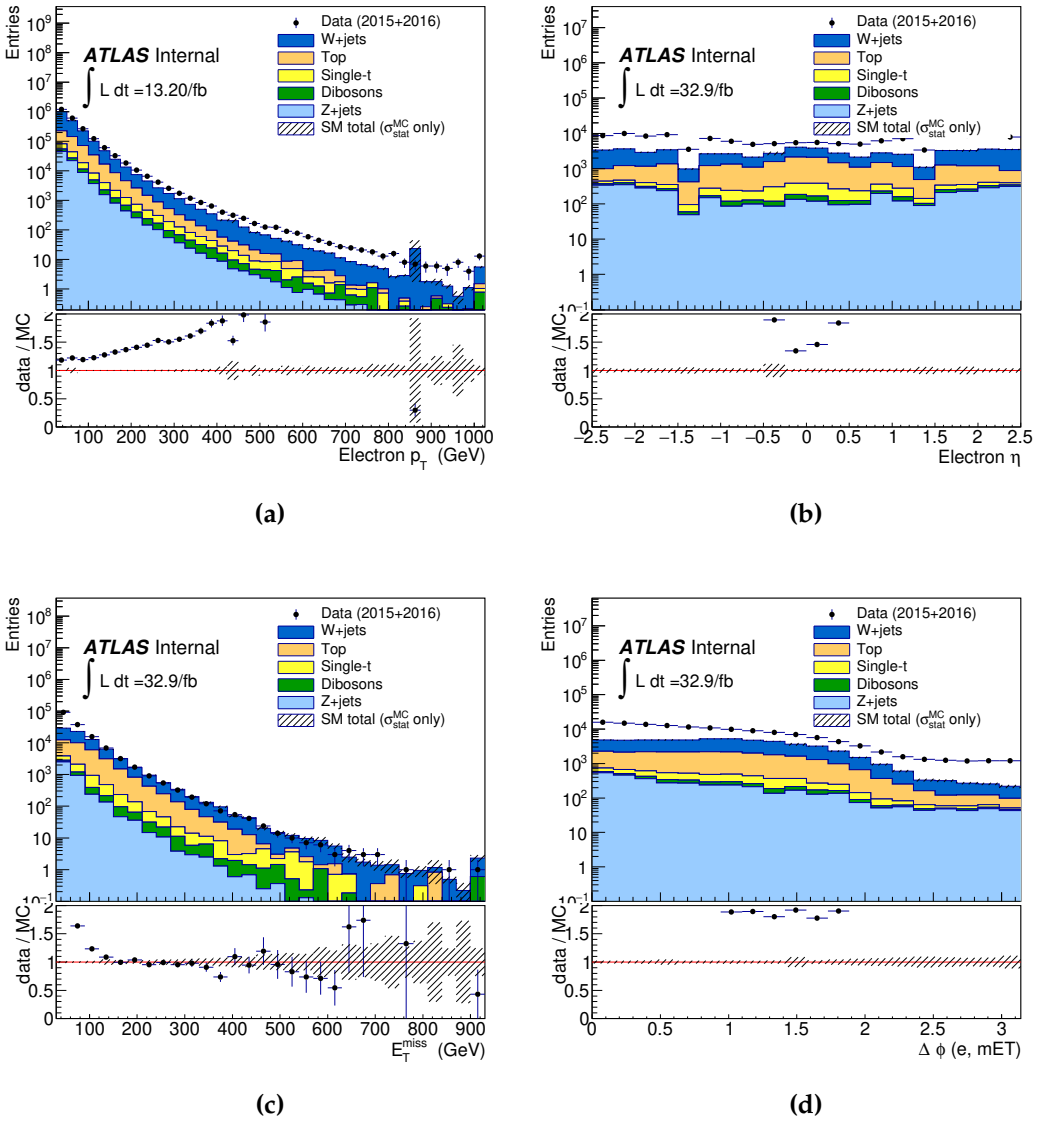

Figure 3.18.: The distribution of lepton p_T, η, E_T^{miss} and $\Delta\phi$(e,E_T^{miss}) in dijet fake control region with inversed lepton for electron channel. The inconsistency is thought to be comprised of multijet events without applying electroweak subtraction.

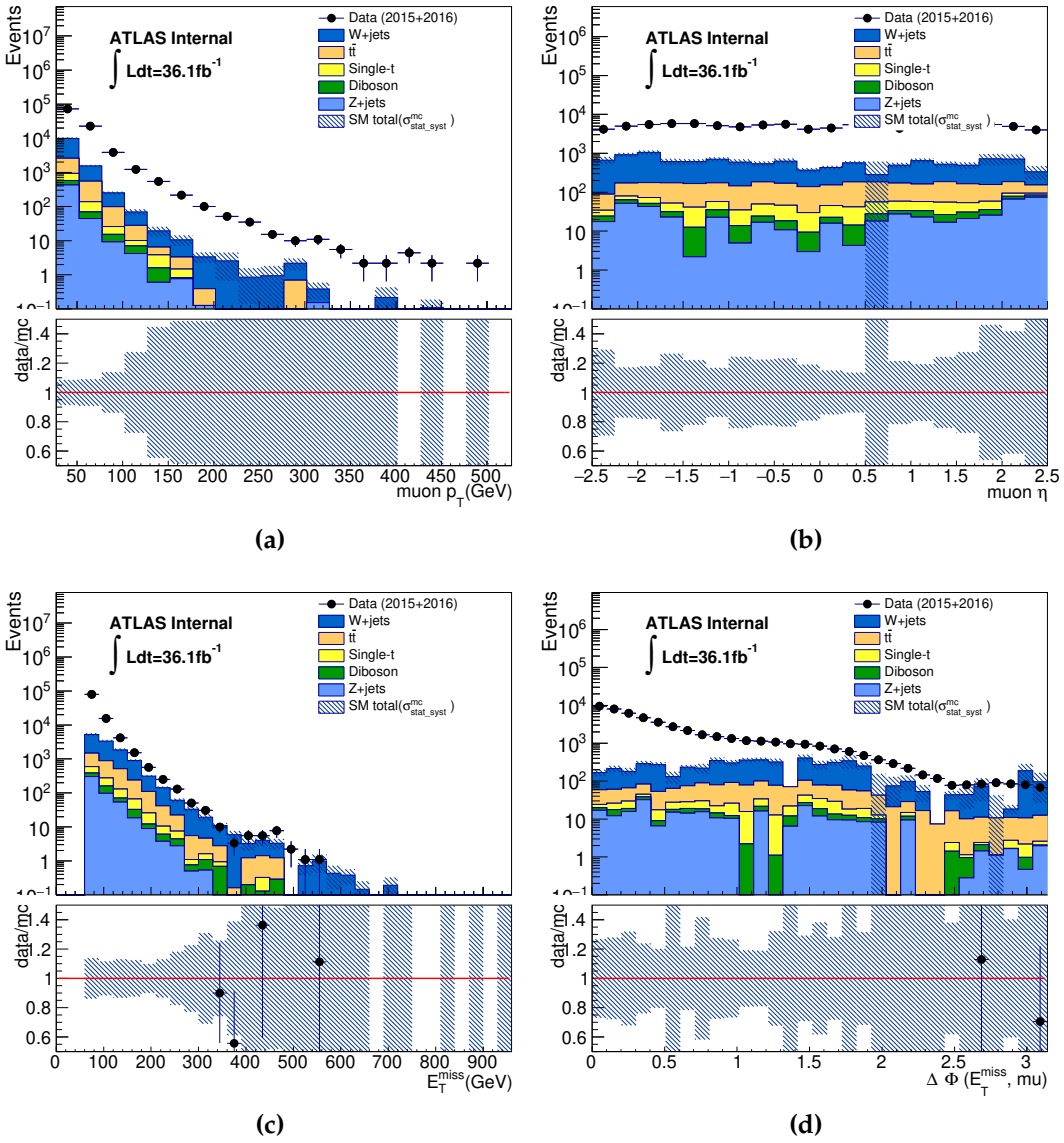

Figure 3.19.: The distribution of lepton p_T, η, E_T^{miss} and $\Delta\phi(\mu, E_T^{miss})$ in dijet fake control region with inversed lepton for muon channel. The inconsistency is thought to be comprised of multijet events without applying electroweak subtraction.

Table 3.11.: Electroweak subtraction factor for electron and muon channels

channels	electron	muon
EW subtraction factor	1.36	1.49

Validation

The method is validated in the dedicated validation region. The definition is similar to the signal region with looser cut to enrich the multijet events. It requires at lease two resolved jets ($p_T^{leading} > 60\ GeV$, $p_T^{subleading} > 45\ GeV$), $30\ GeV < E_T^{miss} < 100\ GeV$, exactly one isolated lepton and the resolved triggers passed for electron and muon channels respectively. This definition is slightly overlapped with signal and control regions, but the upper cut on E_T^{miss} suppress the signal contribution. As the fake factors were derived from two bins of $p_T(l\nu)$, the validation is performed on $p_T(l\nu) < 150\ GeV$ and $p_T(l\nu) > 150\ GeV$ separately. The results are presented in Figures 3.20 - 3.23 with multijet background estimated using fake factor method. In general, data agrees well with backgrounds with tolerable inconsistency within statistic uncertainties. The disagreement in the region of $p_T(l\nu) > 150GeV$ is supposed to be due to the low statistics for fake factor estimation in the single jet control region. This doesn't have a great impact in the final result, as multijet events would just account for around 10% of all the background. The related systematic uncertainties will be discussed in Chapter 4.

3.5. Data Background Comparison

To verify the modelling of background estimation, the data-MC comparison in top and W+jet control regions are performed for both VBF and ggF categories. The consistency is not perfect, as expected, since the fitting in the control regions exists to correct it as discussed in next chapter. The other issue in the background simulation is that a slope in the ratio of data over background is observed in m^{VBF} distribution in VBF category for V+jet samples from Sherpa generator (it could be clearly seen in (d) of Fig. 3.27). In this analysis, it is also taken as one systematic uncertainty contribution to the simulation mismodelling. (Further discussion about this issue will be in Chap. 5.)

Fig. 3.24 and Fig. 3.25 are the comparison plots for m_{WV} in ggF category, while

Fig. 3.26 to Fig. 3.28 are for VBF category. The comparison of m^{VBF} could be found in Fig. 3.27 and Fig. 3.29 to examine the VBF modelling.

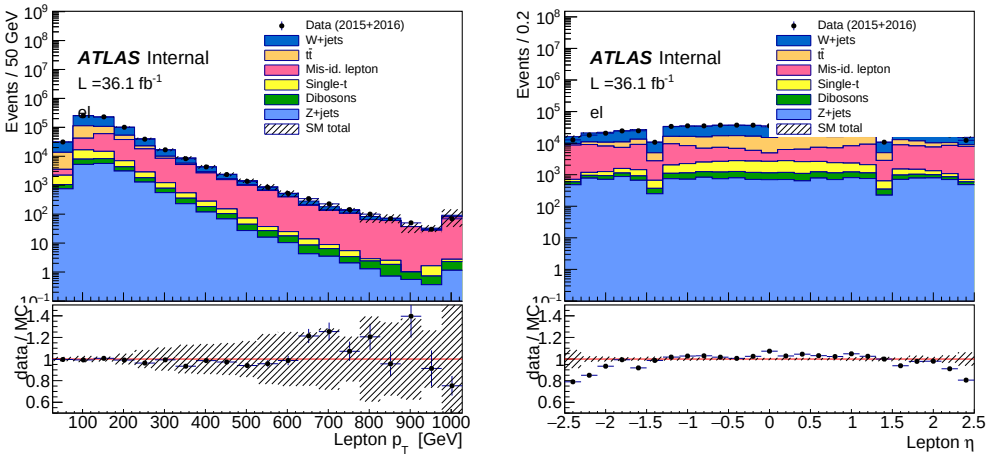

(a)

(b)

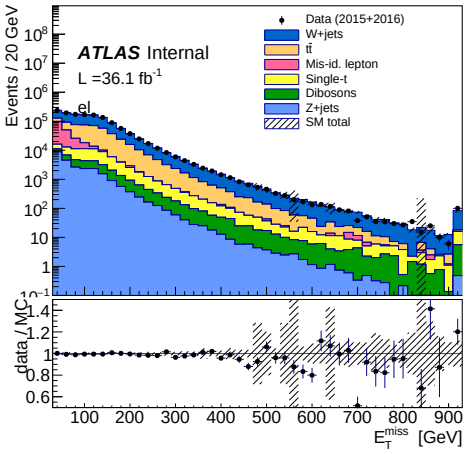

(c)

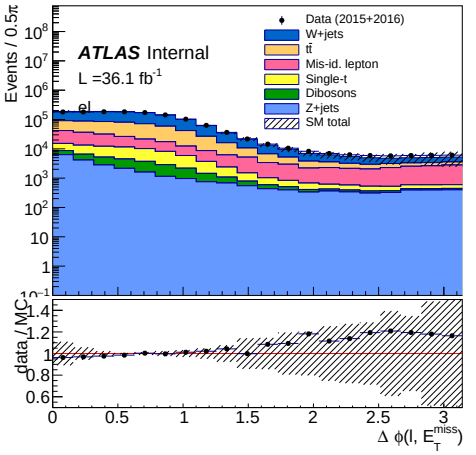

(d)

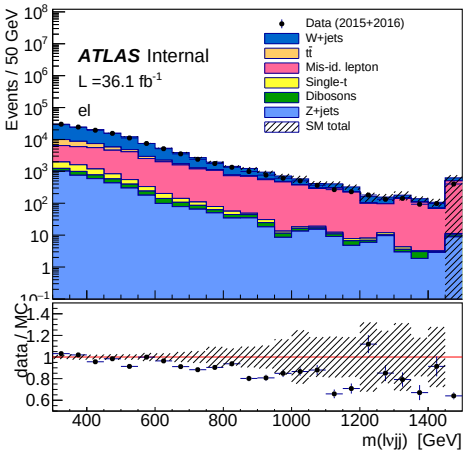

(e)

Figure 3.20.: The distribution of lepton p_T, η, E_T^{miss}, $\Delta\phi(\ell, E_T^{miss})$, and m_{WV} in validation region with $p_T(l\nu) > 150GeV$ in electron channel with multijet background

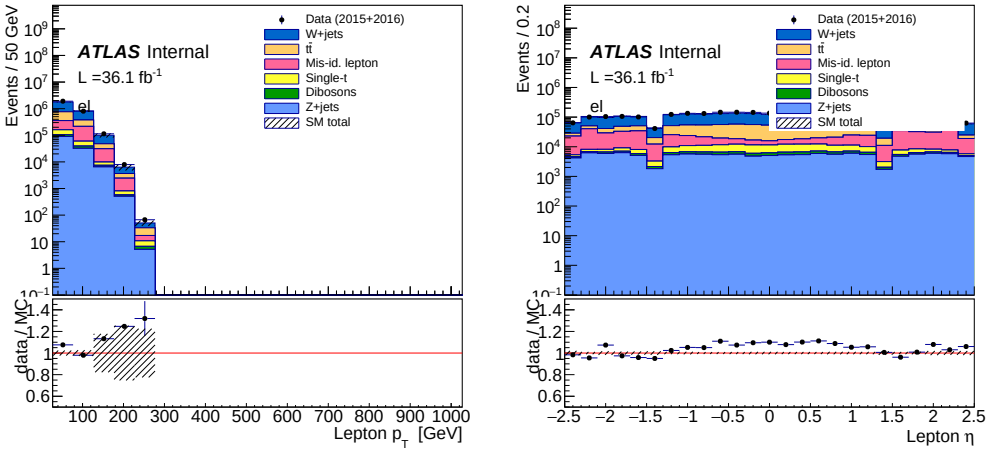

(a) **(b)**

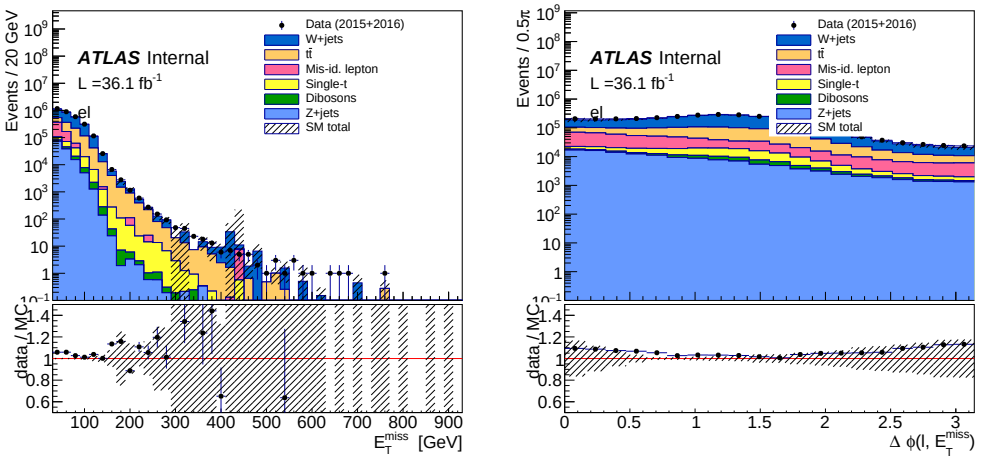

(c) **(d)**

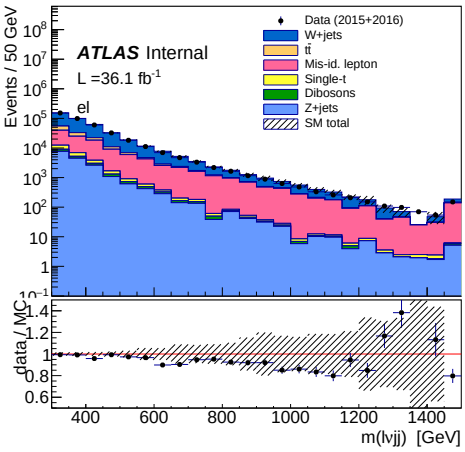

(e)

Figure 3.21.: The distribution of lepton p_T, η, E_T^{miss}, $\Delta\phi(\ell, E_T^{miss})$, and m_{WV} in validation region with $p_T(l\nu) < 150GeV$ in electron channel with multijet background

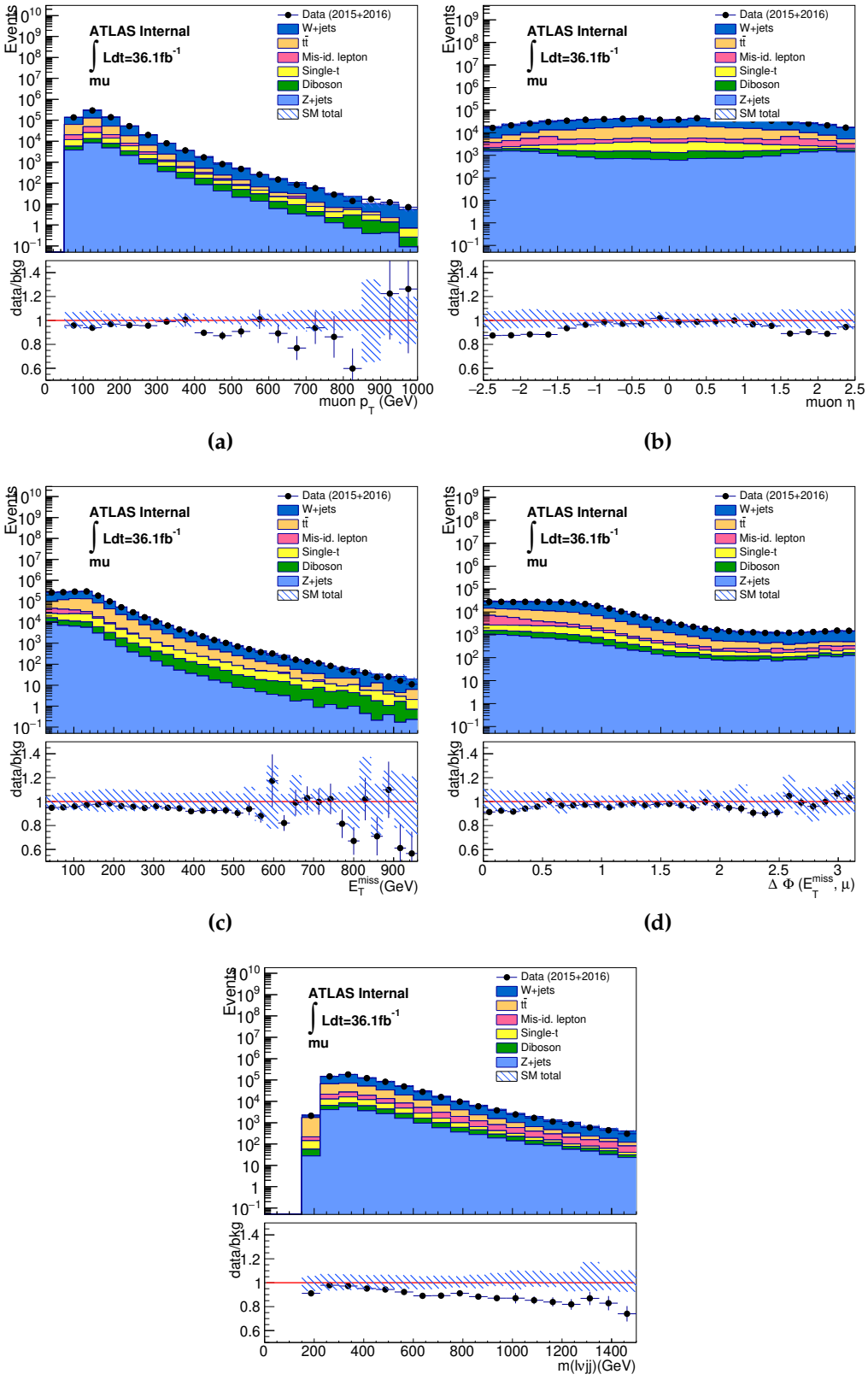

(a) **(b)**

(c) **(d)**

(e)

Figure 3.22.: The distribution of lepton p_T, η, E_T^{miss}, $\Delta\phi(\ell, E_T^{miss})$, and m_{WV} in validation region with $p_T(lv) > 150GeV$ in muon channel with multijet background

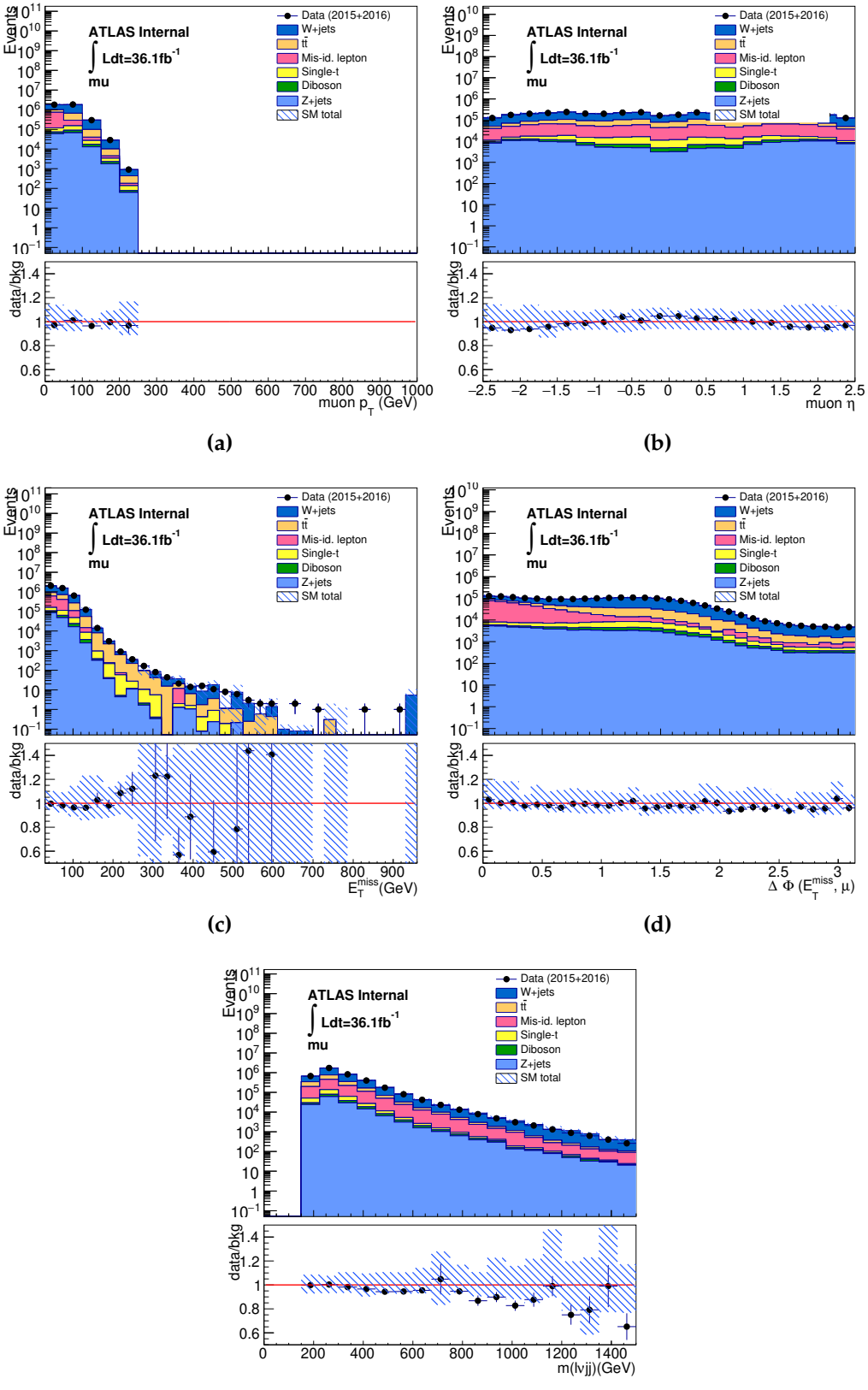

(a) **(b)**

(c) **(d)**

(e)

Figure 3.23.: The distribution of lepton p_T, η, E_T^{miss}, $\Delta\phi(\ell,E_T^{miss})$, and m_{WV} in validation region with $p_T(lv) < 150GeV$ in muon channel with multijet background

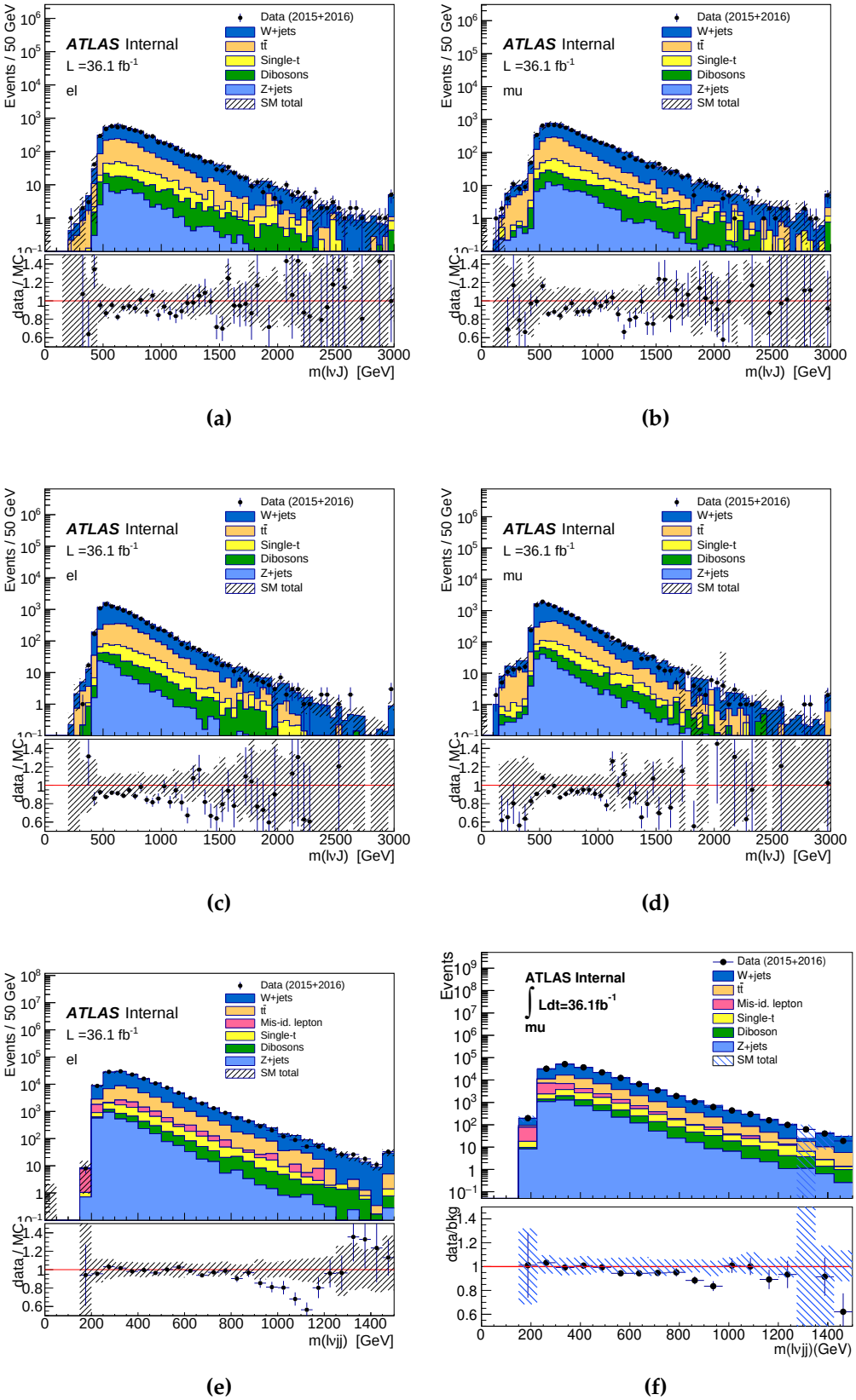

Figure 3.24.: The distribution of m_{WV} in ggF high purity (top), low purity (middle), and resolved (bottom) W+jet control region for electron (left) and muon (right) channels respectively

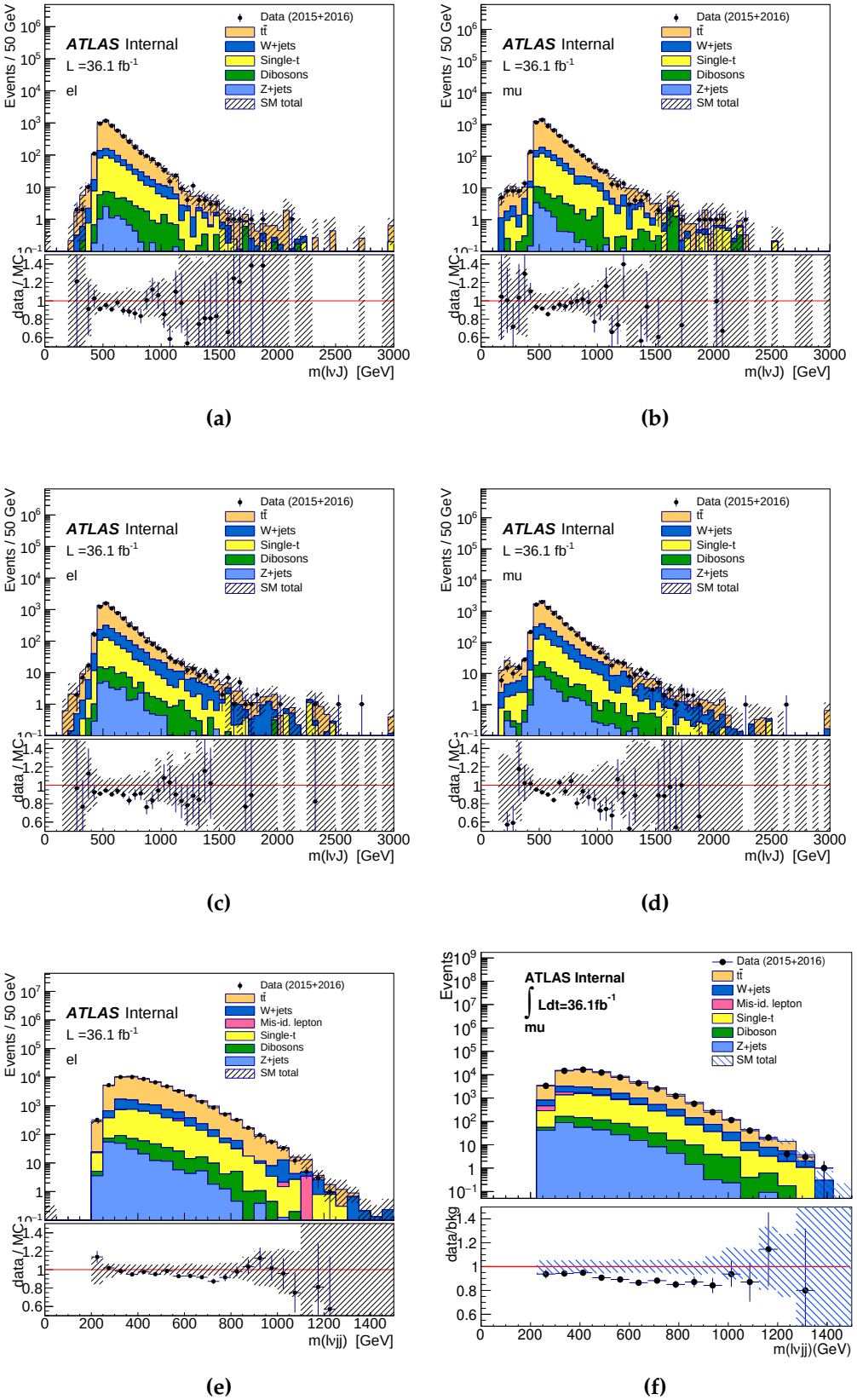

Figure 3.25.: The distribution of m_{WV} in ggF high purity (top), low purity (middle), and resolved (bottom) top control region for electron (left) and muon (right) channels respectively

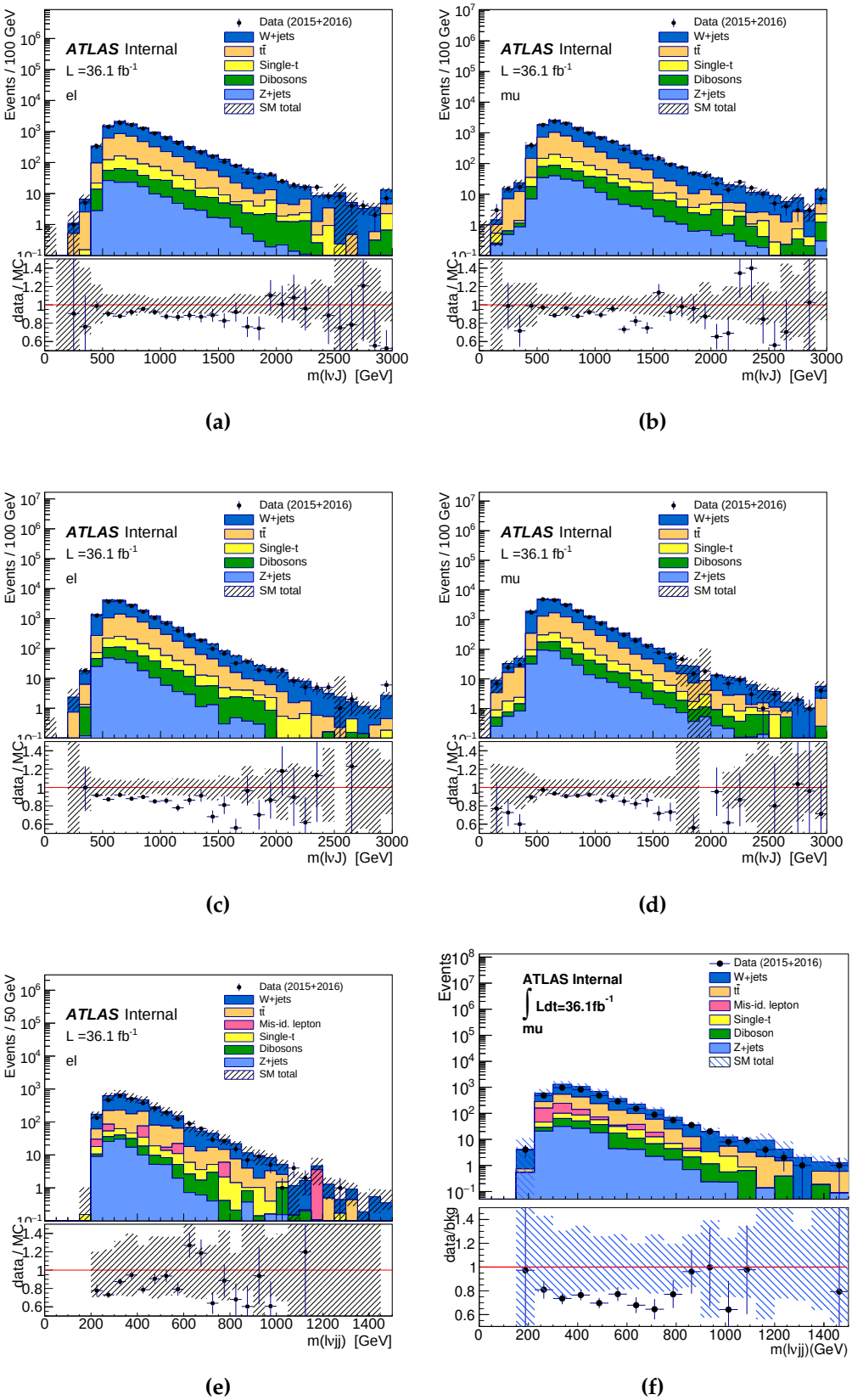

(a) **(b)**

(c) **(d)**

(e) **(f)**

Figure 3.26.: The distribution of m_{WV} in VBF high purity (top), low purity (middle), and resolved (bottom) W+jet control region for electron (left) and muon (right) channels respectively

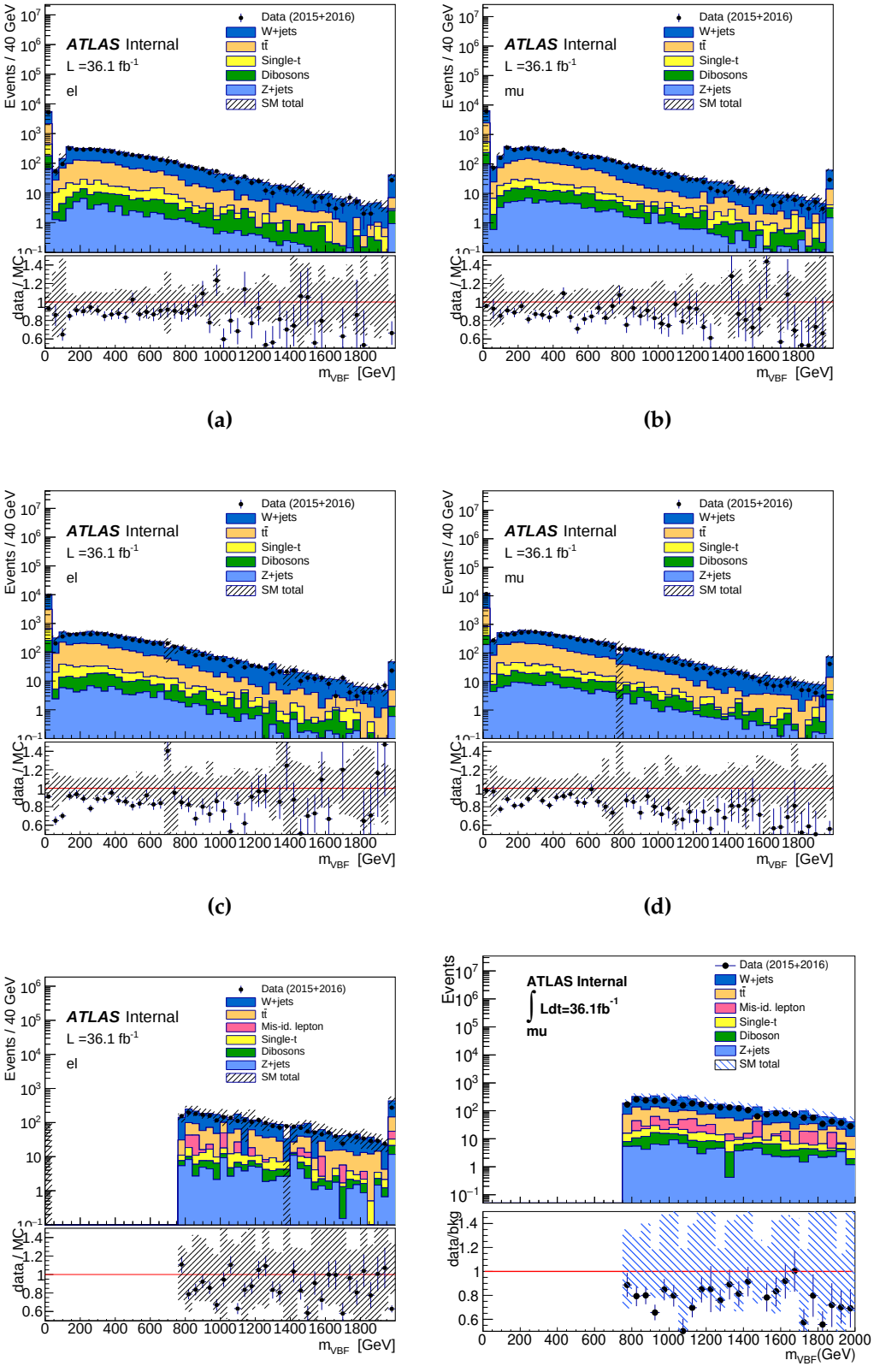

Figure 3.27.: The distribution of m^{VBF} in VBF high purity (top), low purity (middle), and resolved (bottom) W+jet control region for electron (left) and muon (right) channels respectively

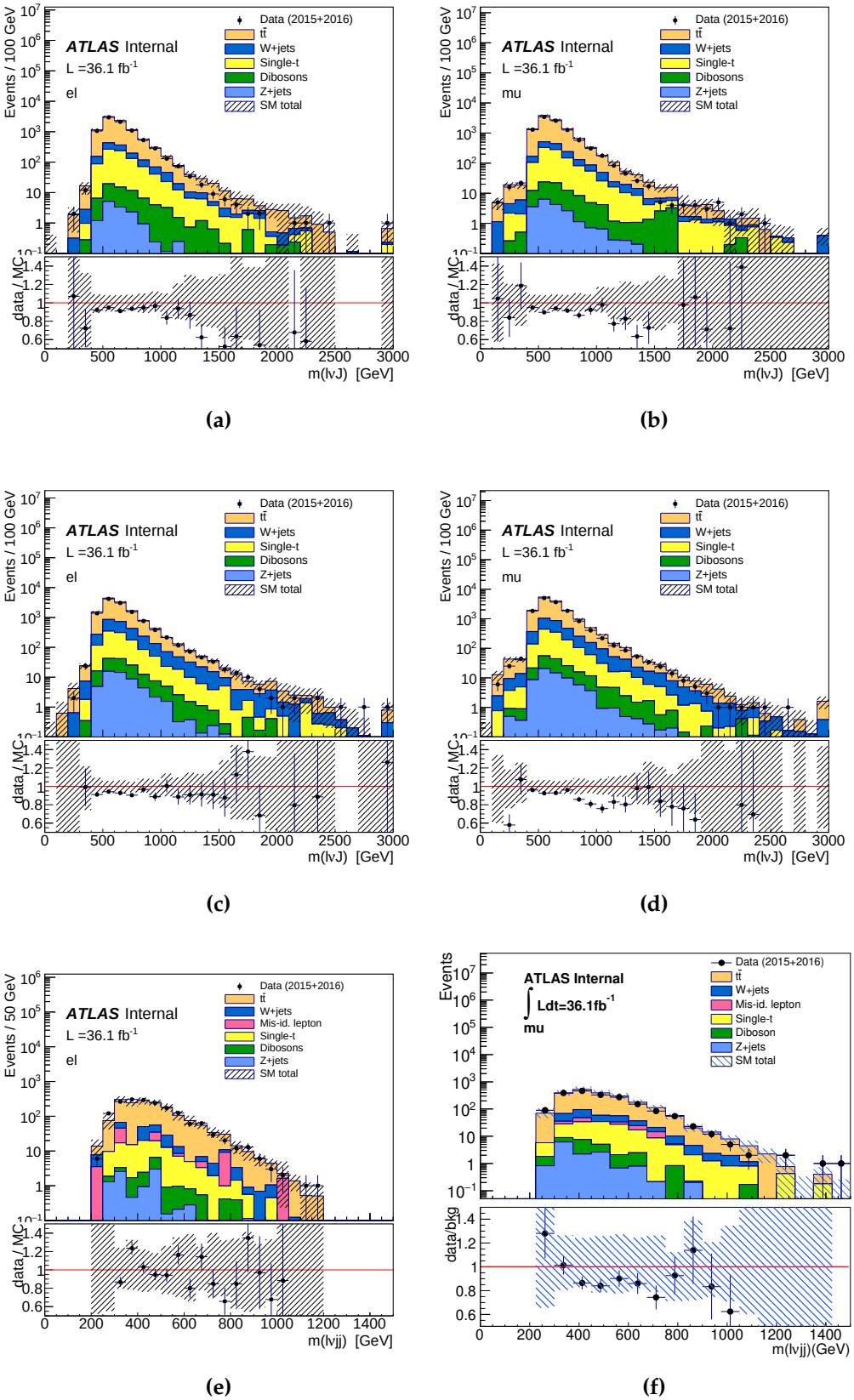

Figure 3.28.: The distribution of m_{WV} in VBF high purity (top), low purity (middle), and resolved (bottom) top control region for electron (left) and muon (right) channels respectively

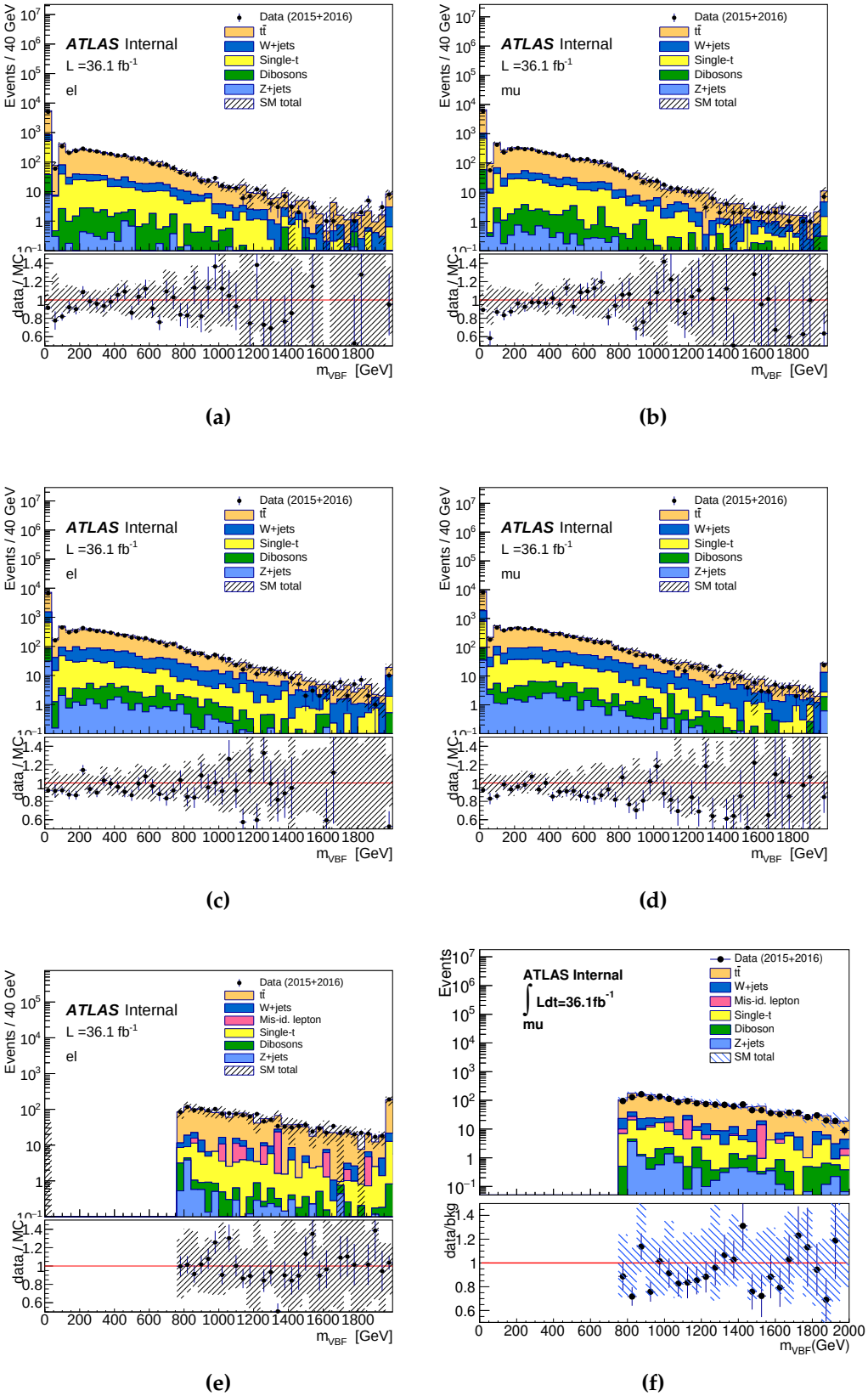

Figure 3.29.: The distribution of m^{VBF} in VBF high purity (top), low purity (middle), and resolved (bottom) top control region for electron (left) and muon (right) channels respectivelyy

Chapter 4.

Interpretation for Resonance Analysis

"The best things happen by chance."
— Dory, Finding Dory

After obtaining the m_{WV} distributions from both control and signal regions, a statistical interpretation is used to determine whether any signal signature is captured in this analysis. The statistical analysis uses the following steps:

- Variation on Histograms: Systematic uncertainties are applied in the analysis to vary the variables like the jet energy or event weight on the simulation samples. This then leads to the variations on distribution of m_WV, and each systematic uncertainty gives one varied m_{WV} histogram. Those histograms are then taken into the statistic interpretation with the one without any variation (this is called "nominal" histogram) for following steps.

- Simultaneous Fitting: a binned maximum-likelihood fitting is performed in control and signal region histograms simultaneously to rescale the backgrounds and signal for a proper agreement to the data. The scaling is performed bin-by-bin in histograms of m_{WV} distribution, which means the shape of m_{WV} distribution would change under this step. Further detail will be discussed later.

- Signal Verification: the signal interpretation is through the CLs method by quantifying the agreement between data and background in signal regions after simul-

taneous fitting. The result will be presented as the exclusion on the mass regions at 95% confidence level or the discovery with a corresponding "p-value".

The details of each step will be discussed in the following sections with the results from this analysis, and the details of the methodology formalism can be referred to [79].

4.1. Systematic Uncertainties

No measurement and theoretical estimation could be 100% accurate, and the uncertainties would propagate to the m_{WV} histograms. In this case, a bump in data might be due to the uncertainty fluctuation but mistaken as a signal. To prevent such a mistake, both systematic and statistic uncertainties are brought into the consideration for the ground fitting and signal interpretation. The following are the systematic uncertainties considered in this analysis and how they are taken into the m_{WV} histograms, and the methods to estimate the uncertainties of each source could be found in [**?**,45,48,80–82].

- **Luminosity Measurement**: the given luminosity of the dataset collected in 2015 and 2016 is accompanied by the uncertainty of 2.1%. It is applied in the histograms from simulations by scaling up and down the total yield of each bin by 2.1%.
- **Selection and Reconstruction Efficiency**: the object reconstruction and selection efficiency of physical objects are not consistent between data and simulation like the trigger efficiency shown in Subsec. 3.4.1. This type of uncertainties are induced by the uncertainties in variables used in tag and probe method. To estimate the impact, the tag and probe criteria are tightened and loosened for scale factor re-estimation, and they replace the nominal scale factors to obtain the new histograms. This type of uncertainties come from the efficiencies of trigger, lepton isolation, lepton identification, jet b-tagging, fat jet boson-tagging, and all physical object reconstruction, and each of them gives one uncertainty contribution with a pair of histograms. (loosened and tightened criteria give two histograms for each source.)

- **Energy Scale and Resolution**: the energy measurement is based on the pulse shapes from the calorimeter cells, but it is not precise enough due to different responses of layers or varied granularities of the calorimeter. The uncertainty estimation of this source for electrons and muons are via the Z boson mass reconstruction in dedicated analysis as a function of p_T. In the case of jets, they are estimated via the comparison of the MC truth and reconstructed E_T from dijet simulation samples with the variation on multiple sources, which contributes 81 uncertainties. However, a simplified scheme is applied to combine related uncertainties into 21 categories, for which details could be found in [45]. The measurement uncertainties of jets also have impact on E_T^{miss} reconstruction, and the variation on jet energy scale is the dominant contribution to E_T^{miss} uncertainty. Each variation is applied on the corresponding object E_T, which gives varied m_{WV} histograms of dedicated uncertainty contributions.

- **Simulation Modelling**: The tuning and modelling parameters are different for generators and showering models due to the varied preference of theoretical approximation. To take this variation into the uncertainty contribution, simulated samples are regenerated with another simulation sets (a different generator or tuning parameters), and the same events selections is applied. New histograms are then obtained after the normalization to total event yield of the nominal sample after the simultaneous fitting (the explanation is in the next section). Each tuning of one SM background process or signal sample gives one uncertainty contribution. For W+jet and $t\bar{t}$ backgrounds, the varied histograms are not taken into the simultaneous fitting directly due to the poor statistics in the region of high m_{WV}. A linear fitting in the dedicated control regions is performed to smooth the m_{WV} distribution based on the event ratio between nominal and varied histograms respectively for each category and each background (the linear fitting of W+jet ($t\bar{t}$) is performed in the W+jet ($t\bar{t}$) control region), which gives weights as a function of m_{WV} in the following form:

$$w = a + b \times m_{WV} \tag{4.1}$$

with a and b as fitting parameters, and w as the given scale factor for each bin to modify the m_{WV} distribution. The rescaled histograms are then taken into the next step for simultaneous fitting. For the signal modelling uncertainty, the generator tuning is to consider additional jets from the initial and final state radiations (ISR and FSR), and histograms from the new tunings are taken into next step without the process done for W+jet and $t\bar{t}$ modelling uncertainties. For other minor SM background contributions, this uncertainty is taken negligible.

- **Multijet Background Modelling**: multijet modelling is sensitive to the lepton isolation criteria and the jet topology. To estimate the uncertainty of this contribution, the fake factors were re-evaluated with loosened and tightened isolations on leptons as well as in the single b-jet control region, and the new fake factors are applied to get the new multijet m_{WV} distribution.

4.2. Likelihood Construction & Fitting

A binned simultaneous fit is conducted to adjust the background and signal to agree well with the data in the m_{WV} distribution. The following is the binning used for boosted (ranged from 500 GeV to 6 TeV, Eq. 4.2) and resolved (ranged from 300 TeV to 2 TeV, Eq. 4.3) category histograms:

$$m_{WV}^{Boosted} = [500, 575, 660, 755, 860, 975, 1100, 1235, 1380, 1535, 1700, 1875, 2060, 2255, 2460, 2675, 2900, 3135, 3380, 3800, 6000] \quad (4.2)$$

$$m_{WV}^{Resolved} = [300, 360, 420, 500, 575, 660, 755, 860, 975, 1100, 1500, 2000] \quad (4.3)$$

For the VBF category, the bins with higher m_{WV} have the statistics too low for the MC samples, so there is only one bin for $m_{WV} > 1535\ GeV (1100\ GeV)$ for the boosted (resolved) region. Then, a maximum likelihood method is performed for the fitting

which could be presented in the full form as:

$$\mathcal{L}(\mu,\boldsymbol{\theta}) = \prod_{k}\left\{\prod_{i=1}^{N_{\text{bins}}^{k}}\left[P(N_i^k|\mu s_i^k + \mu_{t\bar{t},k} b_{t\bar{t},i}^k + \mu_{W,k} b_{W,i}^k + b_{\text{others},i}^k) \times \prod_{j=1}^{N_\theta}\text{Nuis}(\theta_0|\theta_{j,k})\right]\right\} \tag{4.4}$$

where $P(x|y)$ is the Poisson probability distribution function (p.d.f.) to observe "x" number of events (data) when "y" number of events are expected from theory (estimated event number sum of signal event number, s, and background event number, b) in each bin which is indexed by i. To properly normalize the background, μ's are the most important parameter in the formula as floating parameters to rescale the event numbers in each region for background estimation , and they are shared between control and signal regions (simultaneously). The μ to rescale the signal event number is also called "signal strength" which is the primary parameter of interest in the statistical interpretation. The k index in this formula corresponds to the event categories of each control/signal region: ggF merged HP, ggF merged LP, ggF resolved, VBF merged HP, VBF merged LP, and VBF resolved regions for W+jet control regions, $t\bar{t}$ control regions and signal regions. For the last term, $N_\theta\text{Nuis}(\theta_0|\theta_j)$, it is to take systematic uncertainties into the likelihood as nuisance parameters to further vary the probability distribution, which will be discussed next.

Nuisance Parameters

The last term in Eq. 4.4 is to take in the consideration of systematic uncertainties mentioned in the last section. They are called "nuisance parameters" (NP) in the scope of statistics, as they are of the second interest with respect to the primary parameter of interest (POI), μ, the scale factor for signal events. Nuisance parameters are used as addition probabilities multiplying the Poisson distribution function which could be seen in one bin as:

$$p = P(x|\mu n_0) \times \prod_{j=1}^{N_\theta}\text{Nuis}(\theta_0|\theta_j) \tag{4.5}$$

Under this equation, $P(x|\mu n_0)$ is a simplified form of Eq. 4.4, and the nuisance parameter form is taken as the probability to have θ_j variation with respect to an nominal value, θ_0 (j is the index for NPs).

There are three types of nuisance parameters based on their impact on the distribution of m_{WV} [83]. The following are the treatments to them in this analysis, and most of them are taking the constraint as a Gaussian distribution, although the other p.d.f. options are also available. (In the following content, the NP contribution to the likelihood is not normalized to 1, because the normalization factors are cancelled out in the form of a ratio in the next step.)

- Statistical Uncertainty: with the limited event numbers of background estimation, the statistical uncertainties are taken as extra nuisance parameters. A light Beeston-Barlow method is applied which introduces a new scale factor, θ, on each bin with the constraint of a Gaussian distribution with the default value as 1. These nuisance parameters are then contributed to the likelihood in this expression:

$$Nuis(1|\theta) = \exp\left[\frac{(\theta-1)^2}{2\sigma^2}\right] \tag{4.6}$$

  θ is the ratio of the scaled event number to the unscaled (raw) event number in the prediction in one bin with i as the bin index, and the distribution width, σ is computed as the quadratic sum of all the background contributions. Each bin in the histograms makes one contribution in the likelihood with this formulation.

- Overall Normalization: this type of nuisance parameters arise, when yields of m_{WV} histograms are scaled up and down without changing the shape of distributions. They are contributed by uncertainties from the scaling factors and luminosity measurement. The treatment is simply taking a Gaussian distribution for the related probability. It can be presented in the likelihood as:

$$Nuis(N|\theta) = \exp\left[\frac{(\theta-N)^2}{2\sigma^2}\right] \tag{4.7}$$

In this expression, the Gaussian distribution has the mean of estimated event number, N, with the width of observed uncertainty, σ. For the case of luminosity, σ is taken as 2.1% of the estimated event number. In the case of uncertainties for scale factors, Tab. 4.1 is the summary for σ applied on different background scale factors. For $t\bar{t}$ and W+jets backgrounds, no constraint is set, and the deviation of θ from N for their scale factors is always taken as 1σ.

Table 4.1.: The constraints on scaling factors for SM backgrounds

Background	Constraint	Uncertainty (σ)
W+jets	Free	1
$t\bar{t}$	Free	1
single top	Gaussian	0.11
WW+WZ	Gaussian	0.3
Z+jets	Gaussian	0.11

- Shape Related Uncertainty: for the uncertainties which are asymmetrically sided ($\sigma_+ \neq \sigma_-$, σ_+ and σ_- are event numbers in the varied histograms for a given systematic uncertainty), a procedure called "morphing" is applied on each bin respectively which could be presented as:

$$n = \begin{cases} n_0 + \theta(\sigma_+ - n_0) & \theta > 0 \\ n_0 + \theta(n_0 - \sigma_-) & \theta < 0 \end{cases} \tag{4.8}$$

Here, n is the scaled event number, while n_0 is the raw event number. Then, scaled factor is constrained by θ which is under a Gaussian distribution constraint ($G(\mu, \sigma) = G(0, 1)$). This type of nuisance parameters cover the most of systematic uncertainties like selection and reconstruction efficiencies, energy scale, or theoretical modelling.

Quality of Fitting

To find the maximum of likelihood in Eq. 4.4, the logarithmic form, $\log \mathcal{L}$, is used. The

extreme value is then found when:

$$-\frac{\partial}{\partial\mu}\log\mathcal{L}=0 \tag{4.9}$$

However, the phase space of the likelihood is complex constructed with multiple dimensions of the scale factors, so the MINUIT2 [84] method with Hessian matrix[1] is performed under the framework of RooStat [85]. The maximized likelihood is denoted as: $\mathcal{L}(\hat{\mu},\hat{\theta})$

To verify the quality of the process of fitting with the likelihood equation, two properties of the results are verified:

- **Pull** The pull is defined as the deviation of nuisance parameters from the expected mean number:

$$pull=\frac{\hat{\theta}-\theta_0}{\sigma_\theta} \tag{4.10}$$

  with θ_0 as the mean of θ, while the uncertainty of nuisance parameters, σ_θ, is taken from the likelihood phase space. The pull result is verified by the comparison to "Asimov data" which took the expected event number as the observed data. (so the Asimov data has the pull as 0.) The proper fitting should have all the pulls within the 1σ variation with the reasonable uncertainty, or that indicates a huge discrepancy between the background estimation and the observed data.

- **Nuisance Parameter Correlation** The phase space of likelihood is constructed under the assumption that all the nuisance parameters are uncorrelated, but it still needs to be verified. The correlation matrix is then used for this verification which has the elements defined as:

$$Cov(\theta_i,\theta_j)=\frac{\partial^2\log(\mathcal{L})}{\partial\theta_i\partial\theta_j}|_{\theta=\hat{\theta}} \tag{4.11}$$

  This element, $Cov(\theta_i,\theta_j)$, should be close to 0 if $i\neq j$.

[1] Hessian matrix is a square matrix of second-order partial derivatives of a scalar-valued(i.e. the likelihood) function

Control regions		WW		WZ	
		ggF	VBF	ggF	VBF
W+jet CR	Merged HP	0.94 ± 0.07	0.87 ± 0.29	0.95 ± 0.07	0.85 ± 0.28
	Merged LP	0.97 ± 0.07	0.86 ± 0.23	0.98 ± 0.07	0.86 ± 0.22
	resolved	0.87 ± 0.08	N/A	0.90 ± 0.08	0.68 ± 0.23
$t\bar{t}$ CR	Merged HP	0.92 ± 0.07	1.16 ± 0.27	0.93 ± 0.08	1.03 ± 0.21
	Merged LP	0.97 ± 0.07	1.21 ± 0.28	0.96 ± 0.07	1.12 ± 0.24
	resolved	0.90 ± 0.07	N/A	0.92 ± 0.06	1.03 ± 0.27

Table 4.2.: The scale factors for the W+jet (μ_w) and $t\bar{t}$ ($\mu_{t\bar{t}}$) backgrounds for the fitting with the signal strength, μ, set at 0

The pulls are with the signal of ggF 2000 GeV and 500 GeV W' bosons for boosted and resolved categories which are presented in Fig. 4.1 with signal strength (signal scale factor) as 0[2]. Fig. 4.2 is the correlation matrix of the nuisance parameters applied in the ggF HP boosted region. The normalization factors could be seen over-constrained and over-pulled in the fitting, as the scaling factors are allowed to be pulled to the extreme for better data-background agreement after the fitting [76]. And, it could also be observed that the resolved channel has the NPs pulled and constrained much more than the merged channel, and this is due to the fact that the m_{WV} shape was significantly affected by the systematic uncertainty variations in the resolved event categories, and this could also be seen in Tab. 5.9 that the scale factors in the resolved regions have larger deviation from one with respect to the two merged regions. The final yields for the background only fitting are then shown in Tab. 4.3 (WW) and Tab. 4.4 (WZ) for the ggF/DY event category, and the VBF ones are shown in Tab. 4.5 (WW) and Tab. 4.6 (WZ). It could be noted that the total uncertainties in event yields are smaller than the ones shown in Sec. 3.5. The difference here is that the uncertainties in Sec. 3.5 was derived as the quadratic sum over all the uncertainties, but the ones presented in the yields tables are the uncertainties along the statistical uncertainty in the phases space of the likelihood.

[2]The signal sample was used as an essential element for the statistics tool configuration, but the choice does not affect the result

Table 4.3.: Expected and observed yields in signal and control regions for the ggF/DY WW signal hypothesis. Yields and uncertainties are evaluated after a background-only fit to the data in all regions indicated above.

	Boosted, High Purity			Boosted, Low Purity			Resolved		
	SR	W+jets CR	Top CR	Signal Region	W+jets CR	Top CR	SR	W+jets CR	Top CR
W+jets	3116 ± 165	6848 ± 206	540 ± 60	10790 ± 251	10972 ± 255	1424 ± 167	61537 ± 1826	165656 ± 722	7951 ± 925
$t\bar{t}$	2043 ± 142	2920 ± 180	6883 ± 138	2648 ± 187	3790 ± 222	8738 ± 235	23287 ± 1633	31110 ± 2050	78354 ± 1262
Single-t	374 ± 44	487 ± 57	704 ± 84	493 ± 56	553 ± 64	819 ± 97	3822 ± 436	4675 ± 539	5631 ± 669
SM Diboson	353 ± 94	167 ± 45	51 ± 14	431 ± 118	201 ± 55	70 ± 20	2413 ± 656	1500 ± 408	274 ± 77
Z+jets	49 ± 6	143 ± 17	15 ± 3	205 ± 25	215 ± 27	54 ± 9	1748 ± 273	4298 ± 640	275 ± 62
Multijet	–	–	–	–	–	–	3601 ± 720	7627 ± 1671	799 ± 137
Total	5935 ± 70	10565 ± 96	8192 ± 87	14566 ± 120	15730 ± 124	11105 ± 104	96409 ± 310	214866 ± 468	93283 ± 307
Observed	5885	10619	8178	14566	15707	11133	96459	214838	93257

Table 4.4.: Expected and observed yields in signal and control regions for the WZ signal hypothesis. Yields and uncertainties are evaluated after a background-only fit to the data in all regions indicated above.

	Boosted, High Purity			Boosted, Low Purity			Resolved		
	SR	W+jets CR	Top CR	Signal Region	W+jets CR	Top CR	SR	W+jets CR	Top CR
W+jets	3679 ± 173	6958 ± 191	556 ± 61	13356 ± 299	11091 ± 247	1496 ± 173	49052 ± 1294	164656 ± 2692	8066 ± 921
$t\bar{t}$	2283 ± 146	2812 ± 167	6842 ± 141	3447 ± 233	3681 ± 218	8611 ± 241	24376 ± 1272	30589 ± 1955	78012 ± 1269
Single-t	410 ± 50	485 ± 57	749 ± 90	655 ± 75	556 ± 65	854 ± 102	3499 ± 399	4743 ± 549	5762 ± 685
SM Diboson	356 ± 98	162 ± 44	51 ± 14	498 ± 138	193 ± 53	71 ± 21	1672 ± 470	1466 ± 404	267 ± 78
Z+jets	56 ± 7	148 ± 18	15 ± 3	244 ± 31	212 ± 26	55 ± 9	1475 ± 259	4406 ± 659	282 ± 64
Multijet	–	–	–	–	–	–	2650 ± 533	8965 ± 1878	895 ± 153
Total	6784 ± 76	10564 ± 96	8211 ± 88	18201 ± 136	15733 ± 124	11087 ± 104	82722 ± 285	214824 ± 505	93284 ± 308
Observed	6751	10619	8178	18188	15707	11133	82740	214838	93257

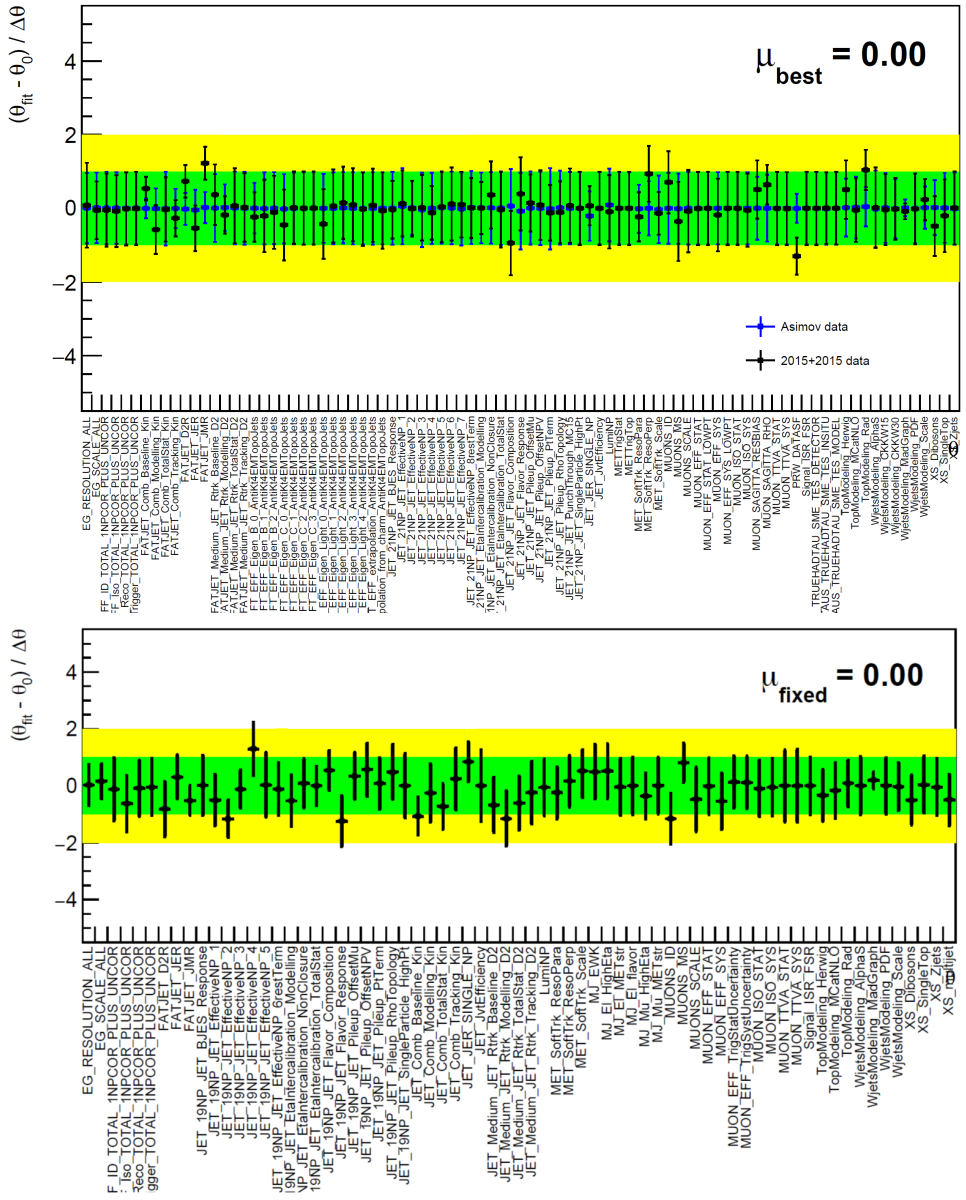

Figure 4.1.: The pulls for the fitting with input signal of ggF 2 *TeV* (up) and 500 *GeV* (down) W' bosons for the boosted and resolved categories respectively.

Combination

This analysis contains several categories (merged and resolved, or VBF and ggF production), and a combination of them could help to increase the sensitivity to set a more stringent limit by the decrease of distribution width in the test statistic p.d.f.

Table 4.5.: Expected and observed yields in signal and control regions for the VBF WW signal hypothesis. Yields and uncertainties are evaluated after a background-only fit to the data in all regions indicated above.

	Boosted, High Purity			Boosted, Low Purity			Resolved		
	SR	W+jets CR	Top CR	Signal Region	W+jets CR	Top CR	SR	W+jets CR	Top CR
W+jets	71 ± 15	183 ± 26	18 ± 4	268 ± 31	294 ± 35	55 ± 11	1093 ± 107	2520 ± 186	215 ± 54
$t\bar{t}$	84 ± 16	179 ± 22	346 ± 19	115 ± 24	225 ± 30	500 ± 27	714 ± 106	1040 ± 144	2442 ± 86
Single-t	13 ± 3	24 ± 6	30 ± 5	23 ± 5	31 ± 6	47 ± 9	66 ± 16	104 ± 24	120 ± 21
SM Diboson	9.8 ± 3.4	13 ± 4	3.3 ± 1.1	17 ± 6	16 ± 5	6.7 ± 3.2	52 ± 19	66 ± 22	14 ± 6
Z+jets	1.6 ± 0.5	4.5 ± 0.9	0.5 ± 0.3	6.7 ± 2.1	8.7 ± 2.1	2.0 ± 0.7	41 ± 10	94 ± 30	12 ± 4
Multijet	–	–	–	–	–	–	44 ± 19	97 ± 39	54 ± 19
Total	178 ± 12	403 ± 19	398 ± 18	431 ± 20	573 ± 23	611 ± 23	2010 ± 47	3920 ± 70	2856 ± 54
Observed	176	402	398	436	567	613	2004	3924	2856

Table 4.6.: Expected and observed yields in signal and control regions for the VBF WZ signal hypothesis. Yields and uncertainties are evaluated after a background-only fit to the data in all regions indicated above.

	Boosted, High Purity			Boosted, Low Purity			Resolved		
	SR	W+jets CR	Top CR	Signal Region	W+jets CR	Top CR	SR	W+jets CR	Top CR
W+jets	75 ± 17	187 ± 27	18 ± 5	323 ± 42	302 ± 41	58 ± 12	773 ± 263	2519 ± 597	196 ± 48
$t\bar{t}$	106 ± 24	175 ± 45	346 ± 36	161 ± 49	224 ± 56	496 ± 52	863 ± 187	1059 ± 264	2460 ± 87
Single-t	12 ± 6	24 ± 10	31 ± 10	26 ± 11	30 ± 9	47 ± 19	75 ± 38	109 ± 59	120 ± 47
SM Diboson	10 ± 5	11 ± 5	2.7 ± 1.1	22 ± 10	14 ± 5	5.9 ± 4.1	37 ± 23	61 ± 27	12 ± 5
Z+jets	1.6 ± 1.5	4.6 ± 2.3	0.4 ± 0.2	7.8 ± 6.0	8.4 ± 3.9	1.9 ± 1.2	53 ± 15	81 ± 39	11 ± 4
Multijet	–	–	–	–	–	–	30 ± 28	94 ± 40	56 ± 20
Total	205 ± 28	402 ± 52	398 ± 41	540 ± 49	578 ± 47	609 ± 66	1833 ± 162	3923 ± 911	2856 ± 59
Observed	201	402	398	550	567	613	1829	3924	2856

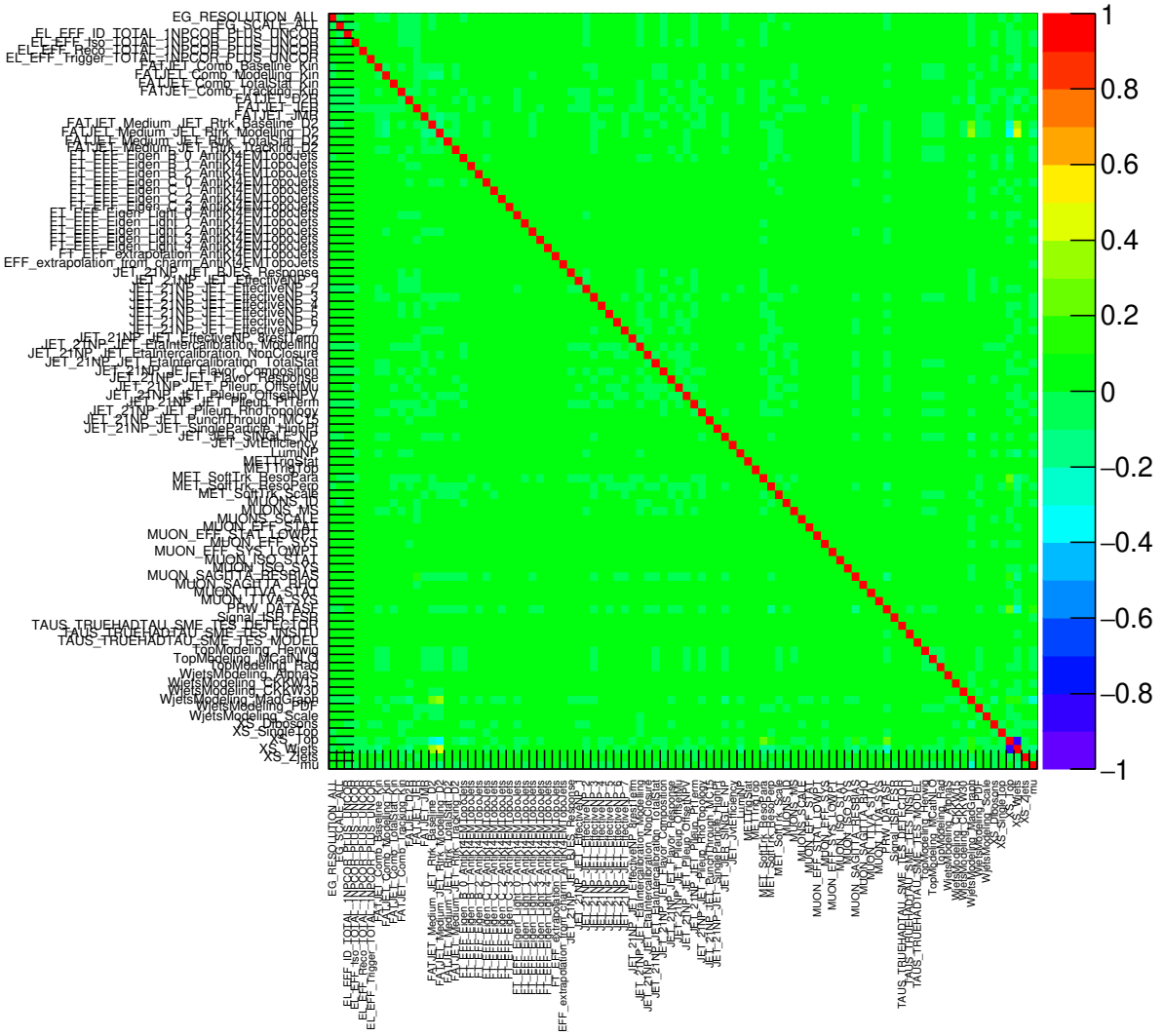

Figure 4.2.: The correlation matrix of boosted high purity region with the ggF event selection

(this will be discussed in the next section). The combination procedure is to simply multiply the likelihoods constructed from different event categories [86]:

$$\mathcal{L} = \prod_{k=1}^{N_{categories}} \mathcal{L}_k(\mu, \theta_k) \tag{4.12}$$

The signal strength,μ, would be common across the likelihoods. For the nuisance parameter terms, if they are from the same source like the uncertainty in object energy measurements, they are also the same among the event categories. In this case, those nuisance parameters are "correlated". For the other case, when the nuisance

parameters are from an independent source which is not considered in the other category like the multijet uncertainties in the resolved category, it would only make the constraint on the likelihood of this category, and they are called "decorrelated".

4.3. Result

After the fitting with no signal strength, the agreement between data and background+signal expectation event numbers should be verified to test whether the "hypothesis" of existence or exclusion of signal is correct for which the signal strength would be floating to find the maximum likelihood. The final interpretation is conduced in two ways: the exclusion for setting limits and the significance of a discovery.

Methodology for a Discovery (p-Value)

This is a counting analysis for which the property we want to measure is to see where a signal bump could be spotted in the diboson mass spectrum, so a profile likelihood with the likelihood built in the last session is formulated [87, 88] (for the case of a precision measurement, the "Neyman–Pearson lemma" is preferred in the format of $\lambda = \mathcal{L}(H_1)/\mathcal{L}(H_0)$ [89]) to simplify the phase space to verify the varied signal strength:

$$\lambda(\mu) = \frac{\mathcal{L}(\mu, \hat{\hat{\theta}})}{\mathcal{L}(\hat{\mu}, \hat{\theta})} \tag{4.13}$$

where $\mathcal{L}(\hat{\mu}, \hat{\theta})$ is the maximized likelihood with $\hat{\mu}$ and $\hat{\theta}$, while $\mathcal{L}(\hat{\mu}, \hat{\theta})$ is the maximized likelihood with a specific μ by giving $\hat{\hat{\theta}}$. The test statistic is then constructed as $-2\ln\lambda(\mu)$. Following by this, a test statistic [90] is built which is given the form:

$$q_0 = \begin{cases} -2\ln\lambda(0) & 0 \leq \hat{\mu} \\ 0 & \hat{\mu} < 0 \end{cases} \tag{4.14}$$

For the second case of $\hat{\mu} < 0$, this is not to reject the background only hypothesis. However, the derivation of a p.d.f. for the test statistic is computationally expensive, so an asymptotic approach is applied. The first step is to apply the Wald approximation, and the test statistic can be simplified to:

$$-2\ln(\lambda(\mu)) = (\frac{\mu - \hat{\mu}}{\sigma})^2 + \mathcal{O}(1/N) \tag{4.15}$$

with σ taken as the uncertainty in the likelihood phase space along the μ direction and N is the observed event number. However, to evaluate σ is computationally expensive, so, in this analysis, the Asimov data is used. With Eq. 4.15, σ could be evaluated as:

$$\sigma^2 = \frac{\mu - \hat{\mu}}{-2\ln(\lambda(\mu))} \tag{4.16}$$

With enough event numbers, the last term in Eq. 4.15 is negligible. From Wilks theorem, if a hypothesized μ' is true, the probability of measuring a specific $\hat{\mu}$ should follow a Gaussian distribution:

$$\hat{\mu} \sim Gaus(\mu', \sigma) \tag{4.17}$$

Then, the probability distribution of the test statistic would be in a "chi-suqare distribution" which is written as $f(q_\mu|\mu')$ with the non-central parameter as:

$$\Lambda = (\frac{\mu - \mu'}{\sigma})^2 \tag{4.18}$$

For a discovery with the test statistic in Eq. 4.14, μ' is set to 0, and a "p-value" is then defined as:

$$p_0 = \int_{q_{0,obs}}^{\infty} f(q_0|\mu' = 0)\,\mathrm{d}\,q_0 \tag{4.19}$$

where $q_{0,obs}$ is taken at the μ value which gives the observed event yield. This is indicating the possibility that the null hypothesis ($\mu' = 0$) is wrong, and it shows great disagreement to data. p-value would also be interpreted into the discovery

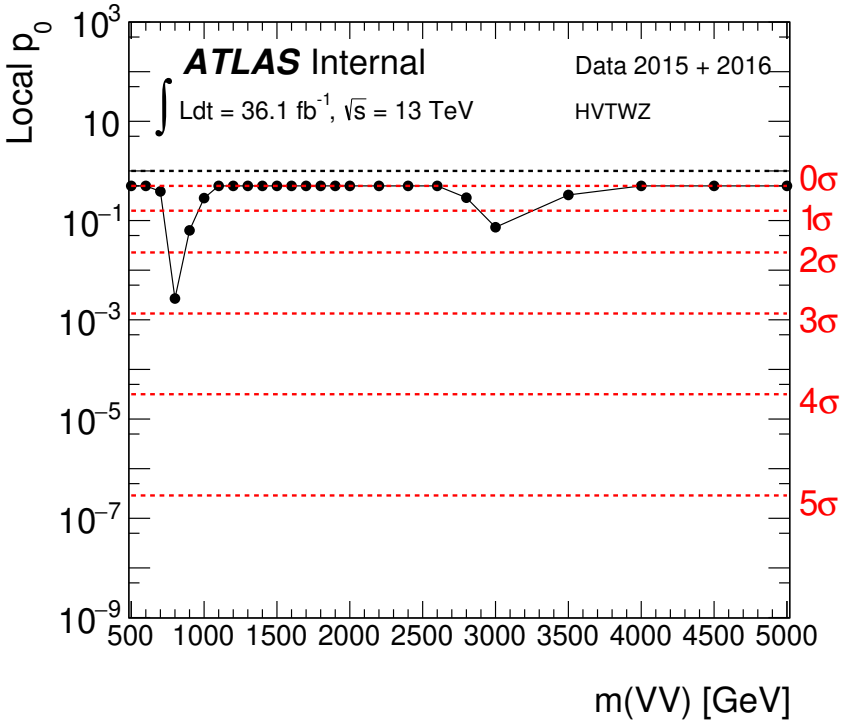

Figure 4.3.: The observed p-value and significance for the W′ boson from the ggF production with the combined data of both resolved and merged channels

significance:

$$Z = \Phi^{-1}(1 - p_0) \tag{4.20}$$

where Φ^{-1} is the quantile for inverse cumulative distribution of a standard Gaussian. Fig. 4.3 shows the p-value and discovery significance for the ggF HVT signal combined with both resolved and boosted regions. The best significance is given at 800 GeV for less than 3σ. In particle physics, the discovery of a new particle could only be claimed with an excess of 5σ which is tight to avoid the so-called "type-I error" defined as making a false discovery. In this case, an exclusion limit is set to make the claim which mass range has no signal at a certain confidence level.

Methodology for an Exclusion (Confidence Interval at 95% Confidence Level)

Without a significant result ($Z < 3\sigma$), an exclusion limit is then set to conclude that a

specific range of theoretical hypotheses (i.e. new particles of varied mass range) has no signal which is within the analysis sensitivity (i.e. the particle production cross-section is significant to be measured).

In the case of an exclusion, an alternative test statistic is formulated as:

$$\tilde{q}_\mu = \begin{cases} -2\ln\lambda(\mu) & 0 \leq \hat{\mu} \leq \mu \\ 0 & \hat{\mu} > \mu \\ -2\ln\lambda(0) & \hat{\mu} < 0 \end{cases} \tag{4.21}$$

For the three cases in the expression, the bottom one is to keep μ positive to have physical meaning, when $\hat{\mu}$ is smaller than 0. For the other two cases, it is to have the μ hypothesis at one side for $\mu > \hat{\mu}$ which is to set the exclusion upper limit on the cross-section, and the lower limit is ignored.

Then, the asymptotic approach is applied again. Under this case, $\tilde{q}^*_\mu$ is chosen with the Asimov data to make:

$$p_\mu = \int_{\tilde{q}^*_\mu}^{\infty} f(\tilde{q}_\mu|\mu = 0)\,\mathrm{d}\,\tilde{q}_\mu = 0.05 \tag{4.22}$$

This is meaning that if the signal exists with a specific signal strength, μ^*, the null hypothesis would be rejected at 95% confidence level (CL). Followed by that, μ^* is taken as the median value for the new p.d.f., $f(\tilde{q}_\mu|\mu = \mu^*)$, and also the expected upper limit of sensitivity to measure the signal. Then, the observed sensitivity is estimated to be the μ in this new p.d.f. corresponding to the observed event yield. This would lead to the claim that there is no signal with the given upper limit on cross-section at 95% confidence, and there is still 5% chance of the occurrence of the "type II error" which means to miss the signal within the expected sensitivity.

The final result is then interpreted by converting the evaluated μ into the produc-

tion cross-section and the decay branch ratio:

$$\sigma \times BR = \frac{\mu \times N^{evt}}{\mathcal{L}} \tag{4.23}$$

with $\mathcal{L}$ as the luminosity

The results with the combination of all the signal regions are presented in Fig. 4.4 for the ggF category with theoretical cross-section overlaid together, and Fig. 4.5 for the VBF category. For the W′ boson, Z′ boson, and the RS graviton, the theoretical cross-section is overlaid together with the expect and observed limits from the experiment which presents that the measurement has the sensitivity on the mass up to 3 TeV, and 1.7 TeV for the HVT bosons and gravitons respectively. And, Fig. 4.6 shows the comparison of power to set a limit on the HVT Z′ boson between resolved, merged, and combined channels. For the range of low mass, resolved channel has dominated the sensitivity, while for $m_{WV} > 800\ GeV$, merged channel has made better performance in terms of the sensitivity.

4.4. Combination of VV/VH/$\ell\ell$/$\ell\nu$

As mentioned before, the combination of multiple signal regions would help to increase the statistics and improve the measured sensitivity. In addition to the final state this analysis is interested in($pp \to WV \to \ell\nu qq$), there are also other analyses which are aiming for the same exotic particles. Therefore, a combination across all the possible final states of those searches was conducted to have a further improvement in the final result. The proposed scheme is to combine the diboson analyses for which the final states of VV (V=W or Z boson) decay are considered to search for the scalar NWA boson, the HVT, and the RS graviton. And, to have a further understanding of the HVT coupling to the SM particles, the dilepton ($\ell\ell$ and $\ell\nu$) and VH ($H \to bb$) channels are also taken into the combination.

The discriminant used in the combination is the fully reconstructed mass, m_{WV}, and

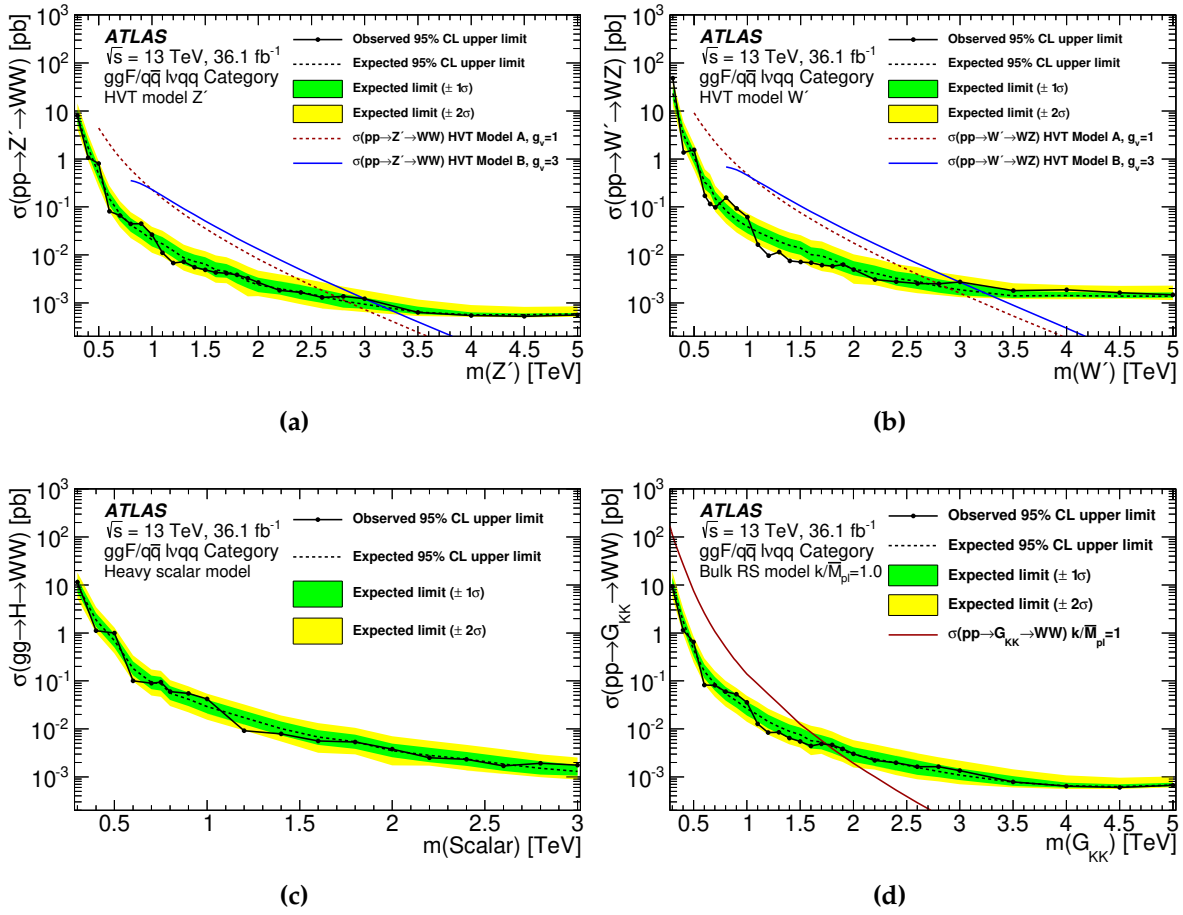

Figure 4.4.: The limits for the BSM particles via ggF/DY production. (a) and (b) are for the HVT Z′ and W′ bosons, while (c) is for the NWA scalar boson, and (d) is for the RS graviton.

the transverse mass, m_T is taken when the mass could not be fully reconstructed. (like $VV \to \nu\nu\ell\ell$ or $X \to \ell\nu$).

As discussed in the last chapter, the signal configuration was set to have a narrow resonance mass window, so the effect of interference on the cross-section is smaller than 15% in the VV and VH channels. Therefore, interference is taken to be negligible. For the dilepton channel, a cut on the resonance (transverse) mass is applied to mitigate the effect. [91]

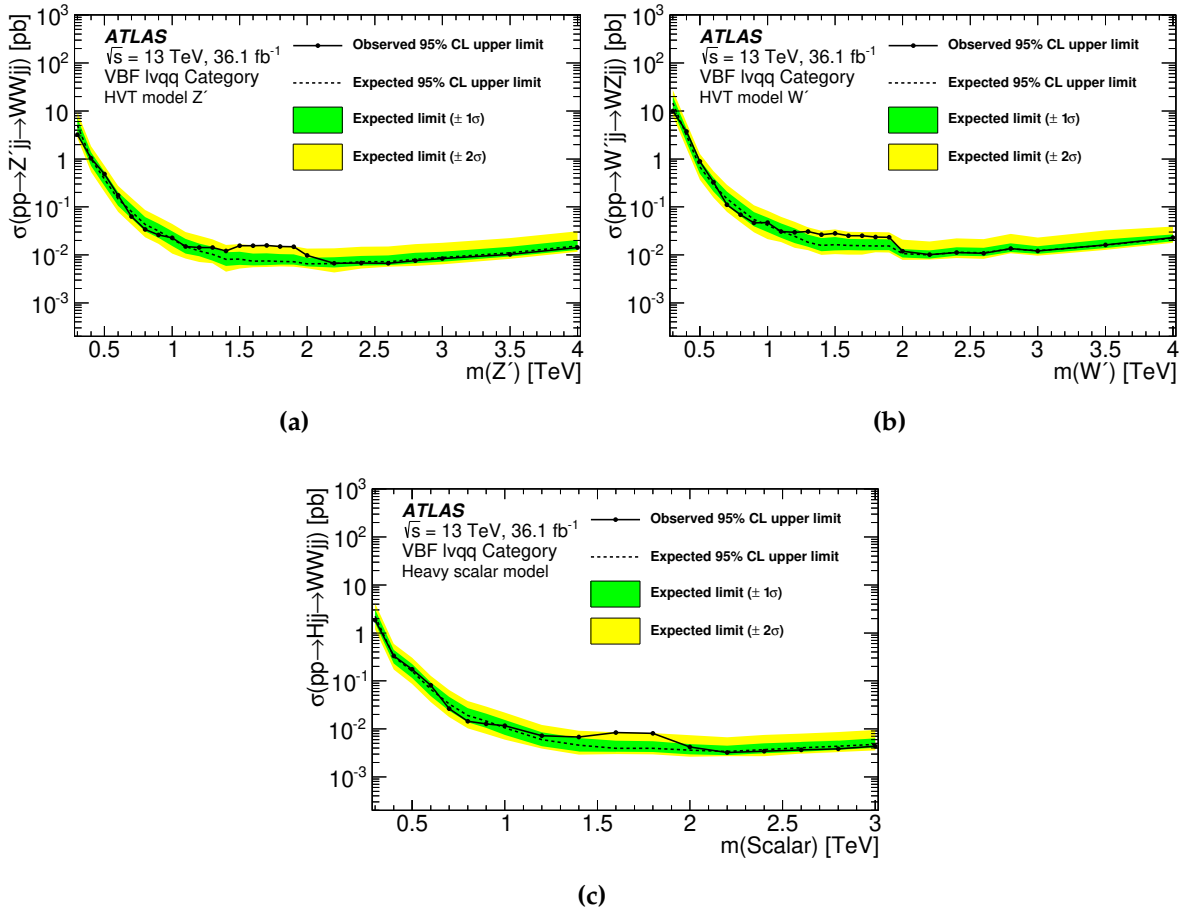

Figure 4.5.: The limits for the BSM particles via VBF production. (a) and (b) are for the HVT Z′ and W′ bosons, while (c) is for the NWA scalar boson. For the RS graviton, the VBF production is not considered

4.4.1. Combination Strategy

The combination scheme could be seen in Fig. 4.7, and the considered analyses with a brief event selection summary is presented in Tab. 4.7.

With the number of involved analyses, the likelihood construction of all the final state would be too complicated, so the procedure was conducted step by step. It started from the combination of channels with same medium states of WW, WZ, or ZZ bosons. For example, there are three analyses involved for $X \to WW$ with final states of $\ell\nu qq$, $\ell\nu\ell\nu$ and qqqq, so they are combined first.Then, the combined results of WW, WZ, and

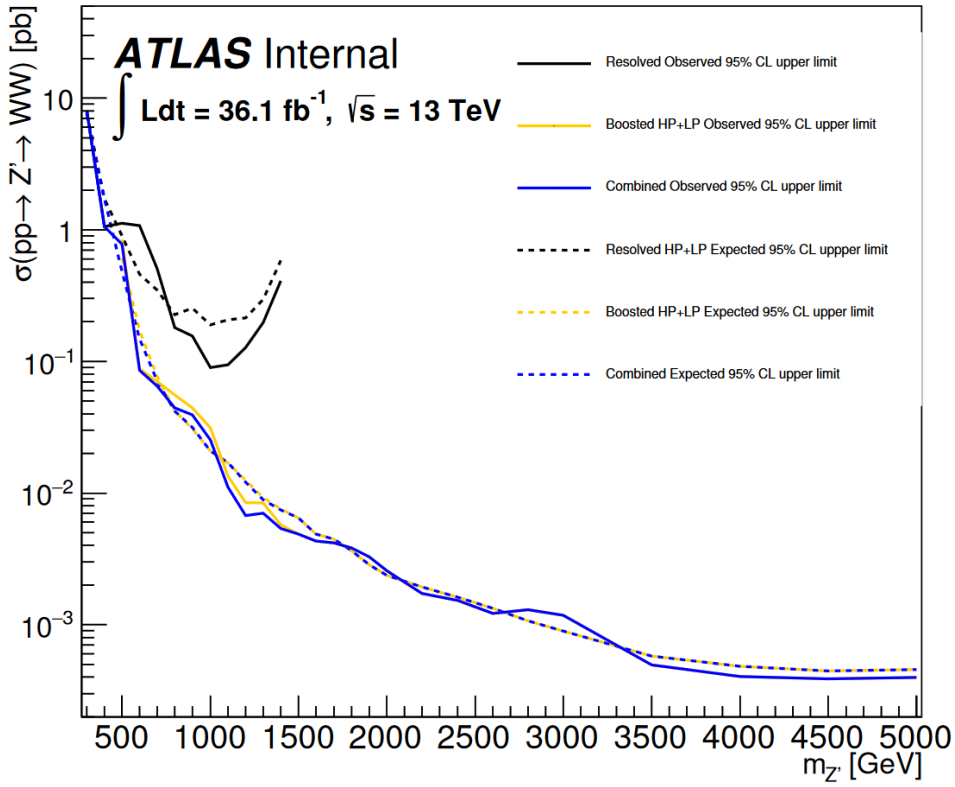

Figure 4.6.: The limit comparison between the merged, resolved, and combined channels.

ZZ are further combined to give the VV combination result. At this stage, the statistic interpretations for RS gravitons and NWA scalar bosons are completed. Following by that, the VV channels are combined together with VH and dilepton channels to set the limit on mass of W′ and Z′ bosons as well as the coupling strength between the HVT and SM particles.

Orthogonality

Within VV and VH channels, the category orthogonality was kept by the cuts on lepton number, E_T^{miss}, and b-jet numbers. However, due to overlapped mass windows between W/Z and Higgs bosons, some events went into both VV and VH signal regions. Tab. 4.8 shows the mass windows used in the hadronically decayed bosons. In this case, the events are given higher priority to go into the VV category and get removed from the VH channels, if the selected dijet system has the mass in the overlapped region. With the comparison to the original event selection, the expected

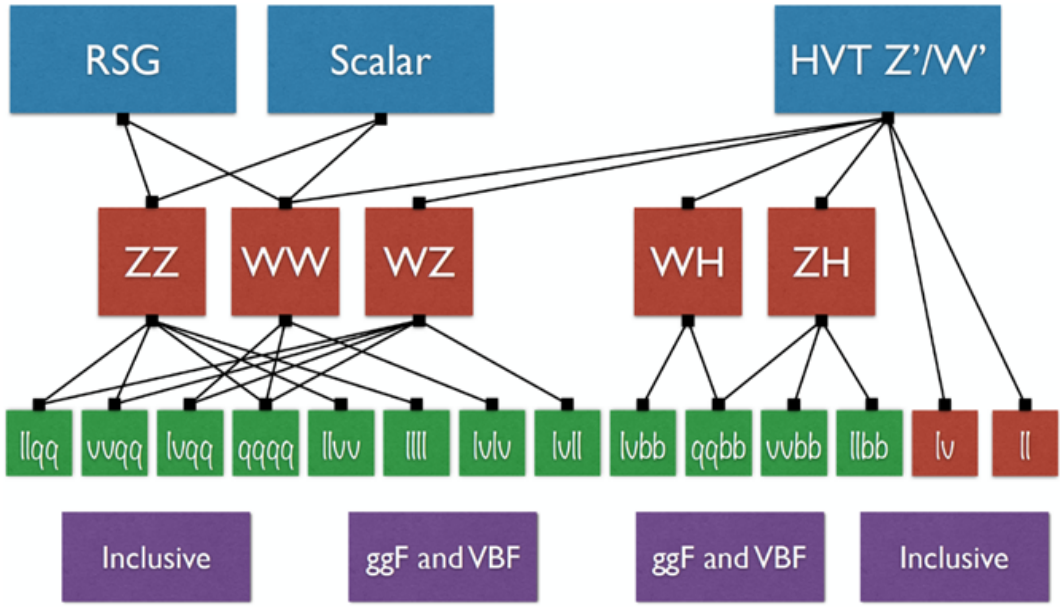

(a)

Figure 4.7.: The scheme for combination of VV, VH, and dilepton analyses with their final states. It could be seen that decays channels for WW, WZ, ZZ, WH, and ZH are combined respectively first. Then, the further combinations are performed to give the final interpretation.

sensitivity does not have significant change ($< 10\%$) which could be seen in Fig. 4.8.

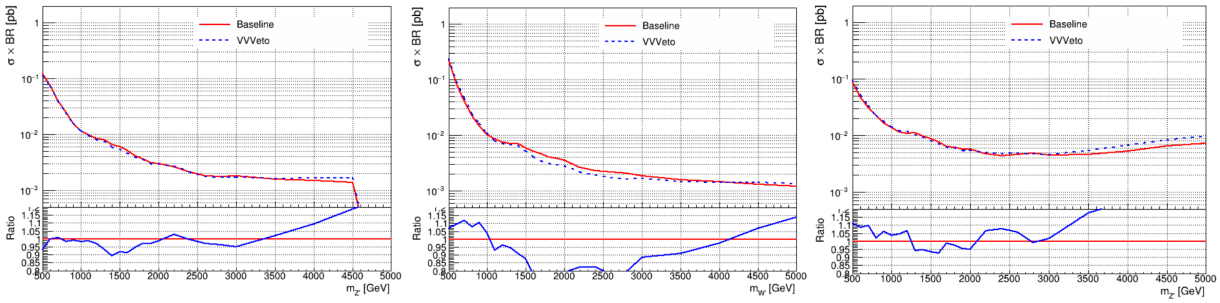

(a) **(b)** **(c)**

Figure 4.8.: The change in expected limits in the VH channels for (a)$VH \to \nu\nu bb$ (b)$VH \to \ell\nu bb$ and (c) $VH \to \ell\ell bb$

Nuisance Parameter Correlation

For each individual analysis, more than 100 nuisance parameters are considered.

Table 4.7.: The list of individual analyses which are taken into the combination

Channel	Diboson state	Selection				VBF cat.	Reference
		Leptons	E_T^{miss}	Jets	b-tags		
$qqqq$	$WW/WZ/ZZ$	0	veto	2J	–	–	[92]
$\nu\nu qq$	WZ/ZZ	0	yes	1J	–	yes	[75]
$\ell\nu qq$	WW/WZ	$1e, 1\mu$	yes	2j, 1J	–	yes	[76]
$\ell\ell qq$	WZ/ZZ	$2e, 2\mu$	–	2j, 1J	–	yes	[75]
$\ell\ell\nu\nu$	ZZ	$2e, 2\mu$	yes	–	0	yes	[93]
$\ell\nu\ell\nu$	WW	$1e$+1μ	yes	–	0	yes	[94]
$\ell\nu\ell\ell$	WZ	$3e$, $2e$+1μ, $1e$+2μ, 3μ	yes	–	0	yes	[95]
$\ell\ell\ell\ell$	ZZ	$4e$, $2e$+2μ, 4μ	–	–	–	yes	[93]
$qqbb$	WH/ZH	0	veto	2J	1, 2	–	[96]
$\nu\nu bb$	ZH	0	yes	2j, 1J	1, 2	–	[97]
$\ell\nu bb$	WH	$1e, 1\mu$	yes	2j, 1J	1, 2	–	[97]
$\ell\ell bb$	ZH	$2e, 2\mu$	veto	2j, 1J	1, 2	–	[97]
$\ell\nu$	–	$1e, 1\mu$	yes	–	–	–	[98]
$\ell\ell$	–	$2e, 2\mu$	–	–	–	–	[99]

Some of them are commonly applied across the analyses, but there are also the ones which only made the contribution to the dedicated analyses. The following is the list of nuisance parameters which are decorrelated from the other analyses:

Jet Uncertainties: The measurement of jets actually have 81 sources of uncertainties, but most of analyses just deploy the simplified schemes for which the 81 sources are combined into 21 or 3 uncertainties. For the analyses using different simplified uncertainty schemes, their jet uncertainties are uncorrelated ($VV \to \ell\nu\ell\ell$&$\ell\ell\nu\nu$)

Electron ID Uncertainty: The $VV \to \ell\nu\ell\nu$ analysis has deployed different identification working points in the electron selection, so the related uncertainties are uncorrelated.

Signal and Background Modelling Uncertainties: The scale factors for the SM background in the likelihood reconstructions are decorrelated as they have differ-

Table 4.8.: The mass windows for the selection on hadronically decayed bosons in VV and VH events

channel	Jet Topo	W	Z	H
$qqqq$	resolved	-	-	-
	merged	[65,95]	[76,106]	-
$\ell\ell qq$	resolved	[62,97]	[70,105]	-
	merged	[65,95]	[76,106]	-
$\ell\nu qq$	resolved	[66,94]	[82,106]	-
	merged	[64,104](LP)	[69,114](LP)	-
$\nu\nu qq$	resolved	-	-	-
	merged	[65,95]	[76,106]	-
$qqbb$	resolved	-	-	-
	merged	-	[70,110] (HP)	[75,145]
$\ell\nu bb/\nu\nu bb$	resolved	[110,140]		
	merged	[75,145]		
$\ell\ell bb$	resolved	[100,145]		
	merged	[75,145]		

ent kinematic properties for varied final states. Furthermore, the uncertainties arising from the data-driven estimation are also decorrelated. As the ISR and FSR effect was not considered in the fully leptonically decayed channels, they are uncorrelated as well.

4.4.2. Result

The combination is aiming for two kinds of results: the limit on the mass of exotic partices (NWA scalar boson, HVT W' and Z' bosons, and RS gravtion), and the limit on the coupling strength between the HVT and SM particles. The first result will follow the asymptotic methodology which was discuss in Sec.4.3 with a cross-check from the toy model[3], and , for the second result, a similar likelihood would be constructed by the parameter of interest would be the coupling constant, $\vec{g}$, instead of the signal

[3] as running the toy model is computationally expensive, it it only performed on the mass points of 1, 2, 3, 4, and 5 TeV

strength, μ. The detail will be coming later.

Mass Limits

The cross-section limits are set with the ggF/DY and VBF productions respectively. For the VBF category, not all analyses have this channel, but they are still combined to provide the upper limit, and the results are shown in Fig. 4.9. Here, a new benchmark for the HVT model is applied with $g_H = 1$ and $g_f = 0$, and this means the production of W′ and Z′ bosons could only be via VBF. With this new configuratio (named as model c), the sensitivity is set as the inclusive (W′ + Z′ bosons) cross-section upper limit ratio between the expectation (observation) and theory. With respect to the single channel analysis presented before, the mass limit has seen a significant improvement from 1.2 TeV(3 TeV) to 2.2 TeV(4.5 TeV) for the RS graviton (HVT boson) interpretation.

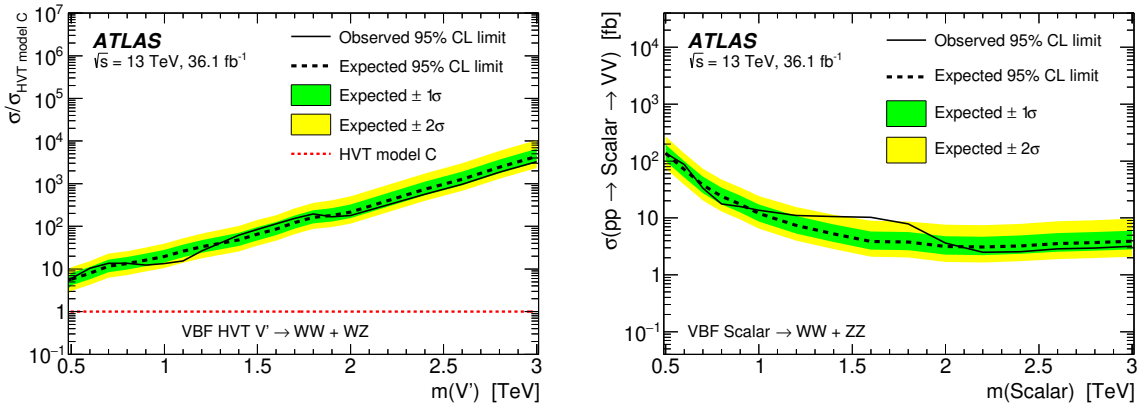

(a) **(b)**

Figure 4.9.: The cross-section upper limit for (a) the HVT model boson (as a ratio to the theoretical one) (b) and the NWA scalar boson

For the ggF result, the VV channel is combined with VH and dilepton channels for the HVT interpretation, while the limits on models of RS graviton and NWA scalar boson are only set with the VV channel. The HVT interpretation is shown in Fig. 4.10 as the ratio of the observed cross-section to the theoretically predicted cross-section. And, the limits on RS graviton and NWA scalar bosons are in Fig. 4.11, while Fig. 4.12 is

presenting the comparison of the sensitivities from the VV+VH and dilepton channels.

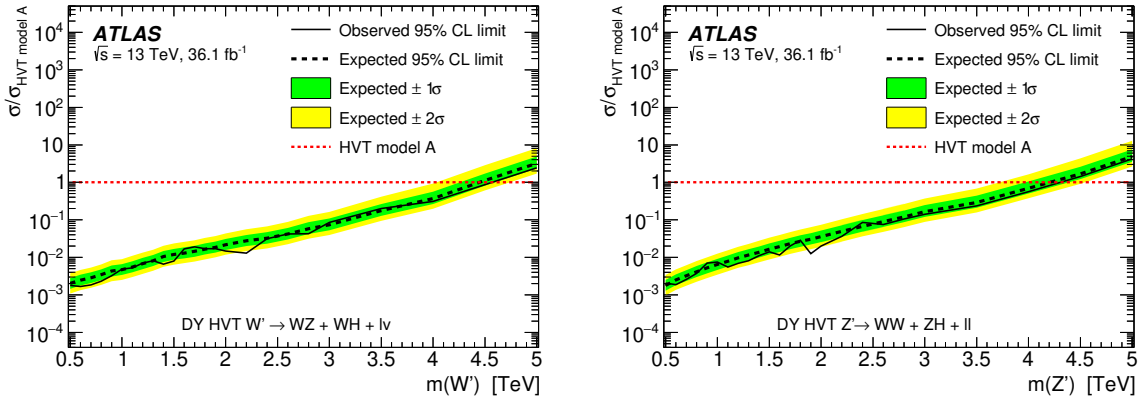

(a) **(b)**

Figure 4.10.: The cross-section upper limit ratio to the HVT model theoretical prediction for (a) the W′ boson (b) the Z′ boson

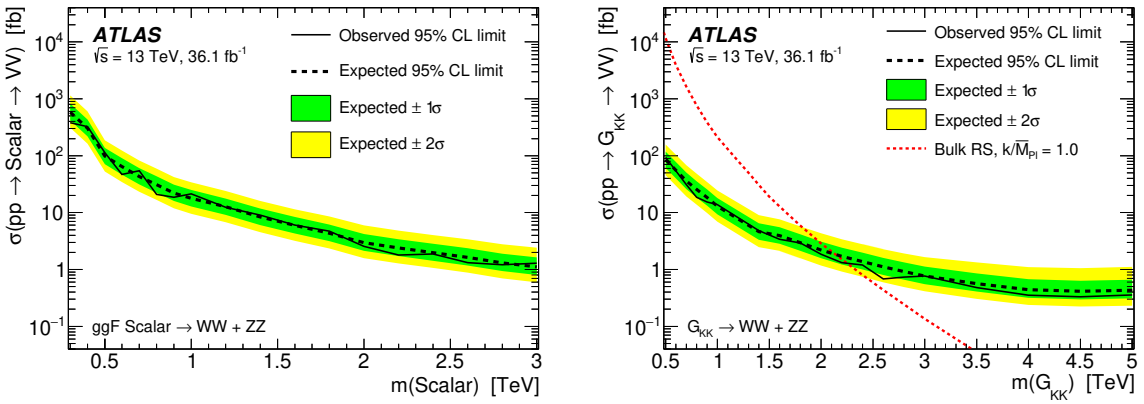

(a) **(b)**

Figure 4.11.: The cross-section upper limit on the (a) NWA scalar boson (b) RS graviton

Coupling Limits

The limits of the HVT couplings are set on a two-dimensional plane with which two pairs of parameters are used:

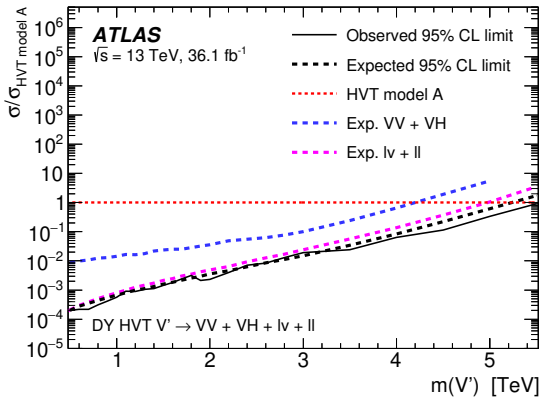

Figure 4.12.: The comparison on the limits on the HVT V′ bosons set by different channels

g_H **and** g_f: they are corresponding to the couplings to the SM bosons (W, Z, and H) and fermions. For the simplicity, the fermionic coupling is set equal between quarks and leptons.

g_l **and** g_q: they are corresponding to the couplings to the leptons and quarks with the coupling to SM bosons set at 0.56 (model A).

For the estimation of the couplings, the same method in Sec.4.3 is applied with the profile likelihood and asymptotic formulae, but the likelihood is constructed with the coupling strengths, $\vec{\mathcal{G}}$:

$$\lambda(\vec{\mathcal{G}}) = \frac{\mathcal{L}(\vec{\mathcal{G}}, \hat{\hat{\theta}})}{\mathcal{L}(\hat{\vec{\mathcal{G}}}, \hat{\theta})} \tag{4.24}$$

Then, the event yields (signal strength) would be parametrized in terms of the couplings, and the following procedure is to set the exclusion limit at the 95% confidence level .

The final results are shown in Fig. 4.13 on which the region outside dotted lines are excluded, and exclusions from the electroweak precision measurements [100] are also overlaid as the coloured exclusion region which has combined the following experiments:

- Z mass pole measurements from LEP [100]
- LEP2 measurements provided in the last joint paper by the ALEPH, DELPHI, L3, and OPAL Collaborations [101]
- Measurements from low-energy experiments, CKM unitarity and α_s [102]
- World average for the top-quark mass measurements from the ATLAS, CMS, CDF, and D0 Collaborations [103]
- World average for the Higgs boson mass measurements with Run 1 data from the ATLAS and CMS Collaborations (the cross-section measurement is not included) [104]

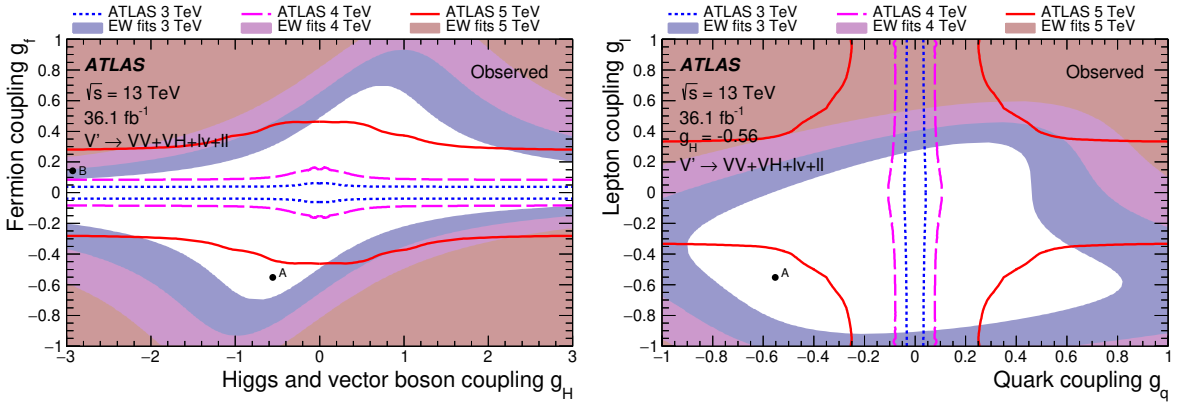

(a) **(b)**

Figure 4.13.: The limits on coupling strength from the full combination with (a) g_H, g_f and (b) g_l, g_q planes

It could be seen that the combination of exotic particle searches has presented the exclusion that the electroweak measurements did not have the sensitivity to achieve. With the low mass HVT boson assumptions, both of the two benchmark models are also excluded by the coupling strength interpretation.

4.5. Summary

In the search for new particles with diboson resonance, the single final state of $WV \to \ell\nu qq$ is chosen to investigate two production modes, ggF/DY (indistinguishable) and VBF, along two jet topologies. The background estimation was performed with the Monte Carlo simulation for the Standard Model process like W+jets and $t\bar{t}$ interactions and the Fake Factor method for the multijet events. After the comparison between background estimation and data with a statistic interpretation, the discovery significance did not confirm the existence of any unknown particle. Therefore, the limits are set via the asymptotic method on the particle mass based the present analysis sensitivity.

For the further enhancement on the sensitivity to new physics, the $\ell\nu qq$ result was combined with the other diboson and dilepton final states. However, there is still no evident existence of the new particles. The limits on the particle mass and their coupling to the SM particle are then set giving an improved constraint on the phase space for the new particle searches.

Chapter 5.

Search with Non-Resonance Signatures (Vector Boson Scattering)

"When something is too hard, there is always another way."
— Charlie, Finding Dory

In addition to the physics with resonance particles, unknown couplings between SM particles are also a portal to new physics. Their signature would be similar to the SM with enhanced or reduced (interference) occurrence rates (cross section) for the physical process of interest. However, the deviation from SM prediction might be marginal, so tests on precision measurement could only be achieved with large amount of data. With the LHC data collected in 2015 and 2016, some of the rare processes predicted by the SM could examined for the first time.

This analysis is aiming for the phenomenology with "vector boson scattering" (VBS) which has the signature like VBF with one back-to-back high-mass jet pair accompanied by two SM gauge bosons ($qq \rightarrow VVqq$). The phenomenon was an interaction with relatively low cross-section predicted by the SM and measured in ATLAS Run1 data analysis (2009-2012) along with the search for the anomalous quadratic gauge coupling (aQGC). However, with the limit number of data, the measurement did not give a promising result for the existence of this interaction (the p-value is less than

3σ) [105]. This analysis is to extend the search with greater luminosity of data collected in 2015 and 2016 for $36.1 fb^{-1}$, and the final state of the dibson system is chosen to be semileptonic. This analysis will focus on one lepton channel ($WV \to lvqq$) just like the resonance search, and the result will be combined with other two semileptonical final states ($ZV \to vvqq/llqq$) for the statistic interpretation.

With the same final state, the object definition was inherited from the resonance search, and the simulation sample and dataset are also reused. However, because the search is aiming for different signal, the optimization was repeated for the thresholds of object and event selection. The most significant change in this analysis is that although m_{WV} is still reconstructed, it cannot be taken as the discriminant because of no resonance particle in the process. Instead, an algorithm of boosted decision tree (BDT) is performed on the experimental observables, and it would give the output of "BDT score" for the discrimination of signal and background.

To maximize the sensitivity, the event categorization employs the same strategy to have boosted HP, boosted LP, and resolved regions for signal, W+jet and $t\bar{t}$ control regions for VBS category only, and the event priority is the same as the resonance search.

5.1. Signal Simulation Samples

Two types of signal signature were generated: SM VBS scattering and anomalous quadratic coupling. As this analysis is a general search for the coupling signature, a couple of physical processes are involved as the signal. In this case, an approximation of effective field theory (EFT) is applied to simplify the simulation.

5.1.1. Standard Model Vector Boson Scattering

Under the SM, the vector boson scattering is through the coupling to a variety of bosons including W/Z bosons, photon, or Higgs boson. The coupling strength is

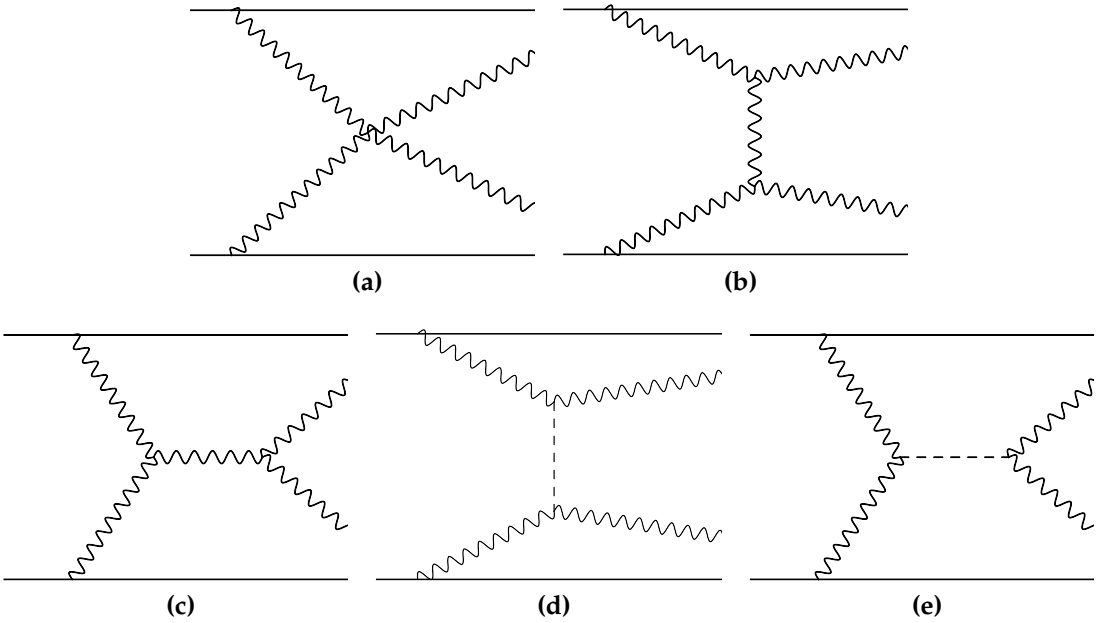

Figure 5.1.: Here are the Feynman diagrams which contribute to the SM VBS signal. The dashed line in figure (b) and (d) are the Higgs boson which couples the interactions. Those interactions are of the order α_{EW}^6 involving the consideration of the decays of the two scattered bosons into fermions.

constrained by the Higgs mass, so the measurement could be another test on the Higgs naturalness and Brout-Englert-Higgs Mechanism [106]. The interactions considered in this analysis are shown in Fig. 5.1 with the order of α_{EW}^6 which also considers the decays of bosons into fermions.

For those interactions, only the longitudinal component of bosons is considered, while the transverse one has relatively low coupling strength, so it is neglected [107]. When the Higgs boson is not involved in the interactions (Fig. 5.1 (a)-(c)), the coupling magnitude [108] could be presented in Mandelstam variables, s and t, as:

$$|\mathcal{M}| = \frac{g^2}{4m_W^2}[s+t] \tag{5.1}$$

with the consideration of only the coupling to W bosons for simplicity. This implies that the coupling strength will diverge when the energy increases, so the unitary of ρ in Eq. 1.23 would be broken due to the enhanced coupling between W and Z bosons. The introduction of the Higgs boson to mediate the bosons could provide a constraint

to prevent the divergence, which makes the coupling magnitude to:

$$|\mathcal{M}| = \frac{g^2 m_H^2}{4m_W^2}\left[\frac{t}{t-m_H^2} + \frac{s}{s-m_H^2}\right] \tag{5.2}$$

This expression is hold at the tree level, and the perturbative terms are neglected with the light Higgs boson [109]. However, the high order terms would remain if the Higgs mass is above 1.2 TeV with $\lambda > 4\pi$:

$$m_H^2 = 2\lambda v^2 > 1.2\ TeV \tag{5.3}$$

where v is 246 GeV measured from experiments. This would then make the cross-section diverge again as shown in Fig. 5.2. Therefore, the cross-section measurement of the SM vector boson scattering could be another verification of the existence of high-mass Higgs boson.

Sample Production

The signal samples are produced with the setting under SM with Higgs boson mass at 125 GeV. MADGRAPH5_aMC@NLO v2.3.3 [69] is the chosen generator interfaced by PYTHIA8 [52] for the fragmentation with the PDF set of NNPDF30LO [59]. The two medium state bosons (WW or WZ) are required to be on-shell with the mass pole from PDG.

As thw physical processes for this analysis is presented as $pp \to VVjj$, some of unwanted interactions would also go into the signal samples. Their coupling is still at the order of α_{EW}^6, but no VBS interaction is involved. With the VBS requirement on event selection, the contribution is well-suppressed.

5.1.2. Anomalous Quadratic Coupling (aQGC)

With the light mass of the discovered SM Higgs boson, the Higgs naturalness turns to be a problem. In addition to the BSM heavy Higgs bosons, the hidden couplings

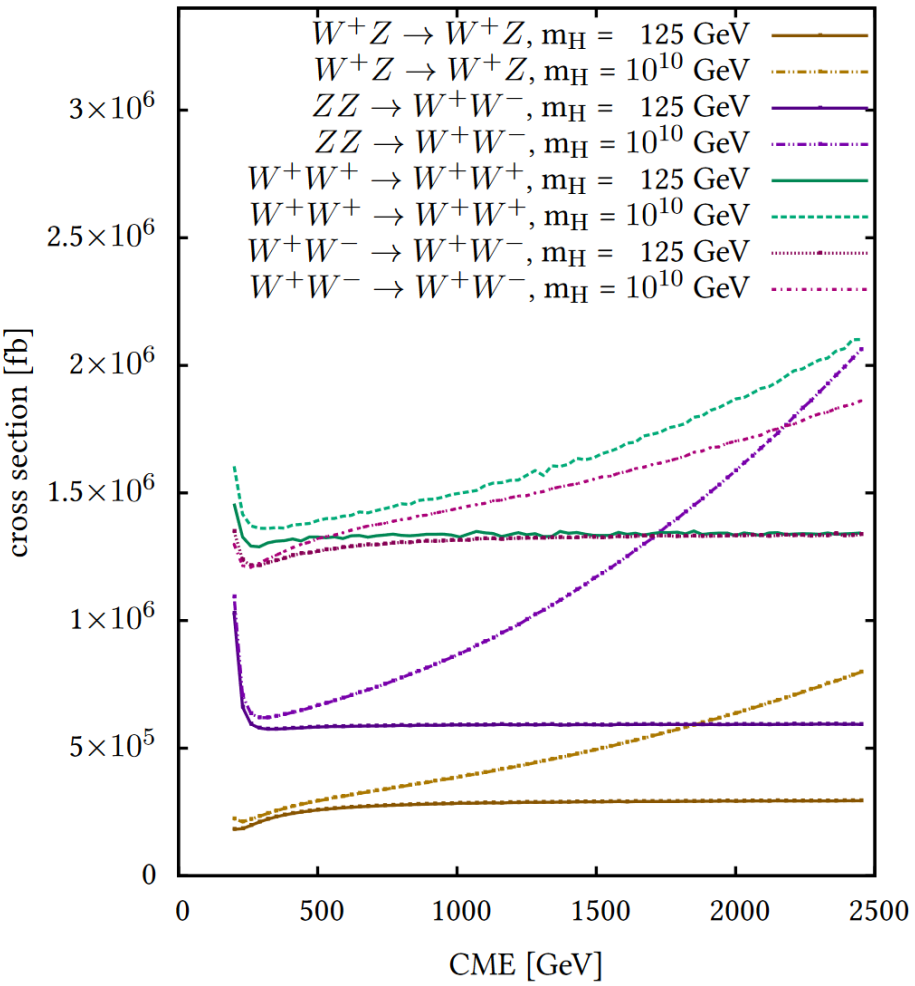

Figure 5.2.: The cross-section of vector boson scattering between gauge bosons with Higgs boson of 125GeV and $10^{10}GeV$ as a function of $\sqrt{s}$. [110]

between bosons is another approach to this issue. It could lead to the fine-tuning to the SM Lagrangian to make high order correction.

To simplify the hidden theory, the approach of EFT is applied which could be presented in Lagrangian as:

$$\mathcal{L}_{EFT} = \mathcal{L}_{SM} + \sum_i \frac{\mathcal{C}_i}{\Lambda_i^{d-4}} \mathcal{O}_i^d \tag{5.4}$$

where the extended term, $\sum_i \frac{\mathcal{C}_i}{\Lambda_i^{d-4}} \mathcal{O}_i^d$, is contributed from the anomalous couplings which are indexed by i. It is constructed by 3 components: Λ as the energy scale for where the coupling is significant, C_i as the coefficient of this interaction and O_i^d is the operator. d is used as the number of dimensions of this coupling. With the constraint of Λ in the power of $d-4$[1], the interactions of higher order could be neglected due to small contribution. When Λ goes to ∞, that would mean the new physics is unapproachable, and SM would be the only observable phenomenon. This approach has been proven working well to have theoretical agreement to experimental data with the example from Fermi theory.

The new physics operators, $\mathcal{O}$, considered here is based on Eboli model [111, 112] which formulates the new interactions with the components:

- Higgs Field Covariant Derivative: $D_\mu \Phi = (\partial_\mu + igW_\mu^j \frac{\sigma^j}{2} + ig' B_\mu \frac{1}{2})\Phi$
- Electroweak W Field Covariant Derivative: $\hat{W}_{\mu\nu} = \sum_i (\partial_\mu W_\nu^i - \partial_\nu W_\mu^i) \frac{\sigma^i}{2}$
- Electroweak B Field Covariant Derivative: $B_{\mu\nu} = \partial_\mu B_\nu - \partial_\nu B_\mu$

The notations used here are the same as the ones used in Chap. 1 with σ^j as the Pauli Matrices, and they all have the same dimension of two:

$$\left[D_\mu \Phi\right] = \left[\hat{W}_{\mu\nu}\right] = \left[B_{\mu\nu}\right] = GeV^2 \tag{5.5}$$

[1] $d-4$ is applied on the energy scale to keep the dimension consistent in the Lagrangian

Then, the BSM interaction is constructed from four of them (the same component could be chosen multiple times) which are combined into one individual operator with the dimension of eight. Three types of operators can then be categorized by the combinations:

- $D_\mu\Phi$ only: the operators are only composed of $D_\mu\Phi$ and denoted as $\mathcal{O}_S^i$ with the free parameters f_S^i. The index, i, ranges from 0 to 2.
- all the elements: the operators are the mix with all the components denoted as $\mathcal{O}_M^i$. The free parameters are denoted as f_M^i with the index, i, ranging from 0 to 7.
- combination of the electroweak fields: the operators have $\hat{W}_{\mu\nu}$ and $B_{\mu\nu}$ which are denoted as $\mathcal{O}_T^i$ with the free parameters, f_T^i. The index, i, has the range from 0 to 9.

Signal Production

It is impossible to investigate all the possible operators, so only one operator of each category is chosen in the signal, which are O_S^0, O_M^0, and O_T^0 with the free parameter, f_S^0, f_M^0, f_T^0, while the other operators are tuned to 0. The chosen coupling strength for the free parameters in the simulation is summarized in Tab. 5.1.

Similar to the SM VBS signal, the production is also via MADGRAPH5_aMC@NLO v2.3.3 [69] interfaced by PYTHIA8 [52] with the PDF set of NNPDF30LO [59]. However, this simple production scheme is not enough for the aQGC statistic interpretation. With the consideration of time scale for a complete sample production (with more benchmarks for Eboli Model parameters), the aQGC statistical interpretation was discard in this analysis.

Table 5.1.: Set-up of parameters in Eboli Model for this analysis

	f_S^0 $\left[10^{-12}TeV\right]$	f_M^0 $\left[10^{-12}TeV\right]$	f_T^0 $\left[10^{-12}TeV\right]$
Signal 1	50	0	0
Signal 2	0	5	0
Signal 3	0	0	1

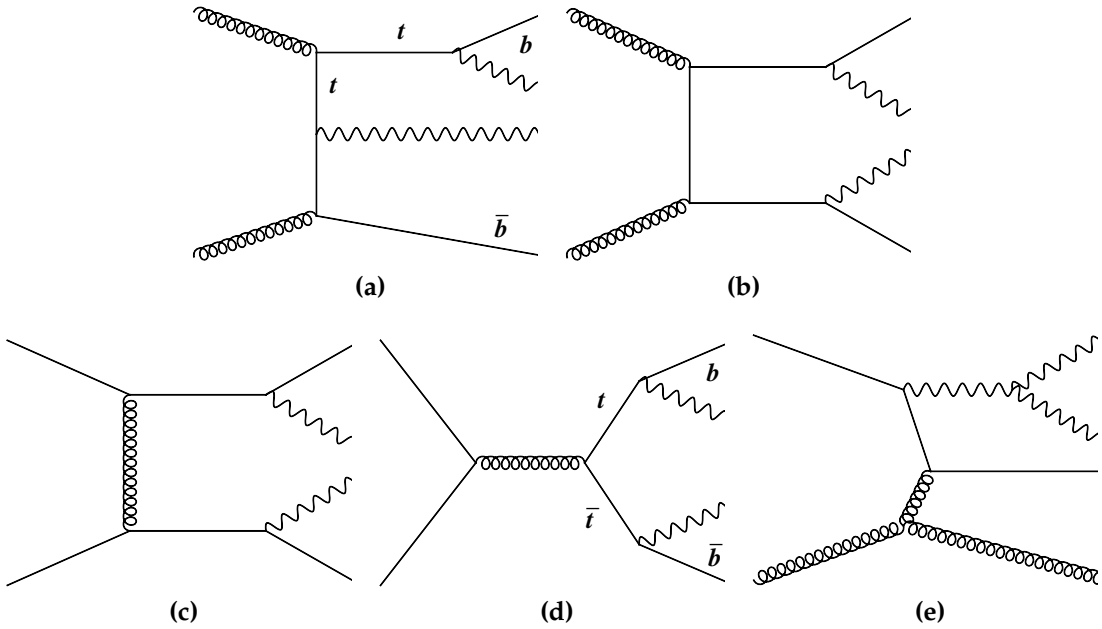

Figure 5.3.: Here are the Feynman diagrams which contribute to the SM VBS signal. The dashed line in figure (b) and (d) are the Higgs boson which couples the interactions. Those interactions are of the order α_{EW}^{6} involving the consideration of the decays of the two scattered bosons into fermions.

5.1.3. Interference Effect on the Signal

Under the Standard Model, the interference on the VBS cross-section would come from the QCD processes which is via the same process, $qq \to VVjj$, under the order of coupling, $\alpha_{EW}^{4}\alpha_{EW}^{2}$. The QCD interactions could be seen in Fig. 5.3. The effect on the cross-section estimation could be presented with the matrix elements, $\mathcal{M}$:

$$|\mathcal{M}|^2 = |\mathcal{M}_1 + \mathcal{M}_2|^2 = |\mathcal{M}_1|^2 + |\mathcal{M}_2|^2 + 2Re(\mathcal{M}_1\mathcal{M}_2) \tag{5.6}$$

with $|\mathcal{M}|^2$ as the total amplitude, and $\mathcal{M}_1$ and $\mathcal{M}_2$ are the amplitudes from the VBS and QCD contributions. The last term is showing the interference effect on the total cross-section. With the estimation by MADGRAPH5_AMC@NLO V2.3.3 [69], this effect is less around 1% for the VBS signal, so it is taken negligible, but it is still taken as one contribution of systematic uncertainty.

5.2. Event Selection

In general, the event selection in this analysis has the same scheme as the resonance search including both trigger and event cleaning. However, as the optimization is conducted with SM VBS signal, some cuts are looser due to the similar kinematic properties with respect to the background. For the same reason, the cuts on topological variables employed in resonance search would also remove significant signal, so they are dropped in this analysis [113].

Not just the event selection scheme but also the event categorization is adopted here from the resonance $WV \to \ell\nu qq$ analysis. Three regions are defined with the jet topology as boosted HP, boosted LP, resolved regions (in the order of selection priority) for W+jet control region, top control region, and signal regions (with higher selection priority than the other two). To achieve better sensitivity for aQGC, the dedicated control region is defined with one additional cut in the signal region with $m^{VBS} > 1\ TeV$.

5.2.1. Batman Veto

In September 2017, a cell saturation problem in high pile-up runs in 2015 and 2016 was reported in the LAr detector endcap (EMEC). This leads to a large number of low p_T jets ($p_T > 20\ GeV$) falsely reconstructed at $|\eta| \sim 2.9$ (which is beyond the range where JVT is applicable), and they also made the contribution to E_T^{miss} reconstruction. Therefore, the events are removed manually by the event and run numbers. Fig. 5.4 shows the jet η distributions before and after the problematic event removal in resolved signal region but with two loose leptons selected, which is another channel along with this 1 lepton analysis. (This issue was noticed after the resonance search was completed, so it was not considered.)

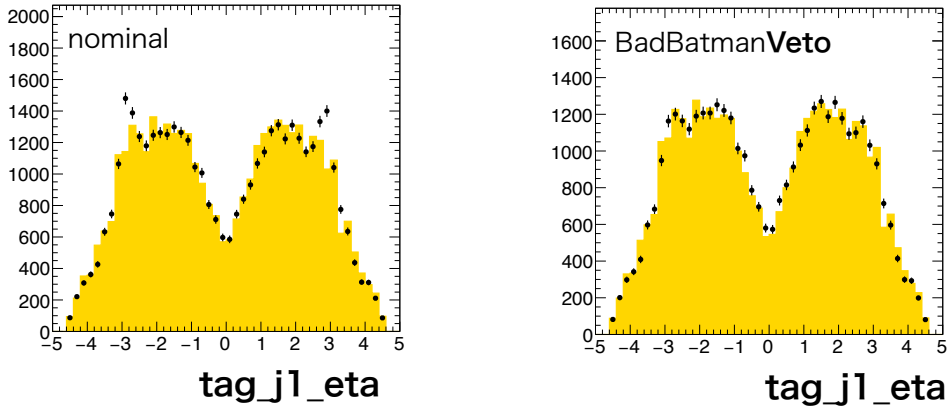

Figure 5.4.: The jet η distribution before (left) and after (right) the problematic event removal

5.2.2. VBS Event Selection

The pairs of VBS jets are still chosen to be the one with highest invariant mass and toward different η direction ($\eta_1 \times \eta_2 < 0$) in an event, but, different to resonance search, the selection was conducted after the pair of signal jets from the boson decay (the pair with invariant mass closet to W/Z mass pole). The full selection of the jet pair is listed below:

- $p_T^{j1} > 30\ GeV \&\& p_T^{j2} > 30\ GeV$
- $m^{VBS} > 400\ GeV$
- $\eta_1 \eta_2 < 0$
- not b-tagged

5.2.3. Boosted & Resolved Event Selection

Tab. 5.2 and 5.3 are showing the cuts applied to select the events into both signal and control regions. The measurement on both aQGC and SM cross-section does not distinguish the processes of WW or WZ, so only one SR is defined for both boosted and resolved jet topologies.

As compared to the resonance search, object selections are kept the same like the

Table 5.2.: Summary of the selection criteria in the definition of the signal region (SR), W+jets control region (W CR) and $t\bar{t}$ control region ($t\bar{t}$ CR), in the high-purity (HP) and low-purity (LP) categories.

Selection		SR		W CR		$t\bar{t}$ CR	
		HP	LP	HP	LP	HP	LP
$W \to l\nu$	Num of signal leptons	1					
	Num of vetoed leptons	0					
	E_T^{miss}	$> 80GeV$					
$W/Z \to J$	Num of large-R jets	≥ 1					
	$D_2^{(\beta=1)}$ 50 % WP	pass	fail	pass	fail	pass	fail
	$D_2^{(\beta=1)}$ 80 % WP	—	pass	—	pass	—	pass
	W/Z mass 50 % WP	pass	fail	—	—	pass	fail
	W/Z mass 80 % WP	—	pass	fail	fail	—	pass
Top-quark veto	Num of b-tagged jets	0				≥ 1	

p_T threshold or lepton isolation requirements. However, the E_{miss}^T cut is lowered to 80 GeV to enhance the statistics for the training sample into the multivariable analysis. Furthermore, the topological cuts are also removed from this analysis, because they are too stringent for the signal sample. And, the b-tagging requirement is also changed in the resolved channel with forbidding any b-tagged jet in the events for signal region.

The definition of W+jet control regions is still defined by the mass side band of the dijet system in resolved channel and failed mass tagging in boosted channel. With the change on number of b-tagged jets, the top control region definition is also simplified as the event with any existence of b-jets.

5.3. Multivariate Analysis

When the new physics and SM interactions have similar kinematics, their detector signatures would have marginal difference. In this case, no individual variable could be taken as the discriminant to distinguish signal from backgrounds. And, this is why

Table 5.3.: Summary of the selection criteria of of the resolved analysis for the WW and WZ signal regions (SR), W+jets control region (WR) and $t\bar{t}$ control region (TR).

cuts		SR	WR	TR
$W \to \ell\nu$ selection	Number of signal leptons	1		
	Number of veto leptons	0		
	E_T^{miss}	$> 80GeV$		
$W/Z \to jj$ selection	Number of small jets	≥ 2		
	$p_T(j1)$	> 60 GeV		
	$p_T(j2)$	> 45 GeV		
	m_{jj}	[64, 106]GeV	$< 66GeV$ or [106, 200]GeV	[64, 106]GeV
Top veto	Number of b-tagged jets	0	0	≥ 1
Existence of VBF jets		yes		

the multivariate analysis is taken into the analysis, and it is based on the framework of TMVA [114].

Two candidate algorithms were considered: adaptive and gradient decision trees. However, the outcome of adaptive decision tree is not robust to prevent overtraining [113], which means the training is too close to the training sample, so it might fail the prediction of additional data. Therefore, gradient boost decision (GBDT) is chosen to be used in this analysis.

Decision Tree

Decision tree is constructed with a series of binary decisions. Those decisions are made by whether the events could pass a cut which can give the best separation between signal and background. The full scheme could be presented as Fig. 5.5. To make the best decision on signal and background separation, the *Gini Index* is defined as:

$$I_G = p(1-p) \tag{5.7}$$

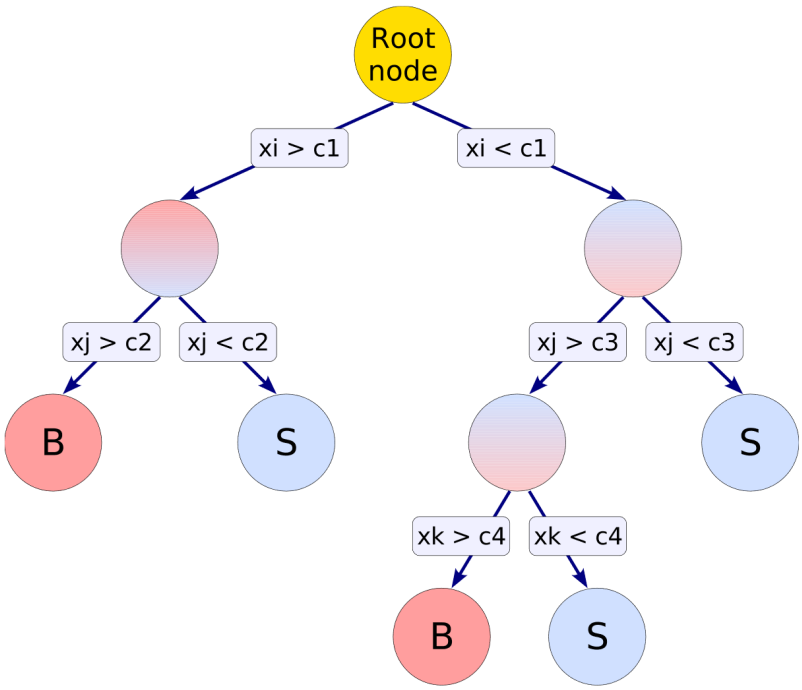

Figure 5.5.: The scheme of a decision tree. The nodes are where the decision are made by whether the event could pass the cut on x_i, x_j, and x_k. The bottom nodes are the final outcomes labeled as S for more signal events categorized into the node, and B for more background events

where p is the percentage of signal events (purity) in the node. The decision would then be made to optimize the increase of I_G in the mother node:

$$Gain = I_G^{\text{mother}} - \frac{n_1}{N} I_G^{\text{daughter1}} - \frac{n_2}{N} I_G^{\text{daughter2}} \tag{5.8}$$

where the two daughter nodes are split from the mother node (event number, N, divided to n_1 and n_2), and their I_G's are reweighted. After repeating this procedure, the events get into the leaf nodes where they are labelled by signal or background depending on which kind of events takes over bigger proportion. To avoid over-training, a further procedure called "pruning" is applied. This procedure is conducted from the bottom, and the node with little increase of the separation power (*Gini Index*) is removed. If the following branches are all removed, the mother node making the decision would be turned into another leaf node.

The other decision tree is also used in this analysis which is called "regression tree" for the prediction of a truth value which is not in the binary format. In this case, the *Gini Index* is not available, and, instead, the average squared error is used:

$$\sigma = \frac{1}{N} \sum^{N} (\hat{y}_i - y_i^{truth}) \tag{5.9}$$

with $\hat{y}_i$ as the average truth value of the events in the same node and y_i^{truth} as the truth value of the events itself. The decision is made with a cut which makes σ as the minimum.

In general, decision tree has the advantage of being handy for use, easy to understand, and flexible, but it also has the disadvantage of being weak to statistic fluctuation and correlation between input variables especially when only one tree is trained. Therefore, there are a couple of methods to train trees into "forests" like random forest, and the one used in this analysis is "Gradient Boost".

Gradient Boost

Due to the insufficiency of a simple decision tree, the approach called "boost" is applied into the sample events after each tree is grown up. The process is determined by deviation of the predicted value from the truth value with a "Loss Function" defined as:

$$L(F(x_i), y_i) = \sum_{i}^{n} \ln(1 + \exp(-2F(x_i)y_i)) \tag{5.10}$$

where $F(x_i)$ is the predicted value from the outcome of decision trees for the ith event, and y_i is its truth value. The training process is then conducted in the following steps:

(a) The first tree is built up with the procedure as mentioned above to optimize the *Gini Index*.

(b) The predicted value of each event, $F_0(x_i)$, is then assigned by the type of nodes. (signal node: $F_0(x_i) = 1$, background node: $F_0(x_i) = -1$)

(c) The gradient of Loss Function, $\partial L(F_0(x_i), y_i)/\partial F_0(x_i)$, is calculated for each event.

(d) The average of the gradient from all the events in a node is assigned as a new label.

(e) Instead of using the label of background (-1) and signal ($+1$), the average of gradient is taken as the new label on the events for next training

(f) The training is conducted as a regression tree by minimizing the average squared error when making each decision

(g) After the tree is constructed, the average expected value of each leaf node, $\hat{y}_i$, is taken to correct $F_0(x_i)$:

$$F_1(x_i) = F_0(x_i) + \beta \hat{y}_i \tag{5.11}$$

with β as the training rate. Smaller β gives better precision, but the training also needs more trees to achieve the required accuracy.

Table 5.4.: The customized parameters in the Gradient Boosted Decision Tree Configuration

Option	Defined Value	Description
NTrees	800	Number of trees
MinNodeSize	5%	Minimum percentage of training events required in a leaf node, or the leaf shall be trimmed off
Shrinkage	0.3	Training rate used in this analysis
nCuts	20	Number of grid points in variable range used in finding optimal cut in node splitting
MaxDepth	4	Max depth of the decision tree allowed
BaggedSampleFraction	0.5	The fraction of events in the full sample for training of each tree.

(h) step (c) to step (g) are then repeated until N tree are built.

The final outcome, $F_N(x_i)$, of this training is then called "BDT score" which is used as the final discriminant for this analysis.

Training

Tab. 5.4 is showing the customized parameter configuration in the training for this analysis, and the ones not mentioned are taken as default value. It could be noted that not all events in the training are used in each tree, but a random sampling ("bagging") is employed. This is to smear the statistic fluctuation to avoid over training.

In this analysis, the SM VBS samples is taken as signal, and the background sample is composed of simulated $t\bar{t}$ and W+jets interaction. Both signal and background events are re-weighted to the relative weight corresponding to their cross-sections. Both of them are split into two samples with equal size: the events of even event numbers are taken as sample A, and odd event number ones are taken as sample B. Then, two trainings are conducted on both samples and evaluated on the other one. Afterwards, data are processed with both of the two trainings also with the event splitting by event numbers. The final result was given as the combination of the two

trainings. With drastically different kinematics, the training is performed on merged and resolved channels respectively.

At the very beginning, the trainings were conducted with more than 50 input variables including 4-vector of the selected objects, topological parameters between them, and various associated observables like jet-width. Only the subsets of uncorrelated variables showing great separation power were chosen. Two variables were newly defined here:

- boson centrality (ζ_V): This is to identify the topology that the two scattered bosons are supposed to be within the η gap of the two scattered jets:

$$\Delta\eta_- = min(\eta(V_{had}), \eta(V_{lep})) - min(\eta(j_1^{VBS}), \eta(j_2^{VBS})) \tag{5.12}$$

$$\Delta\eta_- = max(\eta(V_{had}), \eta(V_{lep})) - max(\eta(j_1^{VBS}), \eta(j_2^{VBS})) \tag{5.13}$$

$$\zeta_V = min(\Delta\eta_-, \Delta\eta_+) \tag{5.14}$$

- jet width: the jet calorimeter width defined as the p_T averaged distance of calorimeter clusters to the jet axis:

$$width = \frac{\sum_i \Delta R(j, c^i) p_T(c^i)}{\sum_i p_T(c_i)} \tag{5.15}$$

  with c^i representing the cluster entities inside the jet.

Tab 5.5 is presenting the variable importance for BDT training with definition as the percentages of variables used to make a decision.

Result

The final result with the output of BDT response (F_{x_i}) is shown in Fig. 5.6. As mentioned above, signal events would have the response close to 1, while background ones tend to have the outcome of -1.

Table 5.5.: The importance of each input variable in Gradent BDT training

SelectionVariable	Importance	
	Resolved	Merged
$M_{VVj^{tag}j^{tag}}$	1.532×10^{-1}	4.726×10^{-1}
$p_T^{sig\ j_2}$	8.833×10^{-2}	NA
$\eta(\ell)$	7.939×10^{-2}	1.366×10^{-1}
ζ_V	7.866×10^{-2}	1.970×10^{-1}
$width(sig\ jet_2)$	7.151×10^{-2}	NA
$width(tag\ jet_1)$	6.933×10^{-2}	NA
$width(sig\ jet_1)$	6.354×10^{-2}	NA
$p_T^{tag\ j_1}$	6.166×10^{-2}	NA
$\Delta\eta(j_1, j_2)$	6.017×10^{-2}	NA
$\Delta R(\ell, \nu)$	5.450×10^{-2}	NA
$p_T^{tag\ j_2}$	5.352×10^{-2}	1.939×10^{-1}
$N_{trk}(sig\ jet_1)$	5.102×10^{-2}	NA
$width(tag\ jet_2)$	4.093×10^{-2}	NA
$N_{trk}(tag\ jet_1)$	3.607×10^{-2}	NA
$N_{trk}(sig\ jet_2)$	2.121×10^{-2}	NA
$N_{trk}(tag\ jet_2)$	1.697×10^{-2}	NA

5.4. Background Modeling

The modelling strategy is similar to the resonance search. The two dominant background interactions, $t\bar{t}$ and W+jets, are constrained using dedicated control regions, while the other minor contributions are without constraint in the signal region fitting. However, to achieve higher precision measurement, some of the cuts are loosened. In this case, the mismodelling of m^{VBS} is not negligible, so an extra event weight is applied on W+jet MC events.

The multijet background contribution in the non-resonance search is higher than the resonance analysis due to the lack of anti-QCD cuts from the topological variables. It is also estimated with the same fake factor from resonance search, because the distribution shape is supposed to remain the same with similar final state. The comparison

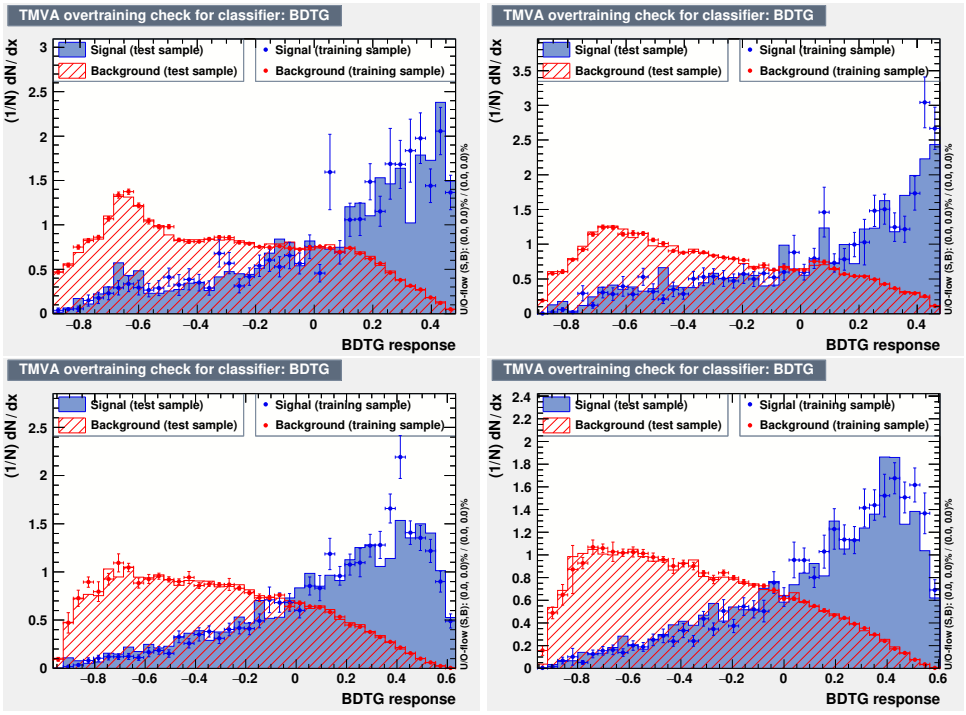

Figure 5.6.: Comparison of test and training BDTG response distributions in 1-lepton channel, for merged (top) and resolved (bottom) regimes. Results obtained with even (odd) event numbers used for training are shown on left (right).

between data and background (pre-fit) will be presented in next section along with the post-fit distribution.

5.4.1. m^{VBS} Modelling

As what was observed in the resonance search, an unknown issue is underlying in the simulation for W+jet events with Sherpa. With the comparison to data, a slope could be seen on the ratio of data to simulation in m^{VBS} distribution shown in Fig. 5.7, and Madgraph sample gives better agreement. However, Sherpa sample has more events for statistics, so it is chosen for the estimation on W+jets background. To remodel the distribution, an extra weight is derived with m^{VBF} distribution in W+jets control region:

$$w(m_{jj}^{VBS}) = \frac{N^{data} - (N^{mc} - N^{mc(W+jets)})}{N^{mc(W+jets)}} \tag{5.16}$$

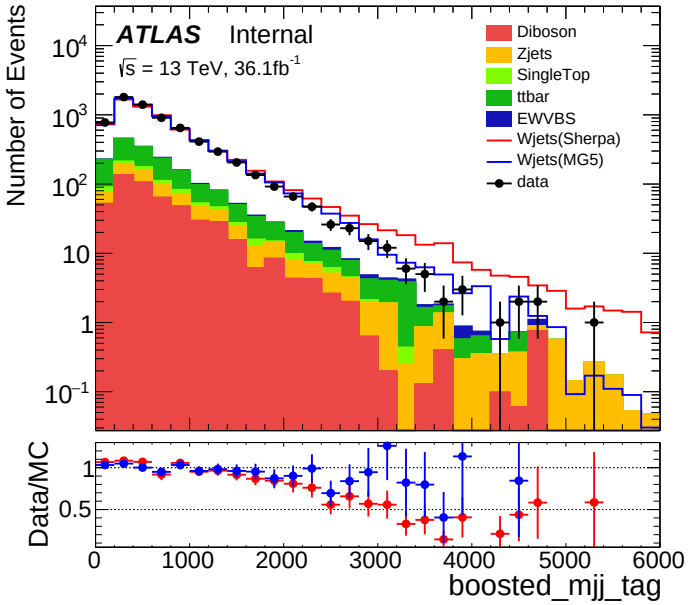

Figure 5.7.: Comparison of m^{VBF} distribution of data and W+jets MC samples from Sherpa and Madgraph 5 in the boosted W+jets control region.

The estimation is performed as a linear fitting in the mass of two small-R signal jets, or the selected large-R signal jet, $m^{V}_{jj(J)}$, bins:

$$m^{V}_{jj(J)} = [50, 60, 70, 100, 150, 200, 300][GeV] \tag{5.17}$$

where the bin of 70-100 GeV is removed because it is defined as signal region. The fitting in multiple bins is to investigate the weight dependence on $m^{V}_{jj(J)}$. The result of fitting could be seen in Fig. 5.8 and 5.9. With consistent results between each $m^{V}_{jj(J)}$ slice, it was determined to perform the fitting only on resolved and boosted regions without further categorisation. The parameters from the best fitting is shown in Tab 5.6 with 1σ uncertainty from statistical fluctuation. As the discrepancy was only seen in

Table 5.6.: Estimated m^{VBS} reweighting functions for W+jets events.

Fitting parameters	Resolved	Merged
p_0 (constant)	1.1 ± 0.04	1.1 ± 0.02
p_1 (slope) $[GeV^{-1}]$	-0.00021 ± 0.00002	-0.00019 ± 0.00003

m^{VBS}, the validation was performed by applying the weight in the other distributions, and the result is in Fig. 5.10 which is showing the agreement is significantly improved for m^{VBS} distribution with little disturbance on the other kinematic properties.

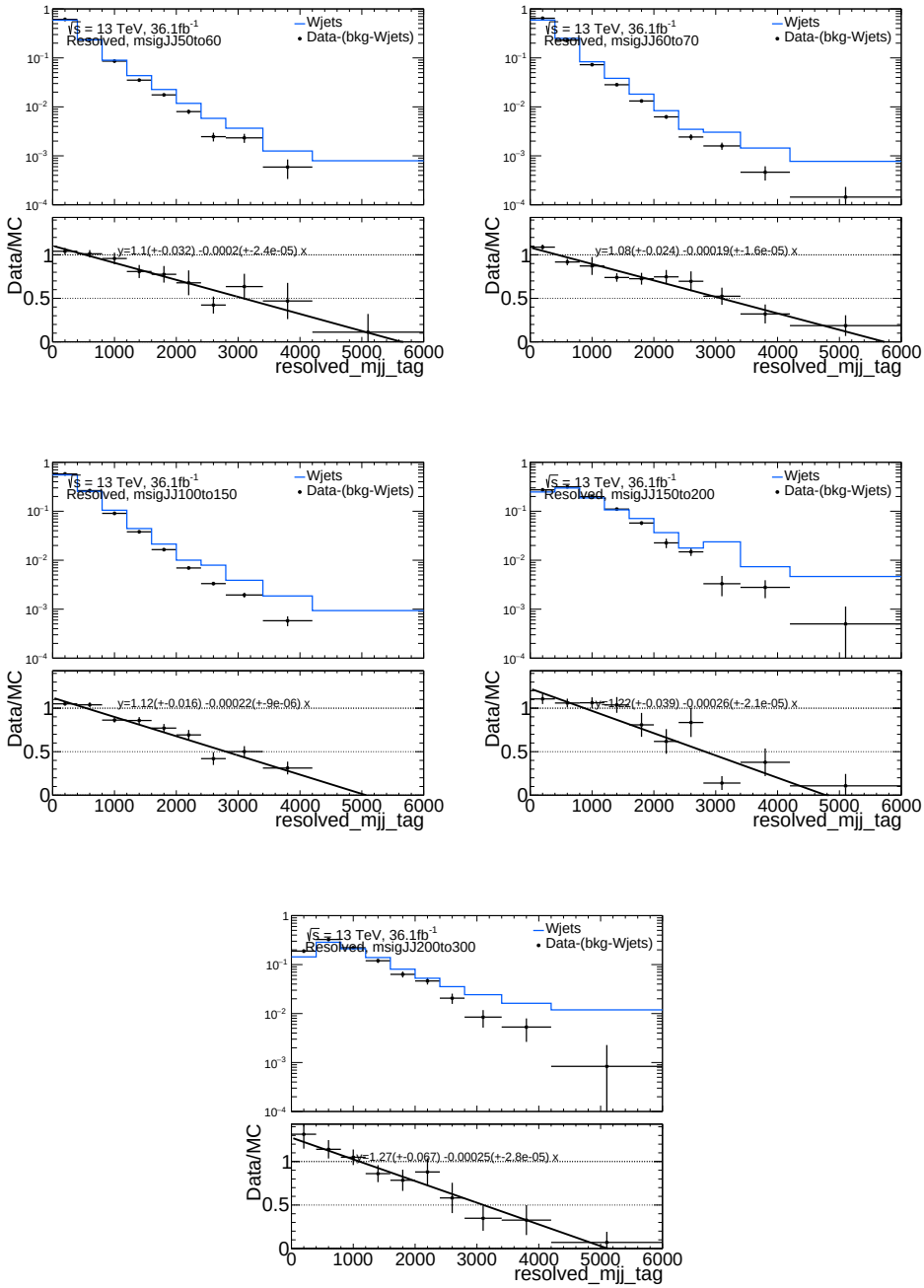

Figure 5.8.: Fit of m^{VBS} (as resolved_m_jj in the plots) slope in W+jets resolved CRs, in different slices of m_{jj}^{V}.

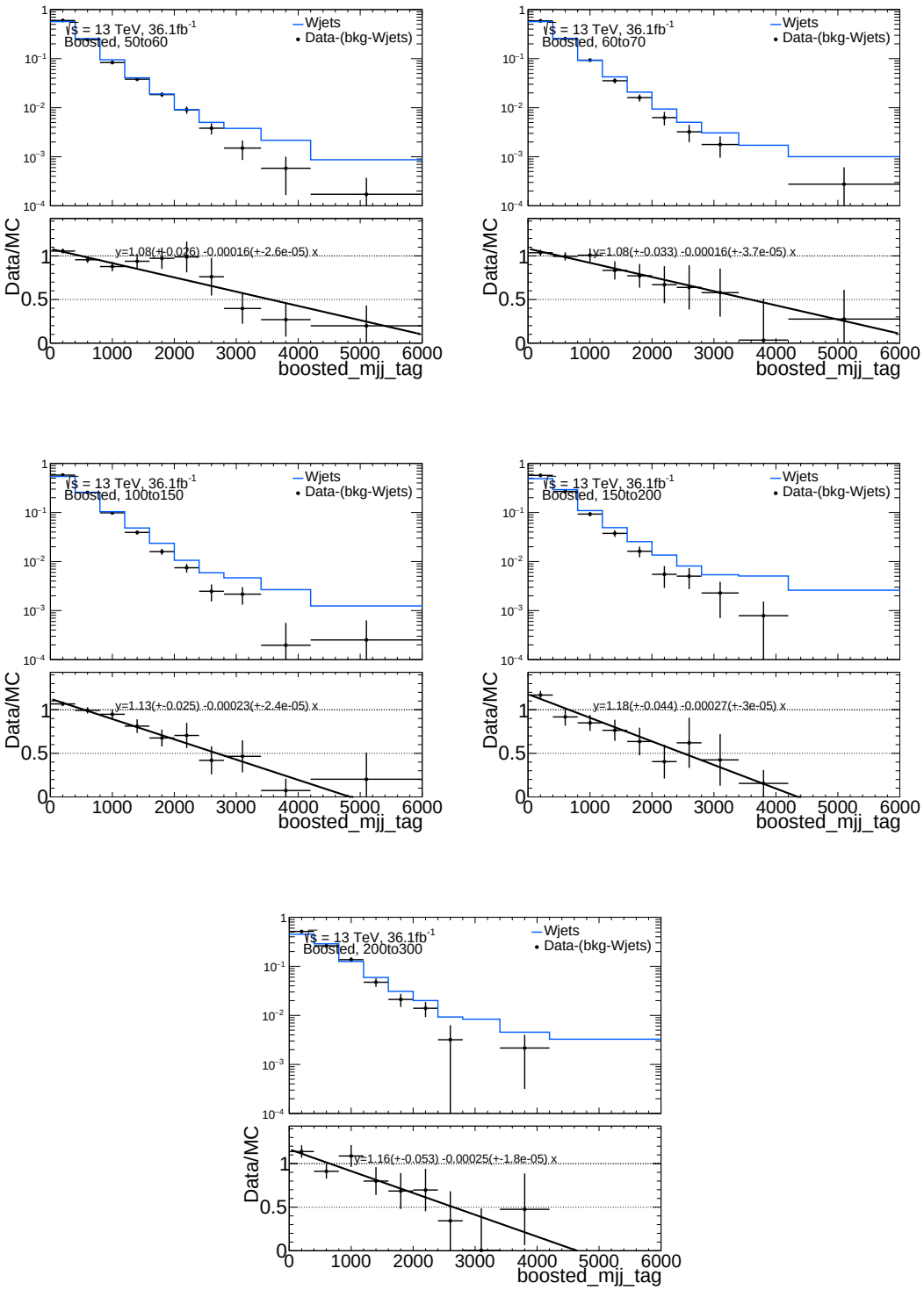

Figure 5.9.: Fit of m^{VBS} (as resolved_m_jj in the plots) slope in W+jets boosted CRs, in different slices of m_J^V.

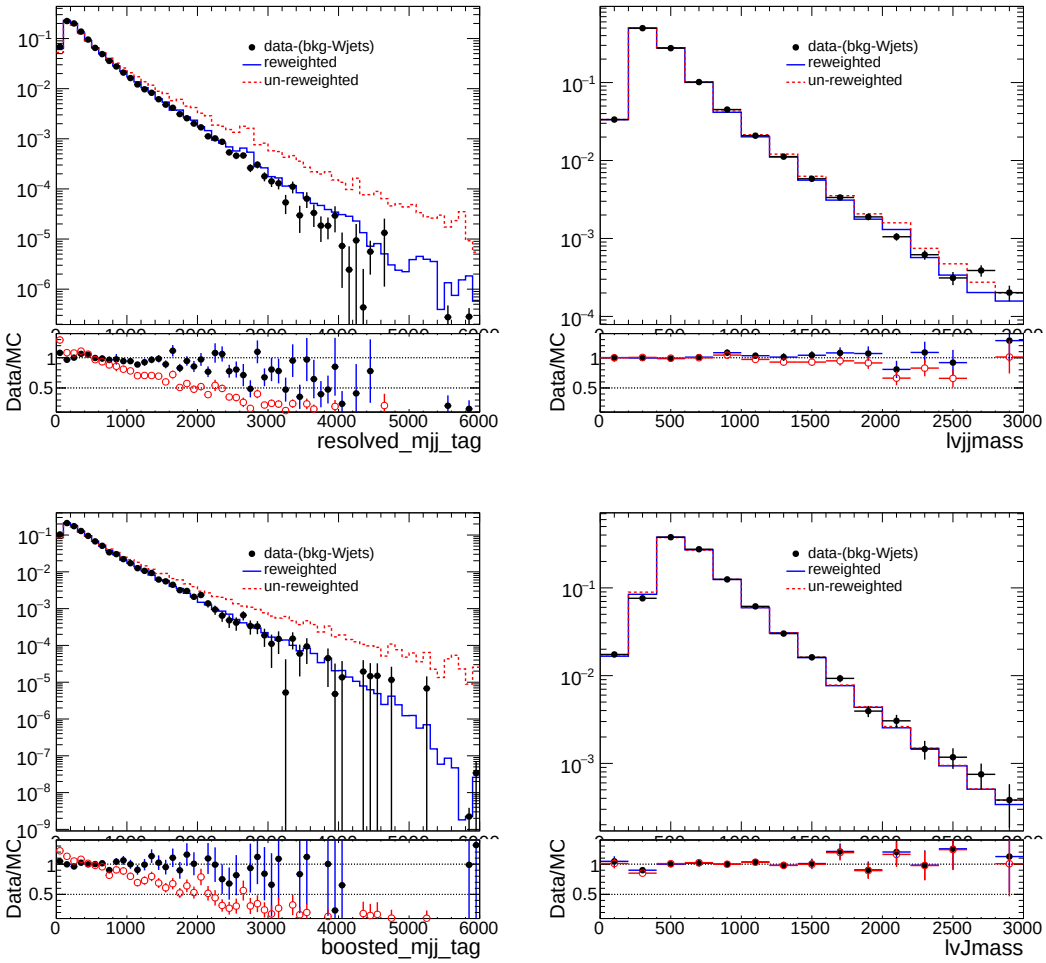

Figure 5.10.: Comparison of m^{VBS} (as resolved_m_jj in the plots) and m_{VV} (as lvjjmass in resolved plots and lvJmass in boosted plots) distributions before and after the m^{VBS} reweighting for events in the resolved (top) and boosted (bottom) W+jets control regions

5.5. Statistical Interpretation

The statistical interpretation of the non-resonance search follows the same strategy as the resonance one in likelihood construction (it has the same structure as Eq. 4.4), fitting, and then the final result. However, as the main focus of this analysis is to observe the vector boson scattering in the semileptonic ($qq \to VVjj \to \ell\ell qq/\ell\nu qq/\nu\nu qq + jj$), the exclusion interpretation is not performed.

The likelihood construction was using two discriminants: the BDT distribution for

signal region (first line in Eq. 4.4) and the m^{VBS} for W+jet control region (third line in Eq. 4.4). The top control region was just taking one bin for the fitting normalization (second line in Eq. 4.4) which has combined both $t\bar{t}$ and single top backgrounds. They are summarized in Tab. 5.7. This choice is to make the m^{VBS} reweighting systematic uncertainty constrained by m^{VBS} distribution shape in the W+jet control region.

Regions	1lep channel fit model		
	Merged high-purity	Merged low-purity	Resolved
SR	BDT	BDT	BDT
WCR	m^{VBS}	m^{VBS}	m^{VBS}
TopCR	One bin	One bin	One bin

Table 5.7.: Summary of the regions from 1lep channel entering the likelihood of the fit models. "One bin" implies that a single bin without any shape information is used in the corresponding fit region.

For the systematic uncertainties, the set from the resonance search is also applied. However, as the analysis employs the m^{VBS} reweight, the additional systematic uncertainty is taken in for the statistic uncertainty from this sources. The other addition systematic uncertainty arises from the interference between the QCD interactions and the VBS process, and it is taken into the uncertainty of signal modelling.

5.5.1. Fitting

The fitting procedure is conducted as the resonance search for which the two dominant backgrounds, W+jets and top, are constrained by the dedicated control regions by a Gaussian distribution. Before having the final result of the signal strength, the background only fitting is performed to test the background modelling and the nuisance parameter effect on the fitting quality.

Post-fit and Pre-fit Distributions

The background and data comparison is presented here to verify the background modelling before the fitting. The post-fit plots are presented together to show the effect of fitting on the histograms. This fitting procedure has applied the background only hypothesis ($\mu = 0$).

Fig. 5.11 and 5.12 are the results in W+jet and top control regions respectively.

Fitting Quality

The fitting quality is also verified in this analysis with the pulls and the correlation matrix. The combined results of merged and resolved channels are in Fig. 5.13 with a reduced scheme presenting only the NPs with significant correlation or pulls on the fitting. There are a coupling of NPs like m^{VBS} reweighting which are highly constrained and pulled, and that is due to the strong impact of the systematic uncertainties on distribution shapes.

5.5.2. Results

This analysis is aiming to provide the vector boson scattering measurement which has been predicted by the SM, so the interpretation has the following two parts: a) the discovery significance b) the cross-section in the intended final states in the fiducial region, and the exclusion limit is not set.

Combination of Semileptonic Channels

For this analysis, all the three semi-leptonic channels are considered. The results will be showing the combination of all the three semileptonical channels through the combination procedure discussed in the last chapter. Most of the systematic uncertainties are correlated among the three semileptonic final states ($\ell\ell qq$, $\ell\nu qq$, and $\nu\nu qq$), but the ones for normalization factors and the multijet background (only in the $\ell\nu qq$

Table 5.8.: Expected and observed yields in signal and control regions for the signal hypothesis. Yields and uncertainties are evaluated after the fitting to the data in all $\ell\nu qq$ regions indicated above.

	Boosted, High Purity			Boosted, Low Purity			Resolved		
	SR	W+jets CR	Top CR	Signal Region	W+jets CR	Top CR	SR	W+jets CR	Top CR
W+jets	1556.66 ± 244.61	1448.88 ± 154.05	749.76 ± 121.50	3931.65 ± 539.85	2002.27 ± 272.88	1822.72 ± 244.59	97489.49 ± 22840.18	25321.33 ± 4730.05	35265.68 ± 7019.05
Top	570.42 ± 123.89	136.60 ± 45.84	5635.05 ± 1198.20	608.91 ± 142.16	166.52 ± 51.80	6670.66 ± 1649.92	11747.76 ± 3529.05	1277.32 ± 634.75	128305.05 ± 36872.78
SM Diboson	238.63 ± 66.59	73.92 ± 20.90	181.79 ± 52.32	339.94 ± 107.33	92.97 ± 30.69	189.66 ± 56.52	4330.69 ± 1287.57	581.58 ± 162.93	2093.22 ± 560.53
Z+jets	53.47 ± 9.96	40.73 ± 6.95	28.42 ± 0	123.62 ± 20.22	57.37 ± 11.74	72.81 ± 14.09	3939.25 ± 1667.54	954.46 ± 350.69	1614.46 ± 432.94
Multijet	–	–	–	–	–	–	15381.16 ± 2292.91	3776.57 ± 471.86	24426.45 ± 4082.85
Background	2477.59 ± 382.38	1705.67 ± 186.99	6642.85 ± 1268.24	5047.75 ± 707.29	2325.75 ± 320.31	8797.59 ± 1784.29	133347.69 ± 26918.73	31959.56 ± 5264.22	192183.01 ± 40519.71
VBS Signal	58.41 ± 8.32	5.53 ± 0.97	47.84 ± 7.76	43.62 ± 6.05	6.53 ± 1.43	41.75 ± 6.24	459.33 ± 54.23	48.30 ± 4.89	478.14 ± 65.29
SM Total	2536.00 ± 382.47	1711.20 ± 186.99	6690.69 ± 1268.26	5091.37 ± 707.32	2332.28 ± 320.31	8839.34 ± 1784.30	133807.02 ± 26918.78	32007.86 ± 5264.22	192661.15 ± 40519.76
Observed	1929	1364	5806	3709	1831	7629	104476	27475	157177

channel	resolved	merged
W+jet CR	0.93 ± 0.07	0.86 ± 0.06
Top CR	0.67 ± 0.10	0.83 ± 0.01

Table 5.9.: The scale factors for the top and W+jet backgrounds for the fitting with signal

channel) are taken decorrelated. The details of the other two channels could be referred to [113]. In addition, the combination performed the simultaneous fitting on the three channels which means that the signal strength and the scaling factors among the three channels are shared: signal strength of three of them, W+jet and top scaling factor are shared between $\ell\nu qq$ and $\nu\nu qq$ which are constrained in $\ell\nu qq$ control regions, and Z+jet scaling factor is shared between $\ell\ell qq$ and $\nu\nu qq$ which is constrained in the $\ell\ell qq$ Z+jet control region. The yields after the fitting with the signal in the $\ell\nu qq$ channel are presented in Tab. 5.8 for the control and signal regions, and the scale factors on W+jets and top backgrounds are shown in Tab. 5.9.

Discovery Significance

The asymptotic formulae was applied here with the same methodology from the resonance search to test the SM VBS hypothesis against the null hypothesis. The discovery significance with the test statistics in Eq. 4.21 before the batman veto is shown in Tab. 5.10 for each channel and combination. However, with the event removal from this cut, the final discovery significance decreased to 2.7σ. Fig. 5.14 is showing the signal strengths denoted, $\hat{\mu}$, giving the best fit in each individual channel

and the combination. The signal and background distributions with observed data are re-binned into the $\log(S/B)$ (S and B are signal and background event numbers) and presented in Fig. 5.15. The final combined result has great agreement with the SM prediction, and the sensitivity is dominated by the systematic uncertainty. The compatibility of the three channels are within the 36% with the estimation from the χ^2 distribution of two degrees of freedom (from systematic and statistical uncertainties).

Channel	Exp. significance(Asimov)	Obs. significance
$\nu\nu qq$	1.35	1.43
$\ell\nu qq$	1.77	0.53
$\ell\ell qq$	1.34	2.07
combined	2.58	3.14

Table 5.10.: Summary of VBS signal significance against null-hypothesis in the semileptonic final states.

VBS Cross-Section Measurement

To measure the inclusive cross-section of the VBS production, the selection efficiency is estimated with the generator truth information through an approach like the tag-and-probe method. Firstly, the events from signal simulation are tagged via the "fiducial region" selection, which means the same signal region cuts are applied on events at the particle truth ("truth") level (without considering their interactions with the detector), but the fat jet D_2 cuts are removed, as it is a variable at the reconstruction level. Then, those tagged events are probed by whether the reconstructed particles ("reco") could also pass the same cuts. This would then give the reconstruction efficiency:

$$\mathcal{C}_{eff} = \frac{N(reco)}{N(truth)} \tag{5.18}$$

To measure the cross-section, the signal strength is set as a free parameter, and the related uncertainty should not affect the fitting procedure, so it is removed from the

likelihood reconstruction in Eq. 4.4. Then, the cross-section could be presented as:

$$\sigma \times BR = \frac{\mu \times (N^{data} - N^{bkg})}{\mathcal{C}_{eff} \times \mathcal{L}} \tag{5.19}$$

The result of the cross-section measurement could be seen in Tab. 5.11.

Fiducial region	Predicted σ_{exp}	Measured σ_{exp}
Total	43.0 ± 2.4 (theo.) fb	45.1 ± 8.6 (stat.) $^{+15.9}_{-14.6}$ (sys.) fb
Merged	11.4 ± 0.7 (theo.) fb	12.7 ± 3.8 (stat.) $^{+4.8}_{-4.2}$ (sys.) fb
Resolved	31.6 ± 1.8 (theo.) fb	26.5 ± 8.2 (stat.) $^{+17.4}_{-17.1}$ (sys.) fb

Table 5.11.: Summary of measured signal strengths, and the predicted and measured fiducial cross section.

5.6. Summary

This analysis is dedicated to spot the vector boson scattering interaction in the semileptonical final states with the analysis strategy inherited from the resonance search. The combination of the three final states ($\ell\ell qq$+$\ell\nu qq$+$\nu\nu qq$) has presented the discovery significance of 2.7σ against the null hypothesis, which is still not yet significant to claim a discovery but still within a reasonable agreement to the SM estimation (2.5σ). For the cross-section measurement, it was given 45.1 fb for the VBS process in agreement with the SM prediction within the uncertainties, and this is also the first measurement of vector boson scattering in semileptonic final states.

The aQGC statistical interpretation is skipped for this analysis due to the need for a more complete signal sample production.

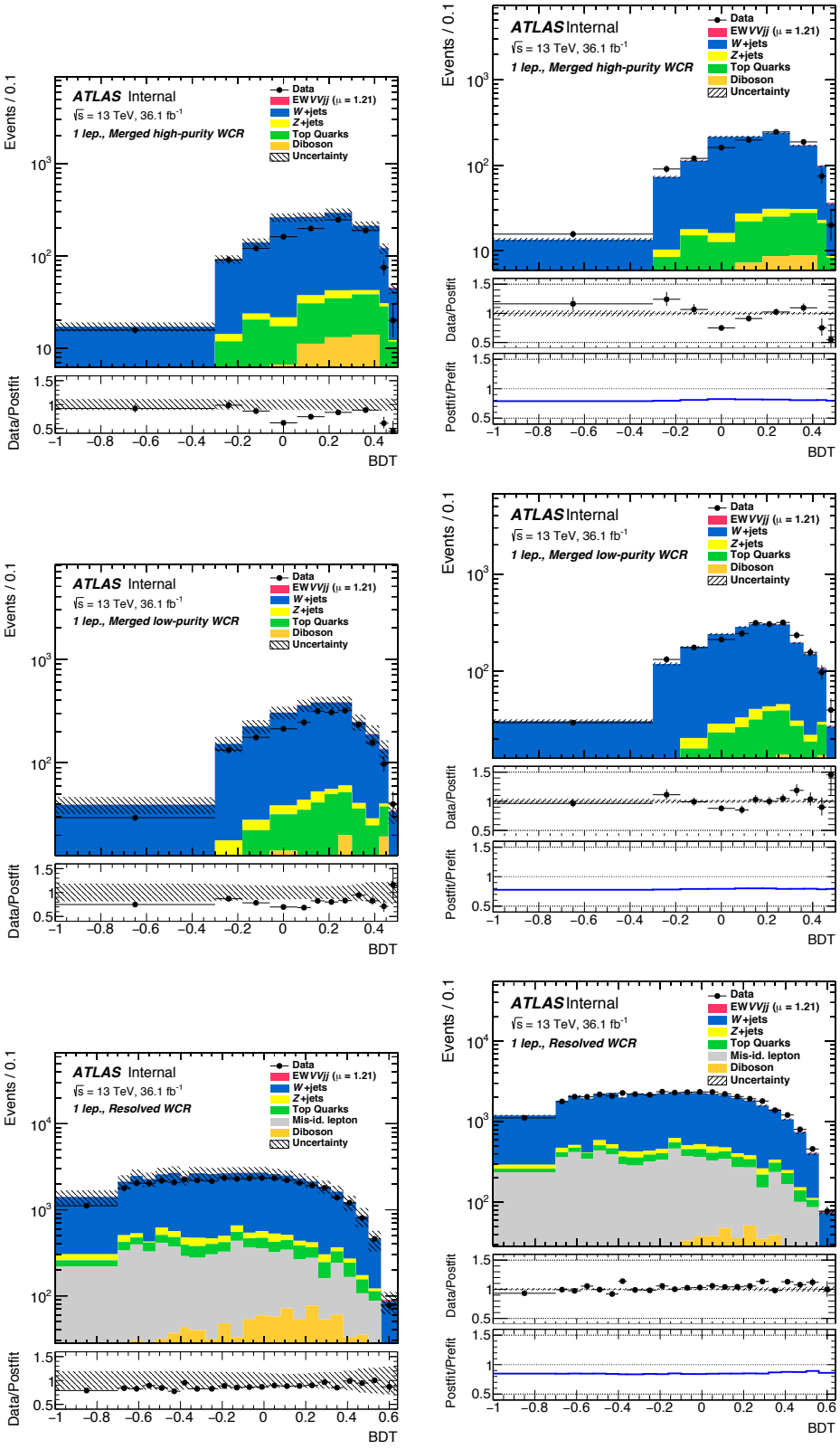

Figure 5.11.: Comparison of the BDT score distributions before and after the fitting in the Boosted HP (top), Boosted LP (middle), resolved (bottom) W+jet control regions. The left and right are the plots for pre-fit and post-fit (with the post-fit over pre-fit ratio) results.

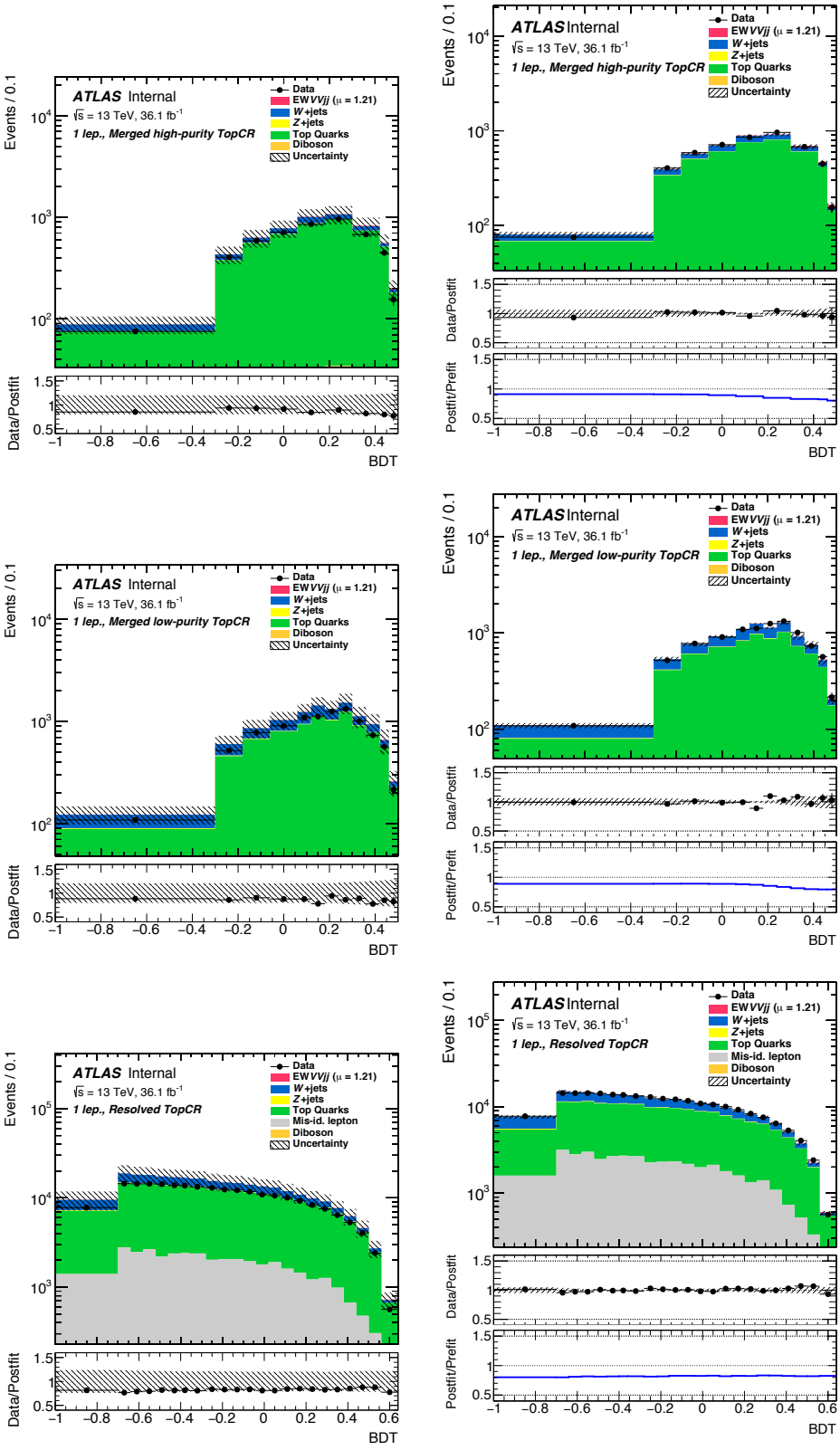

Figure 5.12.: Comparison of the BDT score distributions before and after the fitting in the Boosted HP (top), Boosted LP (middle), resolved (bottom) top control regions. The left and right are the plots for pre-fit and post-fit (with the post-fit over pre-fit ratio) results.

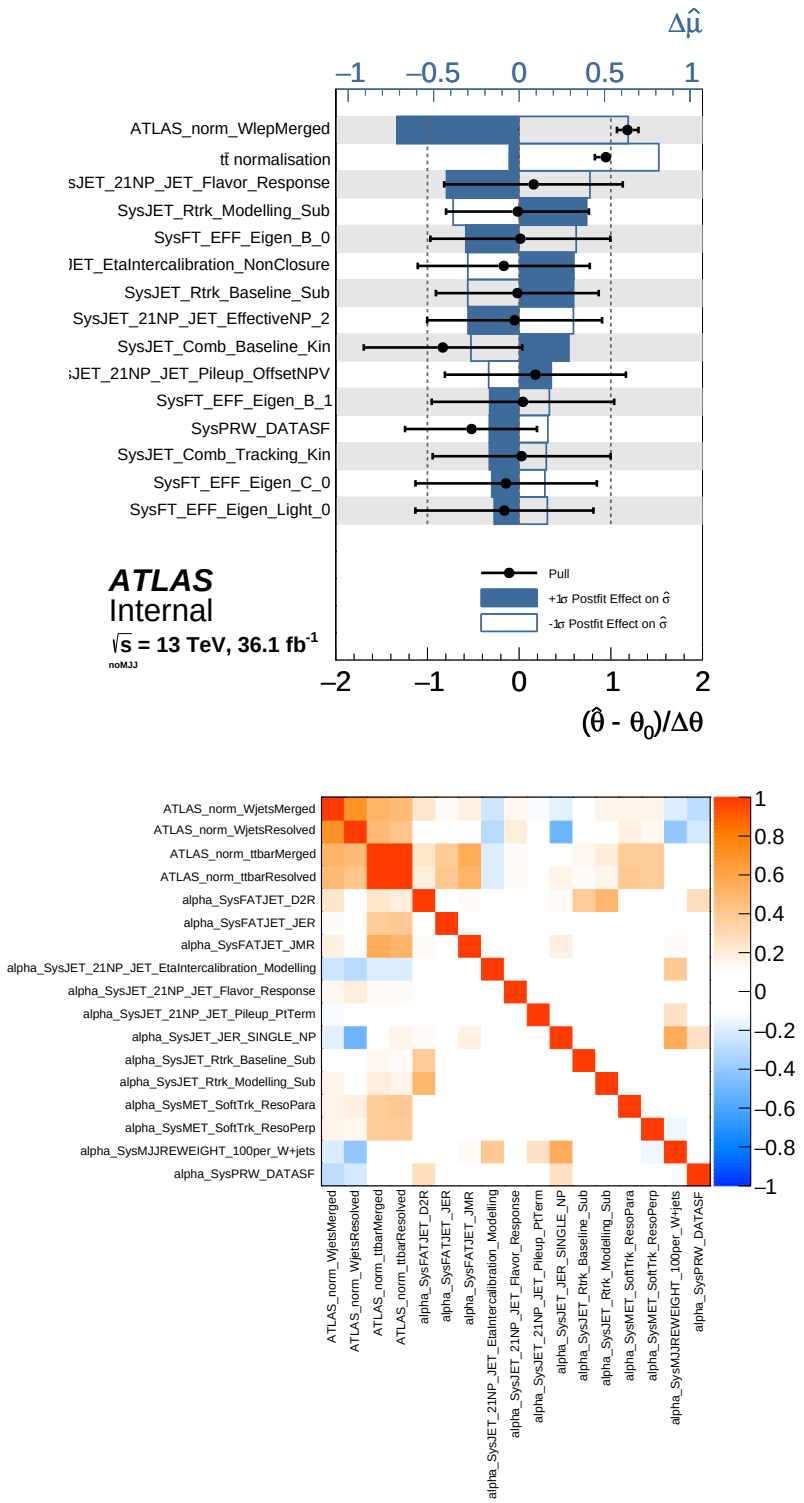

Figure 5.13.: The fitting quality is verified by the pulls (up) and variable correlation (bottom). They are in the reduced scheme to show off the notable ones.

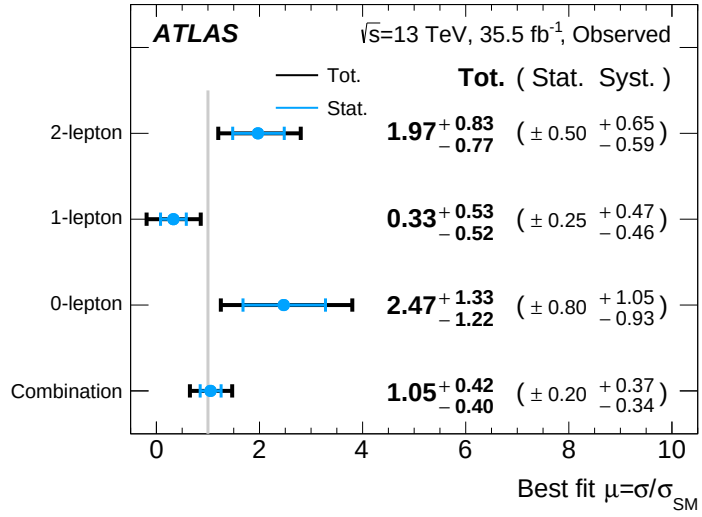

Figure 5.14.: $\hat{\mu}$ for each individual channel and the combined result.

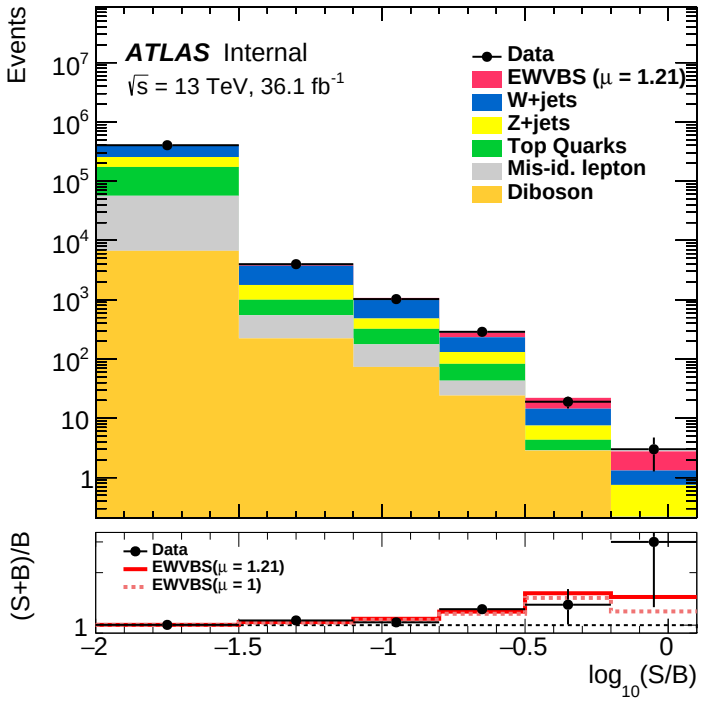

Figure 5.15.: Event yields as a function of $log_{10}(S/B)$. Final-discriminant bins in all regions are combined into bins of $log_{10}(S/B)$, with the expected signal, S and background B.

Chapter 6.

Upgrade of the ATLAS Calorimeter Trigger

"To infinity ... and beyond!"

— Buzz Lightyear (made in Taiwan), Toy Story

Following the period of LHC operation with $\sqrt{s} = 13\ TeV$ from 2015 to 2018, the long-shutdown period (LS2) is scheduled from 2018 to 2021 to prepare for the Run 3 operation which will start in 2021. The major upgrades in this period are to enhance the LHC energy for proton-proton collision as well as the luminosity. Meanwhile, three main upgrades will be also performed on the ATLAS detector: the new small wheels (NSW) in the muon spectrometer [115], the fast tracker at HLT (FTK) [116], and the new L1Calo infrastructure. One of the main purposes of the two upgrades is to improve the trigger rate for better recognition on the physical objects. This chapter will be dedicated to the L1Calo Run 3 upgrade from the hardware design, preparation of the software, to expected performance of the new L1Calo infrastructure, for which I was in charge of the software preparation and also the E_T^{miss} trigger algorithm.

6.1. LHC Run 3 Upgrade

After the operation of Run 2 (2015-2018), the LHC undergoes the Long Shutdown period (LS2) from 2018 to 2021 during which a couple of upgrades and maintenance will be taken to enhance the LHC performance to prepare for the upcoming operation in 2021. This is to bring the LHC to the design energy of 7 TeV for each beam and also enhance the instantaneous luminosity to $2 \times 10^{34}\ cm^{-2}s^{-1}$ with estimated ~ 70 pile-up events per bunch crossing with respect to $1.5 \times 10^{34}\ cm^{-2}s^{-1}$ luminosity during the LHC operation in 2018. The subsequent operation is expected to last for three years delivering the integrated data of 300 fb^{-1} by the end of this period. This upgrade plan could also be taken as the preceding work for the High-Luminosity LHC (HL-LHC) which will keep the beams at 7 TeV, but the instantaneous luminosity will increase to $7.5 \times 10^{34}\ cm^{-2}s^{-1}$ for which the pile-ups will go up to 200 per bunch crossing. The LHC upgrade road map and the estimated instantaneous luminosity can be seen in Fig. 6.1.

The major upgrade of this project is that the linear accelerator of beams will be replaced by the new LINAC4, and the LINAC2 will just retire from 40 years of operation. The major difference between the LINAC2 and LINAC4 is that the LINAC4 will accelerate negatively charged hydrogen ions (H^-), and the electrons will be stripped off in the PSB, whose design is intended to concentrate the beams with better stability [119]. Furthermore, the CERN acceleration complex (Fig. 2.2) will also upgrade the RF cavities for the energy upgrade. For the LHC itself, the upgrade will take place in the magnet systems for which more than 20 magnets will be replaced, and a new superconductor technology using niobium-tin as the cable material will also be employed with the new magnet material which can afford the even higher magnetic field of $\sim 10\ T$ (the original material can only take the magnetic field up to $\sim 9\ T$) [119].

This upgrade project is aiming to refine the present physics results. Firstly, the Higgs boson properties like the couplings to other particles or themselves could be measured with better precision to verify the SM predictions. Secondly, most of the SM interactions have the cross-sections as a function of the collision centre-of-mass energy, and

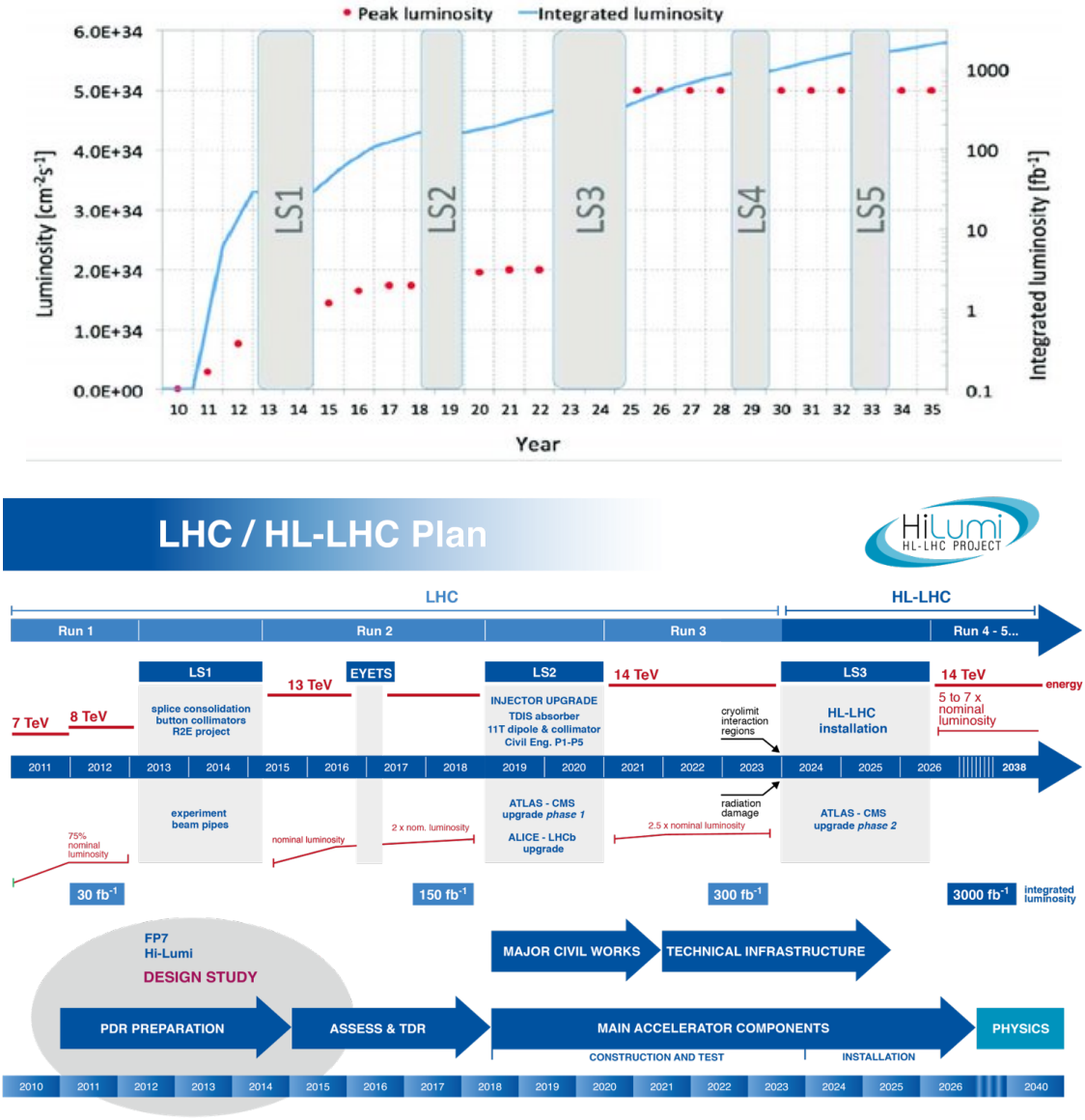

Figure 6.1.: The LHC upgrade plan (top) [117] and the instantaneous luminosity (bottom) [118] for the upcoming 10 years with the estimated integrated data.

the new operation energy can provide other measurement points. Thirdly, the increase of collected data will benefit the new physics search giving a better separation on the test statistics between hypotheses, and this will enhance the sensitivity to the hidden particles. Ref. [118] has summarized all the studies for expected results with the Run 3 LHC data.

6.2. Hardware of the Run 3 ATLAS Calorimeter Trigger

To incorporate the upcoming LHC upgrades, the ATLAS hardware calorimeter trigger system is scheduled to undergo a series of upgrade to cope with the high luminosity in Run 3, and it will also be remained as part of the Run 4 L0 trigger. The full L1Calo trigger scheme in Run 3 can be seen in Fig. 6.2. It could be noted that the Run 2 system

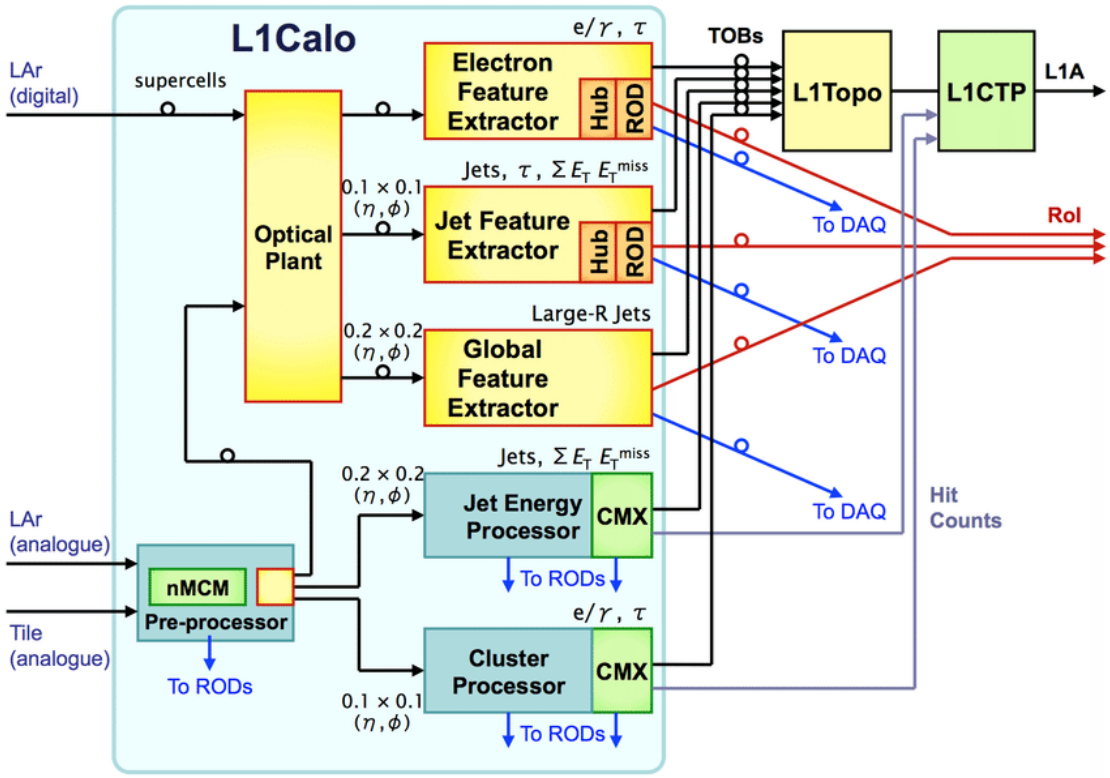

Figure 6.2.: The L1Calo hardware scheme in the Run 3 operation [120]

will still remain in the operation for the tile calorimeter input running in parallel with the new system and also for the purpose of commissioning. This design is because that the calorimeter readout upgrade will only take place in the LAr detector for which the output signal will be digitized, and the tile detector would still use the legacy analogue system. The newly digitized signal from the LAr detector will be processed into the trigger-level object, "supercells" (a new type of trigger tower), in the "LAr Digital Processing Blade" (LDPB) with a granularity of 0.025×0.1 for the middle layer and sent to the optical plant once per 25 ns (the LHC collision rate). Before the transmission into the object processors, two others new types of trigger

towers will be constructed from supercells as well in LDPB, jTowers and gTowers, within the Data Processing System (DPS) which is part of the LDPB. The calorimeter information is herein duplicated into these three types of trigger towers, and they are distributed by the optical plant to the three feature extractors respectively: supercells to the electron feature extractor (eFex), jTowers to the jet feature extractor (jFex), and gTowers to the global feature extractor (gFex). Those Fex systems are designed as FPGA boards written in the reconstruction algorithms which will then output the physical objects to the L1Topo and L1CTP to make the trigger decision along with the outputs from L1MU. Regarding of the tile detector, the analogue signal is processed by a new processor, "Tile Rear Extension Module" (TREX), into "tTowers" with the granularity of 0.1×0.1, and they will be taken into the Fex's as well. In comparison to the Run 2 trigger system, the reconstruction of physical objects could access a better granularity for the background suppression and also have a longer latency for more complicated algorithms of physical object reconstruction.

eFex and Supercells

The eFex is designed to reconstruct the electromagnetic objects like electrons, photons, and taus, with the trigger towers of best granularity, supercells. With respect to the other two trigger tower types (jTowers and gTowers), supercells are constructed within each layer in the LAr calorimeter, and the layer names in each detector region from inside to outside are:

- Barrel ($0 < |\eta| < 1.52$): PreSamplerB, EMB1, EMB2, EMB3
  (EMB stands for "EM Barrel")
- Barrel ($1.52 < |\eta| < 3.2$): PreSamplerE, EME1, EME2, EME3, HEC
  (EME stands for "EM Endcap", and HEC stands for Hadronic Endcap)
- Barrel ($3.2 < |\eta|$): FCAL1, FCAL2, FCAL3

Although the hadronic endcap calorimeter still has several layers, the system would still just sum their energy deposit as one entity. Due to the detector structure, some of the layers might not cover the full designated region. In terms of the granularity,

the middle two layers (EMB1 and EMB2) have the finest one with 0.025×0.1 in the $\Delta\eta \times \Delta\phi$ plane, while it is 0.1×0.1 for the front and back layers (Presampler and EMB3) in the barrel region. However, this supercell arrangement is not employed in the full LAr detector, and the granularity gets coarser when $|\eta|$ increases. In the forward region, the most coarse granularity would degrade to 0.32×0.4 for the back layer of the forward detector (this is a rough number, as the forward supercells are in irregular shapes due to the complicated structure geometry in this region). The comparison between supercells and Run2 trigger towers could be seen in Fig. 6.3. Different from the Run 2 trigger towers, the layer information will be kept in Run 3 L1Calo system, and the middle two layers of supercells have finer granularity. This indicates the accessibility to isolation variables with more complicated algorithm. The full detail of the granularity and the coverage of each layer could be found in [121]. This is the key upgrade for the new L1Calo system. In the Run 2 operation, the single electron trigger has taken around 30% of the total output bandwidth, and this limits the bandwidth budget for the other signatures like jets or taus. Therefore, the eFex upgrade is aiming to make better suppression on the background and keeping the same efficiency for physical signal like $Z \to ee$.

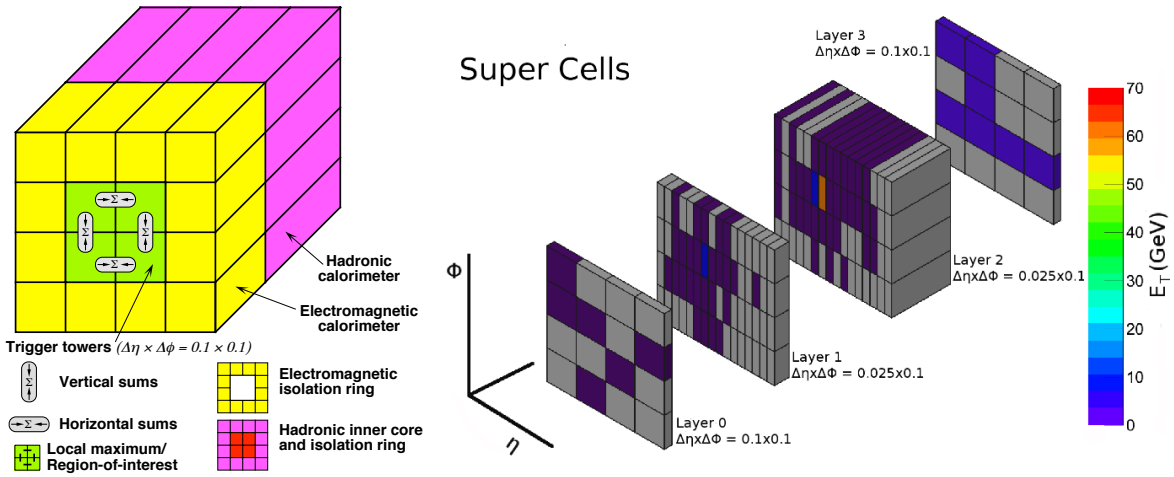

Figure 6.3.: The comparison of the Run 2 trigger towers [121] and the supercells [122] in the barrel region. One block in the Run 2 trigger tower is corresponding to one square in the front layer of supercells.

To evaluate the energy of each supercell, the signal of cells is sent to a processor

called "LATOME" with an optimal filter (OF). The received analogue LAr cell signal is firstly digitalized through the analogue digital converter (ADC) into the number of ADC counts. The energy is then calibrated by the optimal filter to estimated the measured transverse energy ($E_T = E \times \cos\theta$) and also mitigate the noise:

$$E_T = \sum_{i=1}^{i=4} \alpha_i S_i \tag{6.1}$$

$$E_T \cdot \tau = \sum_{i=1}^{i=4} \beta_i S_i \tag{6.2}$$

S is taken as the ADC count with the optimal filter coefficients (OFC), α and β, and τ is the phase shift along the measured time to ensure the energy is assigned to the appropriate bunch crossing. The i is the index for energy sampling every 25 ns within an active window of 100 ns. It should be noted that although the collision rate of LHC is one bunch crossing per 25 ns, the active window for "one" collision is still 100 ns. This means once a channel receives the signal, it will not be available for the following few bunch crossings. In Run 2, the timing assignment was simply applied by checking whether a peak of pulse could be found within the active window [123] (peak finder algorithm):

$$S_{i-1} < S_i > S_{i+1} \tag{6.3}$$

The time is then assigned to the bin centre. However, for the search of long-lived particles, they might arrive in the calorimeter after this time window. Therefore, a more flexible algorithm to extend the time window will be implemented in the Run 3,

$$\begin{cases} -8\ ns < t < 16\ ns & E_T \geq 10\ GeV \\ -8\ ns < t < 8\ ns & E_T < 10\ GeV \end{cases} \tag{6.4}$$

This allows to have the calorimeter receive energy deposits which are not within the active time window triggered by the collisions ($0\ ns < t < 25\ ns$). Although the sampling period is 25 ns, the sampling window could be delayed by maximally 24 ns

with the steps of 1 ns using the PHOS4 chip [124], which can help to achieve the desired temporal resolution. Fig. 6.4 is presenting how the OFC shifts the peak of the origin digitalized ADC input from the beam test and the supercell energy efficiency after the new timing cuts from simulation. They are showing that the new algorithms could successfully recover the peak energy and also reach the signal plateau of 3 GeV energy deposit in a supercell.

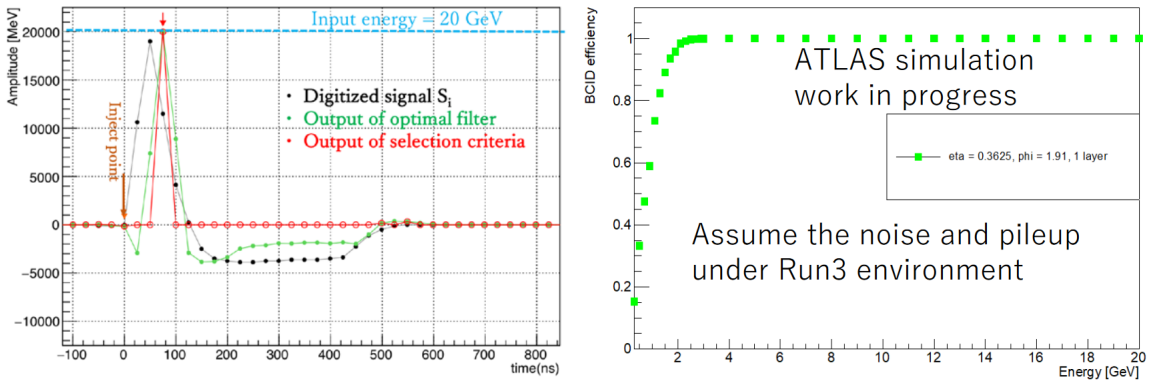

Figure 6.4.: The digitized pulse shape from the ADC and the signal efficiency after the timing window cut. The peak could be seen shifted after the OF is applied, and the timing window properly removes the negative measured energy.

The other correction on the supercells is the "pedestal correction". When the LAr cells start to receive the energy from a bunch train, the cell would deliver strong noise during the first few bunches ($\sim$ 20 bunches), and it leads to a high trigger rate beyond the trigger rate budget. The pedestal correction is applied to mitigate the effect by reducing the energy count from the ADC. Fig. 6.5 is showing the pedestal correction used in the Run 2 operation, while its optimization for Run 3 is still ongoing. Therefore, in the following studies, the first 20 bunches of a bunch train are vetoed in the event selection to remove this noise source. The average noise response (the energy deposit from $pp \rightarrow jj$ for which the two jets have $E_T < 20\ GeV$ at truth level) for each layer in the Run 3 simulated environment ($\mu \sim 80$) could be seen Fig. 6.6, and the noise would increase with $|\eta|$ due to the fact that the supercells are larger in the high $|\eta|$ region.

The calibrated supercells are taken as the input for eFex, and they are reconstructed into electrons/photons, and taus with the coverage of $|\eta|$ up to 2.5 (For physics

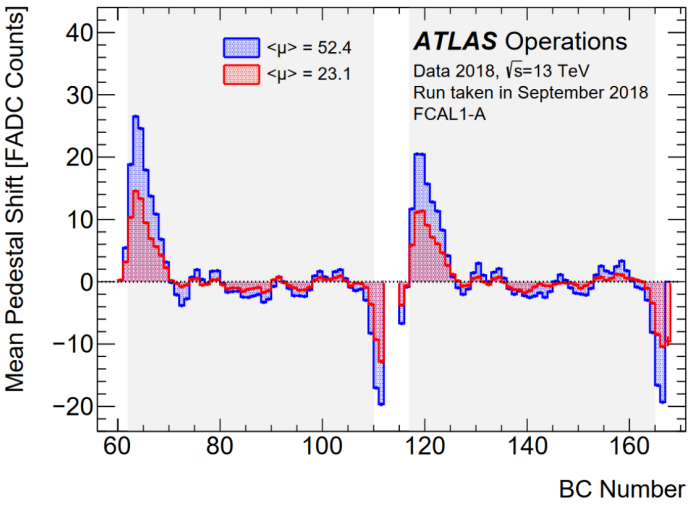

Figure 6.5.: The pedestal correction as a function of bunch crossings for long bunch trains. The shadowed area is within a bunch train [123].

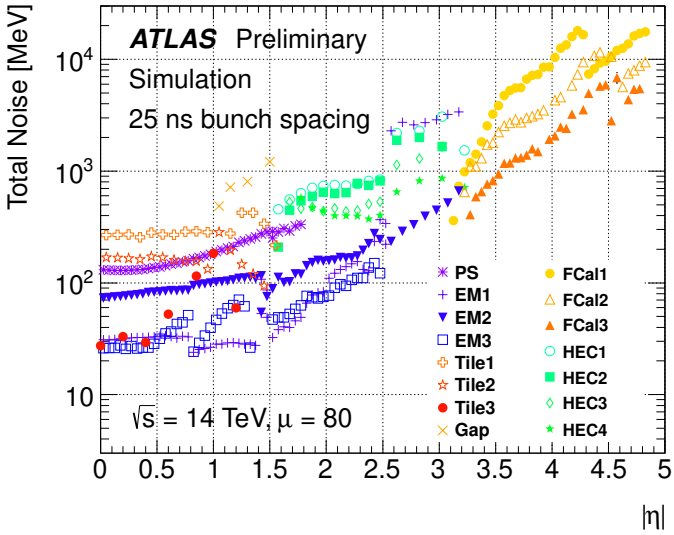

Figure 6.6.: The average E_T of supercell layers as a function of $|\eta|$ with the Run 2 like algorithm with peak finder algorithm [121]

analysis, this is also the $|\eta|$ range for offline electrons due to the coverage of inner detector). It should be noted that in the hardware trigger level, electrons and photons are reconstructed into the same objects for no track information. The reconstruction is performed from seed-finding in the EMB2 layer with the finest granularity and greatest depth. The energy of tTowers behind the ROI are then added into the reconstruction object in EM layers. With the upgraded system, the algorithms could have more

flexibility to explore different cluster shapes and also the isolation variables. Further details will be discussed later.

jFex and jTower

jTowers are in a similar format as the Run 2 trigger towers with the same granularity, 0.1×0.1, but it is not uniform in the whole detector. The granularity of each region in the barrel and endcap regions is summarized in Tab. 6.1. The construction

Table 6.1.: The jTower granularity in the barrel and endcap regions

Index	$\|\eta\|$	Δ	$\Delta\phi$
0	0-2.5	0.1	0.1
1	2.5-3.1	0.2	0.2
2	3.1-3.2	0.1	0.2

of the jTowers are firstly performed by defining the static windows for the jTowers sizes and locations. Then, those windows are simply matched to the supercells whose energy is summed over to build the E_T of jTowers. No additional selection of supercells is applied. However, for the forward region, this construction cannot work because of the irregular shape of supercells, and one supercell might overlap with two other supercells in a back layer. In this case, all the supercells are taken as jTowers directly, so the layer information would still be kept. For the input from the tile detector, the tTowers are processed into independent jTowers in the jFex, so there would be two trigger towers at the same location corresponding to EM and hadronic layers.

When the jFex is processing the jTowers, it is performed in eight FPGA modules which receive data from each ϕ-octant respectively covering the full η range ($0 < |\eta| < 4.9$) from the barrel to forward region, and the jTower data is duplicated to the neighbouring FPGAs [125]. This is to properly reconstruct the physical objects (jets or tau decayed with widely spread signatures) at the transition region between FPGAs. The final outputs of the jFex are taus with larger ROI, small-R jets ($R = 0.45$), E_T^{miss}, and the transverse energy scalar sum (H_T). Different from the Run 2 system, the new sys-

tem can afford more computing-expensive algorithms for the event-by-event pile-up mitigation.

gFex and gTower

The gTowers have similar properties as the jTowers, but they are given a even coarser granularity of 0.2×0.2 without the layer information. Furthermore, not like the jTowers constructed from individual supercells in the forward region, the forward layers of supercells are still summed over to construct the Towers by defining static windows which collect the supercells with their electrodes inside the region. Tab. 6.2 is presenting the gTower granularity in the barrel and endcap regions, while the forward region has the $|\eta|$ binning as:

$$|\eta| = [3.2, 3.5, 4.0, 4.45, 4.9] \tag{6.5}$$

with equal bins in ϕ of $\Delta\phi \sim 0.2$

Table 6.2.: The gTower granularity in the barrel and endcap regions

Index	$\lvert\eta\rvert$	Δ	$\Delta\phi$
0	0-2.5	0.2	0.2
1	2.4-2.5	0.1	0.2
2	2.5-3.1	0.2	0.2
3	3.1-3.2	0.1	0.2

With the coarse granularity, there would be fewer input channels to the gFex, so it can afford some more complicated algorithms and increase the region of interest, which is one of the motivations to have the gFex in the Run 3. In the Run 2, the JEP can only handle the ROI for a narrow jet ($R \sim 0.45$), and it is too small for a large-R jet which is an important signature for a wide range of physics analyses. The comparison of the Run 2 and Run 3 trigger level jets could be seen in Fig. 6.7, and the new system could extend the jet reconstruction to contain all the energy deposits for the decays of

two close-by hadrons. The other advantage of gFex is that it can have more complicated algorithms than the jFex for the pile-up subtraction.

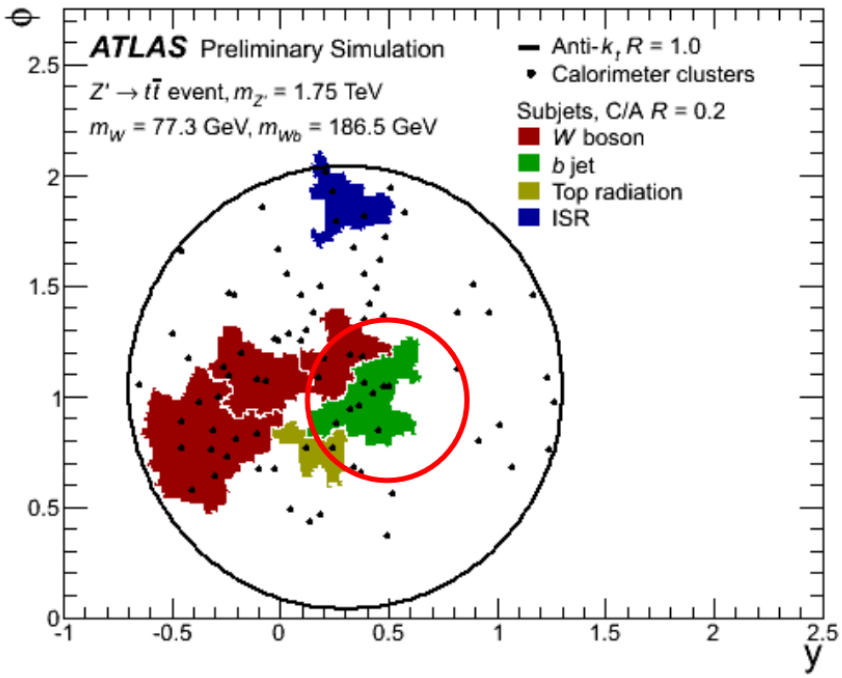

Figure 6.7.: The comparison of the Run 2 (red circle) and Run 3 (black circle) L1Calo jet ROIs for an HVT $Z' \to t\bar{t}$ event. The Z' boson was given a high mass, so the two top quarks were highly boosted and got close to each other. They would form a large-R jet in the offline reconstruction [126].

The processing of gTowers in the gFex is conducted in three FPGAs which correspond to three η ranges of full ϕ rings:

- FPGA #A: $-2.5 < \eta < 0$
- FPGA #B: $0 < \eta < 2.5$
- FPGA #C: $2.5 < |\eta|$

Due to the bandwidth limit for the communication between these FPGAs, no gTower can be duplicated as they might be in the jFex. In this case, when reconstruction objects near the border of FPGAs, the gTowers outside the available range are not considered. In this case, the reconstruction of gFex jets is not yet settled. The outputs from the gFex are the large-R jets and E_T^{miss} with another algorithm different from the jFex one.

6.3. Simulation Software of the Run 3 ATLAS Calorimeter Trigger

The general simulation procedure was already introduced in Sec. 2.4. However, the Run 3 system is still missing in the simulation chain, so I made the contribution to build up the framework with essential components and integrate it into the ATLAS software, Athena. The final output from the simulation should contain both of the trigger-level and offline objects, so they can be distributed to physics analysis groups to decide what trigger items should go into the trigger menu for the ATLAS Run 3 operation.

The trigger simulation receives the digitized data from the LAr detector simulation in the format of supercells, and the trigger simulation is performed afterwards in the following procedure:

- Tower Identification: this process is to define the j/gTower windows in the detector with their locations and granularities through the ATLAS Identifier system.
- Supercell & Tower matching: as the j/gTowers are constructed from the supercells, this is to pair the j/gTowers with the supercells inside the defined windows.
- Construction of Towers: this is performed event by event to collect the energy deposits from supercells into the j/gTowers
- Event Data Model: this is the format to store the reconstructed objects in the output file for both the hardware level (like tracks, energy cluster, or trigger towers) and physical objects. As j/gTowers are new objects in the Run 3, an event data model is created to store them.
- Physical Object Reconstruction: methods for the phyiscal object reconstruction from the trigger towers. As of July 2019, the baseline electrons from eFex, and small-R jets and E_T^{miss} from jFex are already implemented, while the tau recon-

struction and gFex objects are still under study. The algorithms for object reconstruction will be discussed in Sec. 6.4.

- Integration: the last step is to integrate the simulation into the ATLAS simulation chain, *reco_tf* [127], with which the output samples contain all the objects for physics studies with trigger objects.

This simulation is under the ATLAS official software, Athena, which is a Gaudi-based system [128]. All the simulation components are C++ based scripts, and they are accessible and configurable via python interface, "job option", under this framework.

6.3.1. Tower Identification

The ATLAS identifier (ID) infrastructure [129, 130] is used to define and interpret the hardware readout channels for the offline system[1]. It has two components, the dictionary and ID helper. The dictionary is to categorize the hardware readout channels in a hierarchy structure which decomposes the ATLAS detector into several levels, and the ID helper is to interpret the dictionary to construct the readout channels into offline software via the detector storage [131] which is shared between events.

This infrastructure has been used in the Run 2 for a full detector simulation, while the components dedicated for the Run 3 system are still missing like the muon new small wheel, or the L1Calo jFex and gFex. Therefore, although the ATLAS simulation system in the Run 2 has performed well for physics results, it is not yet completed for the full simulation of the new Run 3 system. To incorporate the new system of L1Calo jFex and gFex into the detector simulation, the first step is to construct the identifier system for jFex and gFex readout channels to define the jTowers and gTowers, while the supercells are already implemented within the LAr simulation software. However, the identifier system can only be applied on the readout channels in a regular pattern, so it does not extend to the forward region where supercells are in irregular shapes. Therefore, the forward region towers are defined only in the main construction script, and this information does not go into the detector storage [131].

[1] offline means the system is detached from the detector

Dictionary

The definition dictionary is written in the format of xml, which decomposes the detector in the following order:

the ATLAS detector $\rightarrow$ subdetectors $\rightarrow$ detector sides ($+\eta$, $-\eta$) $\rightarrow$ region (barrel, endcap) $\rightarrow$ sampling layer (EM/Had) $\rightarrow \eta \rightarrow \phi$

Under this structure, each of the readout channel is given a unique hash number with a set of indices representing its hardware location within each level. With the hash numbers, the readout channels could only be recognized by the indices, and the physical meaning like the real η, or ϕ, would still need the further interpretation in the script for a proper construction to make the readout channel into an object (j/gTower in this case). The following is the snippet of how the readout channels of jFex are added and defined in the dictionary:

```
<field name="JTsampling" >
  <label name="EM"         value="0" />
  <label name="Hadronic" value="1" />
</field>

<subregion name="JTower" >
  <range field="DetZside"
       values="negative_lvl1_side positive_lvl1_side" />
  <range field="JTsampling" values="EM Hadronic" />
</subregion>

<!-- Up to eta=2.5 --> \\
<region group="Reg\_JTower" name="JTower\_0"
       eta0="0.0" deta="0.1" phi0="0.0" dphi="0.1">
  <reference subregion="JTower" />
```

```
  <range field="JTregion" value="0" />
  <range field="JTeta" minvalue="0" maxvalue="24" />
  <range field="JTphi" minvalue="0" maxvalue="63"
      wraparound="TRUE" />
</region>
```

The first block in the script defines the two layers of the jTowers, EM and Hadronic layers, and the second block is for the two detector sides. Then, the definition for the central region (region index as 0) granularity and the beginning point of η and ϕ is shown in the third block, and each tower would be given the η indices ranged from 0 to 24 and ϕ indices ranged from 0 to 63. For the jTowers, there are three regions defined corresponding to the granularities presented in Tab. 6.1, while gTowers are categorized into five regions which is summarized in Tab. 6.2. The system would then loop through the combinations of those indices to build up all the trigger towers within those regions, assign the unique hash numbers for each trigger tower via the ID helper, and register them into the detector storage [131].

ID Helper

ID helper is designed to interface the dictionary and the user code for the simulation of the ATLAS detector written in the format of C++. For each system, a dedicated helper is customized due to different architectures of the subdetector designs. During the initialization of the identifiers, the helpers would access its corresponding dictionary and assign the hash identifiers for each channel by the set of indices. The identifier is then enumerated and cached for fast conversion. Under this framework, the memory for the cache of Run 2 identifiers is already fixed and filled, and the direct addition of Run 3 identifiers would occupy the memory. In this case, the identifiers would not be properly configured. To add in the new Run 3 trigger tower identifiers, the Run 2 trigger tower caches are expanded by the method in the snippet shown below:

```
m_full_region_range = m_dict
                    ->build_multirange(reg_id,"Reg_Lvl1" ,prefix, "region");
```

```
m_full_tower_range = m_dict
                    ->build_multirange(reg_id,"Reg_Lvl1" ,prefix, "phi");
m_full_layer_range = m_dict
                    ->build_multirange(reg_id,"Reg_Lvl1" ,prefix);
```

This function is to make the new jTower and gTower identifiers as the extension of the Run 2 trigger towers, so both the Run 2 and Run 3 trigger tower systems could run in parallel. After the identifiers are cached, the users could then access the tower information via the detector StoreGate (DetStore) [131] in the Athena framework.

6.3.2. j/gTower Matching and Construction

The tower definition is then taken to build up the tower windows on the calorimeter for which the locations are fixed. The following snippet is to show how the windows are defined in the software:

```
float jDEta = m_jTowerId->etaGranularity(rid);
float jDPhi = m_jTowerId->phiGranularity(rid);
int nTowers = (int)(TMath::Pi()/jDPhi)+1;
jDPhi = TMath::Pi()/nTowers;

float jEta = (m_jTowerId->eta(jid)+1-0.5)*jDEta*detSide
                                    +m_jTowerId->eta0(rid)*detSide;
float jPhi = (m_jTowerId->phi(jid)+1-0.5)*jDPhi+m_jTowerId->phi0(rid);
if(jPhi>TMath::Pi()) jPhi = jPhi-2*TMath::Pi();
```

Firstly, the granularities are taken from the dictionary by the region with $\Delta\phi$ redefined to ensure the number of ϕ segments is an integer. Then, eta0 and phi0 are used to define the starting point of this region with the granularity to evaluate the centre of trigger towers, and the trigger towers are defined with η, ϕ, and the tower granularity. For the forward region, the j/gTower are not defined in the dictionary, so another

approach is taken. For the jTowers, a simple scheme is deployed to take the forward supercells as individual towers from $|\eta| = 3.1$, while forward gTowers are hard-coded to define the edge and granularity of the towers in the simulation software as the following:

```
float fgT_Etas[5] = {3.2, 3.5, 4.0, 4.45,4.9};
int nTowers = 17;
float fgT_dPhi = 2*TMath::Pi()/nTowers;
```

For the supercells, the supercell identifier is used to retrieve the locations of the electrodes, and the following is the snippet for this purpose:

```
float scEta = dde->eta_raw();
float scPhi = dde->phi_raw();
if(fabs(scEta)>3.2) continue;
if(fabs(fabs(dde->eta_raw())-1.4)<0.001 && m_scid->region(scid) == 0
    && m_scid->sampling(scid) == 2){
  if(scEta > 0) scEta += 0.05;
  else          scEta -= 0.05;
}
```

It could be noted that the η and ϕ are taken "raw", and that means the locations applied in the study are not calibrated for any misalignment in the reality. The last section of the script is showing a special case that the supercells near the transition region between barrel and endcap regions are on the edge of supercells, and the adjustment is to ensure they could be mapped to the trigger towers beginning at $|\eta| = 1.4$.

After both towers and supercells are defined, a matching is performed by verifying whether the supercells are inside the tower windows. If they are matched, the supercell indices are serialized into a vector as one auxiliary parameter of the towers.

Then, the energy of towers is evaluated by simply summing over all the supercells inside the tower window.

6.3.3. Event Data Model for j/gTowers

The ATLAS event data model [132] (EDM) was constructed to store and handle the variables from physical and detector objects. Each type of objects such as electrons, jets, or trigger towers, has one dedicated event data model which is called a container. For the j/gTowers, the Run 2 trigger tower container could not meet all the requirements to store new variables, and its structure also contains some redundant variables for the new Run 3 system which will take unnecessary space for the tower storage. Therefore, for an efficient storage of Run 3 trigger objects, a new type of container was designed and dedicated for the use of Run 3 trigger towers, jTowers and gTowers.

The ATLAS EDM is based on C++, and the scheme is shown in Fig. 6.8. With this infrastructure, the objects are constructed as two components, the object itself, and the object variables like E_T or η. The object variables are then taken into the auxiliary store (it is called "aux-container") of the object, and the object could access the auxiliary store to obtain the variables. When the objects are built up for an event, they are serialized into a vector (transient data) which are then dumped into the container and aux-container (persistent data) respectively via StoreGate [131] and written out into a ROOT file. The StoreGate feature could then also be used to retrieve the object information from the containers.
The new container design is following the same structure as the Run 2 trigger tower container, and the aux container is skimmed by removing the redundant variables. Those removed variables are used for the LAr detector readout calibration like the bunch crossing index and the information about the pulse peak which are now processed in the supercell construction, and they are irrelevant to the j/gTowers. As the j/gTowers are now constructed from the supercells, the indices of supercells inside the towers are now also added into the aux container for the potential use of pulse shape inside the towers.

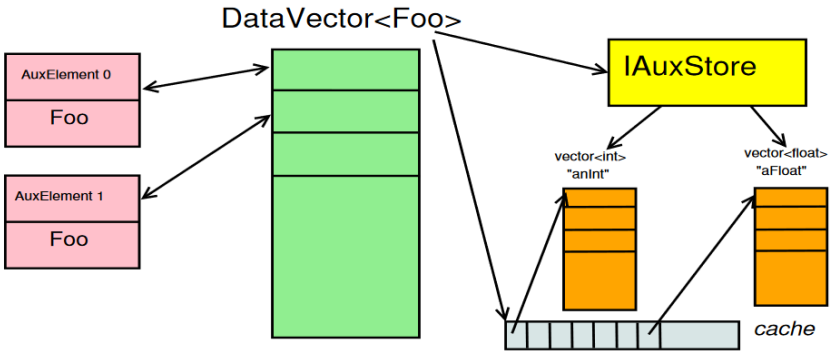

Figure 6.8.: The illustration of the ATLAS EDM scheme for the auxiliary store [132].

6.3.4. Simulation Chain Integration

To study the trigger performance for physics analyses, both trigger-level and offline objects are used to understand the trigger threshold impact on a physics results like the study in Sec. 3.4.1. The offline objects will remain the same from the Run 2 construction algorithms which are already in the simulation chain. However, the Run 3 trigger simulation is still not yet in the simulation chain, although the simulation components are already built up from the procedures mentioned above. In this case, another task to output samples with Run 3 trigger objects is to integrate it into the ATLAS software, Athena.

The ATLAS reconstruction simulation is handled by the *reco_tf* function built in the Athena framework which is presented in the scheme in Fig. 6.9. It is in the form as a python script which calls all the default reconstruction components within the Athena framework using the configurations corresponding to the Athena version (which is called "release" in the ATLAS collaboration). The most important feature in the framework is in the middle block where multiple steps of the reconstruction could be executed sequentially by taking the output file from the last step as a new input. This means although the simulation is complicated as shown in Sec. 2.4, it could still be completed with just a simple command. The other feature of the system is that the completed jobs would send the metadata information such the processed

event numbers and interaction cross-section to the ATLAS Metadata Interface (AMI). The *reco_tf* script could also be extended to include new reconstruction components by the subcommands, preExec and postExec, and this is used to integrate the Run 3 trigger simulation into the simulation chain. The execution order of components from the *reco_tf*, preExec, and postExec is shown in Fig. 6.10 where the execute() is to run the default algorithms in *reco_tf*.

The following is the snippet showing how the Run 3 trigger simulation runs with the *reco_tf* script:

```
Reco_tf.py \
--preExec \
  "from TrigT1CaloFexSim.L1SimulationControlFlags
                    import L1Phase1SimFlags as simflags;\
  simflags.CTP.RunCTPEmulation=False; \
  simflags.Calo.QualBitMask=0x40; \
  simflags.Calo.SCellType=\"Pulse\";
  simflags.Calo.ApplySCQual=True" \
--postInclude \
  "default:PyJobTransforms/UseFrontier.py" \
  "TrigT1CaloFexSim/createL1SimulationSequence.py" \
  "LArROD/LArConfigureCablingSCFolder.py" \
--postExec \
 "StreamAOD.ItemList+=["xAOD::JGTowerContainer#JTower","xAOD::
     JGTowerAuxContainer#JTowerAux."]; \  StreamAOD.ItemList+=["xAOD::
     JGTowerContainer#GTower","xAOD::JGTowerAuxContainer#GTowerAux."]";
--autoConfiguration="everything" \
```

The preExec is to set up the Run 3 configuration for the whole simulation chain, and the postInclude here plays the same role as the postExec with the algorithm components inside joboption files (in python format) which is to run the Run 3 trigger simulation. As the new trigger towers are not set as the default output, they are added by the

postExec to dump the containers and the corresponding auxiliary containers into the output AOD files. The last subcommand is to set the simulation to run with the default configuration for the detector geometry and database which has the information like the employed high voltage in calorimeter or the threshold to receive the cell energy. Then, the final output would be the proper sample for further study on the trigger performance.

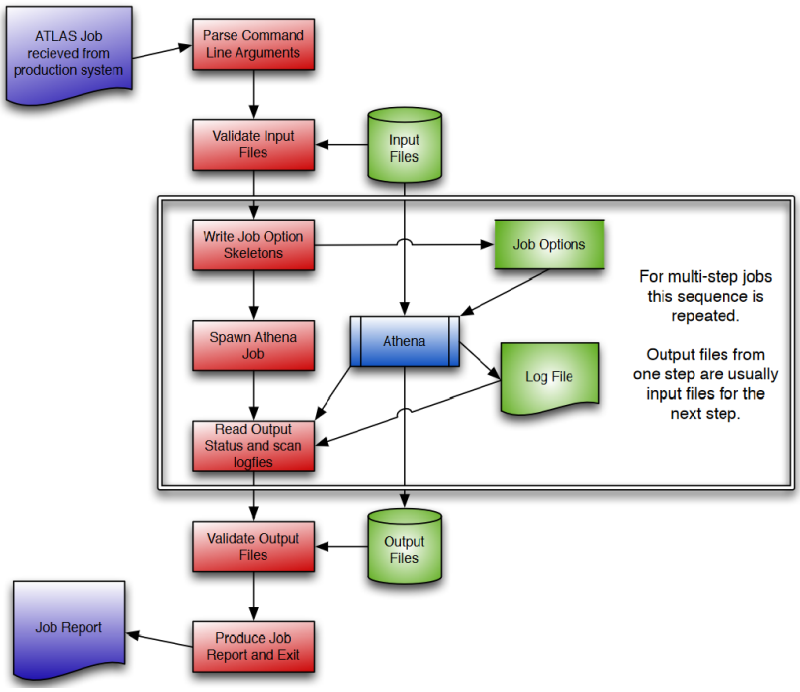

Figure 6.9.: The illustration of the ATLAS simulation flow run by *reco_tf* with the Athena framework [127].

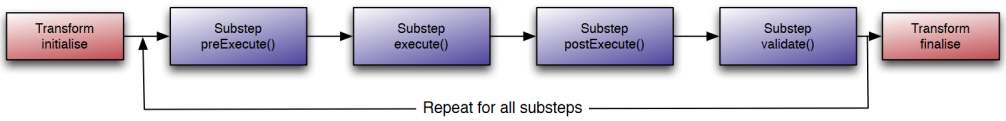

Figure 6.10.: The execution order of *reco_tf* with its subcommands [127].

6.4. Run 3 L1Calo Performance

The output trigger towers are then taken into the physical object reconstructions. This study is to follow the Run 2-like algorithms to verify the performance of object reconstruction under the new Run 3 system, which will be taken as the baseline reconstruction in the firmware. In the study here, three objects will be discussed, which are electrons, small-R jets, and E_T^{miss}, and a deeper insight will be given for E_T^{miss} reconstruction for which I make a thorough study on the thresholds and performance.

The reconstruction of hardware level objects has more constraints than the offline ones. Firstly, the processing of each event must be within the available latency, so a computing-expensive algorithm is not allowed like a machine learning reconstruction with a large-scale structure. Other hardware limits include the restriction on communicating links between the readout channels which are rather important for the gFex algorithms, as the three FPGAs do not share the signal connections between each other. Thirdly, the L1Calo objects should still be consistent to the HLT and offline objects, because they are taken as the seeds for the HLT reconstruction and required to be matched to offline objects.

To investigate the performance of algorithms, two parameters are studied: trigger rate and signal efficiency of an individual L1 trigger item. The trigger rate is estimated from a minimum bias sample with the luminosity corresponding to the pile-up number as 60 per bunch crossing ($\mu = 60$) and $\sqrt{s} = 14\ TeV$, and it is defined as the following:

$$Rate = 40 \times C \times \frac{N^{pass}(trigger(s))}{N^{all}}\ [MHz] \tag{6.6}$$

The "40 MHz" is corresponding to the collision rate of the LHC multiplied by a factor, C, correcting for the fraction of unfilled bunches and the ratio of events passing the trigger requirement (In the following content, the trigger requirements will just be passing "one single" trigger). In the following studies, C was taken as 3/8 from a run in 2017. Each L1Calo item (the objects with corresponding thresholds) should meet the expected individual Run 3 trigger rate budget from the ATLAS TDAQ technical

design report [125] which are presented in Tab. 6.3. After finding a threshold giving a reasonable trigger rate, the trigger efficiency was studied by the offline turn-on curves (definition could be found in Subsec. 3.4.1), which should present a sharp turn-on reaching the plateau at a reasonable offline threshold. The following are the studies with this strategy to verify whether the Run 3 L1Calo system could offer promising physics results with reasonable trigger rates.

Table 6.3.: The expected Run 3 trigger rate budget for the L1Calo items (not all of them)

Object	L1 threshold [GeV]	offline threshold [GeV]	Rate [kHz]
electron/photo	25	32	14
jet	100	200	7
E_T^{miss}	70	200	13

6.4.1. Electron/photon

Due to the lack of the track information, the photons and electrons (egamma) are reconstructed from the calorimeter energy deposits into the same object at L1Calo level. With respect to the other signatures, the energy deposit from the egamma showers is relatively narrow, so the region of interest is defined as a small window of the size, 3×2, on the $\eta - \phi$ plane (as the green area shown in Fig. 6.11 corresponding to 0.075×0.2 for $\Delta\eta \times \Delta\phi$) with the centre cell as a local maximum inside a three by three window. Its energy is given by the summation of energy over all the sampling layer inside this region of both the LAr and tile detectors. However, the electrons are easily faked by the hadronic objects as discussed in Sec. 3.4.7, and a simple cut on energy threshold is not enough to reduce the trigger rate easily. In this case, the shower shape of the energy distribution is taken from three variables for a further background reduction:

- $R_\eta = 1 - E_T^{3\times2}/E_T^{7\times3}$: this variable is defined as the ratio of energy in green over yellow area in Fig. 6.11 to ensure the egamma is well-isolated.

- $R_{had} = E_T^{Had}/E_T^{tot}$: this is the hadronic energy ratio defined in the blue framed region in Fig. 6.11, and it helps to reduce the contamination from the hadronic objects, as they would deposit more energy in the hadronic layers.
- $w_{tot} = \sqrt{\sum_i E_T^{SC_i} \times (\eta^{SC_i} - \eta^{SC_{max}})^2 / \sum E_T^{SC_i}}$: this is to defined the shower distribution within the red framed region in Fig. 6.11.

The final cuts on the three variables are employed with the energy threshold of 20 GeV for the same rate for Run 2 egamma trigger:

- $R_\eta < 0.12$
- $R_{had} < 0.16$
- $w_{tot} < 0.02$

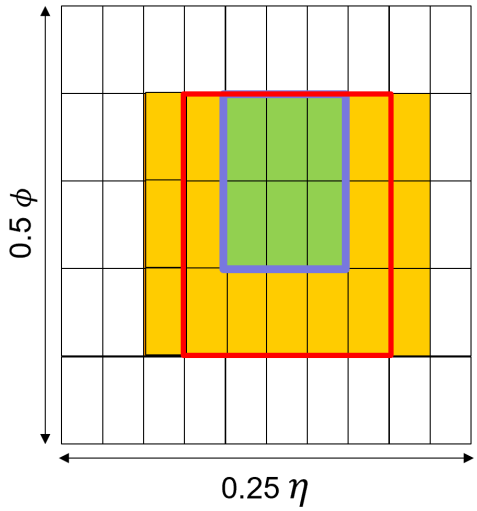

Figure 6.11.: The diagram to illustrate the electron/photon ROI with the areas for the isolation definition.

A sample of $Z \to ee$ simulated by Sherpa generator is taken to verify the signal efficiency. The results are presented in Fig. 6.12. The turn-on curves as a function of the leading truth electron E_T with an event-veto of truth electrons in the transition region of $1.37 < |\eta| < 1.52$ are made from two L1Calo electron E_T cuts: 20 GeV giving the rate of $\sim 30\ kHz$ (the Run 2 single electron trigger rate), and 28 GeV giving the rate of $\sim 10\ kHz$ (the expected rate in the ATLAS TDAQ TDR [125]). With the same rate

as Run 2 electron trigger, the turn-on curves has shown a sharper turn-on which can reach the plateau at 25 GeV which is 7 GeV lower than the Run 2 offline threshold. For the turn-on curve with the cut on 28 GeV, it reaches the plateau at similar E_T as Run 2, but it has much lower rate. Both of them has shown the improvement with respect to the Run 2 electron trigger in terms of either trigger rate or the offline threshold, and it has achieved the performance as the ATLAS TDAQ TDR [125] expected. The other study in the trigger efficiency is to verify the $|\eta|$ dependence which is also shown in Fig. 6.12 with the L1 electron E_T cut at 28 GeV. The result has shown that the electron trigger efficiency has low dependence on η except for the ones in the transition region, and the trigger has almost 100% for electrons with $E_T > 30\ GeV$.

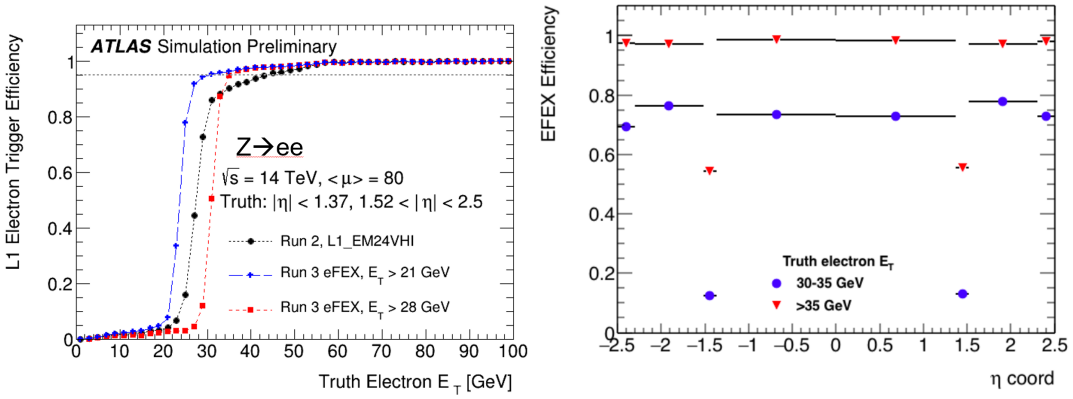

Figure 6.12.: The signal efficiency as a function of truth electron E_T (left) and η (right)

6.4.2. Small-R Jets

The small-R jets are reconstructed from a sliding window algorithm (SLW). Firstly, the jet seed finding was performed by a 3×3 window (0.3×0.3) which went through the jTowers in the LAr detector. The seed is then built if the centre tower is a local maximum, and the energy sum within the window is above 4 GeV and also higher than the surrounding region. Then, the jets is constructed as the region of interest defined as $R = 0.45$ from the central tower with the energy summed over both LAr and tile detector sampling layers. It should be noted that the L1Calo jets has a different radius from the offline and HLT ones which have the radius of $R = 0.4$, because the

number of included towers should be an integer with the centre in a chosen tower. The construction steps are presented in Fig. 6.13 which is also showing another potential algorithm for which the jets are reconstructed from a 9×9 square region of interest.

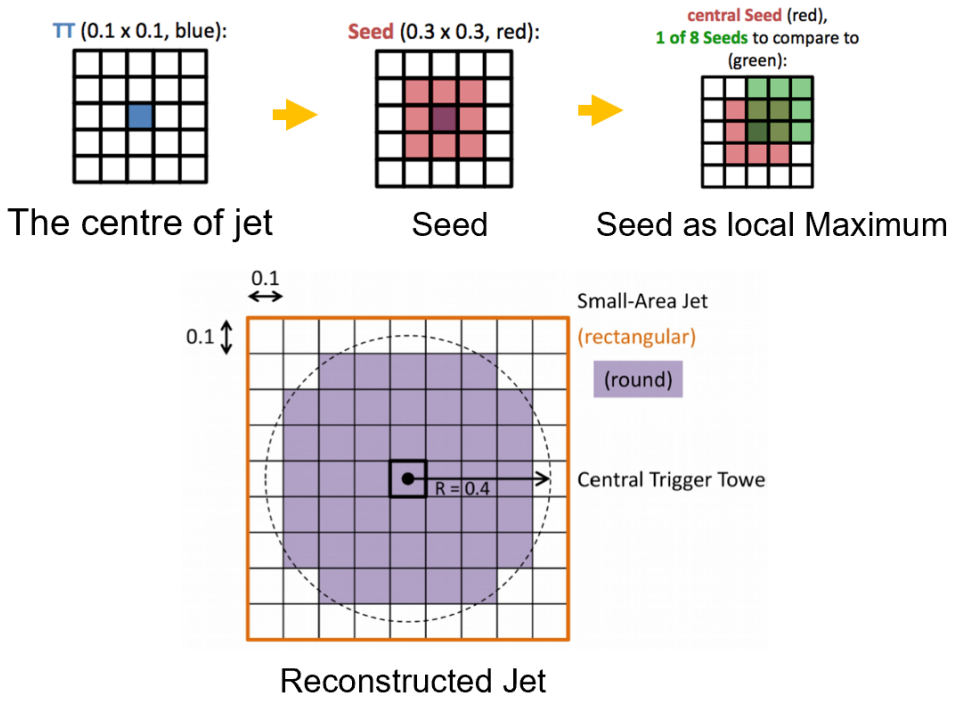

Figure 6.13.: The illustration of how the L1Calo jets are reconstructed.

For the jet triggers, two L1Calo items are proposed, a single jet trigger and a three-jet trigger. Both of the two triggers are studied with a signal sample of $ZH \to \nu\nu bb$ simulated by Sherpa under the collision environment of $\mu = 60$. Although the sample has only two jets from the physical process, the third jet might still be added by the pile-up simulation, so it can also be used for the three-jet trigger study. The performance of these two triggers could be seen in Fig. 6.14 with turn-ons as a function of the offline first (for the single-jet trigger) and third (for the three-jet trigger) leading jet E_T. The performance of Run 3 L1 jets is compared to Run 2 L1 jets and anti-k_T jets which take jTowers as input entities, and the thresholds are all set giving the same trigger rate. For the Run 3 single jet trigger, the threshold was set at 97 GeV, and it has the same performance as the jets reconstructed from the other two algorithms as what we expect from the TDR (7 kHz). For the three jet trigger, the two Run 3 algorithms have

shown better performance than Run 2 jets, as both of them achieve higher efficiency in the turn-on plateau region than Run 2 L1 jets. This is benefited from the improved granularity which provides a better distinguishing power for jet finding within a high pile-up environment.

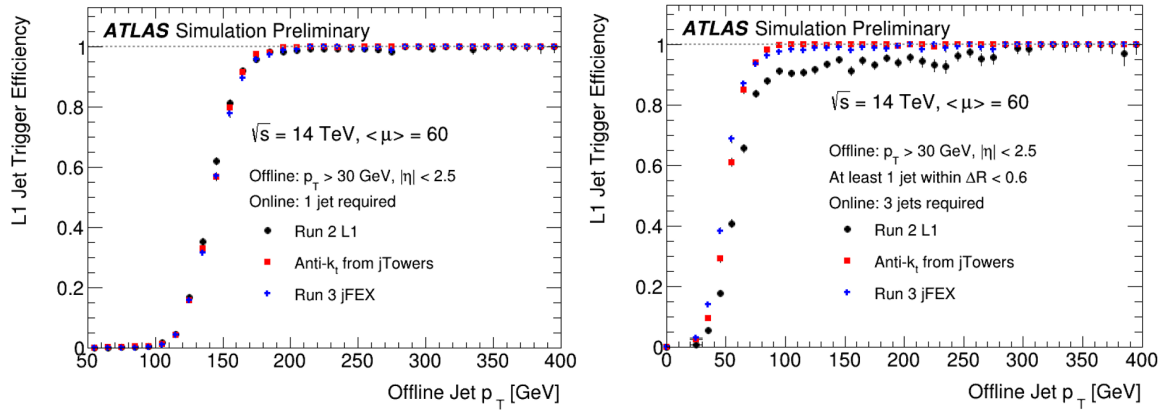

Figure 6.14.: The trigger performance for single-jet (left) and three-jet (right) triggers as turn-on curves as functions of offline jet E_T

6.4.3. Missing Transverse Energy

The missing transverse energy, E_T^{miss}, is constructed as the vector sum of jTowers in the jFex, and the same algorithm proposed here will also be potentially implemented with gTowers which will need further optimization for the trigger tower thresholds. However, most of the energy deposits in the calorimeter are from the pile-up events or electronic noise, so a proper selection on the towers is essential. With broadly ranged granularities, a constant threshold is not appropriate to handle all the jTowers, so a tower-dependent threshold scheme is applied. For this purpose, the minimum bias sample is used to understand the noise behaviour in the jTowers. The first step is to get the E_T histograms for each jTower and take the root mean square (RMS, 1σ) from this histograms, which will be set as the unit of thresholds on jTower selection. Then, the optimization is performed by finding the working point which gives the highest signal efficiency (with the same signal sample for jet trigger study) with the trigger rate at 5 kHz as the Run 2 E_T^{miss} trigger. The working point scan is performed

on a three-dimension phase space constructed by the thresholds on LAr (EM) and tile (Hadronic) sampling layers with one more dimension which levels up the thresholds in the forward region. Fig. 6.15 is presenting the result of signal efficiency at the trigger rate of 5 kHz with the scanning step of 0.5σ for both LAr and tile towers, while the threshold on the forward region is 0.5σ higher than the LAr threshold. After this process, the scheme of thresholds shown in Tab. 6.4 is chosen to reconstruct the jFex E_T^{miss}.

Table 6.4.: jTower thresholds for the E_T^{miss} reconstruction

LAr	Tile	Forward	Efficiency	Threshold
$> 5\sigma$	$> 5.5\sigma$	$> 5.5\sigma$	21.62%	57 GeV

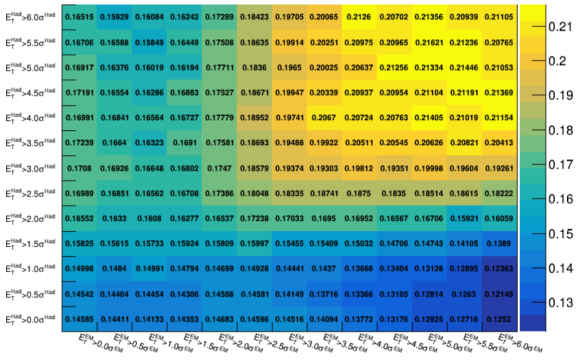

Figure 6.15.: The signal efficiency with the trigger rate at 5 kHz as a function of thresholds on the LAr (x-axis) and tile (y-axis) E_T which are in the unit of σ. The forward region has the threshold for 0.5σ higher than the LAr tower threshold.

To verify the performance for the physics analysis, the $ZH \to \nu\nu bb$ sample is still used. The first verification is for the energy and spatial resolutions with respect to the truth E_T^{miss} which is defined as:

$$Res_{E_T} = \frac{E_T^{jFex} - E_T^{truth}}{E_T^{truth}} \tag{6.7}$$

$$Res_{\phi} = \Delta\phi(E_T^{jFex}, E_T^{truth}) \tag{6.8}$$

The results could be seen Fig. 6.16 with the other thresholds which also give high efficiency with trigger rate at 5 kHz, and they are showing great agreement to the Run 2 L1Calo E_T^{miss}. However, when making the trigger rate comparison to data, a significant inconsistency was found as shown in Fig. 6.17. For this case, the Run 2 simulated L1 E_T^{miss} cannot be used for a proper comparison due to some unknown modelling issue, and, instead, a dataset collected in 2017 with an offline selection of $Z \rightarrow \mu\mu$ is used, as muons are invisible for the L1Calo system and make the contribution to L1 E_T^{miss}. The result is shown in Fig. 6.18, and a great agreement is observed because of the similar algorithm. This is now already taken as the baseline jFex E_T^{miss}, while the other pile-up dependent algorithms are still under investigation for both jFex and gFex.

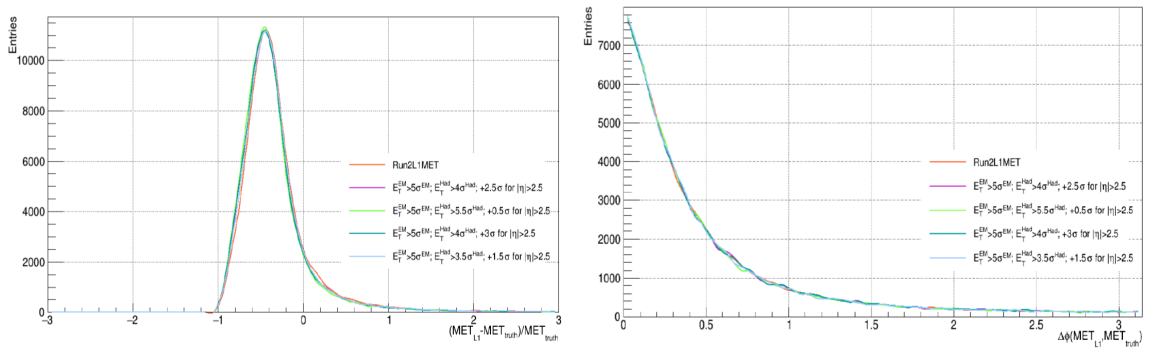

Figure 6.16.: The energy (left) and spatial resolution of the reconstructed jFex E_T^{miss} in comparison to the simulated Run 2 L1Calo E_T^{miss}

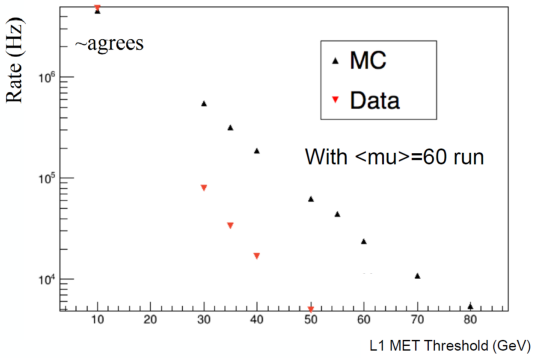

Figure 6.17.: The rate comparison of data and simulated Run 2 L1Calo E_T^{miss}

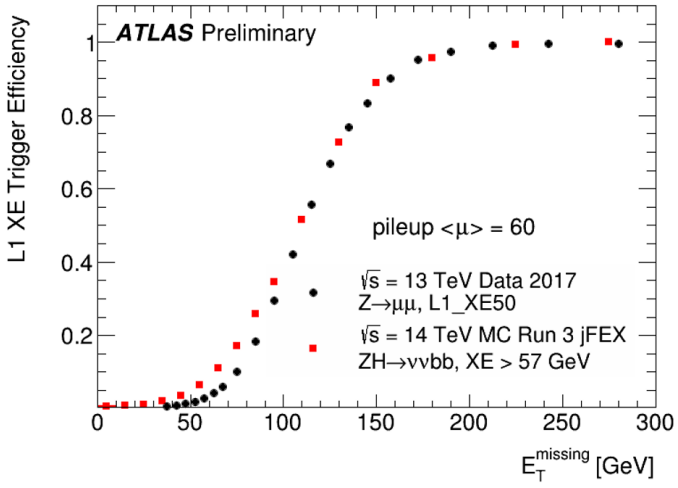

Figure 6.18.: The efficiency turn-on curves as a function of truth E_T^{miss} for data and simulated jFex L1Calo E_T^{miss}

6.5. Summary

The Run 3 L1Calo upgrade plays an important role for the imminent LHC operation to provide a better background suppression and similar signal efficiency with respect to Run 2 under the environment of abundant pile-ups. The new hardware provides a better granularity and a longer latency for the object reconstruction, and it also grants the flexibility to capture new exotic signatures like the long-lived particles by the new design of active time window of calorimeters. To make the best use of the new hardware calorimeter trigger system, I have constructed the simulation software with the new trigger towers and integrated into the ATLAS software, Athena. The preliminary studies with my proposed E_T^{miss} trigger algorithm have shown promising results, and the samples with the new L1Calo physical objects are also under production in preparation for the Run 3 L1 trigger menu.

Chapter 7.

Thesis Remarks

"Git-r-done"

— Mater, Cars

The Standard Model has been a successful description for the constituents of this universe giving precise predictions of how the matters interact with each other. However, we saw that a few puzzles still remain unsolved. I have described how the Large Hadron Collider and the ATLAS detector were built to investigate those mysteries.

New models were proposed in the attempt to solve those problems to complete the SM, and they also predicted the existence of new particles most of which have the couplings to the SM bosons. The $WV \to \ell\nu qq$ final state was therefore chosen to investigate those new models including the heavy-mass Higgs boson, the heavy vector triplet, and also the RS graviton. This analysis has looked into two production modes, VBF and ggF/DY, along with two jet topologies. The analysis strategy was to employ the simulation for the SM background modelling and the fake factor method for the multijet background modelling. After the comparison between data and background estimation, no evidence for new physics was found, and exclusion limits were set on the masses of the new particles. To enhance the sensitivity of this search task, the result was combined with the other diboson and dilepton resonance final states. Unfortunately, there was still no discovery of any new particle, and mass limits were further

updated with the new limit on couplings between the HVT and the SM particles.

In addition to the search for new particles, another way of looking for new physics was to verify the Standard Model predictions toward the interaction cross-sections. This study inheriting the framework from the resonance search, and it was dedicated to the vector boson scattering cross-section measurement which has the semileptonic final states ($pp \to VVjj \to \ell\nu qq$+jj). The final result was combined with the other channels, $\ell\ell qq$ and $\nu\nu qq$, and it made the first measurement on the VBS interaction with semileptonic final states. Although the discovery significance is just 2.7σ which is not enough to claim a discovery, it still showed promising agreement with the SM estimation.

Although no BSM physics was discovered, the ATLAS detector has been through a fruitful Run 2 operation delivering significant physics results. To enhance the sensitivity to new physics, the LHC will undergo the upgrade to increase both the energy and luminosity. To achieve better performance for physics analyses, the ATLAS will also upgrade the hardware calorimeter trigger with new components to process calorimeter signal. I have described my contributions to the software implementation for the simulation of this system including the trigger tower identification and construction. Under this framework, three preliminary physical object algorithms including my proposal of L1 E_T^{miss} reconstruction showed the same or improved performance with the upcoming Run 3 collision environment in comparison to the Run 2 L1 objects. However, it should be noted that there is still the great potential for more complicated algorithms to achieve better performance for pile-up suppression.

In the following decades, the ATLAS detector is expected to collect the data up to 3000 fb^{-1} with hardware upgrades including a full silicon inner tracking system (ITK), an entirely digitized calorimeter readout electronics, and a two-level hardware trigger (L0 and L1). This will shed the light for the underlying new physics and provide a better understanding to the Standard Model at the frontier of human knowledge and technology which include the analyses discussed in this thesis (searches for the diboson resonance and the measurement on the VBS interaction).

"Thanks for the adventure. Now go have a new one"

— Ellie, Up

Appendix A.

Sample List

Here are the lists for the samples used in the analyses in this thesis with the related information for the event normalization.

A.1. Background Samples

Here is the list for samples of background interactions. The V+jets samples are sliced by the leading jet p_T.

Table A.1.: $W \to e\nu$+jets samples used in the analysis. The dataset ID, MC generator, production cross section, filter efficiency and total number of generated events are shown.

DS ID	Name	$\sigma \times$ BR [pb]	k-factor	ϵ_{filter}	Events
364170	Sherpa_221_NNPDF30NNLO_Wenu_MAXHTPTV0_70_CVetoBVeto	19127	0.9702	0.82447	24740000
364171	Sherpa_221_NNPDF30NNLO_Wenu_MAXHTPTV0_70_CFilterBVeto	19130	0.9702	0.1303	9853500
364172	Sherpa_221_NNPDF30NNLO_Wenu_MAXHTPTV0_70_BFilter	19135	0.9702	0.044141	17242400
364173	Sherpa_221_NNPDF30NNLO_Wenu_MAXHTPTV70_140_CVetoBVeto	942.58	0.9702	0.66872	14660500
364174	Sherpa_221_NNPDF30NNLO_Wenu_MAXHTPTV70_140_CFilterBVeto	945.67	0.9702	0.22787	9818400
364175	Sherpa_221_NNPDF30NNLO_Wenu_MAXHTPTV70_140_BFilter	945.15	0.9702	0.10341	9801900
364176	Sherpa_221_NNPDF30NNLO_Wenu_MAXHTPTV140_280_CVetoBVeto	339.81	0.9702	0.59691	9879000
364177	Sherpa_221_NNPDF30NNLO_Wenu_MAXHTPTV140_280_CFilterBVeto	339.87	0.9702	0.28965	7410000
364178	Sherpa_221_NNPDF30NNLO_Wenu_MAXHTPTV140_280_BFilter	339.48	0.9702	0.10898	9880900
364179	Sherpa_221_NNPDF30NNLO_Wenu_MAXHTPTV280_500_CVetoBVeto	72.084	0.9702	0.54441	4923800
364180	Sherpa_221_NNPDF30NNLO_Wenu_MAXHTPTV280_500_CFilterBVeto	72.128	0.9702	0.31675	2963400
364181	Sherpa_221_NNPDF30NNLO_Wenu_MAXHTPTV280_500_BFilter	72.113	0.9702	0.13391	2958000
364182	Sherpa_221_NNPDF30NNLO_Wenu_MAXHTPTV500_1000	15.224	0.9702	1	5916800
364183	Sherpa_221_NNPDF30NNLO_Wenu_MAXHTPTV1000_E_CMS	1.2334	0.9702	1	3947000

Table A.2.: $W \to \mu\nu$+jets samples used in the analysis. The dataset ID, MC generator, production cross section, filter efficiency and total number of generated events are shown.

DS ID	Name	$\sigma \times$ BR [pb]	k-factor	ϵ_{filter}	Events
364156	Sherpa_221_NNPDF30NNLO_Wmunu_MAXHTPTV0_70_CVetoBVeto	19143	0.9702	0.8238	24723000
364157	Sherpa_221_NNPDF30NNLO_Wmunu_MAXHTPTV0_70_CFilterBVeto	19121	0.9702	0.1304	9847000
364158	Sherpa_221_NNPDF30NNLO_Wmunu_MAXHTPTV0_70_BFilter	19135	0.9702	0.044118	17226200
364159	Sherpa_221_NNPDF30NNLO_Wmunu_MAXHTPTV70_140_CVetoBVeto	944.85	0.9702	0.67463	14788000
364160	Sherpa_221_NNPDF30NNLO_Wmunu_MAXHTPTV70_140_CFilterBVeto	937.78	0.9702	0.23456	9853800
364161	Sherpa_221_NNPDF30NNLO_Wmunu_MAXHTPTV70_140_BFilter	944.63	0.9702	0.075648	19639000
364162	Sherpa_221_NNPDF30NNLO_Wmunu_MAXHTPTV140_280_CVetoBVeto	339.54	0.9702	0.62601	9882000
364163	Sherpa_221_NNPDF30NNLO_Wmunu_MAXHTPTV140_280_CFilterBVeto	340.06	0.9702	0.28947	7408000
364164	Sherpa_221_NNPDF30NNLO_Wmunu_MAXHTPTV140_280_BFilter	339.54	0.9702	0.10872	9826000
364165	Sherpa_221_NNPDF30NNLO_Wmunu_MAXHTPTV280_500_CVetoBVeto	72.067	0.9702	0.54647	4940000
364166	Sherpa_221_NNPDF30NNLO_Wmunu_MAXHTPTV280_500_CFilterBVeto	72.198	0.9702	0.31743	2958000
364167	Sherpa_221_NNPDF30NNLO_Wmunu_MAXHTPTV280_500_BFilter	72.045	0.9702	0.13337	2959500
364168	Sherpa_221_NNPDF30NNLO_Wmunu_MAXHTPTV500_1000	15.01	0.9702	1	5910500
364169	Sherpa_221_NNPDF30NNLO_Wmunu_MAXHTPTV1000_E_CMS	1.2344	0.9702	1	3959000

Table A.3.: $W \to \tau\nu$+jets samples used in the analysis. The dataset ID, MC generator, production cross section, filter efficiency and total number of generated events are shown.

DS ID	Name	$\sigma \times$ BR [pb]	k-factor	ϵ_{filter}	Events
364184	Sherpa_221_NNPDF30NNLO_Wtaunu_MAXHTPTV0_70_CVetoBVeto	19152	0.9702	0.82495	24784000
364185	Sherpa_221_NNPDF30NNLO_Wtaunu_MAXHTPTV0_70_CFilterBVeto	19153	0.9702	0.12934	9865600
364186	Sherpa_221_NNPDF30NNLO_Wtaunu_MAXHTPTV0_70_BFilter	19163	0.9702	0.044594	17273200
364187	Sherpa_221_NNPDF30NNLO_Wtaunu_MAXHTPTV70_140_CVetoBVeto	947.65	0.9702	0.67382	14808500
364188	Sherpa_221_NNPDF30NNLO_Wtaunu_MAXHTPTV70_140_CFilterBVeto	946.73	0.9702	0.22222	9860000
364189	Sherpa_221_NNPDF30NNLO_Wtaunu_MAXHTPTV70_140_BFilter	943.3	0.9702	0.10391	9857000
364190	Sherpa_221_NNPDF30NNLO_Wtaunu_MAXHTPTV140_280_CVetoBVeto	339.36	0.9702	0.59622	9899000
364191	Sherpa_221_NNPDF30NNLO_Wtaunu_MAXHTPTV140_280_CFilterBVeto	339.63	0.9702	0.29025	7405000
364192	Sherpa_221_NNPDF30NNLO_Wtaunu_MAXHTPTV140_280_BFilter	339.54	0.9702	0.11799	9834000
364193	Sherpa_221_NNPDF30NNLO_Wtaunu_MAXHTPTV280_500_CVetoBVeto	72.065	0.9702	0.54569	4931200
364194	Sherpa_221_NNPDF30NNLO_Wtaunu_MAXHTPTV280_500_CFilterBVeto	71.976	0.9702	0.31648	2956400
364195	Sherpa_221_NNPDF30NNLO_Wtaunu_MAXHTPTV280_500_BFilter	72.026	0.9702	0.13426	2954100
364196	Sherpa_221_NNPDF30NNLO_Wtaunu_MAXHTPTV500_1000	15.046	0.9702	1	5945000

Table A.4.: $Z \to ee$+jets samples used in the analysis. The dataset ID, MC generator, production cross section, filter efficiency and total number of generated events are shown.

DS ID	Name	$\sigma \times$ BR [pb]	k-factor	ϵ_{filter}	Events
364114	Sherpa_221_NNPDF30NNLO_Zee_MAXHTPTV0_70_CVetoBVeto	1981.8	0.9751	0.82106	7900000
364115	Sherpa_221_NNPDF30NNLO_Zee_MAXHTPTV0_70_CFilterBVeto	1980.8	0.9751	0.11295	4940500
364116	Sherpa_221_NNPDF30NNLO_Zee_MAXHTPTV0_70_BFilter	1981.7	0.9751	0.063809	7883600
364117	Sherpa_221_NNPDF30NNLO_Zee_MAXHTPTV70_140_CVetoBVeto	110.5	0.9751	0.69043	5925000
364118	Sherpa_221_NNPDF30NNLO_Zee_MAXHTPTV70_140_CFilterBVeto	110.63	0.9751	0.18382	1972600
364119	Sherpa_221_NNPDF30NNLO_Zee_MAXHTPTV70_140_BFilter	110.31	0.9751	0.11443	5855000
364120	Sherpa_221_NNPDF30NNLO_Zee_MAXHTPTV140_280_CVetoBVeto	40.731	0.9751	0.61452	4949000
364121	Sherpa_221_NNPDF30NNLO_Zee_MAXHTPTV140_280_CFilterBVeto	40.67	0.9751	0.23044	2962600
364122	Sherpa_221_NNPDF30NNLO_Zee_MAXHTPTV140_280_BFilter	40.694	0.9751	0.14927	12330900
364123	Sherpa_221_NNPDF30NNLO_Zee_MAXHTPTV280_500_CVetoBVeto	8.6743	0.9751	0.56134	1932800
364124	Sherpa_221_NNPDF30NNLO_Zee_MAXHTPTV280_500_CFilterBVeto	8.6711	0.9751	0.26294	988900
364125	Sherpa_221_NNPDF30NNLO_Zee_MAXHTPTV280_500_BFilter	8.6766	0.9751	0.17223	1976850
364126	Sherpa_221_NNPDF30NNLO_Zee_MAXHTPTV500_1000	1.8081	0.9751	1	2973000
364127	Sherpa_221_NNPDF30NNLO_Zee_MAXHTPTV1000_E_CMS	0.14857	0.9751	1	988000

Table A.5.: $Z \to \mu\mu$+jets samples used in the analysis. The dataset ID, MC generator, production cross section, filter efficiency and total number of generated events are shown.

DS ID	Name	$\sigma \times$ BR [pb]	k-factor	ϵ_{filter}	Events
364100	Sherpa_221_NNPDF30NNLO_Zmumu_MAXHTPTV0_70_CVetoBVeto	1983	0.9751	0.8221	7891000
364101	Sherpa_221_NNPDF30NNLO_Zmumu_MAXHTPTV0_70_CFilterBVeto	1978.4	0.9751	0.11308	4917000
364102	Sherpa_221_NNPDF30NNLO_Zmumu_MAXHTPTV0_70_BFilter	1982.2	0.9751	0.064161	7902000
364103	Sherpa_221_NNPDF30NNLO_Zmumu_MAXHTPTV70_140_CVetoBVeto	108.92	0.9751	0.68873	5917000
364104	Sherpa_221_NNPDF30NNLO_Zmumu_MAXHTPTV70_140_CFilterBVeto	109.42	0.9751	0.18596	1969800
364105	Sherpa_221_NNPDF30NNLO_Zmumu_MAXHTPTV70_140_BFilter	108.91	0.9751	0.11375	5900600
364106	Sherpa_221_NNPDF30NNLO_Zmumu_MAXHTPTV140_280_CVetoBVeto	39.878	0.9751	0.60899	4943000
364107	Sherpa_221_NNPDF30NNLO_Zmumu_MAXHTPTV140_280_CFilterBVeto	39.795	0.9751	0.23308	2954400
364108	Sherpa_221_NNPDF30NNLO_Zmumu_MAXHTPTV140_280_BFilter	39.908	0.9751	0.14618	12339300
364109	Sherpa_221_NNPDF30NNLO_Zmumu_MAXHTPTV280_500_CVetoBVeto	8.5375	0.9751	0.55906	1973000
364110	Sherpa_221_NNPDF30NNLO_Zmumu_MAXHTPTV280_500_CFilterBVeto	8.5403	0.9751	0.26528	986000
364111	Sherpa_221_NNPDF30NNLO_Zmumu_MAXHTPTV280_500_BFilter	8.4932	0.9751	0.17559	1971400
364112	Sherpa_221_NNPDF30NNLO_Zmumu_MAXHTPTV500_1000	1.7881	0.9751	1	2960500
364113	Sherpa_221_NNPDF30NNLO_Zmumu_MAXHTPTV1000_E_CMS	0.14769	0.9751	1	988000

Table A.6.: $Z \to \tau\tau$+jets samples used in the analysis. The dataset ID, MC generator, production cross section, filter efficiency and total number of generated events are shown.

DS ID	Name	$\sigma \times$ BR [pb]	k-factor	ϵ_{filter}	Events
364128	Sherpa_221_NNPDF30NNLO_Ztautau_MAXHTPTV0_70_CVetoBVeto	1981.6	0.9751	0.82142	7907000
364129	Sherpa_221_NNPDF30NNLO_Ztautau_MAXHTPTV0_70_CFilterBVeto	1978.8	0.9751	0.11314	4941000
364130	Sherpa_221_NNPDF30NNLO_Ztautau_MAXHTPTV0_70_BFilter	1981.8	0.9751	0.064453	7890600
364131	Sherpa_221_NNPDF30NNLO_Ztautau_MAXHTPTV70_140_CVetoBVeto	110.37	0.9751	0.68883	5935500
364132	Sherpa_221_NNPDF30NNLO_Ztautau_MAXHTPTV70_140_CFilterBVeto	110.51	0.9751	0.1829	1961200
364133	Sherpa_221_NNPDF30NNLO_Ztautau_MAXHTPTV70_140_BFilter	110.87	0.9751	0.1283	5912550
364134	Sherpa_221_NNPDF30NNLO_Ztautau_MAXHTPTV140_280_CVetoBVeto	40.781	0.9751	0.60821	4956000
364135	Sherpa_221_NNPDF30NNLO_Ztautau_MAXHTPTV140_280_CFilterBVeto	40.74	0.9751	0.22897	2973000
364136	Sherpa_221_NNPDF30NNLO_Ztautau_MAXHTPTV140_280_BFilter	40.761	0.9751	0.13442	4932950
364137	Sherpa_221_NNPDF30NNLO_Ztautau_MAXHTPTV280_500_CVetoBVeto	8.5502	0.9751	0.56036	1973000
364138	Sherpa_221_NNPDF30NNLO_Ztautau_MAXHTPTV280_500_CFilterBVeto	8.6707	0.9751	0.26245	986000
364139	Sherpa_221_NNPDF30NNLO_Ztautau_MAXHTPTV280_500_BFilter	8.6804	0.9751	0.17313	1974950
364140	Sherpa_221_NNPDF30NNLO_Ztautau_MAXHTPTV500_1000	1.8096	0.9751	1	2944800
364141	Sherpa_221_NNPDF30NNLO_Ztautau_MAXHTPTV1000_E_CMS	0.14834	0.9751	1	980000

Table A.7.: $t\bar{t}$ and single top samples used in the analysis. The dataset ID, MC generator, production cross section, filter efficiency and total number of generated events are shown.

DS ID	Name	$\sigma \times$ BR [pb]	k-factor	ϵ_{filter}	Events
410000	PowhegPythiaEvtGen_P2012_ttbar_hdamp172p5_nonallhad	831.76	1	0.543	48138600
410011	PowhegPythiaEvtGen_P2012_singletop_tchan_lept_top	43.739	1.0094	1	4986200
410012	PowhegPythiaEvtGen_P2012_singletop_tchan_lept_antitop	25.778	1.0193	1	4989800
410013	PowhegPythiaEvtGen_P2012_Wt_inclusive_top	34.009	1.054	1	4985800
410014	PowhegPythiaEvtGen_P2012_Wt_inclusive_antitop	33.989	1.054	1	4985600
410025	PowhegPythiaEvtGen_P2012_SingleTopSchan_noAllHad_top	2.0517	1.0046	1	997800
410026	PowhegPythiaEvtGen_P2012_SingleTopSchan_noAllHad_antitop	1.2615	1.0215	1	995400

Table A.8.: Diboson samples used in the analysis. The dataset ID, MC generator, production cross section, filter efficiency and total number of generated events are shown.

DS ID	Name	$\sigma \times$ BR [pb]	k-factor	ϵ_{filter}	Events
361091	Sherpa_CT10_WplvWmqq_SHv21_improved	24.885	0.91	1	3993900
361092	Sherpa_CT10_WpqqWmlv_SHv21_improved	24.857	0.91	1	3993700
361093	Sherpa_CT10_WlvZqq_SHv21_improved	11.494	0.91	1	3993600
361094	Sherpa_CT10_WqqZll_SHv21_improved	3.4234	0.91	1	3990500
361095	Sherpa_CT10_WqqZvv_SHv21_improved	6.777	0.91	1	4962400
361096	Sherpa_CT10_ZqqZll_SHv21_improved	16.445	0.91	0.14307	3988900

A.2. Signal Samples for Resonance Search

Here is the list presenting samples which are taken as the signal for the resonance search.

Table A.9.: Graviton samples used in the analysis. The dataset ID, MC generator, production cross section, filter efficiency and total number of generated events are shown.

DS ID	Process	Generator	$\sigma \times$ BR [nb]	ϵ_{filter}	Events
307474	RS $G \to WW \to \ell\nu qq$ $c = 1$ $m = 300$ GeV	MadGraph 2.2.2 + Pythia 8.186	3.172E-02	1.0	29000
307475	RS $G \to WW \to \ell\nu qq$ $c = 1$ $m = 400$ GeV	MadGraph 2.2.2 + Pythia 8.186	7.262E-03	1.0	30000
303224	RS $G \to WW \to \ell\nu qq$ $c = 1$ $m = 500$ GeV	MadGraph 2.2.2 + Pythia 8.186	1.815E-03	1.0	30000
303225	RS $G \to WW \to \ell\nu qq$ $c = 1$ $m = 600$ GeV	MadGraph 2.2.2 + Pythia 8.186	6.132E-04	1.0	29000
303226	RS $G \to WW \to \ell\nu qq$ $c = 1$ $m = 700$ GeV	MadGraph 2.2.2 + Pythia 8.186	2.522E-04	1.0	29000
303227	RS $G \to WW \to \ell\nu qq$ $c = 1$ $m = 800$ GeV	MadGraph 2.2.2 + Pythia 8.186	1.181E-04	1.0	29000
303228	RS $G \to WW \to \ell\nu qq$ $c = 1$ $m = 900$ GeV	MadGraph 2.2.2 + Pythia 8.186	6.054E-05	1.0	30000
303229	RS $G \to WW \to \ell\nu qq$ $c = 1$ $m = 1000$ GeV	MadGraph 2.2.2 + Pythia 8.186	3.3215E-05	1.0	29000
303230	RS $G \to WW \to \ell\nu qq$ $c = 1$ $m = 1100$ GeV	MadGraph 2.2.2 + Pythia 8.186	1.913E-05	1.0	30000
303231	RS $G \to WW \to \ell\nu qq$ $c = 1$ $m = 1200$ GeV	MadGraph 2.2.2 + Pythia 8.186	1.152E-05	1.0	30000
303232	RS $G \to WW \to \ell\nu qq$ $c = 1$ $m = 1300$ GeV	MadGraph 2.2.2 + Pythia 8.186	7.164E-06	1.0	29000
303233	RS $G \to WW \to \ell\nu qq$ $c = 1$ $m = 1400$ GeV	MadGraph 2.2.2 + Pythia 8.186	4.579E-06	1.0	30000
303234	RS $G \to WW \to \ell\nu qq$ $c = 1$ $m = 1500$ GeV	MadGraph 2.2.2 + Pythia 8.186	2.997E-06	1.0	30000
303235	RS $G \to WW \to \ell\nu qq$ $c = 1'm = 1600$ GeV	MadGraph 2.2.2 + Pythia 8.186	2.002E-06	1.0	30000
303236	RS $G \to WW \to \ell\nu qq$ $c = 1$ $m = 1700$ GeV	MadGraph 2.2.2 + Pythia 8.186	1.362E-06	1.0	30000
303237	RS $G \to WW \to \ell\nu qq$ $c = 1$ $m = 1800$ GeV	MadGraph 2.2.2 + Pythia 8.186	9.381E-07	1.0	30000
303238	RS $G \to WW \to \ell\nu qq$ $c = 1$ $m = 1900$ GeV	MadGraph 2.2.2 + Pythia 8.186	6.565E-07	1.0	29000
303239	RS $G \to WW \to \ell\nu qq$ $c = 1$ $m = 2000$ GeV	MadGraph 2.2.2 + Pythia 8.186	4.641E-07	1.0	30000
303240	RS $G \to WW \to \ell\nu qq$ $c = 1$ $m = 2200$ GeV	MadGraph 2.2.2 + Pythia 8.186	2.397E-07	1.0	29000
303241	RS $G \to WW \to \ell\nu qq$ $c = 1$ $m = 2400$ GeV	MadGraph 2.2.2 + Pythia 8.186	1.279E-07	1.0	30000
303242	RS $G \to WW \to \ell\nu qq$ $c = 1$ $m = 2600$ GeV	MadGraph 2.2.2 + Pythia 8.186	7.015E-08	1.0	30000
303243	RS $G \to WW \to \ell\nu qq$ $c = 1$ $m = 2800$ GeV	MadGraph 2.2.2 + Pythia 8.186	3.926E-08	1.0	29000
303244	RS $G \to WW \to \ell\nu qq$ $c = 1$ $m = 3000$ GeV	MadGraph 2.2.2 + Pythia 8.186	2.2365E-08	1.0	30000
303245	RS $G \to WW \to \ell\nu qq$ $c = 1$ $m = 3500$ GeV	MadGraph 2.2.2 + Pythia 8.186	5.831E-09	1.0	29000
303246	RS $G \to WW \to \ell\nu qq$ $c = 1$ $m = 4000$ GeV	MadGraph 2.2.2 + Pythia 8.186	1.613E-09	1.0	30000
303247	RS $G \to WW \to \ell\nu qq$ $c = 1$ $m = 4500$ GeV	MadGraph 2.2.2 + Pythia 8.186	4.658E-10	1.0	30000
303248	RS $G \to WW \to \ell\nu qq$ $c = 1$ $m = 5000$ GeV	MadGraph 2.2.2 + Pythia 8.186	1.403E-10	1.0	30000

Table A.10.: HVT WW samples used in the analysis with Model A and $g_V = 1$. The dataset ID, MC generator, production cross section, filter efficiency and total number of generated events are shown.

307365	$Z' \to WW \to \ell\nu qq$, Model-A $g_V = 1$ $m = 300$ GeV	MadGraph 2.2.2 + Pythia 8.186	1.381E-02	1.0	29000
307366	$Z' \to WW \to \ell\nu qq$, Model-A $g_V = 1$ $m = 400$ GeV	MadGraph 2.2.2 + Pythia 8.186	4.367E-03	1.0	30000
302116	$Z' \to WW \to \ell\nu qq$, Model-A $g_V = 1$ $m = 500$ GeV	MadGraph 2.2.2 + Pythia 8.186	1.745E-03	1.0	25000
302117	$Z' \to WW \to \ell\nu qq$, Model-A $g_V = 1$ $m = 600$ GeV	MadGraph 2.2.2 + Pythia 8.186	8.184E-04	1.0	30000
302118	$Z' \to WW \to \ell\nu qq$, Model-A $g_V = 1$ $m = 700$ GeV	MadGraph 2.2.2 + Pythia 8.186	4.29E-04	1.0	29000
302119	$Z' \to WW \to \ell\nu qq$, Model-A $g_V = 1$ $m = 800$ GeV	MadGraph 2.2.2 + Pythia 8.186	2.434E-04	1.0	30000
302120	$Z' \to WW \to \ell\nu qq$, Model-A $g_V = 1$ $m = 900$ GeV	MadGraph 2.2.2 + Pythia 8.186	1.474E-04	1.0	19000
302121	$Z' \to WW \to \ell\nu qq$, Model-A $g_V = 1$ $m = 1000$ GeV	MadGraph 2.2.2 + Pythia 8.186	9.314E-05	1.0	30000
302122	$Z' \to WW \to \ell\nu qq$, Model-A $g_V = 1$ $m = 1100$ GeV	MadGraph 2.2.2 + Pythia 8.186	6.114E-05	1.0	25000
302123	$Z' \to WW \to \ell\nu qq$, Model-A $g_V = 1$ $m = 1200$ GeV	MadGraph 2.2.2 + Pythia 8.186	4.13E-05	1.0	30000
302124	$Z' \to WW \to \ell\nu qq$, Model-A $g_V = 1$ $m = 1300$ GeV	MadGraph 2.2.2 + Pythia 8.186	2.859E-05	1.0	28000
302125	$Z' \to WW \to \ell\nu qq$, Model-A $g_V = 1$ $m = 1400$ GeV	MadGraph 2.2.2 + Pythia 8.186	2.023E-05	1.0	29000
302126	$Z' \to WW \to \ell\nu qq$, Model-A $g_V = 1$ $m = 1500$ GeV	MadGraph 2.2.2 + Pythia 8.186	1.449E-05	1.0	15000
302127	$Z' \to WW \to \ell\nu qq$, Model-A $g_V = 1$ $m = 1600$ GeV	MadGraph 2.2.2 + Pythia 8.186	1.052E-05	1.0	29000
302128	$Z' \to WW \to \ell\nu qq$, Model-A $g_V = 1$ $m = 1700$ GeV	MadGraph 2.2.2 + Pythia 8.186	7.784E-06	1.0	24000
302129	$Z' \to WW \to \ell\nu qq$, Model-A $g_V = 1$ $m = 1800$ GeV	MadGraph 2.2.2 + Pythia 8.186	5.816E-06	1.0	10000
302130	$Z' \to WW \to \ell\nu qq$, Model-A $g_V = 1$ $m = 1900$ GeV	MadGraph 2.2.2 + Pythia 8.186	4.38E-06	1.0	30000
302131	$Z' \to WW \to \ell\nu qq$, Model-A $g_V = 1$ $m = 2000$ GeV	MadGraph 2.2.2 + Pythia 8.186	3.328E-06	1.0	24000
302132	$Z' \to WW \to \ell\nu qq$, Model-A $g_V = 1$ $m = 2200$ GeV	MadGraph 2.2.2 + Pythia 8.186	1.971E-06	1.0	24000
302133	$Z' \to WW \to \ell\nu qq$, Model-A $g_V = 1$ $m = 2400$ GeV	MadGraph 2.2.2 + Pythia 8.186	1.193E-06	1.0	30000
302134	$Z' \to WW \to \ell\nu qq$, Model-A $g_V = 1$ $m = 2600$ GeV	MadGraph 2.2.2 + Pythia 8.186	7.374E-07	1.0	29000
302135	$Z' \to WW \to \ell\nu qq$, Model-A $g_V = 1$ $m = 2800$ GeV	MadGraph 2.2.2 + Pythia 8.186	4.6252E-07	1.0	23000
302136	$Z' \to WW \to \ell\nu qq$, Model-A $g_V = 1$ $m = 3000$ GeV	MadGraph 2.2.2 + Pythia 8.186	2.949E-07	1.0	30000
302137	$Z' \to WW \to \ell\nu qq$, Model-A $g_V = 1$ $m = 3500$ GeV	MadGraph 2.2.2 + Pythia 8.186	9.894E-08	1.0	30000
302138	$Z' \to WW \to \ell\nu qq$, Model-A $g_V = 1$ $m = 4000$ GeV	MadGraph 2.2.2 + Pythia 8.186	3.45E-08	1.0	25000
302139	$Z' \to WW \to \ell\nu qq$, Model-A $g_V = 1$ $m = 4500$ GeV	MadGraph 2.2.2 + Pythia 8.186	1.224E-08	1.0	30000
302140	$Z' \to WW \to \ell\nu qq$, Model-A $g_V = 1$ $m = 5000$ GeV	MadGraph 2.2.2 + Pythia 8.186	4.383E-08	1.0	30000

Table A.11.: HVT WZ samples used in the analysis with Model A and $g_V = 1$. The dataset ID, MC generator, production cross section, filter efficiency and total number of generated events are shown.

DS ID	Process	Generator	$\sigma \times$ BR [nb]	ϵ_{filter}	Events
307374	$W' \to WZ \to \ell\nu qq$, Model-A $g_V = 1$ $m = 300$ GeV	MadGraph 2.2.2 + Pythia 8.186	3.172E-02	1.0	30000
307375	$W' \to WZ \to \ell\nu qq$, Model-A $g_V = 1$ $m = 400$ GeV	MadGraph 2.2.2 + Pythia 8.186	7.262E-03	1.0	29000
302191	$W' \to WZ \to \ell\nu qq$, Model-A $g_V = 1$ $m = 500$ GeV	MadGraph 2.2.2 + Pythia 8.186	1.891E-03	1.0	30000
302192	$W' \to WZ \to \ell\nu qq$, Model-A $g_V = 1$ $m = 600$ GeV	MadGraph 2.2.2 + Pythia 8.186	8.808E-04	1.0	25000
302193	$W' \to WZ \to \ell\nu qq$, Model-A $g_V = 1$ $m = 700$ GeV	MadGraph 2.2.2 + Pythia 8.186	4.614E-04	1.0	10000
302194	$W' \to WZ \to \ell\nu qq$, Model-A $g_V = 1$ $m = 800$ GeV	MadGraph 2.2.2 + Pythia 8.186	2.627E-04	1.0	30000
302195	$W' \to WZ \to \ell\nu qq$, Model-A $g_V = 1$ $m = 900$ GeV	MadGraph 2.2.2 + Pythia 8.186	1.594E-04	1.0	25000
302196	$W' \to WZ \to \ell\nu qq$, Model-A $g_V = 1$ $m = 1000$ GeV	MadGraph 2.2.2 + Pythia 8.186	1.008E-04	1.0	29000
302197	$W' \to WZ \to \ell\nu qq$, Model-A $g_V = 1$ $m = 1100$ GeV	MadGraph 2.2.2 + Pythia 8.186	6.645E-05	1.0	30000
302198	$W' \to WZ \to \ell\nu qq$, Model-A $g_V = 1$ $m = 1200$ GeV	MadGraph 2.2.2 + Pythia 8.186	4.499E-05	1.0	30000
302199	$W' \to WZ \to \ell\nu qq$, Model-A $g_V = 1$ $m = 1300$ GeV	MadGraph 2.2.2 + Pythia 8.186	3.119E-05	1.0	29000
302200	$W' \to WZ \to \ell\nu qq$, Model-A $g_V = 1$ $m = 1400$ GeV	MadGraph 2.2.2 + Pythia 8.186	2.216E-05	1.0	29000
302201	$W' \to WZ \to \ell\nu qq$, Model-A $g_V = 1$ $m = 1500$ GeV	MadGraph 2.2.2 + Pythia 8.186	1.60E-05	1.0	30000
302202	$W' \to WZ \to \ell\nu qq$, Model-A $g_V = 1$ $m = 1600$ GeV	MadGraph 2.2.2 + Pythia 8.186	1.172E-05	1.0	30000
302203	$W' \to WZ \to \ell\nu qq$, Model-A $g_V = 1$ $m = 1700$ GeV	MadGraph 2.2.2 + Pythia 8.186	8.66E-06	1.0	25000
302204	$W' \to WZ \to \ell\nu qq$, Model-A $g_V = 1$ $m = 1800$ GeV	MadGraph 2.2.2 + Pythia 8.186	6.494E-06	1.0	30000
302205	$W' \to WZ \to \ell\nu qq$, Model-A $g_V = 1$ $m = 1900$ GeV	MadGraph 2.2.2 + Pythia 8.186	4.905E-06	1.0	20000
302206	$W' \to WZ \to \ell\nu qq$, Model-A $g_V = 1$ $m = 2000$ GeV	MadGraph 2.2.2 + Pythia 8.186	3.748E-06	1.0	20000
302207	$W' \to WZ \to \ell\nu qq$, Model-A $g_V = 1$ $m = 2200$ GeV	MadGraph 2.2.2 + Pythia 8.186	2.225E-06	1.0	20000
302208	$W' \to WZ \to \ell\nu qq$, Model-A $g_V = 1$ $m = 2400$ GeV	MadGraph 2.2.2 + Pythia 8.186	1.353E-06	1.0	30000
302209	$W' \to WZ \to \ell\nu qq$, Model-A $g_V = 1$ $m = 2600$ GeV	MadGraph 2.2.2 + Pythia 8.186	8.401E-07	1.0	30000
302210	$W' \to WZ \to \ell\nu qq$, Model-A $g_V = 1$ $m = 2800$ GeV	MadGraph 2.2.2 + Pythia 8.186	5.272E-07	1.0	30000
302211	$W' \to WZ \to \ell\nu qq$, Model-A $g_V = 1$ $m = 3000$ GeV	MadGraph 2.2.2 + Pythia 8.186	3.349E-07	1.0	27000
302212	$W' \to WZ \to \ell\nu qq$, Model-A $g_V = 1$ $m = 3500$ GeV	MadGraph 2.2.2 + Pythia 8.186	1.126E-07	1.0	30000
302213	$W' \to WZ \to \ell\nu qq$, Model-A $g_V = 1$ $m = 4000$ GeV	MadGraph 2.2.2 + Pythia 8.186	3.908E-08	1.0	30000
302214	$W' \to WZ \to \ell\nu qq$, Model-A $g_V = 1$ $m = 4500$ GeV	MadGraph 2.2.2 + Pythia 8.186	1.378E-08	1.0	15000
302215	$W' \to WZ \to \ell\nu qq$, Model-A $g_V = 1$ $m = 5000$ GeV	MadGraph 2.2.2 + Pythia 8.186	4.883E-09	1.0	30000

Table A.12.: VBF HVT WW samples used in the analysis with Model A and $g_V = 1$. The dataset ID, MC generator, production cross section, filter efficiency and total number of generated events are shown.

307563	$q\bar{q} \to Z' (\to WW \to \ell\nu qq)\, jj$, Model-A $g_V = 1$ $m = 300$ GeV	MadGraph 2.2.2 + Pythia 8.186	5.483e-05	1	1	48000
307564	$q\bar{q} \to Z' (\to WW \to \ell\nu qq)\, jj$, Model-A $g_V = 1$ $m = 400$ GeV	MadGraph 2.2.2 + Pythia 8.186	1.359e-05	1	1	47000
307565	$q\bar{q} \to Z' (\to WW \to \ell\nu qq)\, jj$, Model-A $g_V = 1$ $m = 500$ GeV	MadGraph 2.2.2 + Pythia 8.186	5.033e-06	1	1	50000
307566	$q\bar{q} \to Z' (\to WW \to \ell\nu qq)\, jj$, Model-A $g_V = 1$ $m = 600$ GeV	MadGraph 2.2.2 + Pythia 8.186	2.24e-06	1	1	49000
307567	$q\bar{q} \to Z' (\to WW \to \ell\nu qq)\, jj$, Model-A $g_V = 1$ $m = 700$ GeV	MadGraph 2.2.2 + Pythia 8.186	1.108e-06	1	1	50000
307568	$q\bar{q} \to Z' (\to WW \to \ell\nu qq)\, jj$, Model-A $g_V = 1$ $m = 800$ GeV	MadGraph 2.2.2 + Pythia 8.186	5.931e-07	1	1	48000
307569	$q\bar{q} \to Z' (\to WW \to \ell\nu qq)\, jj$, Model-A $g_V = 1$ $m = 900$ GeV	MadGraph 2.2.2 + Pythia 8.186	3.383e-07	1	1	48000
307570	$q\bar{q} \to Z' (\to WW \to \ell\nu qq)\, jj$, Model-A $g_V = 1$ $m = 1000$ GeV	MadGraph 2.2.2 + Pythia 8.186	2.027e-07	1	1	49000
307571	$q\bar{q} \to Z' (\to WW \to \ell\nu qq)\, jj$, Model-A $g_V = 1$ $m = 1100$ GeV	MadGraph 2.2.2 + Pythia 8.186	1.254e-07	1	1	50000
307572	$q\bar{q} \to Z' (\to WW \to \ell\nu qq)\, jj$, Model-A $g_V = 1$ $m = 1200$ GeV	MadGraph 2.2.2 + Pythia 8.186	7.984e-08	1	1	49000
307573	$q\bar{q} \to Z' (\to WW \to \ell\nu qq)\, jj$, Model-A $g_V = 1$ $m = 1300$ GeV	MadGraph 2.2.2 + Pythia 8.186	5.235e-08	1	1	50000
307574	$q\bar{q} \to Z' (\to WW \to \ell\nu qq)\, jj$, Model-A $g_V = 1$ $m = 1400$ GeV	MadGraph 2.2.2 + Pythia 8.186	3.489e-08	1	1	50000
307575	$q\bar{q} \to Z' (\to WW \to \ell\nu qq)\, jj$, Model-A $g_V = 1$ $m = 1500$ GeV	MadGraph 2.2.2 + Pythia 8.186	2.367e-08	1	1	47000
307576	$q\bar{q} \to Z' (\to WW \to \ell\nu qq)\, jj$, Model-A $g_V = 1$ $m = 1600$ GeV	MadGraph 2.2.2 + Pythia 8.186	1.642e-08	1	1	46000
307577	$q\bar{q} \to Z' (\to WW \to \ell\nu qq)\, jj$, Model-A $g_V = 1$ $m = 1700$ GeV	MadGraph 2.2.2 + Pythia 8.186	1.145e-08	1	1	50000
307578	$q\bar{q} \to Z' (\to WW \to \ell\nu qq)\, jj$, Model-A $g_V = 1$ $m = 1800$ GeV	MadGraph 2.2.2 + Pythia 8.186	8.099e-09	1	1	49000
307579	$q\bar{q} \to Z' (\to WW \to \ell\nu qq)\, jj$, Model-A $g_V = 1$ $m = 1900$ GeV	MadGraph 2.2.2 + Pythia 8.186	5.788e-09	1	1	50000
307580	$q\bar{q} \to Z' (\to WW \to \ell\nu qq)\, jj$, Model-A $g_V = 1$ $m = 2000$ GeV	MadGraph 2.2.2 + Pythia 8.186	4.168e-09	1	1	48000
307581	$q\bar{q} \to Z' (\to WW \to \ell\nu qq)\, jj$, Model-A $g_V = 1$ $m = 2200$ GeV	MadGraph 2.2.2 + Pythia 8.186	2.236e-09	1	1	47000
307582	$q\bar{q} \to Z' (\to WW \to \ell\nu qq)\, jj$, Model-A $g_V = 1$ $m = 2400$ GeV	MadGraph 2.2.2 + Pythia 8.186	1.221e-09	1	1	50000
307583	$q\bar{q} \to Z' (\to WW \to \ell\nu qq)\, jj$, Model-A $g_V = 1$ $m = 2600$ GeV	MadGraph 2.2.2 + Pythia 8.186	6.887e-10	1	1	50000
307584	$q\bar{q} \to Z' (\to WW \to \ell\nu qq)\, jj$, Model-A $g_V = 1$ $m = 2800$ GeV	MadGraph 2.2.2 + Pythia 8.186	3.929e-10	1	1	49000
307585	$q\bar{q} \to Z' (\to WW \to \ell\nu qq)\, jj$, Model-A $g_V = 1$ $m = 3000$ GeV	MadGraph 2.2.2 + Pythia 8.186	2.283e-10	1	1	50000
307586	$q\bar{q} \to Z' (\to WW \to \ell\nu qq)\, jj$, Model-A $g_V = 1$ $m = 3500$ GeV	MadGraph 2.2.2 + Pythia 8.186	6.143e-11	1	1	49000
307587	$q\bar{q} \to Z' (\to WW \to \ell\nu qq)\, jj$, Model-A $g_V = 1$ $m = 4000$ GeV	MadGraph 2.2.2 + Pythia 8.186	1.739e-11	1	1	49000

Table A.13.: VBF HVT WZ samples used in the analysis with Model A and $g_V = 1$. The dataset ID, MC generator, production cross section, filter efficiency and total number of generated events are shown.

DS ID	Process	Generator	$\sigma \times$ BR [nb]	ϵ_{filter}	Events	
307647	$q\bar{q} \to W' (\to WZ \to \ell\nu qq)\, jj$, Model-A $g_V = 1$ $m = 300$ GeV	MadGraph 2.2.2 + Pythia 8.186	5.4802e-05	1	1	50000
307648	$q\bar{q} \to W' (\to WZ \to \ell\nu qq)\, jj$, Model-A $g_V = 1$ $m = 400$ GeV	MadGraph 2.2.2 + Pythia 8.186	1.193e-05	1	1	50000
307649	$q\bar{q} \to W' (\to WZ \to \ell\nu qq)\, jj$, Model-A $g_V = 1$ $m = 500$ GeV	MadGraph 2.2.2 + Pythia 8.186	4.1372e-06	1	1	48000
307650	$q\bar{q} \to W' (\to WZ \to \ell\nu qq)\, jj$, Model-A $g_V = 1$ $m = 600$ GeV	MadGraph 2.2.2 + Pythia 8.186	1.789e-06	1	1	49000
307651	$q\bar{q} \to W' (\to WZ \to \ell\nu qq)\, jj$, Model-A $g_V = 1$ $m = 700$ GeV	MadGraph 2.2.2 + Pythia 8.186	8.642e-07	1	1	50000
307652	$q\bar{q} \to W' (\to WZ \to \ell\nu qq)\, jj$, Model-A $g_V = 1$ $m = 800$ GeV	MadGraph 2.2.2 + Pythia 8.186	4.5785e-07	1	1	47000
307653	$q\bar{q} \to W' (\to WZ \to \ell\nu qq)\, jj$, Model-A $g_V = 1$ $m = 900$ GeV	MadGraph 2.2.2 + Pythia 8.186	2.591e-07	1	1	47000
307654	$q\bar{q} \to W' (\to WZ \to \ell\nu qq)\, jj$, Model-A $g_V = 1$ $m = 1000$ GeV	MadGraph 2.2.2 + Pythia 8.186	1.543e-07	1	1	50000
307655	$q\bar{q} \to W' (\to WZ \to \ell\nu qq)\, jj$, Model-A $g_V = 1$ $m = 1100$ GeV	MadGraph 2.2.2 + Pythia 8.186	9.479e-08	1	1	47000
307656	$q\bar{q} \to W' (\to WZ \to \ell\nu qq)\, jj$, Model-A $g_V = 1$ $m = 1200$ GeV	MadGraph 2.2.2 + Pythia 8.186	6.071e-08	1	1	50000
307657	$q\bar{q} \to W' (\to WZ \to \ell\nu qq)\, jj$, Model-A $g_V = 1$ $m = 1300$ GeV	MadGraph 2.2.2 + Pythia 8.186	3.939e-08	1	1	47000
307658	$q\bar{q} \to W' (\to WZ \to \ell\nu qq)\, jj$, Model-A $g_V = 1$ $m = 1400$ GeV	MadGraph 2.2.2 + Pythia 8.186	2.628e-08	1	1	48000
307659	$q\bar{q} \to W' (\to WZ \to \ell\nu qq)\, jj$, Model-A $g_V = 1$ $m = 1500$ GeV	MadGraph 2.2.2 + Pythia 8.186	1.8e-08	1	1	50000
307660	$q\bar{q} \to W' (\to WZ \to \ell\nu qq)\, jj$, Model-A $g_V = 1$ $m = 1600$ GeV	MadGraph 2.2.2 + Pythia 8.186	1.251e-08	1	1	50000
307661	$q\bar{q} \to W' (\to WZ \to \ell\nu qq)\, jj$, Model-A $g_V = 1$ $m = 1700$ GeV	MadGraph 2.2.2 + Pythia 8.186	8.723e-09	1	1	49000
307662	$q\bar{q} \to W' (\to WZ \to \ell\nu qq)\, jj$, Model-A $g_V = 1$ $m = 1800$ GeV	MadGraph 2.2.2 + Pythia 8.186	6.2035e-09	1	1	48000
307663	$q\bar{q} \to W' (\to WZ \to \ell\nu qq)\, jj$, Model-A $g_V = 1$ $m = 1900$ GeV	MadGraph 2.2.2 + Pythia 8.186	4.481e-09	1	1	48000
307664	$q\bar{q} \to W' (\to WZ \to \ell\nu qq)\, jj$, Model-A $g_V = 1$ $m = 2000$ GeV	MadGraph 2.2.2 + Pythia 8.186	3.222e-09	1	1	50000
307665	$q\bar{q} \to W' (\to WZ \to \ell\nu qq)\, jj$, Model-A $g_V = 1$ $m = 2200$ GeV	MadGraph 2.2.2 + Pythia 8.186	1.7372e-09	1	1	50000
307666	$q\bar{q} \to W' (\to WZ \to \ell\nu qq)\, jj$, Model-A $g_V = 1$ $m = 2400$ GeV	MadGraph 2.2.2 + Pythia 8.186	9.602e-10	1	1	48000
307667	$q\bar{q} \to W' (\to WZ \to \ell\nu qq)\, jj$, Model-A $g_V = 1$ $m = 2600$ GeV	MadGraph 2.2.2 + Pythia 8.186	5.446e-10	1	1	49000
307668	$q\bar{q} \to W' (\to WZ \to \ell\nu qq)\, jj$, Model-A $g_V = 1$ $m = 2800$ GeV	MadGraph 2.2.2 + Pythia 8.186	3.131e-10	1	1	49000
307669	$q\bar{q} \to W' (\to WZ \to \ell\nu qq)\, jj$, Model-A $g_V = 1$ $m = 3000$ GeV	MadGraph 2.2.2 + Pythia 8.186	1.8333e-10	1	1	50000
307670	$q\bar{q} \to W' (\to WZ \to \ell\nu qq)\, jj$, Model-A $g_V = 1$ $m = 3500$ GeV	MadGraph 2.2.2 + Pythia 8.186	5.009e-11	1	1	48000
307671	$q\bar{q} \to W' (\to WZ \to \ell\nu qq)\, jj$, Model-A $g_V = 1$ $m = 4000$ GeV	MadGraph 2.2.2 + Pythia 8.186	1.448e-11	1	1	48000

Table A.14.: NWA Higgs samples used in the analysis produced via gluon-gluon fusions. The dataset ID, MC generator, production cross section, filter efficiency and total number of generated events are shown. The cross sections are taken from AMI.

DS ID	Process	Generator	$\sigma \times$ BR [nb]	ϵ_{filter}	Events
341037	$gg \to H(300) \to WW \to \ell\nu qq$, $\Gamma_H = 0.4\,\%$	POWHEG+PYTHIA8	6.6460E-03	4.3692E-01	99600
341038	$gg \to H(400) \to WW \to \ell\nu qq$, $\Gamma_H = 0.4\,\%$	POWHEG+PYTHIA8	6.3551E-03	4.3689E-01	99800
341039	$gg \to H(500) \to WW \to \ell\nu qq$, $\Gamma_H = 0.4\,\%$	POWHEG+PYTHIA8	3.0766E-03	4.3760E-01	99600
341040	$gg \to H(600) \to WW \to \ell\nu qq$, $\Gamma_H = 0.4\,\%$	POWHEG+PYTHIA8	1.3755E-03	4.3695E-01	100000
341041	$gg \to H(700) \to WW \to \ell\nu qq$, $\Gamma_H = 0.4\,\%$	POWHEG+PYTHIA8	6.4050E-04	4.3775E-01	99800
343467	$gg \to H(750) \to WW \to \ell\nu qq$, $\Gamma_H = 0.4\,\%$	POWHEG+PYTHIA8	4.4634E-04	4.3929E-01	98000
341042	$gg \to H(800) \to WW \to \ell\nu qq$, $\Gamma_H = 0.4\,\%$	POWHEG+PYTHIA8	3.1537E-04	4.3736E-01	99800
341043	$gg \to H(900) \to WW \to \ell\nu qq$, $\Gamma_H = 0.4\,\%$	POWHEG+PYTHIA8	1.6359E-04	4.3745E-01	100000
341044	$gg \to H(1000) \to WW \to \ell\nu qq$, $\Gamma_H = 0.4\,\%$	POWHEG+PYTHIA8	8.8946E-05	4.3938E-01	100000
343383	$gg \to H(1200) \to WW \to \ell\nu qq$, $\Gamma_H = 0.4\,\%$	POWHEG+PYTHIA8	2.6436E-05	4.3911E-01	99000
341045	$gg \to H(1400) \to WW \to \ell\nu qq$, $\Gamma_H = 0.4\,\%$	POWHEG+PYTHIA8	9.5454E-06	4.3602E-01	100000
343384	$gg \to H(1600) \to WW \to \ell\nu qq$, $\Gamma_H = 0.4\,\%$	POWHEG+PYTHIA8	3.7775E-06	4.3636E-01	97000
341046	$gg \to H(1800) \to WW \to \ell\nu qq$, $\Gamma_H = 0.4\,\%$	POWHEG+PYTHIA8	1.6065E-06	4.3956E-01	100000
343385	$gg \to H(2000) \to WW \to \ell\nu qq$, $\Gamma_H = 0.4\,\%$	POWHEG+PYTHIA8	7.0844E-07	4.3935E-01	98000
341047	$gg \to H(2200) \to WW \to \ell\nu qq$, $\Gamma_H = 0.4\,\%$	POWHEG+PYTHIA8	3.3466E-07	4.3695E-01	99600
343386	$gg \to H(2400) \to WW \to \ell\nu qq$, $\Gamma_H = 0.4\,\%$	POWHEG+PYTHIA8	1.6438E-07	4.3972E-01	99000
341048	$gg \to H(2600) \to WW \to \ell\nu qq$, $\Gamma_H = 0.4\,\%$	POWHEG+PYTHIA8	8.3436E-08	4.3865E-01	100000
343387	$gg \to H(2800) \to WW \to \ell\nu qq$, $\Gamma_H = 0.4\,\%$	POWHEG+PYTHIA8	4.3535E-08	4.3729E-01	97000
341049	$gg \to H(3000) \to WW \to \ell\nu qq$, $\Gamma_H = 0.4\,\%$	POWHEG+PYTHIA8	2.3253E-08	4.3755E-01	99600

Table A.15.: NWA Higgs samples used in the analysis produced via vector boson fusions. The dataset ID, MC generator, production cross section, filter efficiency and total number of generated events are shown. The cross sections are taken from AMI.

DS ID	Process	Generator	$\sigma \times$ BR [nb]	ϵ_{filter}	Events
341052	$q\bar{q} \to H(300)\,(\to WW \to \ell\nu qq)\,jj, \Gamma_H = 0.4\,\%$	POWHEG+PYTHIA8	1.2220E-03	4.3747E-01	49600
341053	$q\bar{q} \to H(400)\,(\to WW \to \ell\nu qq)\,jj, \Gamma_H = 0.4\,\%$	POWHEG+PYTHIA8	7.4059E-04	4.3614E-01	50000
341054	$q\bar{q} \to H(500)\,(\to WW \to \ell\nu qq)\,jj, \Gamma_H = 0.4\,\%$	POWHEG+PYTHIA8	4.7430E-04	4.3487E-01	49600
341055	$q\bar{q} \to H(600)\,(\to WW \to \ell\nu qq)\,jj, \Gamma_H = 0.4\,\%$	POWHEG+PYTHIA8	3.1797E-04	4.3939E-01	50000
341056	$q\bar{q} \to H(700)\,(\to WW \to \ell\nu qq)\,jj, \Gamma_H = 0.4\,\%$	POWHEG+PYTHIA8	2.2138E-04	4.3941E-01	50000
343468	$q\bar{q} \to H(750)\,(\to WW \to \ell\nu qq)\,jj, \Gamma_H = 0.4\,\%$	POWHEG+PYTHIA8	1.8241E-04	4.3726E-01	49000
341057	$q\bar{q} \to H(800)\,(\to WW \to \ell\nu qq)\,jj, \Gamma_H = 0.4\,\%$	POWHEG+PYTHIA8	1.5801E-04	4.3856E-01	50000
341058	$q\bar{q} \to H(900)\,(\to WW \to \ell\nu qq)\,jj, \Gamma_H = 0.4\,\%$	POWHEG+PYTHIA8	1.1456E-04	4.4044E-01	49800
341059	$q\bar{q} \to H(1000\,() \to WW \to \ell\nu qq)\,jj, \Gamma_H = 0.4\,\%$	POWHEG+PYTHIA8	8.7286E-05	4.3650E-01	49800
343378	$q\bar{q} \to H(1200\,() \to WW \to \ell\nu qq)\,jj, \Gamma_H = 0.4\,\%$	POWHEG+PYTHIA8	4.8397E-05	4.3868E-01	50000
341060	$q\bar{q} \to H(1400\,() \to WW \to \ell\nu qq)\,jj, \Gamma_H = 0.4\,\%$	POWHEG+PYTHIA8	2.8654E-05	4.3795E-01	49800
343379	$q\bar{q} \to H(1600\,() \to WW \to \ell\nu qq)\,jj, \Gamma_H = 0.4\,\%$	POWHEG+PYTHIA8	1.6978E-05	4.4139E-01	50000
341070	$q\bar{q} \to H(1800\,() \to WW \to \ell\nu qq)\,jj, \Gamma_H = 0.4\,\%$	POWHEG+PYTHIA8	1.0408E-05	4.3987E-01	50000
343380	$q\bar{q} \to H(2000\,() \to WW \to \ell\nu qq)\,jj, \Gamma_H = 0.4\,\%$	POWHEG+PYTHIA8	6.7688E-06	4.3715E-01	50000
341071	$q\bar{q} \to H(2200\,() \to WW \to \ell\nu qq)\,jj, \Gamma_H = 0.4\,\%$	POWHEG+PYTHIA8	4.2676E-06	4.3674E-01	50000
343381	$q\bar{q} \to H(2400\,() \to WW \to \ell\nu qq)\,jj, \Gamma_H = 0.4\,\%$	POWHEG+PYTHIA8	2.6168E-06	4.4344E-01	45000
341072	$q\bar{q} \to H(2600\,() \to WW \to \ell\nu qq)\,jj, \Gamma_H = 0.4\,\%$	POWHEG+PYTHIA8	2.3456E-06	4.4122E-01	49800
343382	$q\bar{q} \to H(2800\,() \to WW \to \ell\nu qq)\,jj, \Gamma_H = 0.4\,\%$	POWHEG+PYTHIA8	1.2244E-06	4.3845E-01	48000
341073	$q\bar{q} \to H(3000\,() \to WW \to \ell\nu qq)\,jj, \Gamma_H = 0.4\,\%$	POWHEG+PYTHIA8	8.1174E-07	4.3501E-01	50000

A.3. Signal Samples for non-Resonance Search

Here is the list presenting samples which are taken as signal for the non-resonance search for the VBS signal.

Table A.16.: List of VBS samples used in the analysis.

Process	DSID	Events	Filter efficiency	cross-section (pb)
$W\ell\nu Zqqjj$	364428	487000	1.0	2.3639e-01
$W\ell\nu Wqqjj$	364429	488000	1.0	1.7547e+00

Appendix B.

Run 3 L1Calo E_T^{miss} Trigger Optimization

The E_T^{miss} trigger was optimized by scanning through possible E_T cuts of LAr, tile, and forward jTowers. The scan was performed by the steps of 0.5σ ranged from 0 to 6σ for LAr and tile jTowers, while the forward towers have threshold higher than LAr tower one ranged from 0 to 2.5σ. The result is shown in Fig. B.1.

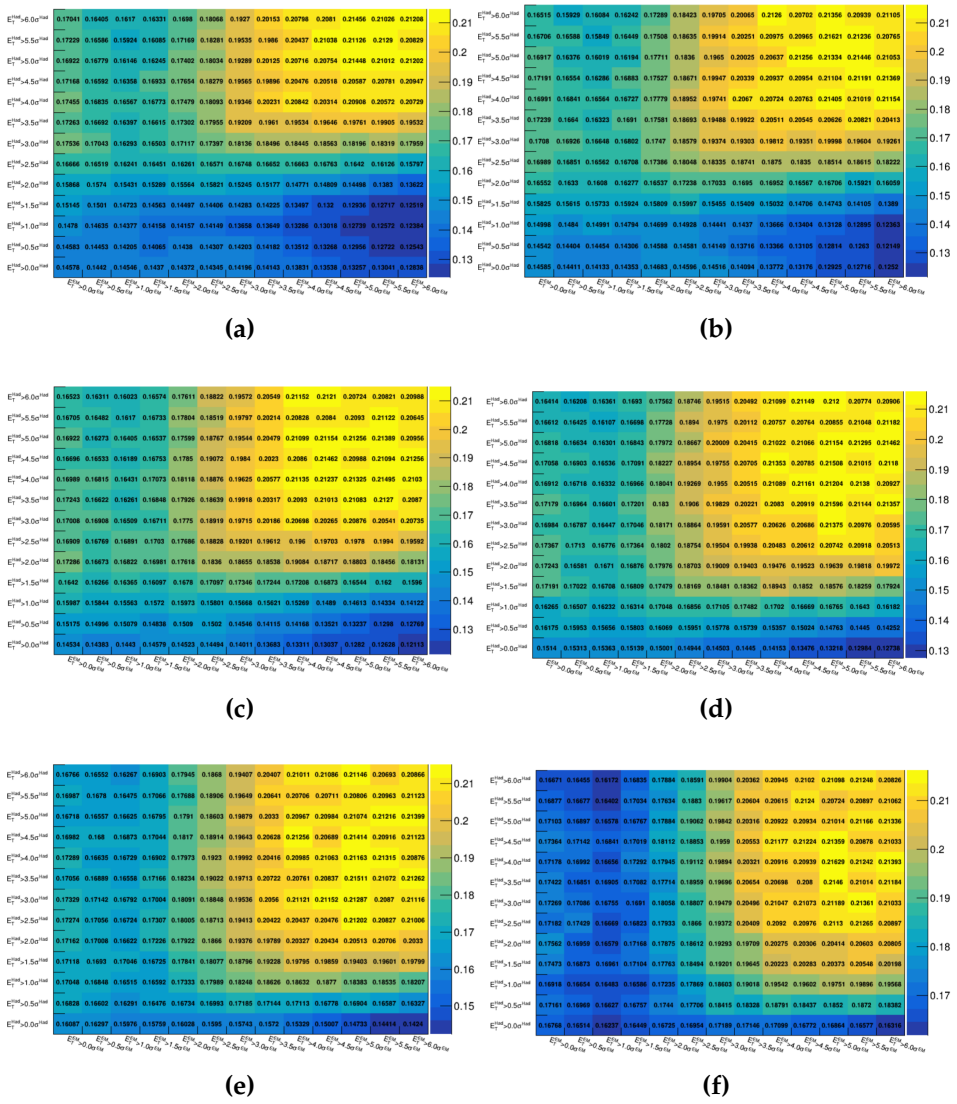

Figure B.1.: The E_T^{miss} trigger signal efficiency with different thresholds on jTowers, when the trigger rate is 5 kHz. The six figures presents different threshold in the forward region: (a) 0σ, (b) 0.5σ, (c) 1.0σ, (d) 1.5σ, (e) 2.0σ, and (f) 2.5σ higher than the LAr jTower E_T thresholds

Appendix C.

Supercells in the ATLAS Forward Region

Here shows the supercell layouts in the forward region. They are in irregular shapes, so the supercell to j/gTower mapping has a complicated scheme.

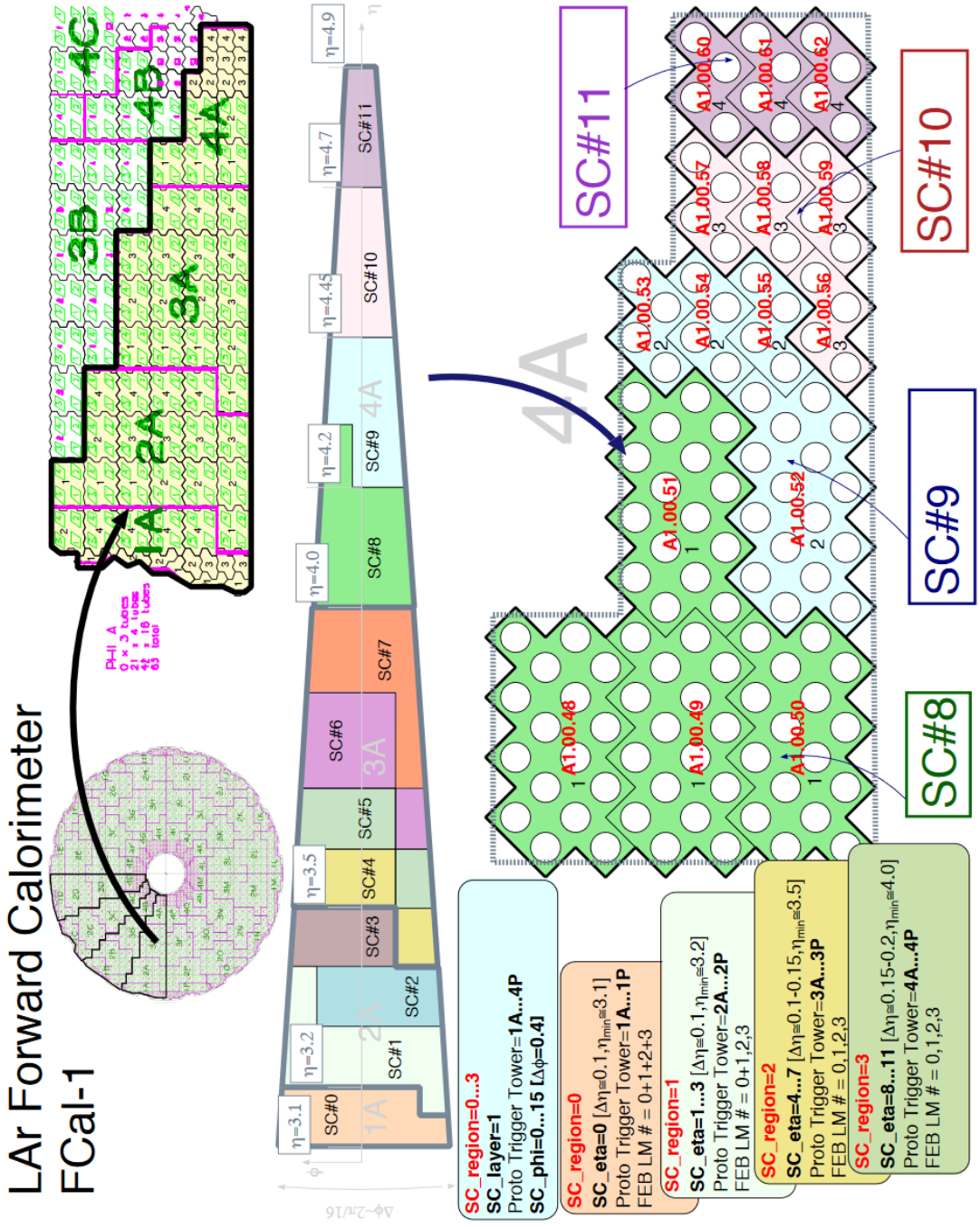

Figure C.1.: The front layer of the forward LAr detector

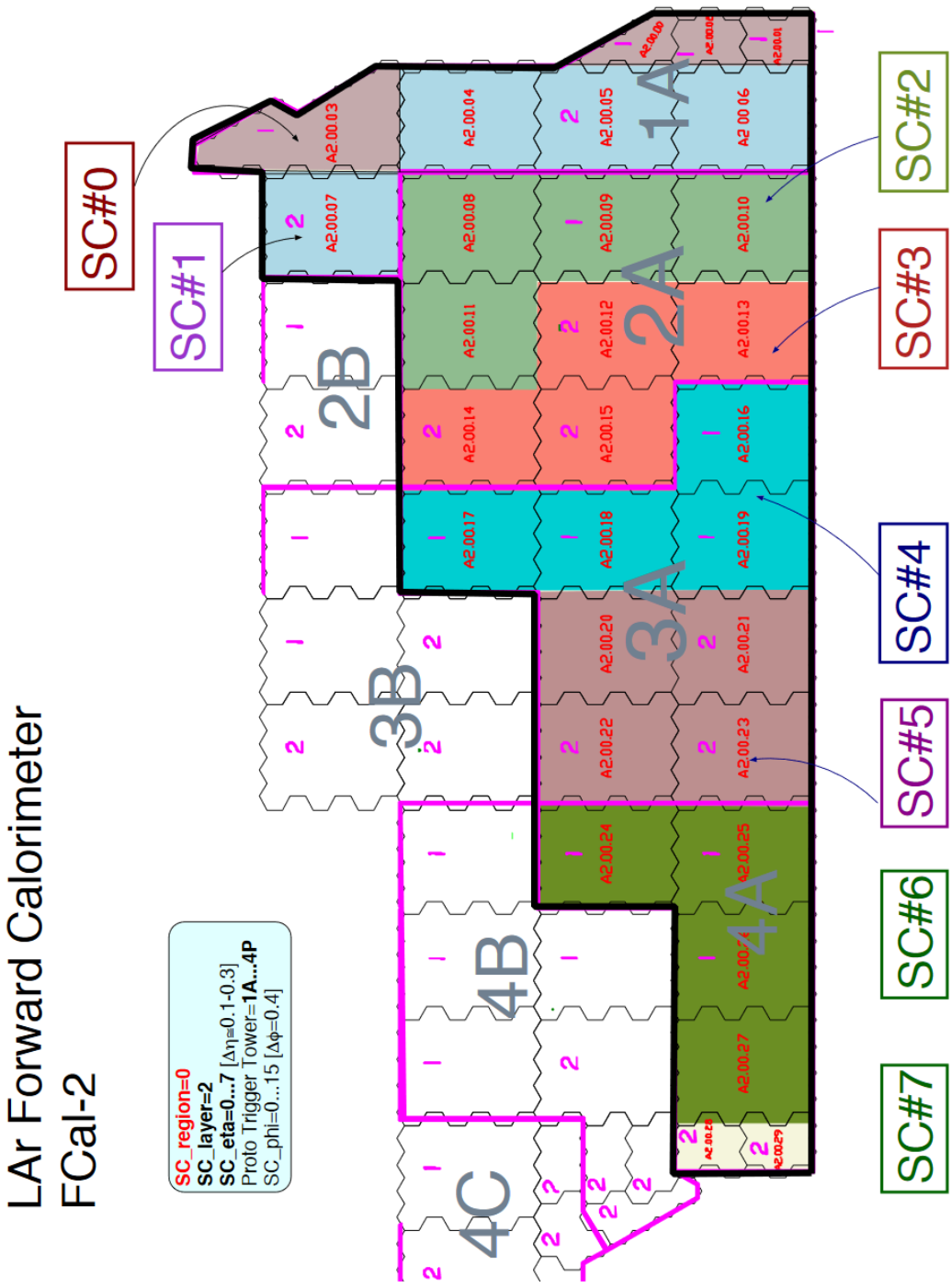

Figure C.2.: The middle layer of the forward LAr detector

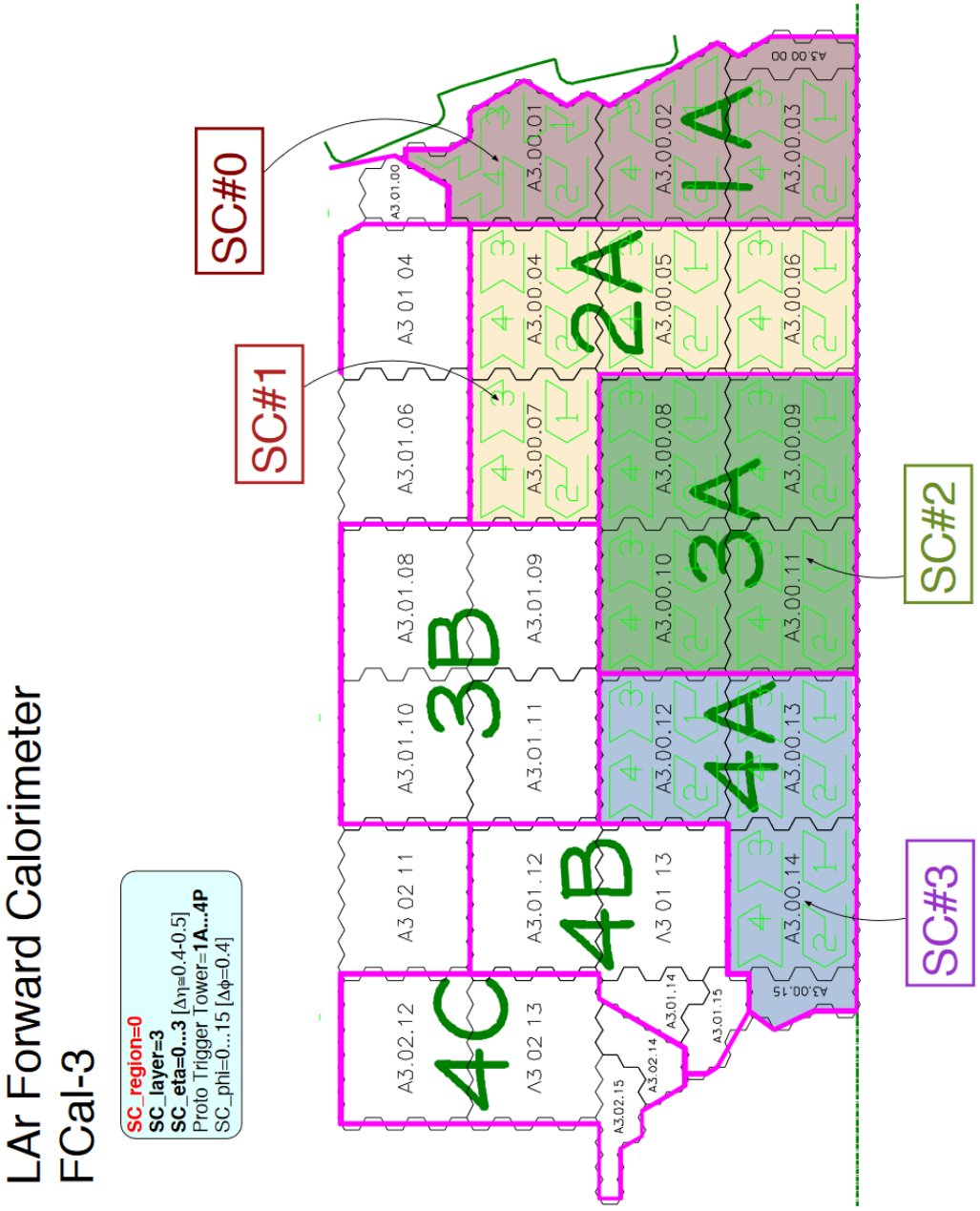

Figure C.3.: The back layer of the forward LAr detector

Colophon

This thesis was made in LaTeX 2_ε using the "hepthesis" class [133].

Bibliography

[1] ATLAS Collaboration, "Observation of a new particle in the search for the Standard Model Higgs boson with the ATLAS detector at the LHC," *Phys. Lett. B* **716** (2012) 1, arXiv:1207.7214 [hep-ex].

[2] CMS Collaboration, "Observation of a new boson at a mass of 125 GeV with the CMS experiment at the LHC," *Phys. Lett. B* **716** (2012) 30, arXiv:1207.7235 [hep-ex].

[3] D. Griffiths, *Introduction to elementary particles; 2nd rev. version*. 2008.

[4] D. Perkins, *Introduction to high energy physics*. 1982.

[5] T. Rias, "Quark weak interactions.svg." https://en.wikipedia.org/wiki/Cabibbo%E2%80%93Kobayashi%E2%80%93Maskawa_matrix#/media/File:Quark_weak_interactions.svg, 2009.

[6] Particle Data Group, "Elementary particles included in the standard model,".

[7] F. Englert, R. Brout, "Broken symmetry and the mass of gauge vector mesons," *Physical Review Letters* (1964) .

[8] P. Higgs, "Broken symmetries and the masses of gauge bosons," *Physical Review Letters* (1964) .

[9] T. K. G. Guralnik, C.R. Hagen, "Global conservation laws and massless particles," *Physical Review Letters* (1964) .

[10] P. Williams, "Naturalness, the autonomy of scales, and the 125gev higgs," *Studies in History and Philosophy of Science Part B: Studies in History and Philosophy of Modern Physics* (2015) .

[11] B. Allanach, "Beyond the standard model lectures," arXiv:1609.02015 [hep-ph].

[12] Super-Kamiokande Collaboration, "Measurements of the solar neutrino flux from Super-Kamiokande's first 300 days," *Phys. Rev. Lett.* **81** (1998) 1158–1162, arXiv:hep-ex/9805021 [hep-ex]. [Erratum: Phys. Rev. Lett.81,4279(1998)].

[13] O. S. Brüning, P. Collier, P. Lebrun, S. Myers, R. Ostojic, J. Poole, and P. Proudlock, *LHC Design Report*. CERN Yellow Reports: Monographs. CERN, Geneva, 2004. http://cds.cern.ch/record/782076.

[14] CERN, "Cern control centre animations 01 "the proton source"." https://videos.cern.ch/record/1750714.

[15] E. Mobs, "The CERN accelerator complex. Complexe des accélérateurs du CERN,". https://cds.cern.ch/record/2197559. General Photo.

[16] CERN, "Radiofrequency cavities,". https://cds.cern.ch/record/1997424.

[17] S. Baird, "Accelerators for pedestrians; rev. version," tech. rep., CERN, Geneva, 2007. http://cds.cern.ch/record/1017689.

[18] ALICE Collaboration, "ALICE Technical Design Report." Cern/lhcc-2001-021, 03 October 2001.

[19] ATLAS Collaboration, "ATLAS Physics TDR: Volume I, Overview, System and Combined Performance," 2 August 1999.

[20] CMS Collaboration, "CMS Physics TDR: Volume I (PTDR1), Detector Performance and Software," 2 February 2006.

[21] LHCb Collaboration, "LHCb: Technical Proposal." Cern-lhcc-98-004, 13 September 2011.

[22] ATLAS Collaboration, "The ATLAS Experiment at the CERN Large Hadron Collider," *JINST* **3** (2008) S08003.

[23] JabberWok, "Pseudorapidity2.png." https://en.wikipedia.org/wiki/Pseudorapidity#/media/File:Pseudorapidity2.png.

[24] ATLAS Collaboration, *ATLAS inner detector: Technical Design Report, 1*. Technical Design Report ATLAS. CERN, Geneva, 1997. https://cds.cern.ch/record/331063.

[25] ATLAS Collaboration, "Performance of the ATLAS track reconstruction

algorithms in dense environments in LHC Run 2," *Eur. Phys. J. C* **77** (2017) 673, arXiv:1704.07983 [hep-ex].

[26] ATLAS Collaboration, "Technical Design Report for the ATLAS Inner Tracker Pixel Detector," Tech. Rep. CERN-LHCC-2017-021. ATLAS-TDR-030, CERN, Geneva, Sep, 2017. https://cds.cern.ch/record/2285585.

[27] A. Miucci, "The ATLAS insertable b-layer project," *Journal of Instrumentation* **9** no. 02, (Feb, 2014) C02018–C02018. https://doi.org/10.1088%2F1748-0221%2F9%2F02%2Fc02018.

[28] B. Mindur, "ATLAS Transition Radiation Tracker (TRT): Straw tubes for tracking and particle identification at the Large Hadron Collider," Tech. Rep. ATL-INDET-PROC-2016-001, CERN, Geneva, Mar, 2016. https://cds.cern.ch/record/2139567.

[29] Thomas Schörner-Sadenius et al., *The Large Hadron Collider:Harvest of Run 1*. 2015.

[30] M. Aleksa, F. Bergsma, P. A. Giudici, A. Kehrli, M. Losasso, X. Pons, H. Sandaker, P. S. Miyagawa, S. W. Snow, J. C. Hart, and L. Chevalier, "Measurement of the ATLAS solenoid magnetic field," *Journal of Instrumentation* **3** no. 04, (Apr, 2008) P04003–P04003. https://doi.org/10.1088%2F1748-0221%2F3%2F04%2Fp04003.

[31] ATLAS Collaboration, "ATLAS liquid argon calorimeter: Technical design report,". https://cds.cern.ch/record/331061.

[32] P. Iengo, "The ATLAS Calorimeters,". http://people.na.infn.it/~elly/TesiAtlas/SeminariAtlas/Detector/IengoAtlasCalo.pdf.

[33] A. Artamonov, D. Bailey, G. Belanger, M. Cadabeschi, T. Y. Chen, V. Epshteyn, P. Gorbounov, K. K. Joo, M. Khakzad, V. Khovanskiy, P. Krieger, P. Loch, J. Mayer, E. Neuheimer, F. G. Oakham, M. O. Neill, R. S. Orr, M. Qi, J. Rutherfoord, A. Savine, M. Schram, P. Shatalov, L. Shaver, M. Shupe, G. Stairs, V. Strickland, D. Tompkins, I. Tsukerman, and K. Vincent, "The ATLAS forward calorimeter," *Journal of Instrumentation* **3** no. 02, (Feb, 2008) P02010–P02010. https://doi.org/10.1088%2F1748-0221%2F3%2F02%2Fp02010.

[34] J. Snuverink, "The atlas muon spectrometer:commissioning and tracking," 2009.

[35] ATLAS Collaboration, "ATLAS trigger system meets the challenges of Run 2,". https://ep-news.web.cern.ch/content/atlas-trigger-system-meets-challenges-run-2.

[36] M. Bruschi, "The new ATLAS/LUCID detector," Tech. Rep. ATL-FWD-PROC-2015-002, CERN, Geneva, Jun, 2015. https://cds.cern.ch/record/2025000.

[37] L. Pontecorvo, "Status of the Experiment: Detector and Phase-II," Tech. Rep. CERN-RRB-2018-075, CERN, Geneva, Sep, 2018. https://cds.cern.ch/record/2638061.

[38] A. Collaboration, "Performance of the ATLAS Track Reconstruction Algorithms in Dense Environments in LHC Run 2," *Eur. Phys. J.* **C77** no. 10, (2017) 673, arXiv:1704.07983 [hep-ex].

[39] ATLAS Collaboration, "Reconstruction of primary vertices at the ATLAS experiment in Run 1 proton–proton collisions at the LHC," *Eur. Phys. J.* **C77** no. 5, (2017) 332, arXiv:1611.10235 [physics.ins-det].

[40] ATLAS Collaboration, "Electron efficiency measurements with the ATLAS detector using the 2015 LHC proton–proton collision data." ATLAS-CONF-2016-024, 2016. https://cds.cern.ch/record/2157687.

[41] W. Lampl *et al.*, "Calorimeter Clustering Algorithms: Description and Performance." ATL-LARG-PUB-2008-002, 2008. https://cds.cern.ch/record/1099735.

[42] T. G. Cornelissen, M. Elsing, I. Gavrilenko, J. F. Laporte, W. Liebig, M. Limper, K. Nikolopoulos, A. Poppleton, and A. Salzburger, "The global chi**2 track fitter in ATLAS," *J. Phys. Conf. Ser.* **119** (2008) 032013.

[43] ATLAS Collaboration, "Improved electron reconstruction in ATLAS using the Gaussian Sum Filter-based model for bremsstrahlung." ATLAS-CONF-2012-047, 2012. https://cds.cern.ch/record/1449796.

[44] ATLAS Collaboration, "Electron identification measurements in ATLAS using $\sqrt{s} = 13$ TeV data with 50 ns bunch spacing." ATL-PHYS-PUB-2015-041, 2015. https://cds.cern.ch/record/2048202.

[45] H. Herde, "Muon reconstruction performance in ATLAS at Run-II," Tech. Rep.

ATL-PHYS-PROC-2015-121, CERN, Geneva, Oct, 2015. https://cds.cern.ch/record/2059849.

[46] R. Atkin, "Review of jet reconstruction algorithms," *J. Phys. Conf. Ser.* **645** no. 1, (2015) 012008.

[47] T. Barillari, E. Bergeaas Kuutmann, T. Carli, J. Erdmann, P. Giovannini, K. J. Grahn, C. Issever, A. Jantsch, A. Kiryunin, K. Lohwasser, A. Maslennikov, S. Menke, H. Oberlack, G. Pospelov, E. Rauter, P. Schacht, F. Spanó, P. Speckmayer, P. Stavina, and P. Strízenec, "Local Hadronic Calibration," Tech. Rep. ATL-LARG-PUB-2009-001-2, CERN, Geneva.

[48] ATLAS Collaboration, "Tagging and suppression of pileup jets with the ATLAS detector." ATLAS-CONF-2014-018, 2014. https://cds.cern.ch/record/1700870.

[49] ATLAS Collaboration, "Expected performance of the ATLAS *b*-tagging algorithms in Run-2." ATL-PHYS-PUB-2015-022, 2015. https://cds.cern.ch/record/2037697.

[50] T. Plehn, "LHC Phenomenology for Physics Hunters," in *Proceedings of Theoretical Advanced Study Institute in Elementary Particle Physics on The dawn of the LHC era (TASI 2008): Boulder, USA, June 2-27, 2008*, pp. 125–180. 2010. arXiv:0810.2281 [hep-ph].

[51] T. Sjostrand, "PYTHIA 8 Status Report," arXiv:0809.0303 [hep-ph].

[52] T. Sjostrand, S. Mrenna, and P. Z. Skands, "A Brief Introduction to PYTHIA 8.1" *Comput. Phys. Commun.* **178** (2008) 852–867, arXiv:0710.3820 [hep-ph].

[53] S. Agostinelli *et al.*, "GEANT4: A Simulation toolkit," *Nucl.Instrum.Meth.* **A506** (2003) 250–303.

[54] E. Fuchs, S. Thewes, G. Weiglein, "Interference effects in bsm processes with a generalised narrow-width approximation," arXiv:1411.4652 [hep-ph].

[55] D. Pappadopulo, A. Thamm, R. Torre, and A. Wulzer, "Heavy Vector Triplets: Bridging Theory and Data," arXiv:1402.4431 [hep-ph].

[56] J. de Blas, J.M. Lizana, M. Perez-Victoria, "Combining searches of Z' and W' bosons," *JHEP* **01** (2013) 166, arXiv:1211.2229 [hep-ph].

[57] L. Randall and R. Sundrum, "A large mass hierarchy from a small extra dimension," *Phys. Rev. Lett.* **83** (1999) 3370–3373, arXiv:hep-ph/9905221 [hep-ph].

[58] T. Gleisberg, S. Hoeche, F. Krauss, M. Schonherr, S. Schumann, F. Siegert, and J. Winter, "Event generation with SHERPA 1.1" *JHEP* **02** (2009) 007, arXiv:0811.4622 [hep-ph].

[59] R. D. Ball *et al.*, "Parton distributions with LHC data," *Nucl. Phys.* **B867** (2013) 244–289, arXiv:1207.1303 [hep-ph].

[60] S. Alioli, P. Nason, C. Oleari, and E. Re, "A general framework for implementing NLO calculations in shower Monte Carlo programs: the POWHEG BOX," *JHEP* **1006** (2010) 043, arXiv:1002.2581 [hep-ph].

[61] J. Gao, M. Guzzi, J. Huston, H.-L. Lai, Z. Li, *et al.*, "The CT10 NNLO Global Analysis of QCD," arXiv:1302.6246 [hep-ph].

[62] P. Artoisenet, R. Frederix, O. Mattelaer, and R. Rietkerk, "Automatic spin-entangled decays of heavy resonances in Monte Carlo simulations," *JHEP* **03** (2013) 015, arXiv:1212.3460 [hep-ph].

[63] ATLAS Collaboration, "Atlas tunes of pythia 6 and pythia 8 for mc11," *ATL-PHYS-PUB-2011-009* (2011) . https://cds.cern.ch/record/1363300.

[64] D. Stump, J. Huston, J. Pumplin, W.-K. Tung, H. L. Lai, S. Kuhlmann, and J. F. Owens, "Inclusive jet production, parton distributions, and the search for new physics," *JHEP* **10** (2003) 046, arXiv:hep-ph/0303013 [hep-ph].

[65] M. Czakon, P. Fiedler, and A. Mitov, "The total top quark pair production cross-section at hadron colliders through O($alpha_S^4$)," arXiv:1303.6254 [hep-ph].

[66] H.-L. Lai, M. Guzzi, J. Huston, Z. Li, P. M. Nadolsky, *et al.*, "New parton distributions for collider physics," *Phys.Rev.* **D82** (2010) 074024, arXiv:1007.2241 [hep-ph].

[67] N. Kidonakis, "Next-to-next-to-leading-order collinear and soft gluon corrections for t-channel single top quark production," *Phys. Rev.* **D83** (2011) 091503, arXiv:1103.2792 [hep-ph].

[68] N. Kidonakis, "Two-loop soft anomalous dimensions for single top quark

associated production with a W- or H-," *Phys. Rev.* **D82** (2010) 054018, arXiv:1005.4451 [hep-ph].

[69] J. Alwall, R. Frederix, S. Frixione, V. Hirschi, F. Maltoni, O. Mattelaer, H. S. Shao, T. Stelzer, P. Torrielli, and M. Zaro, "The automated computation of tree-level and next-to-leading order differential cross sections, and their matching to parton shower simulations," *JHEP* **07** (2014) 079, arXiv:1405.0301 [hep-ph].

[70] M. Borodin, K. De, J. G. Navarro, D. Golubkov, A. Klimentov, T. Maeno, D. South, and A. Vaniachine, "Unified System for Processing Real and Simulated Data in the ATLAS Experiment," 2015. arXiv:1508.07174 [cs.DC].

[71] ATLAS Collaboration, "Data-Quality Requirements and Event Cleaning for Jets and Missing Transverse Energy Reconstruction with the ATLAS Detector in Proton-Proton Collisions at a Center-of-Mass Energy of $\sqrt{s} = 7$ TeV,".

[72] ATLAS Collaboration, "Jet mass reconstruction with the ATLAS Detector in early Run 2 data," *ATLAS-CONF-2016-035* (2016) . https://cds.cern.ch/record/2200211.

[73] A. J. Larkoski, I. Moult, and D. Neill, "Power Counting to Better Jet Observables," *JHEP* **12** (2014) 009, arXiv:1409.6298 [hep-ph].

[74] ATLAS collaboration, "Performance of electron and photon triggers in ATLAS during LHC Run 2," arXiv:1909.00761 [hep-ex].

[75] ATLAS Collaboration, "Searches for heavy ZZ and ZW resonances in the $\ell\ell qq$ and $\nu\nu qq$ final states in pp collisions at $\sqrt{s} = 13$ TeV with the ATLAS detector," *JHEP* **03** (2018) 009, arXiv:1708.09638 [hep-ex].

[76] ATLAS Collaboration, "Search for WW/WZ resonance production in $\ell\nu qq$ final states in pp collisions at $\sqrt{s} = 13$ TeV with the ATLAS detector," *JHEP* **03** (2018) 042, arXiv:1710.07235 [hep-ex].

[77] ATLAS Collaboration, "Search for the Standard Model Higgs boson produced in association with a vector boson and decaying to a $b\bar{b}$ pair in pp collisions at 13 TeV using the ATLAS detector," *ATLAS-CONF-2016-091* (2016) . https://cds.cern.ch/record/2206813.

[78] ATLAS Collaboration, "Search for a Standard Model Higgs boson produced in association with a vector boson and decaying to a pair of b-quarks ."

ATL-COM-PHYS-2016-429, 2016. https://cds.cern.ch/record/2150252.

[79] G. Cowan, *Statistical Data Analysis*. 1998.

[80] ATLAS Collaboration, "Electron efficiency measurements with the ATLAS detector using 2012 LHC proton–proton collision data," *Eur. Phys. J. C* **77** (2017) 195, arXiv:1612.01456 [hep-ex].

[81] ATLAS Collaboration, "Muon reconstruction performance in early $\sqrt{s} = 13$ TeV data." ATL-PHYS-PUB-2015-037, 2015. https://cds.cern.ch/record/2047831.

[82] ATLAS Collaboration, "Jet energy scale measurements and their systematic uncertainties in proton–proton collisions at $\sqrt{s} = 13$ TeV with the ATLAS detector," *Phys. Rev. D* **96** (2017) 072002, arXiv:1703.09665 [hep-ex].

[83] J. Conway, "Nuisance parameters in likelihoods for searches," 2011. https://indico.cern.ch/event/107747/contributions/32677/attachments/24367/35056/Conway-PhyStat2011.pdf.

[84] F. James, *MINUIT Tutorial on Function Minimization*. 1972.

[85] L. Moneta, K. Belasco, K. S. Cranmer, S. Kreiss, A. Lazzaro, D. Piparo, G. Schott, W. Verkerke, and M. Wolf, "The RooStats Project," *PoS* **ACAT2010** (2010) 057, arXiv:1009.1003 [physics.data-an].

[86] G. Cowan, K. Cranmer, E. Gross, and O. Vitells, "Asymptotic formulae for likelihood-based tests of new physics," *Eur. Phys. J. C* **71** (2011) 1554.

[87] T. Amemiya, *"Advanced Econometrics"*. 1985.

[88] R. Davidson; J.G. MacKinnon, *"Concentrating the Loglikelihood Function"*. 1983.

[89] J. Neyman and E.S. Pearson, "IX. On the problem of the most efficient tests of statistical hypotheses," *Phil. Trans. R. Soc. Lond. A.* (1933) .

[90] R.L. Berger, G. Casella., *Statistical Inference, Duxbury Press, Second Edition*. 2001.

[91] ATLAS Collaboration, "Combination of searches for heavy resonances decaying into bosonic and leptonic final states using 36 fb^{-1} of proton-proton collision data at $\sqrt{s} = 13$ TeV with the ATLAS detector," *Phys. Rev.* **D98** no. 5, (2018) 052008, arXiv:1808.02380.

[92] ATLAS Collaboration, "Search for diboson resonances with boson-tagged jets in pp collisions at $\sqrt{s} = 13$ TeV with the ATLAS detector," *Phys. Lett. B* **777** (2018) 91, arXiv:1708.04445 [hep-ex].

[93] ATLAS Collaboration, "Search for heavy ZZ resonances in the $\ell^+\ell^-\ell^+\ell^-$ and $\ell^+\ell^-\nu\bar{\nu}$ final states using proton–proton collisions at $\sqrt{s} = 13$ TeV with the ATLAS detector," *Eur. Phys. J. C* **78** (2018) 293, arXiv:1712.06386 [hep-ex].

[94] ATLAS Collaboration, "Search for heavy resonances decaying into WW in the $e\nu\mu\nu$ final state in pp collisions at $\sqrt{s} = 13$ TeV with the ATLAS detector," *Eur. Phys. J. C* **78** (2018) 24, arXiv:1710.01123 [hep-ex].

[95] ATLAS Collaboration, "Search for resonant WZ production in the fully leptonic final state in proton–proton collisions at $\sqrt{s} = 13$ TeV with the ATLAS detector," *Phys. Lett. B* **787** (2018) 68, arXiv:1806.01532 [hep-ex].

[96] ATLAS Collaboration, "Search for heavy resonances decaying to a W or Z boson and a Higgs boson in the $q\bar{q}^{(\prime)}b\bar{b}$ final state in pp collisions at $\sqrt{s} = 13$ TeV with the ATLAS detector," *Phys. Lett. B* **774** (2017) 494, arXiv:1707.06958 [hep-ex].

[97] ATLAS Collaboration, "Search for heavy resonances decaying into a W or Z boson and a Higgs boson in final states with leptons and b-jets in 36 fb^{-1} of $\sqrt{s} = 13$ TeV pp collisions with the ATLAS detector," arXiv:1712.06518 [hep-ex].

[98] ATLAS Collaboration, "Search for a new heavy gauge boson resonance decaying into a lepton and missing transverse momentum in 36 fb^{-1} of pp collisions at $\sqrt{s} = 13$ TeV with the ATLAS experiment," arXiv:1706.04786 [hep-ex].

[99] ATLAS Collaboration, "Search for new high-mass phenomena in the dilepton final state using 36 fb^{-1} of proton–proton collision data at $\sqrt{s} = 13$ TeV with the ATLAS detector," *JHEP* **10** (2017) 182, arXiv:1707.02424 [hep-ex].

[100] F. del Aguila, J. de Blas, and M. Perez-Victoria, "Electroweak Limits on General New Vector Bosons," *JHEP* **09** (2010) 033, arXiv:1005.3998 [hep-ph].

[101] ALEPH, DELPHI, L3, OPAL, LEP Electroweak Working Group, "Electroweak Measurements in Electron-Positron Collisions at W-Boson-Pair Energies at LEP," *Phys. Rept.* **532** (2013) 119–244, arXiv:1302.3415 [hep-ex].

[102] K. Olive, "Review of particle physics," *Chinese Physics C* **40** no. 10, (Oct, 2016) 100001. https://doi.org/10.1088%2F1674-1137%2F40%2F10%2F100001.

[103] ATLAS, CDF, CMS, D0 Collaboration, "First combination of Tevatron and LHC measurements of the top-quark mass," arXiv:1403.4427 [hep-ex].

[104] ATLAS and C. Collaboration, "Combined Measurement of the Higgs Boson Mass in pp Collisions at $\sqrt{s} = 7$ and 8 TeV with the ATLAS and CMS Experiments," *Phys. Rev. Lett.* **114** (2015) 191803, arXiv:1503.07589 [hep-ex].

[105] ATLAS Collaboration, "Measurement of $W^{\pm}W^{\pm}$ vector-boson scattering and limits on anomalous quartic gauge couplings with the ATLAS detector," *Phys. Rev. D* **96** (2017) 012007, arXiv:1611.02428 [hep-ex].

[106] D. A. Dicus and V. S. Mathur, "Upper bounds on the values of masses in unified gauge theories," *Phys. Rev. D* **7** (May, 1973) 3111–3114. https://link.aps.org/doi/10.1103/PhysRevD.7.3111.

[107] S. Brass, C. Fleper, W. Kilian, J. Reuter, and M. Sekulla, "Transversal Modes and Higgs Bosons in Electroweak Vector-Boson Scattering at the LHC," *Eur. Phys. J.* **C78** no. 11, (2018) 931, arXiv:1807.02512 [hep-ph].

[108] V. D. Barger, K.-m. Cheung, T. Han, and R. J. N. Phillips, "Strong W^+W^+ scattering signals at pp supercolliders," *Phys. Rev.* **D42** (1990) 3052–3077.

[109] S. D. Rindani, "Strong gauge boson scattering at the LHC," in *Physics at the Large Hadron Collider*, A. Datta, B. Mukhopadhyaya, A. Raychaudhuri, A. K. Gupta, C. L. Khetrapal, T. Padmanabhan, and M. Vijayan, eds., pp. 145–155. 2009. arXiv:0910.5068 [hep-ph].

[110] U. Schnoor, "Vector Boson Scattering and Electroweak Production of Two Like-Charge W Bosons and Two Jets at the Current and Future ATLAS Detector," Nov, 2014. https://cds.cern.ch/record/2000941. Presented 30 Jan 2015.

[111] O. J. P. Éboli and M. C. Gonzalez–Garcia, "Classifying the bosonic quartic couplings," *Phys. Rev.* **D93** no. 9, (2016) 093013, arXiv:1604.03555 [hep-ph].

[112] O. J. P. Eboli, M. C. Gonzalez-Garcia, S. M. Lietti, and S. F. Novaes, "Anomalous quartic gauge boson couplings at hadron colliders," *Phys. Rev.* **D63** (2001) 075008, arXiv:hep-ph/0009262 [hep-ph].

[113] ATLAS Collaboration, "Search for the electroweak diboson production in

association with a high-mass dijet system in semileptonic final states in pp collisions at $\sqrt{s} = 13$ TeV with the ATLAS detector," arXiv:1905.07714 [hep-ex].

[114] A. Hocker *et al.*, "TMVA - Toolkit for Multivariate Data Analysis," arXiv:physics/0703039 [physics.data-an].

[115] B. Stelzer, "The new small wheel upgrade project of the atlas experiment," *Nuclear and Particle Physics Proceedings* **273-275** (2016) 1160 – 1165. http://www.sciencedirect.com/science/article/pii/S2405601415006719. 37th International Conference on High Energy Physics (ICHEP).

[116] M. Shochet, L. Tompkins, V. Cavaliere, P. Giannetti, A. Annovi, and G. Volpi, "Fast TracKer (FTK) Technical Design Report," Tech. Rep. CERN-LHCC-2013-007. ATLAS-TDR-021, Jun, 2013. https://cds.cern.ch/record/1552953.

[117] CERN, "project-schedule." https://project-hl-lhc-industry.web.cern.ch/content/project-schedule.

[118] ATLAS and CMS Collaborations, "Report on the Physics at the HL-LHC and Perspectives for the HE-LHC," in *HL/HE-LHC Physics Workshop: final jamboree Geneva, CERN, March 1, 2019*. 2019. arXiv:1902.10229 [hep-ex].

[119] L. Diamante, "Key plans for the next two years of the lhc." https://home.cern/news/news/accelerators/key-plans-next-two-years-lhc.

[120] R. Schwienhorst, "The Phase-1 upgrade of the ATLAS first level calorimeter trigger," *JINST* **11** no. 01, (2016) C01018.

[121] M. C. Aleksa, W. P. Cleland, Y. T. Enari, M. V. Fincke-Keeler, L. C. Hervas, F. B. Lanni, S. O. Majewski, C. V. Marino, and I. L. Wingerter-Seez, "ATLAS Liquid Argon Calorimeter Phase-I Upgrade Technical Design Report," Tech. Rep. CERN-LHCC-2013-017. ATLAS-TDR-022, Sep, 2013. http://cds.cern.ch/record/1602230. Final version presented to December 2013 LHCC.

[122] ATLAS Collaboration, "Performance of the ATLAS Trigger System in 2015," *Eur. Phys. J.* **C77** no. 5, (2017) 317, arXiv:1611.09661 [hep-ex].

[123] J. Jongmanns and M. Wessels, "Performance of the upgraded PreProcessor of

the ATLAS Level-1 Calorimeter Trigger," Tech. Rep. ATL-COM-DAQ-2019-035, CERN, Geneva, Feb, 2019. https://cds.cern.ch/record/2661780.

[124] T. Toifl, P. Moreira, A. Marchioro, and R. Vari, "4-channel rad hard delay generation ASIC with 1ns timing resolution for LHC," *IEEE Trans. Nucl. Sci.* **46** (1999) 139–143.

[125] ATLAS collaboration, "Technical Design Report for the Phase-I Upgrade of the ATLAS TDAQ System,". http://cds.cern.ch/record/1602235. Final version presented to December 2013 LHCC.

[126] S. Tang, M. Begel, H. Chen, K. Chen, F. Lanni, H. Takai, and W. Wu, "The development of Global Feature eXtractor (gFEX) - the ATLAS calorimeter Level 1 trigger for ATLAS at High Luminosity LHC," Tech. Rep. ATL-DAQ-PROC-2017-035, CERN, Geneva, Oct, 2017. https://cds.cern.ch/record/2289434.

[127] G. A. Stewart, W. B. Breaden-Madden, H. J. Maddocks, T. Harenberg, M. Sandhoff, and B. Sarrazin, "ATLAS Job Transforms: A Data Driven Workflow Engine," *J. Phys. Conf. Ser.* **513** (2014) 032094.

[128] P. Mato and E. Smith, "User-friendly parallelization of GAUDI applications with python," *J. Phys. Conf. Ser.* **219** (2010) 042015.

[129] R. Schaffer and S. C. M. Bentvelsen, "Definition of Offline Readout Identifiers for the ATLAS detector," Tech. Rep. ATL-SOFT-2001-004, CERN, Geneva, Feb, 2001. http://cds.cern.ch/record/684167.

[130] C. Arnault and A. Schaffer, "Use of a generic identification scheme connecting events and detector description in the ATLAS experiment," *eConf* **C0303241** (2003) THJT008, arXiv:physics/0306141 [physics].

[131] P. Calafiura, C. G. Leggett, D. R. Quarrie, H. Ma, and S. Rajagopalan, "The StoreGate: A Data model for the Atlas software architecture," *eConf* **C0303241** (2003) MOJT008, arXiv:cs/0306089 [cs-se].

[132] A. Buckley, T. Eifert, M. Elsing, D. Gillberg, K. Koeneke, A. Krasznahorkay, E. Moyse, M. Nowak, S. Snyder, and P. van Gemmeren, "Implementation of the ATLAS Run 2 event data model," *J. Phys. Conf. Ser.* **664** no. 7, (2015) 072045.

[133] A. Buckley, "The hepthesis LaTeX class.".

List of figures

List of tables